



**HAL**  
open science

# Geometrical frustration and quantum origin of spin dynamics

Alexandre Bertin

► **To cite this version:**

Alexandre Bertin. Geometrical frustration and quantum origin of spin dynamics. Other [cond-mat.other]. Université Grenoble Alpes, 2015. English. NNT : 2015GREAY014 . tel-01172689

**HAL Id: tel-01172689**

**<https://theses.hal.science/tel-01172689>**

Submitted on 7 Jul 2015

**HAL** is a multi-disciplinary open access archive for the deposit and dissemination of scientific research documents, whether they are published or not. The documents may come from teaching and research institutions in France or abroad, or from public or private research centers.

L'archive ouverte pluridisciplinaire **HAL**, est destinée au dépôt et à la diffusion de documents scientifiques de niveau recherche, publiés ou non, émanant des établissements d'enseignement et de recherche français ou étrangers, des laboratoires publics ou privés.

## THÈSE

Pour obtenir le grade de

### DOCTEUR DE L'UNIVERSITÉ DE GRENOBLE

Spécialité : **Physique de la matière condensée et du rayonnement**

Arrêté ministériel : 7 août 2006

Présentée par

**Alexandre BERTIN**

Thèse dirigée par **Pierre Dalmas de Réotier**  
et codirigée par **Björn Fåk**

préparée au sein du **Service de Physique Statistique, Magnétisme et Supraconductivité (CEA-Grenoble/INAC/SPSMS)**  
et de l' **Ecole Doctorale de Physique, Grenoble**

## Geometrical frustration and quantum origin of spin dynamics

Thèse soutenue publiquement le **Judi 21 Mai 2015**,  
devant le jury composé de :

**M. Olivier ISNARD**

Professeur à l'Université Joseph Fourier, Président

**M. Hans-Henning KLAUSS**

Professeur à l'Université technique de Dresde, Rapporteur

**M. Andrew WILDES**

Chercheur à l'Institut Laue-Langevin, Rapporteur

**M. Fabrice BERT**

Professeur à l'Université Paris XI, Examineur

**M. Pierre DALMAS DE REOTIER**

Chercheur au CEA-Grenoble, Directeur de thèse

**M. Björn FÅK**

Chercheur à l'Institut Laue-Langevin, Co-Encadrant de thèse





# Remerciements

Enfin la page de remerciements, la page la plus simple à écrire (et la plus lue par certains d'entre vous, le français s'arrête à la fin de cette page!!) marquant la fin de la rédaction!!

En tout premier lieu, je remercie très chaleureusement mon directeur de thèse **Pierre Dalmas de Réotier** pour toute ton aide si précieuse tant dans le domaine de la physique que de l'informatique, toute ce que tu as pu m'apprendre au cours de ces quatre années, mais surtout pour ta patience, ta gentillesse et ton implication quotidienne. Bien évidemment, je remercie également très sincèrement mon encadrant **Björn Fåk** pour ta disponibilité, ton omniscience du neutron et ta sympathie (et pour les bureaux à l'ILL!!). Un immense merci à vous deux pour m'avoir permis d'en arriver jusque là!!

Je remercie tout particulièrement les membres du jury qui m'ont fait l'honneur d'évaluer ma thèse. Je commencerai bien sûr par **Olivier Isnard** qui a accepté de présider le jury, mais surtout mon premier maître de stage à l'Institut Néel au cours duquel j'ai pu découvrir le monde de la recherche, et qui m'a donné le goût de poursuivre dans cette voie. Un grand merci à mes deux rapporteurs, **Hans-Henning Klauss** et **Andrew Wildes**, qui ont eu la tâche d'évaluer le manuscrit. Enfin, je remercie vivement **Fabrice Bert** pour son oeil critique en tant qu'examinateur.

Je remercie **Jean-Pascal Brison** de m'avoir accepté au sein du service de physique statistique, magnétisme, et supraconductivité (SPSMS), ainsi que toutes les personnes que j'ai pu y côtoyer, en commençant bien évidemment par **Alain Yaouanc**. Merci pour ton implication, pour tout ce que tu as pu m'apprendre sur le muon et le magnétisme, mais surtout pour m'avoir poussé durant toutes ces années! Un immense merci également à **Christophe Marin** pour sa gentillesse, pour les échantillons (merci également à Anne Forget du CEA-Saclay), mais également pour m'avoir accompagné régulièrement durant les manips d'aimantation et de DRX. Un très chaleureux merci à **Marielle Perrier**, pour entre autre s'être occupé de toute sorte de problèmes administratifs, mais surtout pour les moments très sympathiques au C5. Je remercie également **Stéphanie Pouget** pour les manips DRX, **Jean-Francois Jacquot** pour les mesures d'aimantation, sans oublier **Frédéric Bourdarot** pour ses nombreux conseils, scientifiques ou non. Enfin je remercie les "jeunes", postdocs ou thésards, que j'ai pu rencontrer au SPSMS, en particulier le néo-papa Ahmad SULTAN (Félicitations!!!) — Merci pour ton soutien et tes nombreux conseils! — mais aussi Driss, Caro, Nico, Justin, Alex, Benoit, Vladimir, Mounir...

Un certain nombre d'expériences ont été réalisées aux seins des grands instruments. Je remercie donc tout les contacts locaux qui m'ont accueilli et accompagné, tout d'abord à l'Institut Laue-Langevin, **Peter Fouquet** (IN11), **Bernhard Frick** (IN16), **Clemens Ritter** (D1B); à l'Institut Paul Scherrer, **Chris Baines** (LTF), **Alex Am-**

ato (GPS), et **Denis Scheptyakov** (HRPT); et enfin à ISIS, **Peter Baker** (MuSR), **Jon Taylor** et **Ross Stewart** (MARI).

Un clin d'oeil bien évidemment aux collègues que j'ai rencontré à AITAP et qui ont rendu cette aventure très agréable. Je pense tout particulièrement, (et dans le désordre), à Heimanu, Raph, Seb B et Seb G, Larissa, Emilie, Kevin, Jacques, Pierre, Matteo, Guillaume, Emanuella, Lucia, Thomas, Clément, Benoit, Marion...et tous ceux que j'oublie (désolé).

Un IMMENSE merci à mon plus fidèle dude, Pimousse, présent depuis le début de l'ère grenobloise, mes aussi les anciens avec qui tout a commencé: Simon l'homme-wagon, JS et JuJu, Bilou, Dark Polo, el Presidente...et de manière général l'équipe des Tadors. A très bientôt! Un très gros bisous à ZZ et Céline — a este momento de escritorio, nos vemos pronto en Quito tios!! Les remerciements se doivent d'indiquer tout particulièrement les personnes sans qui cette thèse n'aurait pas vu le jour, mes pensées se tournent alors naturellement vers mes deux colocs Clem' et Ju: merci les gars d'avoir été là dans les moments difficiles (mais surtout dans les bons!!). Un grand merci à toute cette petite clique formidable: Dim, Mathieu, Jerem', Carole, Benou, Julie... Un clin d'oeil également à mes vieux lozériens Domi et Francois: on se reverra plus souvent maintenant que la thèse est finie! Bref un grand merci à tous!!!

Enfin je terminerai par ceux qui me sont le plus cher, qui m'ont toujours soutenu — et supporté! —, et sur qui j'ai toujours trouvé soutien et réconfort: mes parents et la petite fratrie (pas ordre d'âge décroissant, pas de jaloux!!): Fred, Charles, Camille et le petit Raphou pour qui il faudra attendre quelques années avant de feuilleter ces pages. Merci mille fois!! Une pensée particulière pour toi papa qui t'es toujours acharné à me remettre sur pied quand le globule se faisait la malle.

En bref, merci à tous!!

# Contents

<b>Glossary</b>	<b>6</b>
<b>1 Introduction</b>	<b>15</b>
1.1 Geometrical frustration . . . . .	15
1.2 The pyrochlore compounds . . . . .	17
1.3 The classical spin-ice . . . . .	20
1.3.1 The water ice model . . . . .	20
1.3.2 The dipolar spin-ice model (DSM) . . . . .	21
1.3.3 Magnetic monopoles . . . . .	24
1.3.4 Experimental evidence for magnetic monopoles . . . . .	26
1.4 The quantum spin-ice . . . . .	27
1.4.1 Beyond the classical spin ice . . . . .	27
1.4.2 The exchange Hamiltonian . . . . .	29
1.5 A large variety of magnetic ground state . . . . .	31
1.5.1 $\text{Tb}_2\text{Ti}_2\text{O}_7$ vs $\text{Tb}_2\text{Sn}_2\text{O}_7$ . . . . .	31
1.5.2 $\text{Yb}_2\text{Ti}_2\text{O}_7$ vs $\text{Yb}_2\text{Sn}_2\text{O}_7$ . . . . .	32
1.5.3 $\text{Er}_2\text{Ti}_2\text{O}_7$ vs $\text{Er}_2\text{Sn}_2\text{O}_7$ . . . . .	35
1.5.4 $\text{Gd}_2\text{Ti}_2\text{O}_7$ vs $\text{Gd}_2\text{Sn}_2\text{O}_7$ . . . . .	36
1.6 Content of the manuscript . . . . .	38
<b>2 Experimental techniques</b>	<b>40</b>
2.1 Bulk measurements . . . . .	41
2.1.1 Specific heat . . . . .	41
2.1.2 Magnetometry . . . . .	43
2.2 Facilities for microscopic probe measurements . . . . .	45
2.2.1 Institut Laue Langevin (ILL), a continuous neutron source . . . . .	45
2.2.2 ISIS, a muon and neutron pulsed source . . . . .	46
2.2.3 A neutron and muon pseudo-continuous source at PSI . . . . .	46
2.2.4 A third generation synchrotron at PSI . . . . .	46
2.3 Diffraction experiments . . . . .	47
2.3.1 Introduction to diffraction . . . . .	47
2.3.2 Nuclear or charge scattering . . . . .	47
2.3.3 Magnetic scattering . . . . .	49
2.3.4 Powder diffractometers . . . . .	50
2.3.5 X-ray experiments . . . . .	50
2.3.6 Neutron experiments . . . . .	51
2.3.7 The Rietveld refinement . . . . .	52

2.4	Neutron time-of-flight spectroscopy . . . . .	54
2.4.1	The MARI spectrometer . . . . .	54
2.4.2	Energy resolution . . . . .	55
2.5	Neutron backscattering spectroscopy . . . . .	56
2.5.1	The IN16 spectrometer . . . . .	56
2.5.2	The backscattering process . . . . .	57
2.5.3	Spectroscopy . . . . .	59
2.6	Muon spectroscopy . . . . .	59
2.6.1	Introduction . . . . .	60
2.6.2	Experimental details . . . . .	60
2.6.3	Pseudo-continuous versus pulsed source . . . . .	61
2.6.4	Muon spectrometers . . . . .	62
2.6.5	Polarisation functions . . . . .	63
2.6.6	Muon Knight shift measurements . . . . .	65
<b>3</b>	<b>CEF study of the pyrochlore series <math>R_2M_2O_7</math></b>	<b>68</b>
3.1	Introduction . . . . .	69
3.1.1	Rare earth properties . . . . .	69
3.1.2	The Stevens Hamiltonian . . . . .	71
3.1.3	Neutron cross section . . . . .	74
3.2	CEF of the titanate series $R_2Ti_2O_7$ . . . . .	75
3.2.1	Published CEF parameters . . . . .	75
3.2.2	Proposal of a single CEF solution . . . . .	75
3.2.3	Analysis of $Tb_2Ti_2O_7$ . . . . .	79
3.2.4	Analysis of $Er_2Ti_2O_7$ . . . . .	81
3.2.5	Analysis of $Ho_2Ti_2O_7$ . . . . .	83
3.2.6	Conclusions . . . . .	86
3.3	CEF of the stannate series $R_2Sn_2O_7$ . . . . .	88
3.3.1	Published CEF parameters . . . . .	88
3.3.2	Analysis of $Ho_2Sn_2O_7$ . . . . .	90
3.3.3	Analysis of $Tb_2Sn_2O_7$ . . . . .	94
3.3.4	Analysis of $Er_2Sn_2O_7$ . . . . .	95
3.3.5	Conclusions . . . . .	98
<b>4</b>	<b>Experimental study of <math>Nd_2Sn_2O_7</math></b>	<b>100</b>
4.1	Introduction . . . . .	101
4.2	Powder synthesis . . . . .	101
4.3	Crystal structure analysis . . . . .	102
4.4	Neutron time-of-flight spectroscopy . . . . .	103
4.5	Bulk measurements . . . . .	104
4.5.1	Specific heat . . . . .	104
4.5.2	Magnetisation . . . . .	107
4.6	Determination of the magnetic structure . . . . .	110
4.7	Neutron backscattering measurements . . . . .	114
4.7.1	Spin Hamiltonian for $^{143}Nd$ . . . . .	114
4.7.2	Incoherent scattering cross-section . . . . .	115
4.7.3	Magnetic scattering cross-section . . . . .	116

4.7.4	Data analysis . . . . .	117
4.8	$\mu$ SR spectroscopy . . . . .	120
4.8.1	Evidence of long-range order . . . . .	121
4.8.2	Persistence of spin dynamics . . . . .	125
4.8.3	$\lambda_Z$ behaviour in the paramagnetic phase . . . . .	127
4.8.4	Anomalously slow paramagnetic fluctuations . . . . .	130
4.9	Conclusions . . . . .	132
<b>5</b>	<b>Insights into <math>\text{Tb}_2\text{Ti}_2\text{O}_7</math></b>	<b>133</b>
5.1	Introduction . . . . .	133
5.2	$\text{Tb}_2\text{Ti}_2\text{O}_7$ : a Jahn-Teller transition? . . . . .	136
5.2.1	Context . . . . .	136
5.2.2	X-ray synchrotron radiation measurements . . . . .	139
5.3	$\text{Tb}_2\text{Ti}_2\text{O}_7$ : a quantum spin-ice realisation? . . . . .	140
5.3.1	The exchange Hamiltonian . . . . .	140
5.3.2	Prediction of a magnetisation plateau . . . . .	145
5.3.3	$\mu$ SR frequency shift measurements . . . . .	148
5.4	Conclusions . . . . .	152
<b>6</b>	<b>General conclusions</b>	<b>154</b>
6.1	Beyond the Stevens Hamiltonian . . . . .	154
6.2	Observation of spontaneous oscillations . . . . .	156
6.3	Origin of spin dynamics . . . . .	157
6.4	A magneto-elastic mode: solving the $\text{Tb}_2\text{Ti}_2\text{O}_7$ case . . . . .	159
6.5	New perspectives: the spinel compounds . . . . .	159
<b>A</b>	<b>Crystallography of the pyrochlore compounds</b>	<b>161</b>
<b>B</b>	<b>The point charge model</b>	<b>164</b>
<b>C</b>	<b>Neutron absorption correction</b>	<b>168</b>
C.1	Rectangular geometry . . . . .	168
C.2	Annular geometry . . . . .	168
<b>D</b>	<b>Complements to magnetic diffraction</b>	<b>171</b>
D.1	Elements of group theory . . . . .	171
D.2	BasIREPS vs SARAh . . . . .	173
D.3	Analytical evidence for IR $\Gamma_3$ selection in $\text{Nd}_2\text{Sn}_2\text{O}_7$ . . . . .	173
<b>E</b>	<b>Complements to <math>\mu</math>SR</b>	<b>176</b>
E.1	Derivation of the spin lattice relaxation rate . . . . .	176
E.2	Relaxation by excitations . . . . .	178
E.2.1	Ferromagnetic magnons . . . . .	178
E.2.2	Antiferromagnetic magnons . . . . .	182
	<b>List of publications</b>	<b>185</b>
	<b>Bibliography</b>	<b>186</b>

# Glossary

Symbol	Definition
$a_i^\dagger, a_i$	Boson creation and annihilation operators at rare earth site $i$
$a_{as}(\varepsilon)$	Asymmetry parameter varying with the kinetic energy $\varepsilon$
$a_{bg}$	Time-independent background term
$a_d$	Distance between the center of two neighbouring tetrahedra
$a_{lat}$	Lattice parameter
$a_{mag}(\mathbf{q})$	Amplitude of the magnetic interaction
$a_0$	Initial muon asymmetry or Bohr radius, depending on the context
$A_{\mathbf{h}}(\equiv A)$	Absorption factor
$A_{inc}$	Weighing factor for incoherent nuclear intensity
$A_{mag}$	Weighing factor quasielastic magnetic intensity
$A_n^m(\equiv A_n^m(R))$	CEF parameters of rare earth $R$
$\mathcal{A}_{hyp}^{143}$	Hyperfine constant of isotope $^{143}\text{Nd}$
$b_{g,i}$	Background intensity at the experimental point $i$
$b_j$	Fermi length of atom $j$
$\mathbf{B}_{dem}$	Demagnetising field
$\mathbf{B}_{dip}$	Dipolar magnetic field
$\mathbf{B}'_{dip}$	Dipolar magnetic field arising from magnetic moments inside the Lorentz sphere
$\mathbf{B}_{hyp}$	Hyperfine magnetic field
$\mathbf{B}_{int}$	Internal field
$B_j$	Parameter describing the amplitude of the isotropic displacement around the atomic mean position, and involved in the Debye-Waller factor
$B_J(x)$	Brillouin function
$\mathbf{B}_{loc}$	Local magnetic field
$\mathbf{B}_{Lor}$	Lorentz magnetic field
$B_{max}$	Maximum amplitude of the local field $B_{loc}$
$B_n^m$	CEF parameters: $B_n^m = A_n^m \langle r^n \rangle \Theta_n$
$c_a, c_x$	Heat capacity of the platform and of the sample, respectively
$c_p$	Heat capacity at constant pressure
$C$	Constant
$C_{el}$	Electronic specific heat
$C_{ex}$	Specific heat of magnon-like excitations
$C_{nuc}$	Nuclear specific heat

Symbol	Definition
$C_p$	Specific heat at constant pressure
$C_{\text{ph}}$	Lattice contribution to the specific heat
$C_{\text{sh}}$	Constant
$C_v$	Specific heat at constant volume
$C^{\alpha,\beta}(\mathbf{q})$	Analytical function of $\mathbf{q}$
$d$	Dimension of a system/matrix/representation
$d_{\text{hkl}}(\equiv d)$	Interplanar spacing
$\mathbf{d}_{\text{pair}}$	Vector joining a magnetic ion to one of its nearest neighbours
$d_1, d_2$	Interlaced sublattices describing a Heisenberg collinear antiferromagnet
$d_\nu^{(\mu)}(g_i)$	Matrix representation of the symmetry element $g_i$ in the representation $\Gamma_\nu^{(\mu)}$
$\hat{d}_\nu^{(\mu)}(g_i)$	Matrix representation of the symmetry element $g_i$ in the representation $\hat{\Gamma}_\nu^{(\mu)}$
$D$	Dipolar energy scale
$D_c(B_{\text{loc}})$	Field distribution
$D_{\text{diff}}$	Diffusion coefficient
$\mathbf{D}_{\text{DM}}$	Dzyaloshinskii-Moriya vector
$D_{\text{nn}}$	Dipolar energy scale between two nearest neighbours
$D_{\mathbf{r}_i}^{\alpha\beta}$	Components of the field dipole tensor associated with site $\mathbf{r}_i$
$\mathcal{D}$	Constant
$\mathcal{D}_t$	Scale of the distortion
$e^+$	Positron
$E_{\text{ex}}$	Excitation energy
$E_f$	Neutron final energy
$E_i$	Neutron incident energy or CEF energy levels, depending on the context
$E_m$	Nuclear energy levels
$E_{\text{max}}$	Maximal energy of a magnon excitation
$f$	Frustration index or filling factor, depending on the context
$f_j(q)$	Atomic form factor (Fourier transform of the electronic density)
$f_{\text{mag}}(\mathbf{q})$	Magnetic form factor
$F(x)$	Function describing a CEF transition and taken as the convolution of a Gaussian and a Lorentzian function
$\mathbf{F}_{\text{mag}}(\mathbf{q})$	Magnetic structure factor
$F_n(\mathbf{q})$	Neutron structure factor
$F'_n(\mathbf{q})$	Unit-cell structure factor
$F_p(\mathbf{q})$	X-ray structure factor
$g$	Spectroscopic splitting factor or order of $G_k$ , depending on the context
$g(\omega)$	Density of states
$g_{\text{eff}}$	Effective spectroscopic factor
$g_i$	Symmetry operation
$g_J$	Landé factor

Symbol	Definition
$g_m(E)$	Magnetic density of states
$g_{\parallel}$	Longitudinal spectroscopic factor
$g_{\perp}$	Transverse spectroscopic factor
$G(x)$	Gaussian function
$G_k$	Little group: subgroup of the space group leaving the magnetic propagation wavevector invariant
$G_{\mathbf{r}_i}^{\alpha\beta}$	Components of the tensor $\mathbf{G}$ representing the coupling between the muon spin and the spins of the system
$\mathbf{h}$	Label of the Bragg peaks positions at the angle $\theta_{\mathbf{h}}$ , or translational part of a symmetry operator, depending on the context
$\hbar$	Reduced Planck constant (or Dirac constant)
$\mathbf{H}_{\text{applied}}$	Real applied magnetic field at the sample
$H_c$	Critical magnetic field inducing a phase transition
$\mathbf{H}_{\text{ext}}$	External magnetic field
$H_G$	Full width at half maximum of the Gaussian function
$H_L$	Full width at half maximum of the Lorentzian function
$\mathcal{H}_{\text{AF}}$	Heisenberg collinear antiferromagnetic Hamiltonian
$\mathcal{H}_{\text{CEF}}$	CEF Hamiltonian
$\mathcal{H}_{\text{CEF}}^{(J)}$	CEF Hamiltonian acting on the multiplet defined by a total angular momentum $J$
$\mathcal{H}_{\text{CEF}}^{(J),\text{mix}}$	CEF Hamiltonian acting on the multiplet defined by a total angular momentum $J$ taking into account the $J$ -mixing effect arising from the coupling with other multiplets
$\mathcal{H}_{\text{CSI}}$	Classical spin-ice Hamiltonian (longitudinal exchange Hamiltonian)
$\mathcal{H}_{\text{DB}}$	Dipolar spin-ice Hamiltonian in terms of the dumbbell model notation
$\mathcal{H}_{\text{DSM}}$	Dipolar spin-ice Hamiltonian
$\mathcal{H}_{\text{ex}}$	Anisotropic exchange Hamiltonian
$\mathcal{H}_{\text{FM}}$	Hamiltonian for a ferromagnetic system
$\mathcal{H}_{\text{per}}$	Perturbative Hamiltonian
$\mathcal{H}_Q$	Quadrupolar Hamiltonian
$\mathcal{H}_{\text{QSI}}$	Quantum spin-ice Hamiltonian (XXZ model)
$\mathcal{H}_{\text{XYZ}}$	Anisotropic exchange Hamiltonian of the XYZ model
$\mathcal{H}_Z$	Zeeman Hamiltonian
$\mathcal{H}_{\perp}$	Transverse exchange Hamiltonian (XXZ model)
$\mathbf{I}$	Nuclear spin vector operator
$I_{\text{bg}}$	Background contribution
$I_c$	Critical current in a Josephson junction
$I_{\mathbf{h}}$	Intensity at the Bragg position $\mathbf{h}$
$\mathcal{I}$	Isotropic exchange coupling constant
$\mathcal{I}_{\text{eff}}$	Effective nearest-neighbour isotropic exchange coupling constant
$\mathcal{I}_{\text{nn}}(\equiv J_{\text{nn}})$	Nearest-neighbour isotropic exchange coupling constant

Symbol	Definition
$I_0$	Scaling factor
$\{\mathcal{I}_1, \dots, \mathcal{I}_4\}$	Anisotropic exchange constants involved in $\mathcal{H}_{\text{ex}}$ Notations $\{\mathcal{I}_{zz}, \mathcal{I}_{\pm}, \mathcal{I}_{\pm\pm}, \mathcal{I}_{z\pm}\}$ are also used
$\mathcal{I}_{\perp}$	Transverse exchange coupling constant
$\mathbf{J}_i$	Total angular momentum vector operator of rare earth at site $i$
$J_1(x)$	Bessel function of the first kind
$\mathbf{J}_{\pm}$	Raising and lowering spin operators
$\{\tilde{J}_x, \tilde{J}_y, \tilde{J}_z\}$	Exchange constants involved in $\mathcal{H}_{\text{XYZ}}$
$\{\mathcal{J}_1, \dots, \mathcal{J}_4\}$	Anisotropic exchange constants involved in the effective spin-1/2 exchange Hamiltonian
$\mathbf{k}$	Vector in the reciprocal space
$k_{\text{B}}$	Boltzmann constant
$\mathbf{k}_i, \mathbf{k}_f$	Incident and final wavevectors, respectively
$\mathbf{k}_{\text{mag}}$	Magnetic propagation wavevector
$K$	Dissociation constant for the nucleation of magnetic monopoles
$K_{\text{exp}}$	Normalised muon frequency shift
$K'_{\text{dip}}$	Muon Knight shift that arises only from the dipolar field created by the magnetic moments inside the Lorentz sphere
$K_0$	Complex conjugation operator
$K_1, K_2$	Thermal conductance between the cryostat and the platform, and between the platform and the sample, respectively
$K_{\mu}$	Muon Knight shift
$L$	Neutron flight path
$L(x)$	Lorentzian function
$\mathbf{L}_i$	Total orbital momentum vector operator of rare earth at site $i$
$L_{p,\mathbf{h}}$	Lorentz factor
$m_e$	Electron mass
$m_n$	Neutron mass
$m_{\text{pm}}$	Paramagnetic moment
$m_{\text{sat}}$	Saturation value of the magnetic moment
$m_{\text{sp}}$	Spontaneous magnetic moment
$m_{111}$	Projection of the spontaneous magnetic moment over the [111] axis
$m_{\mu}$	Muon mass
$\mathbf{M}$	Bulk magnetisation
$\mathbf{M}_d$	Divergence-free part of the Helmholtz decomposition
$M_{\mathbf{h}}$	Multiplicity of the reflection $\mathbf{h}$
$\mathbf{M}_{\text{Lor}}$	Magnetisation inside the Lorentz sphere
$\mathbf{M}_m$	Curl-free part of the Helmholtz decomposition
$\mathbf{M}_{\perp}(\mathbf{q})$	Projection of the Fourier transform of the total magnetisation density on a plane perpendicular to $\mathbf{q}$
$n$	Order of the operators or number of free parameters, depending on the context
$n(x)$	Distribution function

Symbol	Definition
$n(4f)$	Number of $4f$ electrons
$n_b$	Number of bound magnetic monopoles
$n_{BE}(x)$	Bose-Einstein distribution function
$n_{FD}(x)$	Fermi-Dirac distribution function
$n_P(x)$	Planck distribution
$n_u$	Number of dissociated magnetic monopoles
$n_0$	$n_0 = n_b + n_u$
$N$	Number of magnetic ions in the system
$N(t)$	Positron counts in a detector
$\mathbf{N}$	Demagnetising field tensor
$N_c$	Number of unit cells in the system
$N_{Cu}$	Number of Cu nuclei in the sample holder
$N_f$	Number of formula unit in the unit cell
$N_L$	Number of magnetic moments inside the Lorentz sphere
$N_{mag}$	Number of magnetic cells
$N_{Nd}$	Total number of $^{143}\text{Nd}$ nuclei in the sample
$N_p$	Number of experimental points
$N_0$	Scale of the positron count
$N_{\pm}$	Positron counts in the forward (+)/backward (-) detectors
$N^{ZZ}$	Longitudinal component of the diagonal tensor $\mathbf{N}$
$\mathcal{N}_A$	Avogadro number
$O_n^m$	Stevens operators
$p$	Magnetic scattering length for a magnetic moment of $1 \mu_B$ at $q = 0$
$p$	Pressure or proton, depending on the context
$p_i$	Relative abundance of isotope $i$
$p_n^m$	Prefactor
$P$	Thermal power
$P(\theta)$	Polarisation factor
$P_n(x)$	Legendre polynomials
$P_n^m(x)$	Associated Legendre polynomials
$P_X(t), P_Y(t)$	Transverse muon polarisation functions
$P_X^{\text{exp}}(t)$	Experimentally measured transverse muon polarisation function
$P_Z(t)$	Longitudinal muon polarisation function
$P_Z^{\text{exp}}(t)$	Experimentally measured longitudinal muon polarisation function
$P_Z^{\text{stat}}(t)$	Static longitudinal muon polarisation function
$\mathbf{q}$	Scattering vector
$q_{BZ}$	Radius of the first Brillouin zone considered as a sphere
$q_i$	Electric charge
$q_m$	Magnetic charge arising from the fragmentation of the magnetic moment
$Q$	Quadrupolar moment
$Q_{\text{ex}}$	Quadrupole moment of the excited Mössbauer state

Symbol	Definition
$Q_{\text{gs}}$	Quadrupole moment of the Mössbauer ground state
$Q_{\text{h}}$	Heat input brought to the sample
$Q_{\alpha}(\equiv Q)$	Total magnetic monopole charge in a tetrahedron $\alpha$
$\tilde{Q}_{\text{eff}}$	Effective magnetic charge carried by a magnetic monopole
$r$	Spin anisotropy ratio: $r = g_{\perp}/g_{\parallel}$
$\mathbf{r}_i$	Vector linking the muon to the rare earth site $i$
$\mathbf{r}_{ij}$	Vector linking rare earth sites $i$ and $j$
$r_{\text{nn}}$	distance between nearest neighbours
$\langle r^n \rangle$	Expectation values of the $n$ th power distance between the nucleus of the magnetic ion and the $4f$ electronic shell
$R$	Ideal gas constant or rare earth ion, depending on the context
$R(x)$	Instrumental resolution function
$R_{\text{exp}}, R_p, R_{\text{wp}}$	Profile, weight profile, and expected weight profile factors, respectively
$\mathbf{R}_i$	Distance between an electric charge and the rare earth
$S(\mathbf{q}, \omega)$	Scattering function
$\mathbf{S}'(\equiv \mathbf{S}^{\mu})$	Effective spin-1/2
$S_{\text{el}}$	Electronic entropy
$\mathbf{S}_i$	Total spin vector operator of rare earth at site $i$
$S_{\text{iso}}(\mathbf{q}, \hbar\omega)$	Isotope-incoherent scattering function
$S_{\text{mag}}(\mathbf{q}, \hbar\omega)$	Magnetic scattering function
$S_{\text{spin}}(\mathbf{q}, \hbar\omega)$	Spin-incoherent scattering function
$\mathbf{S}_{\mu}$	Muon spin
$T$	Temperature
$T_{\text{C}}$	Curie temperature
$T_{\text{c}}$	Transition temperature
$T_0, T_a, T_x$	Temperatures of the cryostat, the platform, and the sample, respectively
$\{U, V, W\}$	Half-width free parameters describing the resolution function
$U_{\alpha\beta}$	Anisotropic displacement parameters involved in the Debye-Waller factor
$v_c(\equiv v_0)$	Volume of the unit cell
$v_c^*$	Volume of the first Brillouin zone
$v_{\text{D}}$	Doppler velocity
$v_{\text{ex}}$	Excitation velocity
$v_i, v_f$	Neutron incident and final velocity, respectively
$v_{\text{mag}}$	Volume of the magnetic cell
$v_{\text{Tb}}$	Volume per terbium ion
$V(r_{\alpha\beta})$	Magnetic Coulomb interaction between two magnetic monopoles separated by a distance $r_{\alpha\beta}$
$V_{\text{CEF}}$	CEF potential
$V_{\text{F}}(\mathbf{r})$	Fermi pseudo-potential at the $\mathbf{r}$ real space position
$V_{\text{mag}}$	Potential of magnetic interaction
$V_{\text{p}}(x)$	Pseudo-Voigt function

Symbol	Definition
$V_{zz}$	Principal component of the electric-field gradient tensor
$W(\theta)$	Probability of the positron to be emitted in a direction $\theta$
$x$	Position of oxygen atom O1
$X$	Isotropic strain parameter
$y_{c,i}$	Calculated intensity at the experimental point $i$
$y_{c,0}$	Scaling factor
$y_{o,i}$	Observed intensity at the experimental point $i$
$Y$	Isotropic size parameter
$Y_n^m(x)$	Spherical harmonics
$z$	Quantisation axis [111]
$z_{nn}$	Number of nearest neighbours
$Z_i(\equiv Z)$	Partition function of isotope $i$
$Z(\theta)$	Peak profile function
$Z_n^m(x)$	Tesseral harmonics
$\alpha$	Parameter set involving the $n$ free parameters: $\alpha = (\alpha_1, \dots, \alpha_n)$
$\alpha_c$	Critical exponent involved in the critical behaviour of $C_{el}$
$\alpha_d$	Instrumental balance parameter
$\alpha_m$	$\alpha_m = n_u/n_0$
$\beta_c$	Critical exponent involved in the critical behaviour of $m_{sp}$
$\alpha_D$	Constant
$\beta_{se}$	Exponent of the stretched exponential function
$\delta_i$	Unit vector belonging to a $\langle 111 \rangle$ axis at rare earth site $i$
$\chi$	Bulk magnetic susceptibility
$\chi(\mathbf{q}, \hbar\omega)$	Dynamical susceptibility
$\chi'_{ac}$	Real part of the a.c. magnetic susceptibility
$\chi''(\mathbf{q}, \hbar\omega)$	Imaginary part of the dynamical susceptibility $\equiv \mathcal{I}m\{\chi^{\alpha\beta}(\mathbf{q}, \omega)\}$
$\chi'(q)$	$q$ -dependent static susceptibility
$\delta(x)$	Dirac function
$\delta_{CEF}$	Energy splitting between the low-lying CEF energy levels
$\delta_{i,j}$	Kronecker symbol
$\Delta$	Anisotropic energy gap
$\Delta_a$	Strength of the spin anisotropy
$\Delta_G$	Standard deviation of a Gaussian field distribution
$\Delta_{N,i}$	Energy splitting between nuclear levels of isotope $i$
$\Delta_Q$	Nuclear quadrupole splitting
$\Delta_{so}$	Energy splitting between the CEF ground state and the first CEF excited energy level
$\Delta S_{elec}$	Electronic entropy variation
$\Delta t$	Time scale
$\Delta_X$	Standard deviation of the field distribution
$\eta$	Mixing parameter involved in the pseudo-Voigt function
$\varphi$	Phase shift
$\phi_n$	Neutron flux

Symbol	Definition
$\Phi^{\alpha\beta}(t)$	Symmetrised correlation function of the fluctuating part of the local magnetic field at the muon site
$\Phi_0^\pm$	Ground state wavefunctions
$\gamma_i$	Gyromagnetic ratio of isotope $i$
$\gamma_\mu$	Muon gyromagnetic ratio
$\gamma_\infty$	Sternheimer coefficient
$\Gamma(x)$	Gamma function
$\Gamma_{i,i'}$	Linewidths of the Lorentzian function accounting for the lifetime of the $i'$ CEF energy level during the transition $i \rightarrow i'$
$\Gamma_q$	Quasielastic Lorentzian linewidth
$\Gamma_Z$	Inverse lifetime of the nuclear level
$\Gamma_\nu^{(\mu)} (\equiv \Gamma_\nu)$	Irreducible representation of order $\mu$ and labelled by the index $\nu$
$\hat{\Gamma}_\nu^{(\mu)}$	Loaded irreducible representation
$\kappa_{\alpha_m}$	Magnetic conductivity illustrating the motion of the magnetic monopoles
$\lambda_{so}$	Spin-orbit coupling constant
$\lambda_X$	Transverse (or spin-spin) relaxation rate
$\lambda_Z$	Spin-lattice relaxation rate
$\lambda_Z^{\text{exp}}$	Expected spin-lattice relaxation rate
$\lambda_{Z,0}$	Constant
$\Lambda^{\alpha\beta}(\mathbf{q}, \omega)$	Symmetrised spin correlation function
$\mu$	Magnetic moment or chemical potential, depending on the context
$\mu_0$	Permeability of free space
$\mu_B$	Electronic Bohr magneton
$\mu^{\text{CF}}$	CEF magnetic moment
$\mu_{\parallel}^{\text{CF}}$	CEF magnetic moment along the $z$ axis
$\mu_{\perp}^{\text{CF}}$	CEF magnetic moment perpendicular to the $z$ axis
$\boldsymbol{\mu}_n$	Magnetic moment of the neutron
$\mu_N$	Nuclear Bohr magneton
$\mu^+$	Muon with positive electric charge
$\nu_e$	Neutrino associated to the positron
$\nu_{\text{ext}}$	Muon precession frequency around the external magnetic field $B_{\text{ext}}$
$\nu_{\text{FC}}$	Fermi chopper frequency
$\nu_M$	Relaxation rate of the magnetisation
$\nu_0$	Self energy accounting for the dipolar and exchange energy between nearest neighbours
$\nu_{\alpha_m}$	Relaxation rate for recombination of the nucleated magnetic monopoles
$\nu_\mu$	Muon neutrino or muon precession frequency around the local magnetic field $B_{\text{loc}}$ , depending on the context
$\bar{\nu}_\mu$	Antineutrino associated to the muon

Symbol	Definition
$\omega_\mu$	Muon precession angular frequency
$\Omega$	Solid angle
$\Omega_m$	Number of microstates
$\Psi_i^j (\equiv \Psi_i)$	Basis vectors of the irreducible representations taken at atom $j$ (the index $i$ labels the different basis vectors)
$\Psi^\pm$	CEF wavefunctions of a given doublet state
$\pi^+$	Positive pion
$\sigma$	Neutron spin
$\sigma_{a,i}$	Neutron absorption cross section of atom $i$
$\sigma_i$	Standard deviation of $y_i$
$\sigma_{\text{spin}}^i, \sigma_{\text{iso}}^i$	Spin-incoherent and isotope-incoherent cross sections of atom $i$
$\sigma_2$	Screening coefficient
$\Sigma, \Sigma'$	Incident and final total absorption cross sections, respectively
$\tau$	Reduced temperature: $\tau = \frac{T-T_c}{T_c}$
$\tau_c$	Magnetic correlation time: $\tau_c = 1/\nu_c$
$\tau_0$	Spin fluctuation time: $\tau_0 = 1/\nu_0$
$\tau_1$	Relaxation time of the sample temperature
$\tau_\mu$	Muon lifetime
$\hat{\theta}$	Odd time-reversal symmetry operator
$\theta_{\text{CW}}$	Curie-Weiss temperature
$\theta_{\text{h}}$	Bragg peak angle
$\Theta_{\text{D}}$	Debye temperature
$\Theta_n$	Stevens multiplicative factors
$\xi(x)$	Riemann function
$ i\rangle$	Eigenvectors of $\mathcal{H}_{\text{CEF}}$
$ m\rangle$	Zeeman states ( $-I \leq m \leq I$ , $I$ nuclear spin)
$ m_J\rangle$	Zeeman states ( $-J \leq m_J \leq J$ , $J$ total angular momentum)
$\frac{d\sigma}{d\Omega}$	Differential neutron cross section
$\frac{d\sigma_{\text{coh}}(\mathbf{q})}{d\Omega}$	Differential coherent neutron cross section
$\frac{d\sigma_{\text{inc}}(q)}{d\Omega}$	Differential incoherent neutron cross section
$\frac{d\sigma_{\text{mag}}(\mathbf{q})}{d\Omega}$	Differential magnetic neutron cross section
$\frac{d^2\sigma}{d\Omega dE'}$	Double differential neutron cross section
$\left(\frac{d^2\sigma}{d\Omega dE}\right)_{\text{inc}}$	Double differential incoherent neutron cross section
$\left(\frac{d^2\sigma}{d\Omega dE}\right)_{\text{mag}}$	Double differential magnetic neutron cross section
$\left(\frac{d^2\sigma}{d\Omega dE}\right)_{\text{se}}$	Double differential neutron cross section from the sample environment
$[\mathbf{A}, \mathbf{B}]$	Commutator of operators $\mathbf{A}$ and $\mathbf{B}$ : $[\mathbf{A}, \mathbf{B}] = \mathbf{AB} - \mathbf{BA}$
$\{\mathbf{A}, \mathbf{B}\}$	Symmetrised correlation function of operators $\mathbf{A}$ and $\mathbf{B}$ : $2\{\mathbf{A}, \mathbf{B}\} = \mathbf{AB} + \mathbf{BA}$
$\langle \dots \rangle$	Thermal average

# Chapter 1

## Introduction

### Contents

---

<b>1.1</b>	<b>Geometrical frustration . . . . .</b>	<b>15</b>
<b>1.2</b>	<b>The pyrochlore compounds . . . . .</b>	<b>17</b>
<b>1.3</b>	<b>The classical spin-ice . . . . .</b>	<b>20</b>
1.3.1	The water ice model . . . . .	20
1.3.2	The dipolar spin-ice model (DSM) . . . . .	21
1.3.3	Magnetic monopoles . . . . .	24
1.3.4	Experimental evidence for magnetic monopoles . . . . .	26
<b>1.4</b>	<b>The quantum spin-ice . . . . .</b>	<b>27</b>
1.4.1	Beyond the classical spin ice . . . . .	27
1.4.2	The exchange Hamiltonian . . . . .	29
<b>1.5</b>	<b>A large variety of magnetic ground state . . . . .</b>	<b>31</b>
1.5.1	Tb <sub>2</sub> Ti <sub>2</sub> O <sub>7</sub> vs Tb <sub>2</sub> Sn <sub>2</sub> O <sub>7</sub> . . . . .	31
1.5.2	Yb <sub>2</sub> Ti <sub>2</sub> O <sub>7</sub> vs Yb <sub>2</sub> Sn <sub>2</sub> O <sub>7</sub> . . . . .	32
1.5.3	Er <sub>2</sub> Ti <sub>2</sub> O <sub>7</sub> vs Er <sub>2</sub> Sn <sub>2</sub> O <sub>7</sub> . . . . .	35
1.5.4	Gd <sub>2</sub> Ti <sub>2</sub> O <sub>7</sub> vs Gd <sub>2</sub> Sn <sub>2</sub> O <sub>7</sub> . . . . .	36
<b>1.6</b>	<b>Content of the manuscript . . . . .</b>	<b>38</b>

---

A general introduction on magnetic geometrical frustration and a non exhaustive review of the different exotic magnetic states encountered in the two pyrochlore series  $R_2M_2O_7$  ( $M = \text{Ti, Sn}$ ) of interest in this work are provided in the following. Moreover, a brief description of the content of the manuscript is given at the end of this chapter.

### 1.1 Geometrical frustration

Magnetic compounds usually undergo a transition to establish at low temperatures a long-range magnetic order and stabilise in a well-known magnetic state such as ferromagnetic order where all the spins are parallel, antiferromagnetic order where spins are antiparallel or ferrimagnetism order where magnetic moments of different magnitudes

are antiparallel. For instance, the ferromagnetic order should appear below the Curie temperature  $T_C \approx \theta_{CW}$ , where  $\theta_{CW}$  is the Curie-Weiss temperature characterising the nature and strength of the magnetic interactions.

The notion of frustration in magnetism refers to the inability to simultaneously satisfy all the magnetic interactions. This originates from the competition of several exchange paths between two magnetic ions, i.e. frustration of interactions, or from the topology of the lattice where the spatial arrangement of the magnetic atoms precludes the satisfaction of the magnetic interactions simultaneously. The latter case, of interest here, is called geometrical frustration. An example is given in Fig. 1.1 where Ising spins, i.e. spins allowed to point up or down, with nearest-neighbour antiferromagnetic interactions are located at the corner of a square and a triangle. In the former case, all the antiferromagnetic interactions are satisfied whereas in the triangular case, if one antiferromagnetic interaction is satisfied with two spins antiparallel, the orientation of the third spin is uncertain since it cannot satisfy simultaneously the two antiferromagnetic bonds with its two neighbours.

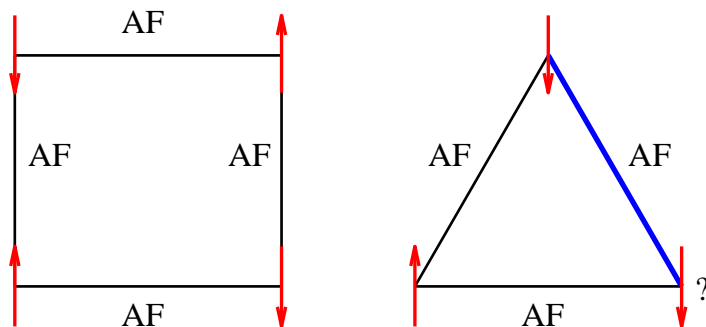


Figure 1.1: *Ising spins are located at the corner of a square lattice (left) where all the antiferromagnetic interactions between the first neighbours can be satisfied and on a triangle (right) where one of the AF bonds displayed by the blue bond is not satisfied.*

Geometrical frustration has focused a lot of attention from an experimental and theoretical point of view in the past decades in front of the richness of the magnetic ground states. This concept leads to unconventional magnetic states, such as complex magnetic structures or prevention of the long-range magnetic order. Frustration usually forbids the establishment of a single state, and the lowest energy spin configuration is realised by minimising the interaction energies in several manners, i.e. the ground states of frustrated compounds are usually highly degenerated. The degree of frustration can be evaluated through the ratio  $f = |\theta_{CW}|/T_c$ , where  $T_c$  denotes the temperature of the transition, if any, to a magnetic order or a glassy state. Among the various lattices leading to frustration, the most popular two-dimensional structures are the triangular and the Kagome lattice, illustrated in the left and right panels of Fig. 1.2, respectively. Wannier [1] firstly introduced this concept noticing that ferromagnetic and antiferromagnetic interactions between Ising spins have very different properties on a triangular lattice: in the latter case, no magnetic transition is predicted down to the lowest temperatures. Three-dimensional geometrically frustrated lattices are displayed

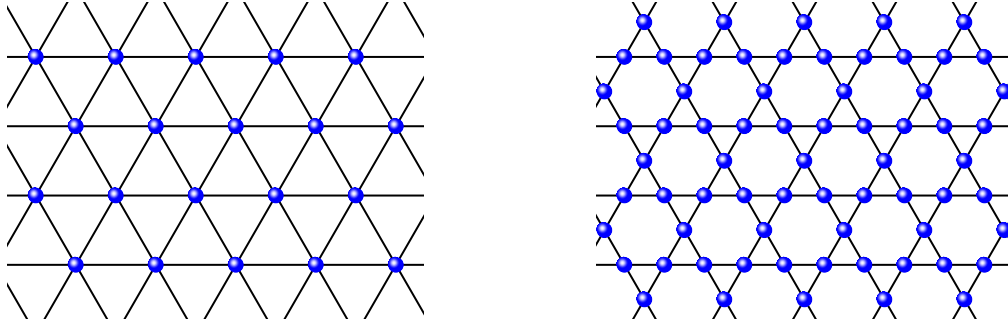


Figure 1.2: Two dimensional geometrically frustrated systems: the triangular (left) and Kagome (right) lattice.

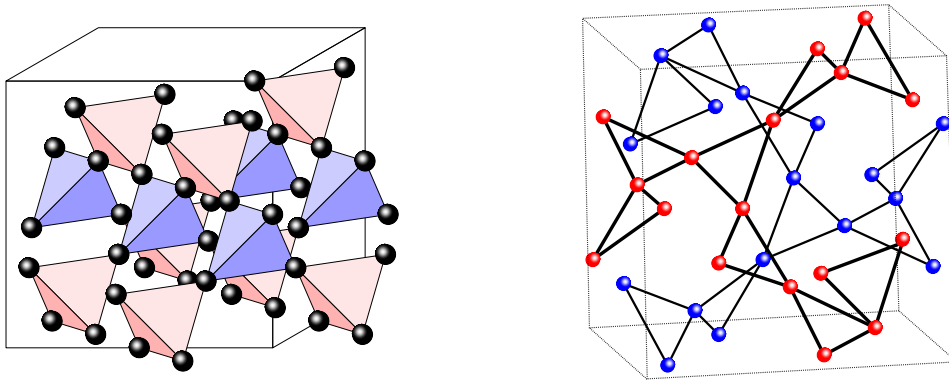


Figure 1.3: Examples of three-dimensional geometrically frustrated systems: the pyrochlore lattice composed of corner-sharing tetrahedra. Magnetic ions are drawn by black spheres located at the corners of tetrahedra. Reprinted figure with permission from Ref. [2]. Copyright 2015 by the American Physical Society. Right: hyperkagomé lattice (corner-sharing triangles) as found in the gadolinium garnet compound  $Gd_3Ga_5O_{12}$  [3].

in Fig. 1.3 in the case of a corner-sharing tetrahedra (left) or triangles (right) network.

## 1.2 The pyrochlore compounds

A realisation of a three-dimensional frustrated network is the pyrochlore lattice, illustrated in the left panel of Fig. 1.3 where magnetic ions are located in the vertices of a corner-sharing tetrahedra network. We will focus on insulator compounds of chemical formula  $R_2M_2O_7$  where  $R$  is a rare earth magnetic ion, and  $M = \text{Ti}$  or  $\text{Sn}$  in this work. They crystallise in the face centred cubic lattice of space group  $Fd\bar{3}m$ . More details of the unit cell crystallography are provided in App. A. However, we need to notice that the  $[111]$  direction is a local trigonal symmetry axis which will be taken as the quantisation axis  $z$  in the following. Some rare earth properties will be given in the introduction of Chapter 3.

The simplest model which can be considered is the classical isotropic nearest-neigh-

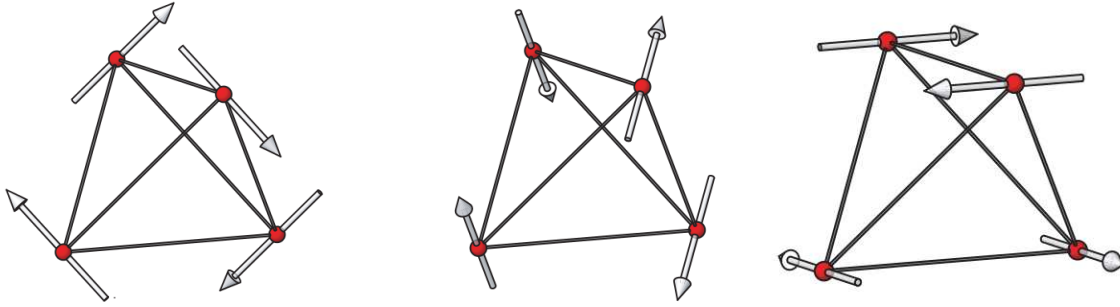


Figure 1.4: The three spin configurations of the irreducible representation  $\Gamma_7$  defined by the basis vectors  $\Psi_4$  (left),  $\Psi_5$  (middle), and  $\Psi_6$  (right), see Tab. D.1. Picture reproduced from Ref. [9] with kind permission of IOP Publishing.

bour exchange Hamiltonian:

$$\mathcal{H} = -\mathcal{I} \sum_{i,j} \mathbf{S}_i \cdot \mathbf{S}_j, \quad (1.1)$$

where  $\mathcal{I}$  is the nearest-neighbour exchange coupling, i.e.  $\mathcal{I} > 0$  in the case of ferromagnetic interactions and  $\mathcal{I} < 0$  for antiferromagnetic ones, and  $\mathbf{S}_i$  is a Heisenberg spin located at site  $i$ . In the antiferromagnetic case, the authors of Refs. [4–6] show through Monte Carlo simulations that the system remains disordered at any finite temperature, i.e. a classical spin liquid. Note that the ferromagnetic case does not lead to frustration since the minimal energy configuration is achieved when all the spins are parallel.

Nevertheless, still considering classical Heisenberg spins interacting through nearest-neighbour antiferromagnetic interactions, and taking into account dipolar interactions, Palmer and Chalker [7] show that the degeneracy associated to the infinite number of spin configurations, previously predicted in Ref. [8], is lifted. For a specific range of the ratio of the dipolar energy scale over the exchange energy, the system enters a four-sublattice long-range magnetic order with a magnetic propagation wavevector  $\mathbf{k}_{\text{mag}} = (0, 0, 0)$  and a coplanar spin configuration illustrated in Fig. 1.4 by the three basis vectors of the  $\Gamma_7$  irreducible representation (see Tab. D.1).

However other aspects need to be considered. One important feature of the investigated pyrochlore compounds is the strong spin-orbit coupling, larger than the crystal-electric-field acting at the rare earth site and created by the surrounding electric charges. As we will see in Chapter 3, the crystal field perturbation splits the ground state multiplet, leading in most cases to a ground state magnetic doublet. This enforces a strong anisotropy of the spin. With regard to the local axis  $[111]$  at the rare earth site, spins could lie along or perpendicular to this axis, i.e. the Ising or XY anisotropy, respectively. Considering Ising classical spins, the Hamiltonian is written as:

$$\mathcal{H}_{\text{ex}} = -\mathcal{I} \sum_{i,j} \mathbf{S}_i \cdot \mathbf{S}_j - \Delta_a \sum_i (\boldsymbol{\delta}_i \cdot \mathbf{S}_i)^2, \quad (1.2)$$

where  $\Delta_a > 0$  scales the strength of the anisotropy and  $\boldsymbol{\delta}_i$  is a unit vector belonging to a  $\langle 111 \rangle$  axis. Monte-Carlo calculations predict [10, 11], within the approximation that a strong anisotropy enforces spins to lie along the  $\langle 111 \rangle$  axis ( $|\mathcal{I}| \ll \Delta_a$ ), that with nearest-neighbour antiferromagnetic interactions a long-range magnetic order occurs at

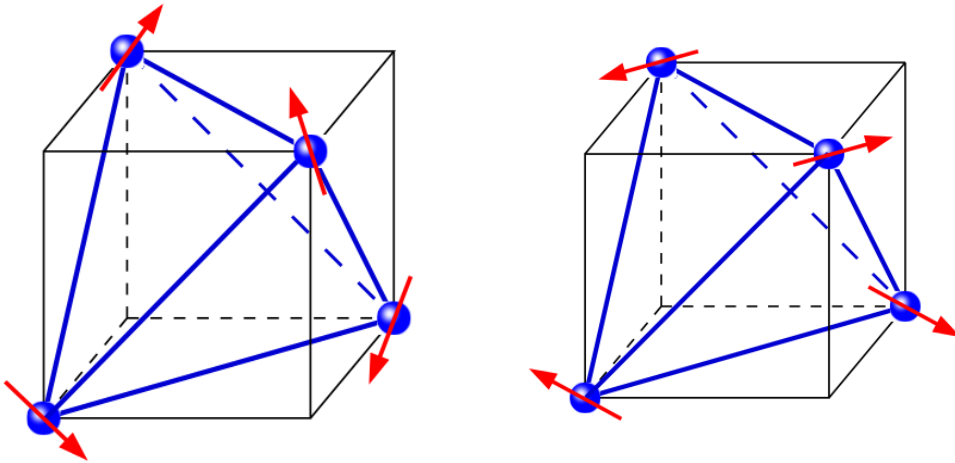


Figure 1.5: Spins configuration for a planar anisotropy in a single tetrahedron: the non coplanar  $\Psi_2$  state (left) and the coplanar  $\Psi_3$  state (right). Blue spheres indicate rare earth ions sitting on the corner of a tetrahedron and red arrows show the orientation of the spins. Reprinted figure with permission from Ref. [14]. Copyright 2015 by the American Physical Society.

$T_c \approx |\mathcal{I}|$  with a magnetic propagation wavevector  $\mathbf{k}_{\text{mag}} = (0, 0, 0)$  and a configuration where all the spins are pointing into or out the center of the tetrahedra; the first experimental realisation of this magnetic order has been found in the corner-sharing tetrahedra compound  $\text{FeF}_3$  [12]. On the contrary, in the case of nearest-neighbour ferromagnetic interactions, the system does not display any long-range magnetic order: two spins are pointing into and two spins are pointing out the center of a tetrahedron, i.e. the classical spin-ice case (see below) [13]. This absence of order results from the high degeneracy of the ground state since several energy equivalent spin configurations fulfil the "two-in/two-out" constraint, see Sec. 1.3.

In the case of an XY spin anisotropy with nearest-neighbour antiferromagnetic interactions, two magnetic structures can be achieved where spins lie in a plane perpendicular to the local axis  $[111]$ , as shown in Fig. 1.5: a non coplanar spin configuration defined as the  $\Psi_2$  state (left panel) and a coplanar spin arrangement characterised by the  $\Psi_3$  state (right panel). Note that these two states are the basis vector of the irreducible representation  $\Gamma_5$  allowed by the space group  $Fd\bar{3}m$ , see Tab. D.1. These states are energy equivalent leading to the degeneracy of the ground state. However, in a so-called order by disorder mechanism [15], thermal fluctuations select the  $\Psi_2$  states, i.e. whereas the internal energy of the two states are equal, minimising the free energy which takes into account thermal fluctuations will select the aforementioned state [16]. Therefore a first-order magnetic transition is predicted to occur with a magnetic propagation wavevector  $\mathbf{k}_{\text{mag}} = (0, 0, 0)$ . When quantum fluctuations are considered, a second-order magnetic transition is predicted [14, 17].

In summary, the magnetic ground state of the pyrochlore is ruled by numerous physical aspects: the nature of the nearest-neighbour exchange interaction and the character of the spin anisotropy need to be considered, but also dipolar and further neighbour interactions, anisotropic exchange interactions, and whether the spins are

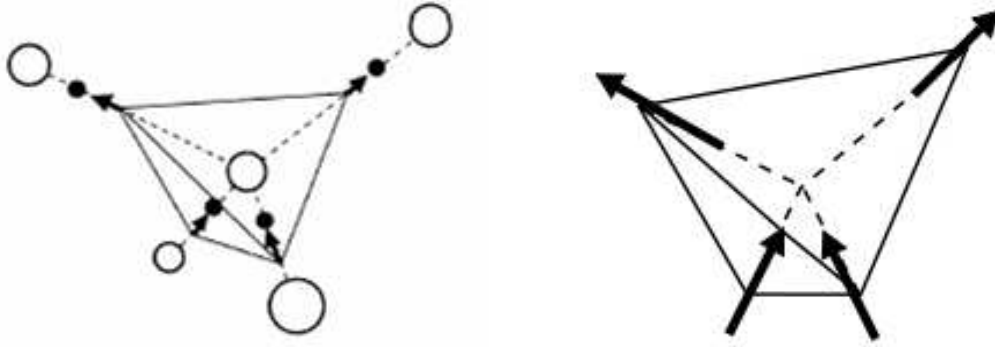


Figure 1.6: *Illustration of the analogy between the spin-ice and the water ice model. Left: Water ice structure where the oxygen ions ( $O^{2-}$ ) are displayed by the empty spheres and the protons ( $H^+$ ) by the black ones. Arrows show the proton displacement from the middle of two oxygen atoms where two are near the central oxygen ion whereas the other two are far from it. Reprinted figure with permission from Ref. [24]. Copyright 2015 by the American Physical Society. Right: Single tetrahedron obeying the ice rule: two Ising spins are pointing into the center of the tetrahedron and two spins are pointing out. Reprinted figure with permission from Ref. [18]. Copyright 2015 by the American Physical Society.*

classical or quantum. The subtle balance between these considerations is at the origin of the various exotic magnetic states encountered in the pyrochlore series. In the following, we endeavour ourselves to summarise briefly different magnetic ground states at play in the  $R_2M_2O_7$  families where  $M = \text{Ti}$  or  $\text{Sn}$ .

### 1.3 The classical spin-ice

The terminology of *spin-ice* was first introduced by Harris *et al.* [18] for the pyrochlore compound  $\text{Ho}_2\text{Ti}_2\text{O}_7$  where no long-range order was evidenced down to 50 mK by  $\mu\text{SR}$  spectroscopy [19]. Other pyrochlore compounds, namely  $\text{Dy}_2\text{Ti}_2\text{O}_7$  [20],  $\text{Ho}_2\text{Sn}_2\text{O}_7$  [21] and  $\text{Dy}_2\text{Sn}_2\text{O}_7$  [22] have also been unambiguously classified as classical spin-ice. In the following, we will present some peculiar properties of these compounds.

#### 1.3.1 The water ice model

The crystal-electric-field acting on the rare earth site constrains the spins to lie along the local [111] direction, i.e. defining the Ising model. The configuration on a single tetrahedron is two spins pointing into the center of the tetrahedra and two spins pointing out, defining the so-called *ice rule*. This denomination originates from the analogy made with the model of the water ice  $I_h$  originally proposed by Bernal and Fowler [23], as illustrated in Fig. 1.6, where two protons are close to the central oxygen position and two far from it.

The degeneracy of the ground state of frustrated materials is a consequence of the peculiar lattice topology. For a given tetrahedron obeying the ice rule, only six configurations are available as illustrated in Fig. 1.7. The corresponding entropy can be

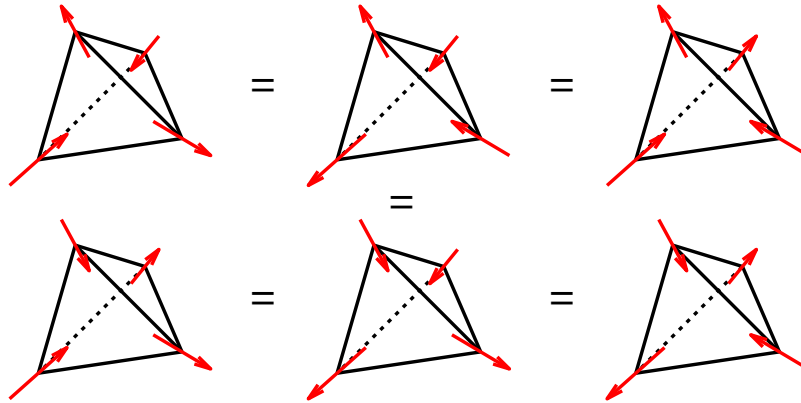


Figure 1.7: The six possible spin configurations obeying the ice rule illustrate the degeneracy of the ground state in a spin-ice compound.

calculated [25]: a system of  $N$  spins corresponds to  $\frac{N}{2}$  tetrahedra since a spin belongs to two tetrahedra. As Ising spins are considered, i.e. up or down,  $2^4$  configurations should be considered for a single tetrahedron but only 6 of them are available in order to satisfy the ice rule. Thus the number of microstates accessible to the spin-ice is calculated as  $\Omega_m = 2^N \left(\frac{6}{16}\right)^{\frac{N}{2}}$  and the entropy per spin is  $S_{\text{el}}/N = k_B \ln \Omega_m = \frac{k_B}{2} \ln \frac{3}{2}$ , corresponding to Pauling's result for water ice [26]. The magnetic entropy is deduced from specific heat measurements down to 0.2 K on  $\text{Dy}_2\text{Ti}_2\text{O}_7$  [20], illustrated in the left panel of Fig. 1.8, and down to 0.34 K on  $\text{Ho}_2\text{Ti}_2\text{O}_7$  [27], after subtraction of the nuclear contribution arising from strong hyperfine interactions acting on the nucleus, and is in agreement with this prediction. The sibling stannate compounds present the same residual magnetic entropy in  $\text{Ho}_2\text{Sn}_2\text{O}_7$  [28] and  $\text{Dy}_2\text{Sn}_2\text{O}_7$  [29].

The spin-ice compounds do not exhibit any magnetic long-range order as for instance in  $\text{Ho}_2\text{Ti}_2\text{O}_7$  where no spontaneous oscillations and no drop in the initial asymmetry of the muon polarisation function are resolved by zero-field  $\mu\text{SR}$  experiments [19]. The electronic specific heat exhibits a broad hump roughly around  $T = 1$  K below which it drops to almost zero, indicative of a spin freezing in  $\text{Ho}_2\text{Ti}_2\text{O}_7$  [27] and  $\text{Dy}_2\text{Ti}_2\text{O}_7$  [20]. This property was confirmed by magnetisation measurements with the presence of an hysteresis effect between zero-field and field cooling procedures at 0.65 K for  $\text{Dy}_2\text{Ti}_2\text{O}_7$  [30], and 0.75 K for  $\text{Ho}_2\text{Sn}_2\text{O}_7$  [31], the latter case being illustrated in the right panel of Fig. 1.8. An additional proof of this spin freezing lies in the presence of a peak in the real part of the a.c. susceptibility in  $\text{Dy}_2\text{Ti}_2\text{O}_7$  [30] and  $\text{Dy}_2\text{Sn}_2\text{O}_7$  [22] indicative of the development of spin correlations.

### 1.3.2 The dipolar spin-ice model (DSM)

As discussed above, the case of classical spins with a strong Ising anisotropy, see the Hamiltonian in Eq. 1.2, leads to the spin-ice configuration if ferromagnetic interactions are at play, which is in agreement with the positive Curie-Weiss temperature deduced from susceptibility measurements:  $\theta_{\text{CW}} \approx 1.9, 0.5, 1.8,$  and  $1.7$  K for  $\text{Ho}_2\text{Ti}_2\text{O}_7$  [18],  $\text{Dy}_2\text{Ti}_2\text{O}_7$  [20],  $\text{Ho}_2\text{Sn}_2\text{O}_7$  [31], and  $\text{Dy}_2\text{Sn}_2\text{O}_7$  [33], respectively.

However, magnetic ions carry a large magnetic moment of about  $\approx 10 \mu_B$ . There-

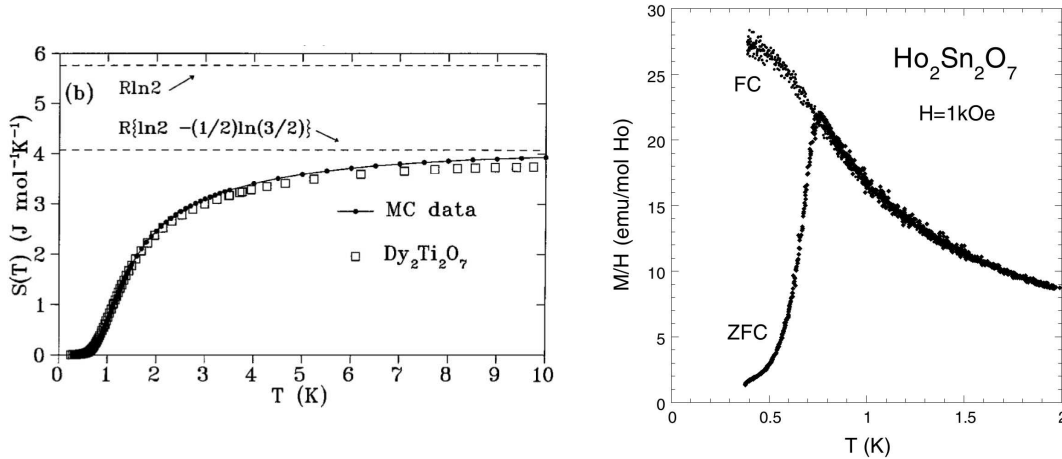


Figure 1.8: *Left: Temperature dependence of the magnetic entropy of  $\text{Dy}_2\text{Ti}_2\text{O}_7$  revealing the same residual entropy as explained by Pauling in water ice [26]. A fit to the data is achieved using the dipolar spin-ice model, see Eq. 1.3. Experimental data are from Ref. [20]. Reprinted figure with permission from Ref. [32]. Copyright 2015 by the American Physical Society. Right: Temperature dependence of the magnetisation of  $\text{Ho}_2\text{Sn}_2\text{O}_7$  recorded in ZFC-FC and showing a spin freezing behaviour. Copyright IOP Publishing. Picture reproduced from Ref. [31] by permission of IOP Publishing. All rights reserved.*

fore, dipolar interactions are not negligible compared to the weak exchange interaction inferred from the Curie-Weiss temperature. An estimation of the dipolar energy scale between two nearest neighbours is given by  $D_{\text{nn}} = \frac{5}{3} \frac{\mu_0 \mu^2}{4\pi r_{\text{nn}}^3} \approx 2.4 \text{ K}$  [34], where  $r_{\text{nn}} = a_{\text{lat}} \sqrt{2}/4$  is the nearest-neighbour distance and  $\mu = 10 \mu_{\text{B}}$ . Therefore, an effective nearest-neighbour energy scale is put forward to take into account both the effect of the exchange and dipolar interactions:  $\mathcal{I}_{\text{eff}} \equiv \mathcal{I}_{\text{nn}} + D_{\text{nn}}$ , where  $\mathcal{I}_{\text{nn}}$  is the nearest-neighbour exchange constant. Analysing specific heat data, a negative value of the exchange constant is inferred indicative of nearest-neighbour antiferromagnetic exchange interactions, i.e.  $\mathcal{I}_{\text{nn}} = -0.52$  and  $-1.24 \text{ K}$  for  $\text{Ho}_2\text{Ti}_2\text{O}_7$  [27] and  $\text{Dy}_2\text{Ti}_2\text{O}_7$  [32], respectively. Therefore, dipolar interactions are of prime importance since they restore the ferromagnetic nature of the net nearest-neighbour interactions, a mandatory condition to recover the spin-ice case.

The dipolar spin-ice Hamiltonian was introduced in order to describe the low temperature properties of the classical spin-ice compounds [32]:

$$\mathcal{H}_{\text{DSM}} = -\mathcal{I} \sum_{\langle i,j \rangle} S_i S_j \mathbf{z}_i \cdot \mathbf{z}_j + D r_{\text{nn}}^3 \sum_{j>i} S_i S_j \left( \frac{\mathbf{z}_i \cdot \mathbf{z}_j}{|\mathbf{r}_{ij}^3|} - \frac{3(\mathbf{z}_i \cdot \mathbf{r}_{ij})(\mathbf{z}_j \cdot \mathbf{r}_{ij})}{|\mathbf{r}_{ij}^5|} \right), \quad (1.3)$$

where the first term accounts for the nearest-neighbour exchange interaction ( $\mathcal{I} = 3\mathcal{I}_{\text{nn}}$ )<sup>1</sup> and the vector  $\mathbf{z}_i$  refers to local  $\langle 111 \rangle$  direction of spin  $S_i$  located at the rare earth site  $i$ . The second term arises from the dipolar interaction ( $D = 3D_{\text{nn}}/5$ )<sup>2</sup>. The

<sup>1</sup>The factor 3 comes from the scalar product between the local  $\langle 111 \rangle$  directions of two nearest neighbour Ising spins located at sites  $i$  and  $j$ .

<sup>2</sup>The  $\frac{3}{5}$  factor comes from the scalar product between the  $\langle 111 \rangle$  directions and the vector direction connecting two nearest neighbours.

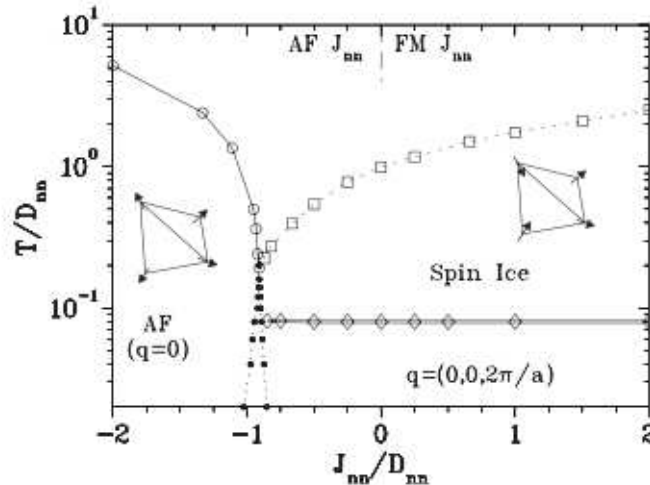


Figure 1.9: Zero-field phase diagram of the dipolar spin-ice model predicted by Melko *et al.* [38] with Monte Carlo simulations.  $J_{nn}$  and  $D_{nn}$  have been defined in the main text and refer to the nearest-neighbor exchange and dipolar energy scales, respectively. Here,  $J_{nn} \equiv \mathcal{I}_{nn}$ . Copyright IOP Publishing. Picture reproduced from Ref. [38] by permission of IOP Publishing. All rights reserved.

role of the long-range dipolar interactions was at stake for these frustrated systems to understand why they do not lift the degeneracy to establish a long-range ordering. If the first Monte Carlo simulations fail to describe the specific heat and magnetic entropy results [35, 36], due to a truncated sum over the dipolar term [37], bulk properties of the spin-ice compound were finally consistent with simulations using the dipolar spin-ice Hamiltonian for  $\text{Ho}_2\text{Ti}_2\text{O}_7$  [37] and  $\text{Dy}_2\text{Ti}_2\text{O}_7$  [32], the latter case being illustrated in the left panel of Fig. 1.8.

The corresponding phase diagram of the Hamiltonian written in Eq. 1.3 has been computed in Refs. [32, 38], see Fig. 1.9. When the nearest neighbour exchange energy becomes sufficiently large compared to the dipolar one, we recover the all-in-all-out antiferromagnetic state with a magnetic propagation wavevector  $\mathbf{k}_{\text{mag}} = (0, 0, 0)$ . Above this value, the ferromagnetic spin-ice case is evidenced where the upper dotted line refers to the broad peak in specific heat measurements corresponding to a slowing down of the spin fluctuations. Decreasing the temperature, the spin-ice compound is predicted to undergo a first order transition at  $T/D_{nn} \leq 0.08$  with  $\mathbf{k}_{\text{mag}} = (0, 0, 1)$ , which has never been evidenced experimentally.

The experimental evidence of a signature of the existence of dipolar spin correlations was a challenge over the past few years. Dipolar correlations in the real space are characterised by a  $1/r^3$  decay, which corresponds in the reciprocal space by Fourier transformation to [39]:

$$\langle S_i(-\mathbf{k})S_j(\mathbf{k}) \rangle \propto \left( \delta_{ij} - \frac{k_i k_j}{k^2} \right), \quad (1.4)$$

where  $\mathbf{k}$  is a vector of the reciprocal space. This leads to singularities at the Brillouin zone centres, the so-called *pinch points* in neutron scattering measurements. Whereas these pinch points were hardly seen with unpolarised neutron experiments on the spin-ice compounds  $\text{Ho}_2\text{Ti}_2\text{O}_7$  [34, 40] and  $\text{Dy}_2\text{Ti}_2\text{O}_7$  [41], Fennell *et al.* [42] succeeded to

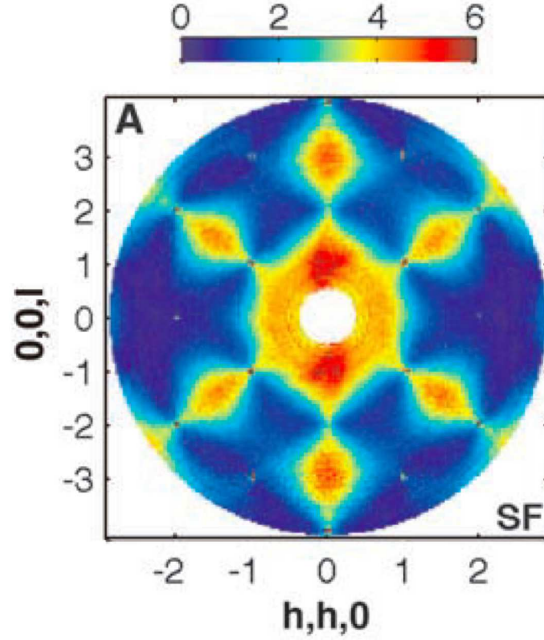


Figure 1.10: Diffuse magnetic scattering map recorded on the spin-ice compound  $\text{Ho}_2\text{Ti}_2\text{O}_7$  at 1.7 K in the  $(hhl)$  plane in order to evidence pinch points. From Ref. [42]. Reprinted with permission from AAAS.

evidence these peculiar pinch points on  $\text{Ho}_2\text{Ti}_2\text{O}_7$  using polarised neutrons, see Fig. 1.10, revealing the dipolar nature of the spin correlations. The comparison of data recorded in the spin flip and non spin-flip channels explains why previous measurements could not resolve these pinch points with unpolarised neutrons.

### 1.3.3 Magnetic monopoles

The notion of magnetic monopoles was firstly introduced by Ryzhkin [43] in order to describe excitations in spin-ice. Then, the dumbbell model, see for instance Ref. [44], has been developed in order to illustrate the DSM Hamiltonian and to describe the thermal fluctuations breaking of the ice rule with emergent quasiparticles, i.e. the magnetic monopoles [43]. The principle lies on the fragmentation of the magnetic dipole into two magnetic monopoles of opposite charges  $\pm q_m$  (dumbbell) as illustrated in Fig. 1.11, and separated by a length  $a_d = \sqrt{3}a_{\text{lat}}/2$  which is the distance separating the center of two neighbouring tetrahedra. Thus, the magnetic moment carried by the dipole  $\mu = q_m a_d$  is recovered. Therefore, the total magnetic charge in a tetrahedron  $\alpha$  is  $Q_\alpha = \sum_i q_{m,i}$ , where the sum runs over the four magnetic charges inside the tetrahedra. This resulting total magnetic charge is the so-called magnetic monopole. Note that in the ice rule ground state  $Q_\alpha = 0$  and if a spin is flipped  $Q_\alpha = \pm 2q_m$ . According to Refs. [44, 45], the magnetic Coulomb interaction between two monopoles is written as:

$$V(r_{\alpha\beta}) = \begin{cases} \frac{\mu_0 Q_\alpha Q_\beta}{4\pi r_{\alpha\beta}} & \text{if } \alpha \neq \beta \\ \frac{\nu_0 Q_\alpha^2}{2} & \text{if } \alpha = \beta, \end{cases} \quad (1.5)$$

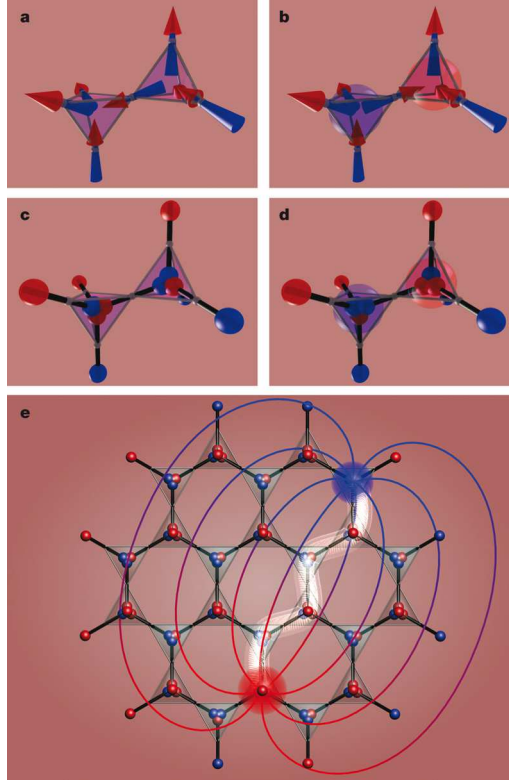


Figure 1.11: (a) Two neighbouring tetrahedra obeying the ice rule. (b) The spin shared by the two tetrahedra is thermally flipped to create a pair of magnetic monopoles of opposite charge. Panels (c) and (d) are the illustration of panel (a) and (b) in terms of the dumbbell model: a magnetic moment is replaced by two opposite magnetic charges  $\pm q_m$ . (e) Propagation of two magnetic monopoles along a Dirac string. Reprinted by permission from Macmillan Publishers Ltd: Nature [44], copyright 2015.

where  $r_{\alpha\beta}$  denotes the distance between two monopoles. The first line of Eq. 1.5 refers to the dipolar interaction of the DSM and the introduction of the *self energy*  $\nu_0$  in the second line accounts for the dipolar and exchange energy between nearest neighbours. The DSM Hamiltonian can be rewritten in terms of the dumbbell notation such as:

$$\mathcal{H}_{\text{DB}} = \frac{\mu_0}{4\pi} \sum_{\alpha \neq \beta} \frac{Q_\alpha Q_\beta}{r_{\alpha\beta}} + \frac{\nu_0}{2} \sum_{\alpha} Q_\alpha^2 \quad (1.6)$$

When the ice rule is satisfied, the spin-ice state is defined as a Coulomb phase since the three criteria stated by Henley [46] are fulfilled: (i) the system is highly disordered since no long-range order is established, (ii) each dumbbell is associated to a magnetic flux, and (iii) the magnetic flux at the centre of the tetrahedron vanishes. The last condition can be rewritten as a divergence free coarse-grained field, i.e.  $\nabla \cdot \mathbf{B} = \mu_0 \sum_{\alpha} Q_\alpha = 0$  in the spin-ice ground state. We should notice that in a more usual *cooperative paramagnet*, the system enters in a phase without long-range magnetic order with spin correlations decreasing exponentially, whereas in the so-called Coulomb phase spin correlations are algebraic.

Therefore, this model allows to describe spin dynamics in such a system: to a spin thermally flipped corresponds the nucleation of two magnetic monopoles of opposite

charge located in two corner-sharing tetrahedra. These monopoles interact through a magnetic Coulomb potential. The divergence-free condition is broken, i.e. the ice rule is not fulfilled anymore. Thus, once magnetic monopoles are nucleated, their diffusion along a path of reversed spins, i.e. the so-called Dirac string, see panel (e) of Fig. 1.11, corresponds to the propagation of a zero energy cost spin reversal along the string, since each tetrahedron tends to recover the ground state defined by the ice rule configuration.

### 1.3.4 Experimental evidence for magnetic monopoles

Bramwell *et al.* [47] have recently proposed by muon spectroscopy the presence of magnetic monopoles interacting through a magnetic potential in the spin-ice pyrochlore compound  $\text{Dy}_2\text{Ti}_2\text{O}_7$ . The principle lies on the increase of the magnetic monopoles density when applying a magnetic field, inspired from Onsager's work [48] on the second Wien effect which predicts the increase of the dissociation constant of water molecule into  $\text{H}_3\text{O}^+$  and  $\text{OH}^-$  ions under an applied electric field which overcomes the Coulomb energy barrier. Pursuing this analogy, the dissociation constant  $K$  for the nucleation of magnetic monopoles was assumed to take a similar form as in Onsager's theory for weak magnetic field  $B$  [47]:

$$K(B) = K(0) \left( 1 + b + \frac{b^2}{3} \dots \right), \quad (1.7)$$

where  $b = \frac{\mu_0 Q^3 B}{8\pi k_B^2 T^2}$ .<sup>3</sup> At the equilibrium, i.e. without applied magnetic field, the number of bound magnetic monopoles  $n_b$  is predominant compared to the dissociated ones  $n_u$ . According to Ref. [47], the dissociation constant is written as:

$$K(0) = n_0 \frac{\alpha_m^2}{1 - \alpha_m}, \quad (1.8)$$

where  $n_0 = n_b + n_u$  and  $\alpha_m = n_u/n_0$ . The recombination of nucleated magnetic monopoles follows an exponential decay with a relaxation time  $1/\nu_{\alpha_m}$ . Since  $\nu_{\alpha_m} \propto \kappa_{\alpha_m}$ , where  $\kappa_{\alpha_m}$  is the magnetic conductivity (illustrating the motion of the magnetic monopoles) proportional to the density of magnetic monopoles, and recalling that  $\alpha_m \ll 1$ , it follows [47]:

$$\frac{\nu_{\alpha_m}(B)}{\nu_{\alpha_m}(0)} = \frac{\kappa_{\alpha_m}(B)}{\kappa_{\alpha_m}(0)} = \frac{\alpha_m(B)}{\alpha_m(0)} = \sqrt{\frac{K(B)}{K(0)}} \approx 1 + \frac{b}{2}. \quad (1.9)$$

Furthermore, Bramwell *et al.* [47] put forward that the fluctuations of the magnetic monopole density produces fluctuations of the local field. Therefore after a magnetic field perturbation, the relaxation rate of the magnetisation  $\nu_M$  is proportional to the relaxation rate of the magnetic monopole density  $\nu_{\alpha_m}$ .

$$\frac{\nu_{\alpha_m}(B)}{\nu_{\alpha_m}(0)} = \frac{\nu_M(B)}{\nu_M(0)} \quad (1.10)$$

---

<sup>3</sup>Note that the index  $\alpha$  labelling a tetrahedron has been dropped now,  $Q$  refers to the magnetic charge of an effective monopole.

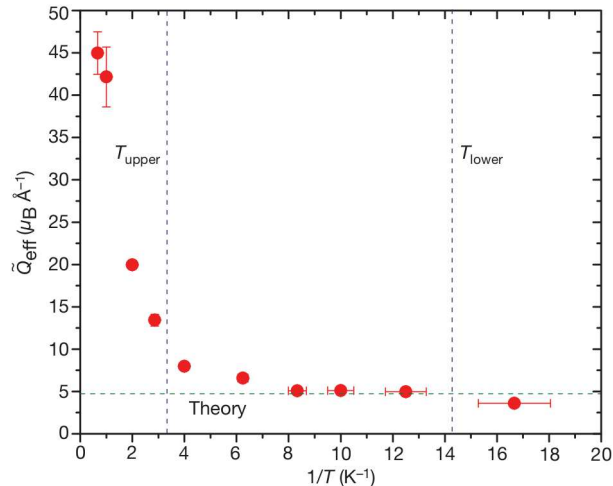


Figure 1.12: Temperature dependence of the calculated value of the effective magnetic charge  $\tilde{Q}_{\text{eff}}$  inferred from the field dependence of the muon spin relaxation rate in the case of  $\text{Dy}_2\text{Ti}_2\text{O}_7$ . Reprinted by permission from Macmillan Publishers Ltd: Nature [47], copyright 2015.

In the transverse field muon spin relaxation technique, see Sec. 2.6, the muon polarisation function is characterised by oscillations illustrating the precession of the muon spin around the local field, and an envelope giving information on dynamics of the local field at the muon site: in the case of slow fluctuations of the local field, the relaxation rate  $\lambda$ , characteristic of the exponential decay of the envelope, is proportional to  $\nu_M$ . Therefore, Bramwell *et al.* find an ingenious way to measure the magnetic charge carried by the magnetic monopoles. Hence, measuring the field dependence of  $\lambda$  allows to extract the effective magnetic charge carried by the monopoles, see Fig. 1.12. A typical value of  $\tilde{Q}_{\text{eff}} = 5 \mu_B \text{ \AA}^{-1}$  has been inferred in good agreement with Ref. [44] within the temperature range  $T_{\text{lower}} \leq T \leq T_{\text{upper}}$  where Onsager's theory remains valid. The authors of Ref. [49] draw the same conclusions with  $\mu\text{SR}$  experiments on the spin-ice compound  $\text{Ho}_2\text{Ti}_2\text{O}_7$ .

Whereas these results were strongly debated [50, 51] in a first instance, additional experimental proofs evidenced a signature of magnetic monopoles in spin-ice as for instance the observation of Dirac strings in  $\text{Dy}_2\text{Ti}_2\text{O}_7$  with neutron scattering experiments under a magnetic field applied along [100] [52]. Existence of such strings were previously suggested in Ref. [42] from the broadening of pinch points. Furthermore, the temperature dependence of the relaxation time inferred from a.c. susceptibility on  $\text{Dy}_2\text{Ti}_2\text{O}_7$  [30], previously misunderstood, has been described in terms of the motion of magnetic monopoles [53].

## 1.4 The quantum spin-ice

### 1.4.1 Beyond the classical spin ice

The quantum spin-ice is defined by the same properties as its classical counterpart: Ising spins along the trigonal axis [111] fulfil the ice rule constraint, defining the same

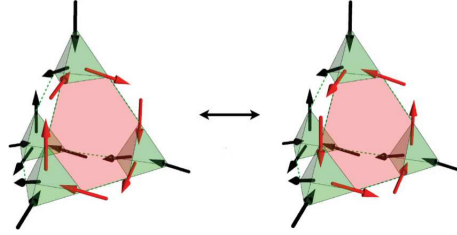


Figure 1.13: *Illustration of the tunnelling between two spin configurations on an hexagonal plaquette, preserving the ice rule constraint. Reprinted figure with permission from Ref. [56]. Copyright 2015 by the American Physical Society.*

divergence free condition, i.e.  $\nabla \cdot \mathbf{B} = 0$ . However, in the former case, additional transverse nearest-neighbour exchange interaction  $\mathcal{I}_\perp$  are at play with the usual longitudinal coupling  $\mathcal{I}_{zz}$ . To these in-plane interactions result slight tilts of the spins away from their initial direction, since  $\mathcal{I}_\perp \ll \mathcal{I}_{zz}$ . Note that the U(1) symmetry is preserved since a rotation around the local [111] axis leaves the system invariant. Hermele *et al.* [54] firstly introduced this planar interaction as a perturbation of the classical spin-ice ground state. Following notations of Ref. [55], the nearest-neighbour exchange Hamiltonian with effective spin-1/2 (or XXZ model) is thus written:

$$\begin{aligned} \mathcal{H}_{\text{QSI}} &= \mathcal{H}_{\text{CSI}} + \mathcal{H}_\perp \quad \text{where,} \\ \mathcal{H}_{\text{CSI}} &= \mathcal{I}_{zz} \sum_{\langle i,j \rangle} S_i^z S_j^z \quad \text{and,} \\ \mathcal{H}_\perp &= \mathcal{I}_\perp \sum_{\langle i,j \rangle} (S_i^+ S_j^- + S_i^- S_j^+). \end{aligned} \quad (1.11)$$

The introduction of this small perturbation lifts the degeneracy associated to the classical spin-ice. Using perturbation theory on  $\mathcal{H}_\perp$  shows that the first and second order terms lead to a vanishing or constant contribution to the energy. The third order term involves, in order to preserve the ice rule constraint, a tunnelling between a specific spin configuration: a ring exchange running on an hexagonal plaquette as illustrated in Fig. 1.13. The authors of Ref. [54] show that, for a finite range of the ratio of the strength of the tunnelling matrix element (which involves the transverse component of the nearest-neighbour interaction) over the number of flippable plaquettes in the system, the U(1) quantum spin liquid phase is predicted, the quantum spin ice state being a peculiar case of the latter.

Since the ice rule is preserved, the divergence free condition of the magnetic field allows to introduce a gauge field  $\mathbf{A}$ , such as  $\nabla \times \mathbf{A} = \mathbf{B}$ . Therefore, the tunnelling between ice configurations introduces time fluctuations of  $\mathbf{A}$  resulting on the emergence of an electric field  $\mathbf{E} = -\frac{\partial \mathbf{A}}{\partial t}$  [57]. Due to the U(1) symmetry, only transverse fluctuations are allowed for this gauge field. This state supports several kinds of excitations: magnetic monopoles, or spinons in the spin liquid literature, resulting from a spin flip

breaking the ice rule constraint which, unlike the classical spin-ice, interact through magnetic and electric fields. By construction of the spin loops on a hexagonal plaquette, electric loops appear. Flipping a spin will not only generate magnetic monopoles but also will break these electric loops: the extremities of these strings become source of electric charges, the so called visons (see Ref. [55] and references therein). Finally, at low temperatures, the emergence of a gapless magnetic photon resulting from the transverse fluctuations of  $\mathbf{A}$  is predicted in Ref. [56].

### 1.4.2 The exchange Hamiltonian

As we will see in Chapter 3, the crystal electric field acts as a perturbation of the spin-orbit multiplet in the pyrochlore compounds, leading for most of them to a well isolated magnetic ground state doublet which enforces a strong anisotropy of the spins. Therefore, the low temperature properties can be described by an effective spin-1/2. Looking for a realisation of the quantum spin ice state, compounds with a strong anisotropy of the exchange interactions is an asset to the existence of quantum fluctuations, as introduced above. Therefore, an anisotropic effective spin-1/2 Hamiltonian within the ground state doublet was firstly derived on symmetry grounds in Ref. [58] and mostly taken over in the quantum spin ice literature.<sup>4</sup> Following the notations introduced in Ref. [60], this exchange Hamiltonian takes the form:

$$\begin{aligned} \mathcal{H}_{\text{ex}} = & \sum_{\langle ij \rangle} \mathcal{I}_{zz} S_i^z S_j^z - \mathcal{I}_{\pm} (S_i^+ S_j^- + S_i^- S_j^+) \\ & + \mathcal{I}_{\pm\pm} [\gamma_{ij} S_i^+ S_j^+ + \gamma_{ij}^* S_i^- S_j^-] + \mathcal{I}_{z\pm} [S_i^z (\xi_{ij} S_j^+ + \xi_{ij}^* S_j^-) + i \leftrightarrow j], \end{aligned} \quad (1.12)$$

where the effective spin is written in terms of local coordinates, i.e. the  $z$  direction is taken along the trigonal axis [111] at the rare earth site,  $\gamma$  is a  $4 \times 4$  complex matrix (see Ref. [60]), and  $\xi = -\gamma^*$ . The space described by the four coupling constants constitutes a challenge in order to theoretically describe the exotic magnetic phases observed in the pyrochlore compound. Note that the case where  $\mathcal{I}_{\pm\pm} = \mathcal{I}_{z\pm} = 0$  has been treated in Ref. [54] and presented in the former section. We recognise  $\mathcal{I}_{zz}$ , the longitudinal or Ising exchange constant. According to Refs. [55, 61], the three other exchange coupling terms illustrate different interacting processes at play. Linear combinations of these parameters allow to retrieve an isotropic exchange interaction, a pseudo-dipolar nearest-neighbour interaction of the form  $\mathbf{S}_i \mathbf{S}_j - 3(\mathbf{S}_i \cdot \mathbf{r}_{ij})(\mathbf{S}_j \cdot \mathbf{r}_{ij})$  where  $\mathbf{r}_{ij}$  is a unitary vector connecting two nearest neighbours and the Dzyaloshinskii-Moriya interaction of the form  $\mathbf{D}_{\text{DM}} \cdot (\mathbf{S}_i \times \mathbf{S}_j)$  [62, 63]. The latter interaction depends on the symmetry of the crystal: Moriya's rules [64] state that if the middle point between the two magnetic sites is a center of inversion, there is no Dzyaloshinskii-Moriya interaction. The authors of Refs. [62, 63] have shown that only two cases are allowed in the pyrochlore lattice: in both cases, vectors  $\mathbf{D}_{\text{DM}}$  must be perpendicular to the  $\{110\}$  planes.

The anisotropic exchange Hamiltonian in Eq. 1.12 has been analysed by means of gauge mean field theory gMFT in order to compute the phase diagram in the Kramers (half-integer spin) [65] or non-Kramers (integer spin) [66] cases, illustrated in the left and

---

<sup>4</sup>Note that a similar Hamiltonian is derived based on the superexchange interaction—the hybridization of the  $4f$  orbital of the magnetic ion and the  $2p$  orbital of an oxygen—and calculating the probability of an electron (or a hole) to hop between the aforementioned orbitals [59].

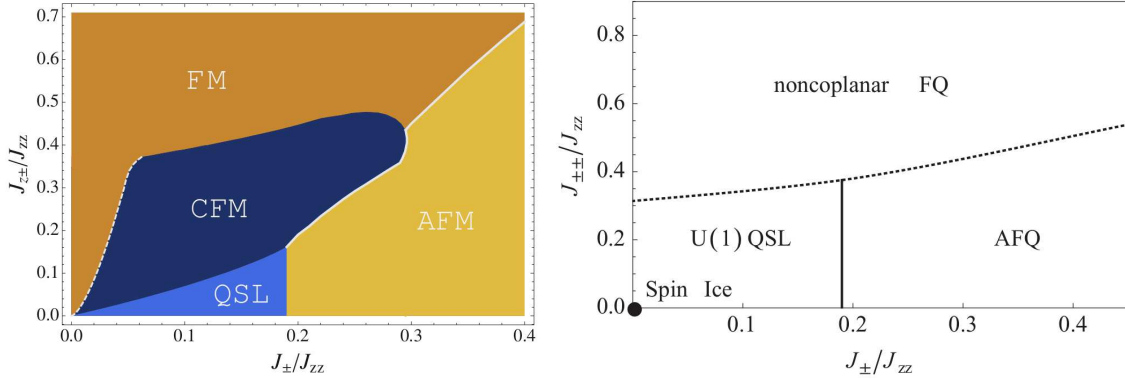


Figure 1.14: *Left: Zero temperature phase diagram resulting from gMFT analysis of the Hamiltonian written in Eq. 1.12 in the case of Kramers (left) and non-Kramers ions (right). Here  $J_{zz} \equiv \mathcal{I}_{zz}$ ,  $J_{z\pm} \equiv \mathcal{I}_{z\pm}$ ,  $J_{\pm} \equiv \mathcal{I}_{\pm}$ , and  $J_{\pm\pm} \equiv \mathcal{I}_{\pm\pm}$ . Reprinted figures with permission from Refs. [65, 66] for left and right panels, respectively. Copyright 2015 by the American Physical Society.*

right panels of Fig. 1.14, respectively. In Ref. [65],  $\mathcal{I}_{zz} > 0$  has been taken, i.e. the spin ice ground state manifold, and  $\mathcal{I}_{\pm\pm} = 0$  to restrain the space to two parameters. FM and AFM denote the Higgs ferromagnetic and antiferromagnetic long-range order, QSL refers to the quantum spin liquid (or quantum spin-ice case since  $\mathcal{I}_{zz} > 0$ ) presented in Sec. 1.4.1— defined as a deconfined phase since Coulombic interaction between effective particles is weak —, and CFM names the Coulomb ferromagnetic state which displays the same excitations as in the quantum spin-ice and a dipolar long-range order [65]. Note that the non zero temperature phase diagram has been studied recently in Ref. [67]. On the other hand, the non-Kramers case has been treated in Ref. [66], using  $\mathcal{I}_{zz} > 0$ . The coupling between the Ising and planar components of the effective spin does not contribute to the Hamiltonian in the non Kramers case since  $|\langle \phi_0^{\pm} | S^{\pm} | \phi_0^{\mp} \rangle| = 0$ , where  $\phi_0^{\pm}$  are the wavefunctions of the ground state. The resulting phase diagram leads to the quantum spin-ice state, and two ordered phases: an XY antiferroquadrupolar order and a non coplanar ferroquadrupolar order.

The most propitious and studied compound over the past few years which could exhibit a quantum spin liquid phase is  $\text{Tb}_2\text{Ti}_2\text{O}_7$ : we will present a non exhaustive review of it in Chapter 5. Other candidates to the quantum spin-ice state are  $\text{Pr}_2\text{Sn}_2\text{O}_7$  and  $\text{Pr}_2\text{Zr}_2\text{O}_7$  [68]. The latter compound belongs to a pyrochlore series which will not be discussed in this work. On the former compound, inelastic neutron scattering measurements reveal a non Kramers ground state doublet well isolated from the excited ones, and crystal field calculations taking account the low lying multiplets arising from the spin-orbit coupling show an Ising anisotropy and a magnetic moment  $\approx 2.6 \mu_B$  [69], implying that dipolar interactions are much weaker than in the classical spin-ice. Ferromagnetic interactions are dominant since  $\theta_{\text{CW}} = 0.3$  K [33]. The authors of Ref. [70] show a broad hump in the specific heat at  $T = 0.86$  K indicative of the development of short range correlations, as confirmed by neutron diffraction where no magnetic Bragg peaks are evidenced down to 0.2 K but rather a diffuse magnetic scattering intensity. The residual entropy at 0.37 K is higher than the one found in spin ice, attesting the dy-

namical nature of the ground state. A characteristic correlation time  $\approx 2$  ps is inferred from the quasielastic signal observed by inelastic neutron scattering measurements. A small hysteresis in the field dependence of the magnetisation at  $T = 90$  mK indicates a slowing down of the fluctuations, confirmed by a.c. susceptibility measurements [71]. Note that due to the non-Kramers nature of the ground state, fluctuations have been proposed to originate from quadrupolar interactions [69, 72].

## 1.5 The pyrochlore series $R_2M_2O_7$ : a large variety of magnetic ground states

We present here a short review of the magnetic states existing in the pyrochlore compounds  $R_2M_2O_7$  ( $M=\text{Ti, Sn}$ ) which were not discussed yet. Note that the case of the thulium ion will not be discussed since it exhibits a non magnetic singlet ground state, see Chapter 3. We first focus on compounds having an Ising anisotropy, namely  $\text{Tb}_2M_2O_7$  and then briefly describe those having a dominant planar anisotropy.

### 1.5.1 $\text{Tb}_2\text{Ti}_2\text{O}_7$ vs $\text{Tb}_2\text{Sn}_2\text{O}_7$

As already mentioned,  $\text{Tb}_2\text{Ti}_2\text{O}_7$  is a candidate for the quantum spin-ice phase and will be largely discussed in Chapter 5. It does not display any magnetic order. On the contrary,  $\text{Tb}_2\text{Sn}_2\text{O}_7$  is characterised by a long-range magnetic order at  $T_c = 0.87$  K as seen by magnetic susceptibility measurements. The high temperature range ( $100 \leq T \leq 300$  K) of the susceptibility follows a Curie-Weiss law leading to  $\theta_{\text{CW}} \approx -12$  K, indicative of antiferromagnetic interactions,<sup>5</sup> and a paramagnetic moment close to the value of the free ion [33]. Powder neutron diffraction experiments show that nearest-neighbour antiferromagnetic correlations appearing below 100 K are progressively replaced by the development of ferromagnetic correlations below  $T = 2$  K. This reminds us the case of the classical spin-ice compounds where dipolar interactions overcome the nearest-neighbour antiferromagnetic exchange coupling resulting in an overall ferromagnetic interactions. An ordered magnetic phase is evidenced with a magnetic propagation wavevector  $\mathbf{k}_{\text{mag}} = (0, 0, 0)$  at  $T_c$ .<sup>6</sup> The magnetic structure is seen with magnetic moments canted away from the local axis [111] with an angle of  $\approx 13^\circ$  and their longitudinal components are arranged in the two-in/two-out configuration, i.e. an ordered spin-ice state, see the left panel of Fig. 1.15. A spontaneous magnetic moment of  $5.9 \mu_B$  is found [74]. However, whereas a peak is observed at the transition in specific heat measurements [74, 75], the analysis of the low temperature part raises some questions. Ions  $\text{Tb}^{3+}$  carry a nuclear spin  $I = \frac{3}{2}$ , and nuclear levels are split by Zeeman effect from the hyperfine field and a quadrupolar term arising from the electric field gradient acting at the rare earth site. Estimation of the hyperfine field leads to a smaller magnetic moment, i.e.  $4.5 \mu_B$ , compared to the one found by neutron diffraction [74, 76]. This feature was understood considering the spin fluctuations — or fluctuation of the

<sup>5</sup>Note that an estimation of the crystal-electric-field contribution yields a weaker but still antiferromagnetic Curie-Weiss constant  $\theta_{\text{CW}} \approx -6$  K [73]

<sup>6</sup>Note that irreducible representations allowed by the pyrochlore space group  $\text{Fd}\bar{3}m$  cannot account for the magnetic diffraction pattern and a solution was found by lowering the symmetry of the crystal (space group  $I4_1/amd$ ), i.e. magnetoelastic effects distort the crystal [74].

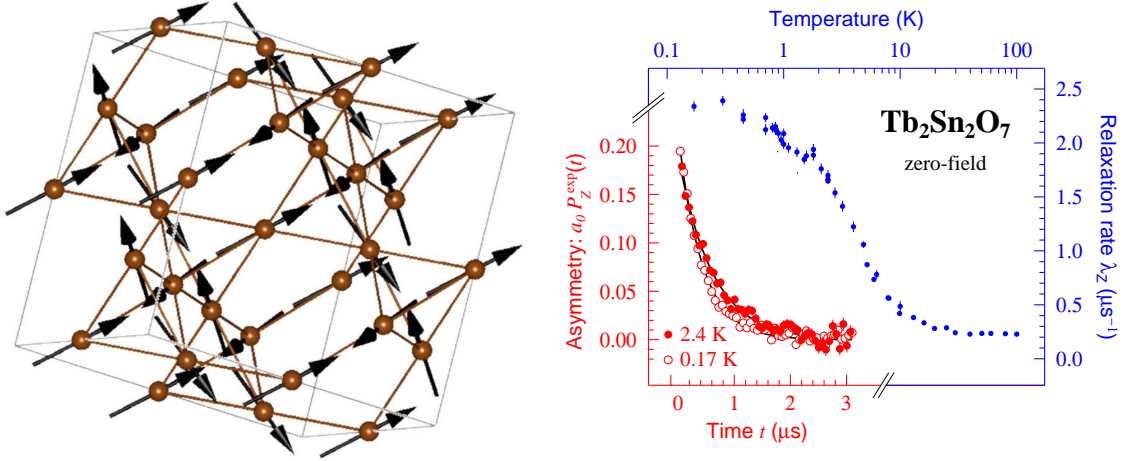


Figure 1.15: *Left: Magnetic structure of  $\text{Tb}_2\text{Sn}_2\text{O}_7$ : spins are slightly canted away from the  $[111]$  axis and their longitudinal components are in the "two-in/two-out" configuration. All tetrahedra are identical, defining the ordered spin-ice state. Reprinted from Ref. [76], copyright 2015, with permission from Elsevier. Right: Temperature dependence of the muon spin-lattice relaxation rate in zero-field  $\mu\text{SR}$  measurements and  $\mu\text{SR}$  spectra recorded in zero-field at  $T = 0.17$  and  $2.4$  K. No spontaneous oscillations are seen in the ordered phase. Data reproduced from Fig. 2 of Ref. [75].*

hyperfine field — leading to the non thermal equilibrium of the nuclear levels, and thus to a decrease of the nuclear specific heat [74]. Spin dynamics was confirmed by  $\mu\text{SR}$  experiments where no spontaneous oscillations are observed in the ordered phase and no clear evidence of a transition is seen in the temperature dependence of the spin-lattice relaxation rate [75, 77], see the right panel of Fig. 1.15. A characteristic fluctuation time  $\tau_c \approx 10^{-10}$  s was found. Additional measurements with the neutron spin-echo technique show the coexistence of static ( $q = 0.08 \text{ \AA}^{-1}$ ) [78] and dynamical spins [79] at larger wavevectors with a fluctuation time  $\tau_c = 2 \times 10^{-11}$  s. Polarised neutron diffraction experiments show that 60% of the spins remain static, contributing to the observation of magnetic Bragg peaks, whereas the remaining are responsible for the liquid-like diffuse magnetic background and fluctuating at  $\tau_c \approx 5 \times 10^{-11}$  s [80]. Finally, the analysis of the Bragg peak widths, the diffuse magnetic scattering and the small angle neutron scattering at  $T = 0.1$  K yield several spin correlation lengths [81], using high-resolution neutron diffraction experiments. In the same reference, neutron backscattering spectroscopy evidences a fluctuation time  $\tau_c = 1.3 \times 10^{-9}$  s. Therefore, the ground state of  $\text{Tb}_2\text{Sn}_2\text{O}_7$  is characterised by long and short-range correlation lengths and a distribution of fluctuation times, attesting the presence of dynamic spins coexisting with a long-range magnetic order.

### 1.5.2 $\text{Yb}_2\text{Ti}_2\text{O}_7$ vs $\text{Yb}_2\text{Sn}_2\text{O}_7$

$\text{Yb}_2\text{Ti}_2\text{O}_7$  is believed to be a realisation of a three-dimensional quantum spin-liquid system. It possesses a Kramers ground state doublet well isolated from the excited ones and a dominant planar anisotropy, see Chapter 3. A sharp peak in the temperature dependence of the specific heat indicates a transition at  $T_c = 0.24$  K [82]. A broad

hump is also observed at  $T \approx 2$  K, attributed to the development of short-range spin correlations and not to a Schottky anomaly since the first excited crystal-electric-field energy level is predicted to lie above 50 meV, see Chapter 3. Ferromagnetic interactions are inferred from the Curie-Weiss temperature  $\theta_{\text{CW}} = 0.75(10)$  K [83]. From the hyperfine field measured by Mössbauer spectroscopy, the magnetic moment carried by the  $\text{Yb}^{3+}$  moments is found to be equal to  $\approx 1.15 \mu_{\text{B}}$  and therefore, dipolar interactions are negligible [84]. In the same reference, magnetic moments are shown to be canted away from the local axis [111] with an angle of  $44(5)^\circ$ . The sharp transition observed in the temperature dependence of the  $\text{Yb}^{3+}$  magnetic moments, and the coexistence of paramagnetic and static moments, are indicative of a first-order transition [84]. This feature is confirmed by  $\mu\text{SR}$  and Mössbauer spectroscopies since the spin fluctuation rate undergoes a sharp decrease at  $T_c$  of three orders of magnitude, with a persistence of spin dynamics down to 40 mK with a characteristic fluctuation time  $\tau_c \approx 10^{-6}$  s [84], see left panel of Fig. 1.16. However, originally unpolarised and polarised neutron diffraction experiments seem to preclude the existence of a long-range magnetic ordering, see Refs. [84, 85]. Therefore, this candidate attracts a lot of attention in order to understand its magnetic ground state as a possible candidate to a quantum spin-liquid. The determination of the exchange couplings introduced in Eq. 1.12 becomes of prime importance. Analysing the spin wave dispersion measured by inelastic neutron scattering at  $T = 30$  mK under applied magnetic field, the authors of Ref. [60] find a set of values given in meV, i.e.  $\mathcal{I}_{zz} = 0.17(4)$ ,  $\mathcal{I}_{\pm} = 0.05(1)$ ,  $\mathcal{I}_{\pm\pm} = 0.05(1)$ , and  $\mathcal{I}_{z\pm} = -0.14(1)$ , putting this compound deep in the ferromagnetic state<sup>7</sup> shown in the left panel of Fig. 1.14. Note that despite the strong planar anisotropy, the Ising exchange coupling is dominant. These results allow to well describe zero-field specific heat data above 0.7 K [86] and the temperature dependence of the magnetisation under different applied magnetic fields [87]. The prediction of a long-range ferromagnetic order state is in agreement with some earlier measurements: Yasui *et al.* [88] have evidenced magnetic Bragg peaks at  $T = 0.03$  K with a reduction of the magnetic moment ( $1.1 \mu_{\text{B}}$ ) compared to the saturation value of the magnetisation measured at  $T = 5$  K ( $1.8 \mu_{\text{B}}$ ), indicative of canted magnetic moments. These results were strongly debated at the time since they contradict the conclusions of the aforementioned Refs. [84, 85]. Besides, neutron spin echo measurements at  $T = 0.18$  K show that the relaxation of the intermediate scattering function occurs out of the neutron spin echo time window, i.e. spin dynamics characterised by a fluctuation time  $\tau_c \leq 4$  ps [85] much faster than the one inferred from  $\mu\text{SR}$  ( $\tau_c \approx 10^{-6}$  s). However, polarised neutron experiments [89] supports the existence of a ferromagnetic state since a magnetic Bragg peak has been undoubtedly evidenced below  $T_c$ . An explanation for such different experimental results could arise from the possibility of stuffing, i.e. site exchange between ytterbium and titanium ions, or evaporation of the titanium, while growing single crystals by the optical floating zone technique [90]. This goes in line with specific heat measurements where a sharp peak at  $T_c$  is observed or not for powder samples or single crystals [91].

On the other hand, the sibling compound  $\text{Yb}_2\text{Sn}_2\text{O}_7$  exhibits very similar physical properties: ferromagnetic interactions deduced from  $\theta_{\text{CW}} = 0.51$  K [33], a sharp transition at  $T_c = 0.15$  K [92] in the temperature dependence of the specific heat, together

---

<sup>7</sup>According to Ref. [65], the phase diagram shown in the left panel of Fig. 1.14 is symmetric in  $\mathcal{I}_{z\pm} \rightarrow -\mathcal{I}_{z\pm}$ .

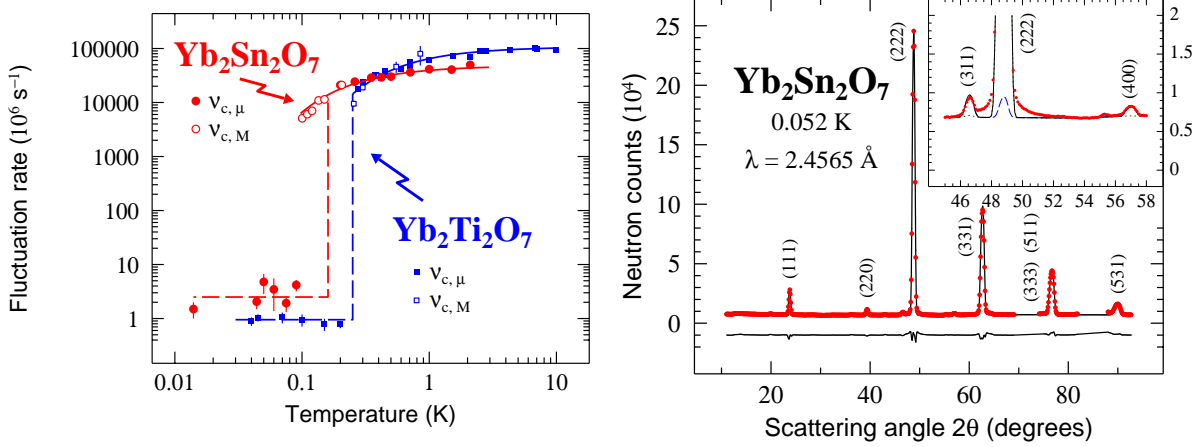


Figure 1.16: *Left: Fluctuation rate of spin dynamics measured by  $\mu\text{SR}$  ( $\nu_{c,\mu}$ ) and Mössbauer ( $\nu_{c,M}$ ) spectroscopies for  $\text{Yb}_2\text{Ti}_2\text{O}_7$  [83] (blue symbols) and  $\text{Yb}_2\text{Sn}_2\text{O}_7$  [92] (red symbols). Note that  $\mu\text{SR}$  experiments are necessary to probe slower spin dynamics since the Mössbauer time windows is limited to time  $t \leq 10^{-8} \text{ s}$ . Right: Powder neutron diffraction pattern of  $\text{Yb}_2\text{Sn}_2\text{O}_7$  recorded at 52 mK. Reprinted figures with permission from Ref. [92]. Copyright 2015 by the American Physical Society.*

with a broad hump around 2 K [92, 93]. The first-order nature of the transition is confirmed by  $\mu\text{SR}$  and Mössbauer spectroscopies where, similarly to  $\text{Yb}_2\text{Ti}_2\text{O}_7$ , a sharp increase in the temperature dependence of the  $\text{Yb}^{3+}$  magnetic moments, the coexistence of paramagnetic and static magnetic moments and an abrupt reduction of several orders of magnitude of the spin fluctuation rate is observed at the transition [92], see left panel of Fig. 1.16 for the latter property. A persistence of spin dynamics down to the lowest temperatures with a typical spin correlation time  $\tau_c \approx 3 \times 10^{-6} \text{ s}$  is also evidenced [92]. From the measurement of the hyperfine field with Mössbauer spectroscopy, the spontaneous magnetic moment  $m_{\text{sp}} = 1.1 \mu_{\text{B}}$  is tilted away from the [111] axis with an angle of  $65^\circ$ , leading to a stronger planar anisotropy compared to  $\text{Yb}_2\text{Ti}_2\text{O}_7$  [92, 94]. The main difference compared to the titanate compound resides in the presence of magnetic Bragg peaks with a magnetic propagation wavevector  $\mathbf{k}_{\text{mag}} = (0, 0, 0)$ : the diffraction pattern, see the right panel of Fig. 1.16, is very well refined using the  $\Gamma_9$  irreducible representation allowed by the  $Fd\bar{3}m$  space group: a spontaneous magnetic moment  $m_{\text{sp}} = 1.05(2) \mu_{\text{B}}$  has been inferred, very close to the Mössbauer value, with magnetic moments canted away from the  $z$  axis with the aforementioned angle [92]. Therefore, the name of splayed ferromagnetic state is coined [92]. However, no spontaneous oscillations are seen by  $\mu\text{SR}$  spectroscopy due to the persistence of spin dynamics [92, 94]. The latter assumption is supported by a.c. susceptibility measurements where a behaviour of spin freezing rather than a magnetic long-range order is put forward from the analysis of the imaginary part of the susceptibility, with a characteristic time of spin fluctuations  $\tau_c \approx 1.5 \times 10^{-6} \text{ s}$  at 0.13 K, compatible with the value inferred from  $\mu\text{SR}$  measurements [94]. Therefore, the magnetic ground state of  $\text{Yb}_2\text{Sn}_2\text{O}_7$  is one of the ferromagnetic states (Coulomb ferromagnet or Higgs ferromagnetic state) predicted in Ref. [65], see left panel of Fig. 1.14. The persistence of spin dynamics should place  $\text{Yb}_2\text{Sn}_2\text{O}_7$  close to the quantum spin liquid state [94].

### 1.5.3 $\text{Er}_2\text{Ti}_2\text{O}_7$ vs $\text{Er}_2\text{Sn}_2\text{O}_7$

$\text{Er}_2\text{Ti}_2\text{O}_7$  has a strong planar anisotropy, i.e. spins lie in a plane perpendicular to the local [111] axis, see Chapter 3. A sharp peak at  $T = 1.2$  K in the temperature dependence of the specific heat indicates a magnetic transition [82]. The analysis of the high temperature range of the magnetic susceptibility yields strong antiferromagnetic interactions deduced from the Curie-Weiss temperature  $\theta_{\text{CW}} = -15.9$  K and a paramagnetic moment close to the value of the free ion [95]. Powder neutron diffraction reveals the second-order nature of the transition and a long-range magnetic order with a magnetic propagation wavevector  $\mathbf{k}_{\text{mag}} = (0, 0, 0)$  [96]. The magnetic structure is characterised by the so-called  $\Psi_2$  state, see Tab. D.1, basis vector of the irreducible representation  $\Gamma_5$  [97]. The corresponding spin configuration over a tetrahedron is shown in the left panel of Fig. 1.5. The authors of Refs. [96, 98] show that an order by disorder mechanism [15] through thermal fluctuations selects the  $\Psi_2$  state. However the transition is predicted to be first order in contradiction with experimental results. The four symmetry-allowed exchange couplings introduced in Eq. 1.12 are determined from the analysis of spin wave dispersion under magnetic fields [17] and given in  $10^{-2}$  meV:  $\mathcal{I}_{zz} = -2.5(1.8)$ ,  $\mathcal{I}_{\pm} = 6.5(8)$ ,  $\mathcal{I}_{\pm\pm} = 4.2(5)$ , and  $\mathcal{I}_{z\pm} = -0.88(1.5)$ . Note here that the transverse exchange constants are dominant. We can mention that these parameters are roughly similar to those determined from zero-field diffuse neutron scattering intensity maps [2]. More importantly, the second order nature of the phase transition is restored with the introduction of quantum fluctuations [14, 17, 99].<sup>8</sup>

Coexistence of short-range spin correlations and long-range order has been evidenced in Ref. [101] from the sharpening of the magnetic Bragg peaks and reduction of the diffuse scattering when applying a magnetic field. The presence of spin dynamics in the ordered phase has been confirmed by the absence of spontaneous oscillations by  $\mu\text{SR}$  spectroscopy [2, 102], similarly to the ordered compound  $\text{Tb}_2\text{Sn}_2\text{O}_7$ . However, zero-field  $\mu\text{SR}$  spectra cannot be described by usual muon depolarisation functions, and the origin of its shape remains mysterious. Applying strong longitudinal magnetic field — but lower than the critical field  $H_c = 2$  T inducing a phase transition [103]— allows to recover a usual exponential decay of the muon depolarisation spectrum, as displayed in the left panel of Fig. 1.17.

On the other side, the XY stannate counterpart  $\text{Er}_2\text{Sn}_2\text{O}_7$  does not display any long-range magnetic order down to  $T = 0.13$  K from magnetic susceptibility measurements [33] and down to  $T = 0.02$  K from  $\mu\text{SR}$  experiments [102] which suggests a dynamical nature of the ground state. In the former reference, the analysis of the high temperature range of the magnetic susceptibility reveals that  $\text{Er}_2\text{Sn}_2\text{O}_7$  has a paramagnetic moment very close to the value of the free ion while the Curie-Weiss temperature  $\theta_{\text{CW}} = -14$  K indicates antiferromagnetic interactions smaller than those in  $\text{Er}_2\text{Ti}_2\text{O}_7$ . The absence of magnetic order was also confirmed later by neutron diffraction down to  $T = 100$  mK, but diffuse magnetic scattering was evidenced starting from  $T = 5$  K down to the lowest temperatures, indicative of the apparition of short-range spin correlations [105]. This freezing of spin dynamics is confirmed by the hysteresis effect in field cooling/zero-field cooling below  $T = 0.2$  K in the temperature dependence of the

---

<sup>8</sup>We should mention that authors of Ref. [100] propose an alternative explanation to the order by disorder mechanism selecting the  $\Psi_2$  state and stabilizing a long-range magnetic order by considering an admixture of the low-lying excited crystal-electric-field energy levels.

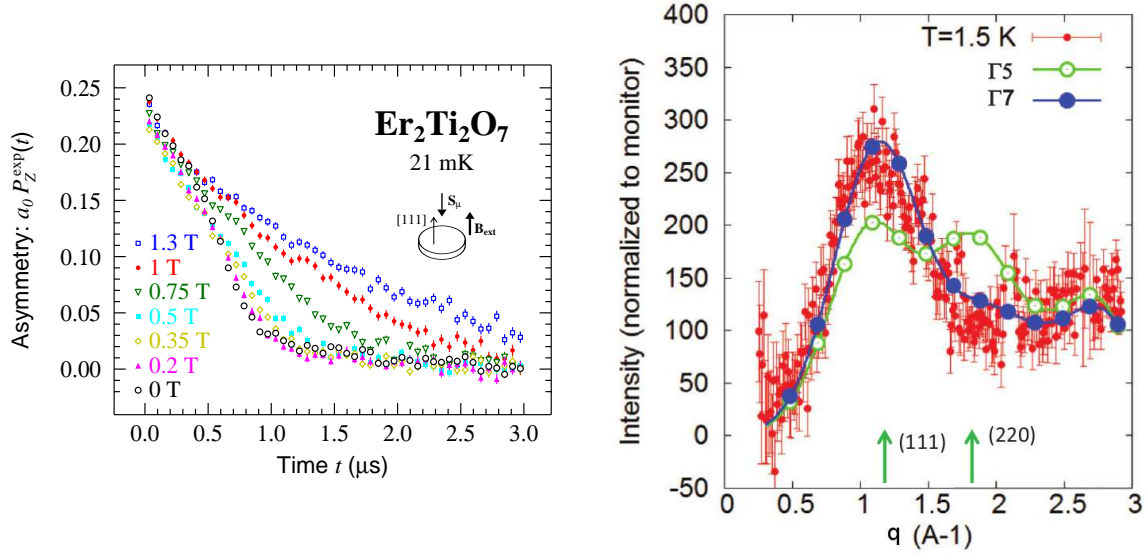


Figure 1.17: *Left: Zero and longitudinal fields  $\mu$ SR spectra of a  $\text{Er}_2\text{Ti}_2\text{O}_7$  crystal sample recorded deep into the ordered phase at  $T = 21$  mK. For magnetic fields  $H \geq 0.5$  T, an exponential decay is recovered. Reprinted figure with permission from Ref. [2]. Copyright 2015 by the American Physical Society. Right: Diffuse magnetic scattering of  $\text{Er}_2\text{Sn}_2\text{O}_7$  analysed following spin correlations described by the  $\Gamma_5$  (green line) or the  $\Gamma_7$  (blue line) irreducible representations, the latter corresponding to the Palmer-Chalker state. Reprinted figure with permission from Ref. [104]. Copyright 2015 by the American Physical Society.*

magnetisation and the frequency dependence of the peak observed in the imaginary part of the a.c. susceptibility [104]. In the latter reference, the magnetic diffuse scattering recorded at  $T = 1.5$  K is analysed in terms of spin correlations according to the spin configuration corresponding to the three-dimensional  $\Gamma_7$  irreducible representation,<sup>9</sup> i.e. the Palmer-Chalker state introduced in Sec. 1.2, as shown in the right panel of Fig. 1.17. However, it should be noted that an experimental report from ILL [106] suggests from neutron diffraction experiments on  $\text{Er}_2\text{Ti}_{2-x}\text{Sn}_x\text{O}_7$  that  $\text{Er}_2\text{Sn}_2\text{O}_7$  enters a long-range magnetic order at  $T_c \approx 0.1$  K.

#### 1.5.4 $\text{Gd}_2\text{Ti}_2\text{O}_7$ vs $\text{Gd}_2\text{Sn}_2\text{O}_7$

The case of pyrochlore compounds with gadolinium ion is slightly apart from the other rare earths since Gd does not possess an orbital momentum (the  $4f$  electronic shell is half-filled). Therefore, the spin anisotropy resulting from the crystal-electric-field should not play any role: thus, spins are expected to be Heisenberg. Still, electron paramagnetic resonance measurements reveal an XY anisotropy of the spins and with a strength non negligible compared to exchange and dipolar energies for  $\text{Gd}_2\text{Ti}_2\text{O}_7$  [107] and  $\text{Gd}_2\text{Sn}_2\text{O}_7$  [108]. In the latter compound, the strength of the anisotropy is about one-third lower than in the titanate one.

Both compounds display antiferromagnetic interactions with a Curie-Weiss temper-

<sup>9</sup>Note that this analysis does not allow to distinguish which basis vectors  $\Psi_{4,5,6}$  are involved.

ature  $\theta_{\text{CW}} \approx -9.5$  and  $-9.4$  K for  $\text{Gd}_2\text{Ti}_2\text{O}_7$  [8, 109] and  $\text{Gd}_2\text{Sn}_2\text{O}_7$  [109, 110]. The paramagnetic moment is very close to the expected value of the free ion, i.e.  $7.94 \mu_{\text{B}}$ .

$\text{Gd}_2\text{Ti}_2\text{O}_7$  exhibits two transitions in specific heat measurements [8, 111, 112] at  $T_{\text{c},1} = 1$  K and  $T_{\text{c},2} = 0.74$  K. The computed magnetic entropy reaches  $\approx 90\%$  of the expected  $R\ln(2S + 1) = R\ln 8$  value for the free ion. Powder neutron diffraction experiments initially revealed below  $T_{\text{c},2}$  a single  $\mathbf{k}_{\text{mag}} = (\frac{1}{2}, \frac{1}{2}, \frac{1}{2})$  magnetic structure where magnetic moments lying in the Kagome planes are static whereas those belonging to the triangular planes remain dynamic [113].<sup>10</sup> However, the authors of Ref. [114] show that the only possible configuration allowing to account for a supplementary magnetic Bragg peak located at  $(\frac{1}{2}, \frac{1}{2}, \frac{1}{2})$  and to be consistent with the correlation length deduced from magnetic diffuse scattering intensity recorded with polarised neutrons is a  $4\text{-}k_{\text{mag}}$  structure with spins perpendicular to the local [111] axis. Furthermore, 25% of the spins are not ordered in the temperature range  $T_{\text{c},2} \leq T \leq T_{\text{c},1}$  and this fraction of the spins partially orders at  $T = T_{\text{c},2}$ , i.e. they carry a magnetic moment of  $1.9 \mu_{\text{B}}$  whereas the fully ordered spins carry a magnetic moments close to the value expected for the free ion. Hence, the magnetic ground state is very peculiar, exhibiting a partially ordered magnetic structure with spins remaining strongly fluctuating. The latter property was confirmed by  $\mu\text{SR}$  spectroscopy: whereas spontaneous oscillations are observed in zero-field measurements as a signature of a long-range magnetic order, persistence of spin dynamics is evidenced down to 20 mK with a characteristic fluctuation time  $\tau_c = 0.7(2)$  ns [112].<sup>11</sup> With the purpose of confirming the proposed magnetic ground state, neutron spin echo measurements show at  $T = 110$  mK that 80% of the intermediate scattering function is constant as a proof of static spins behaviour. The remaining 20% of the signal is missing, meaning that spins fluctuate faster than the NSE window time [115].

On the other hand,  $\text{Gd}_2\text{Sn}_2\text{O}_7$  undergoes a single transition at  $T \approx 1$  K [117]. From Mössbauer spectroscopy, the spontaneous magnetic moment in the ordered phase is found to be  $\approx 7 \mu_{\text{B}}$ , and its temperature dependence indicates a first order transition [117]. Neutron diffraction measurements reveals a magnetic structure with  $\mathbf{k}_{\text{mag}} = (0, 0, 0)$  and magnetic moments with an XY anisotropy lying parallel to the edges of the tetrahedron [9]. This magnetic structure correspond to the Palmer-Chalker state [7] described earlier in Sec. 1.2 for classical Heisenberg spins interacting through nearest-neighbour antiferromagnetic exchange and dipolar interactions. An explanation to the difference observed between the magnetic ground states of these two gadolinium compounds could arise from a different third-neighbour exchange coupling [9]. Despite the magnetic long-range order confirmed by the presence of spontaneous oscillations observed by  $\mu\text{SR}$  spectroscopy [116, 118], persistent spin dynamics down to  $\approx 20$  mK is deduced in Mössbauer spectroscopy from the analysis of the relative intensities of Mössbauer lines leading to a population of the nuclear levels more even than predicted by the Boltzmann population factor, indicative of spins fluctuations [119, 120]. These spin fluctuations are characterised by a characteristic time out of the Mössbauer time window, i.e.  $\tau_c < 1.2 \times 10^{-8}$  s for  $\text{Gd}^{3+}$ . The latter feature is confirmed by the non vanishing

<sup>10</sup>We refer to Fig. A.2 to see that looking in the  $\langle 111 \rangle$  directions, magnetic ions belong alternately to triangular and Kagome planes.

<sup>11</sup>A stretched exponential function is used to analyse  $\mu\text{SR}$  data with an exponent  $\beta_{\text{se}} \approx 0.5$  and  $\beta_{\text{se}} \approx 0.75$  for  $T \leq T_{\text{c},2}$  and  $T \leq T_{\text{c},1}$ , respectively [112].

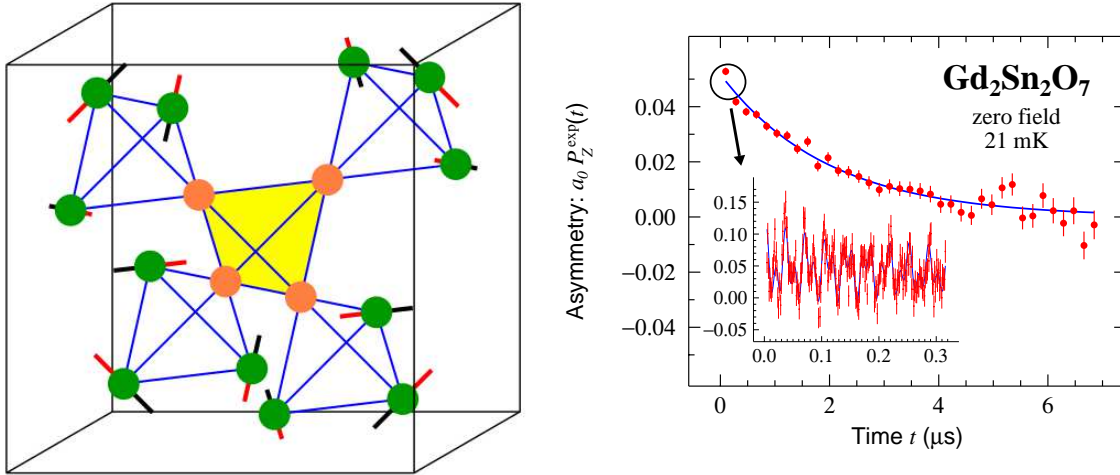


Figure 1.18: *Left: Illustration of the  $4-k_{\text{mag}}$  magnetic structure in  $\text{Gd}_2\text{Ti}_2\text{O}_7$ . The green spheres show magnetic ions ordering for  $T_{c,2} \leq T \leq T_{c,1}$  and the orange ones those remaining dynamics in this temperature range, and which partially order below  $T_{c,2}$ . Copyright IOP Publishing. Picture reproduced from Ref. [114] by permission of IOP Publishing. All rights reserved. Right: zero field  $\mu\text{SR}$  spectrum of  $\text{Gd}_2\text{Sn}_2\text{O}_7$  recorded at 21 mK. A zoom over the shortest times displays the spontaneous oscillations of the muon spin attesting from the long-range nature of the magnetic state, but still an exponential decay is observed at longer times as a signature of persistent spin dynamics. Reprinted from Ref. [116], copyright 2015, with permission from Elsevier.*

plateau of the spin-lattice relaxation rate revealed by  $\mu\text{SR}$  spectroscopy [116, 118].

## 1.6 Content of the manuscript

The present work focuses on low temperature properties of geometrically frustrated magnetic compounds: the two pyrochlore series  $R_2\text{Ti}_2\text{O}_7$  and  $R_2\text{Sn}_2\text{O}_7$  where  $R$  is a rare earth. We will outline in this section the content of each following chapters.

The second chapter will introduce the different experimental techniques used in this work in order to characterise the physical properties of the investigated compounds. Laboratory experiments have been conducted at INAC, CEA-Grenoble, which include X-ray diffraction and bulk measurements such as specific heat and magnetisation measurements. Large scale facilities — the Institut Laue-Langevin (ILL), the Rutherford Appleton laboratory (ISIS) and the Paul Scherrer Institut — allowed us to perform experiments with a wide panel of techniques: X-ray synchrotron radiation, neutron diffraction, neutron time-of-flight, neutron backscattering and  $\mu\text{SR}$  experiments will be described.

The third chapter is devoted to the study of the crystal-electric-field acting at the rare earth site, which is of prime importance since it provides the energy levels scheme of the rare earth, the spin anisotropy, and the wavefunctions of the different states for instance. Within the approximation that only the ground state term arising from the spin-orbit coupling needs to be taken into account, i.e. using the Stevens Hamiltonian,

a global analysis of published and measured inelastic neutron scattering spectra aims to characterise each pyrochlore series of interest with a single set of crystal-electric-field parameters.

The fourth chapter will present numerous results obtained on the pyrochlore compound  $\text{Nd}_2\text{Sn}_2\text{O}_7$  with a wide panel of techniques. This compound undergoes a second-order magnetic transition at  $T_c = 0.91$  K, with an all-in-all-out spin configuration. The long-range order nature is confirmed by the observation of spontaneous oscillations in  $\mu\text{SR}$  experiments. However, persistent spin dynamics is observed in the ordered state and ascribed to low-energy spin loops excitations. Anomalously slow spin fluctuations are also evidenced in the paramagnetic state.

The following chapter deals with one of the most intriguing pyrochlore compound over the past few years:  $\text{Tb}_2\text{Ti}_2\text{O}_7$ . A review of its different physical properties will be presented before a discussion on the two possible magnetic ground states: X-ray synchrotron radiation and  $\mu\text{SR}$  Knight shift measurements are brought to shed light if a Jahn-Teller transition occurs or if this compound is a realisation of a quantum spin-ice state.

General conclusions and some perspectives for future work are given in the last chapter.

Finally, several appendices are provided in order to give further information on: (i) the crystallography of the pyrochlore compounds, (ii) the point charge model supporting the existence of a scaling law between crystal-electric-field parameters of different compounds and mandatory to a global analysis of the crystal-electric-field properties, (iii) the correction of the neutron absorption included in the analysis of neutron time-of-flight data, (iv) some basics of group theory for the determination of magnetic structures and an analytical evidence confirming the selection of the irreducible representation for  $\text{Nd}_2\text{Sn}_2\text{O}_7$ , and finally (v) some necessary theoretical tools to understand and analyse  $\mu\text{SR}$  data.

We finish the overview of the manuscript by mentioning some other aspects investigated during this PhD thesis which are not included in the manuscript. The spin dynamics of  $\text{Er}_2\text{Ti}_2\text{O}_7$  in the ordered and paramagnetic states has been probed using the neutron spin-echo technique and results are currently being analysed at the time of writing. Spinel compounds of chemical formula  $\text{Cd}_2\text{R}_2\text{X}_4$ , where  $R = \text{Ho}$  or  $\text{Yb}$  and  $X = \text{S}$  or  $\text{Se}$ , which present the same frustrated network as the pyrochlore compounds, have been studied by means of X-ray diffraction, specific heat, magnetisation, and  $\mu\text{SR}$  measurements. These results are not discussed here in order to keep the coherence of the manuscript, focusing on the pyrochlore series.

# Chapter 2

## Experimental techniques

### Contents

---

<b>2.1</b>	<b>Bulk measurements</b>	<b>41</b>
2.1.1	Specific heat	41
2.1.2	Magnetometry	43
<b>2.2</b>	<b>Facilities for microscopic probe measurements</b>	<b>45</b>
2.2.1	Institut Laue Langevin (ILL), a continuous neutron source	45
2.2.2	ISIS, a muon and neutron pulsed source	46
2.2.3	A neutron and muon pseudo-continuous source at PSI	46
2.2.4	A third generation synchrotron at PSI	46
<b>2.3</b>	<b>Diffraction experiments</b>	<b>47</b>
2.3.1	Introduction to diffraction	47
2.3.2	Nuclear or charge scattering	47
2.3.3	Magnetic scattering	49
2.3.4	Powder diffractometers	50
2.3.5	X-ray experiments	50
2.3.6	Neutron experiments	51
2.3.7	The Rietveld refinement	52
<b>2.4</b>	<b>Neutron time-of-flight spectroscopy</b>	<b>54</b>
2.4.1	The MARI spectrometer	54
2.4.2	Energy resolution	55
<b>2.5</b>	<b>Neutron backscattering spectroscopy</b>	<b>56</b>
2.5.1	The IN16 spectrometer	56
2.5.2	The backscattering process	57
2.5.3	Spectroscopy	59
<b>2.6</b>	<b>Muon spectroscopy</b>	<b>59</b>
2.6.1	Introduction	60
2.6.2	Experimental details	60

2.6.3	Pseudo-continuous versus pulsed source . . . . .	61
2.6.4	Muon spectrometers . . . . .	62
2.6.5	Polarisation functions . . . . .	63
2.6.6	Muon Knight shift measurements . . . . .	65

---

In this chapter are detailed the different techniques used in this work: specific heat and magnetisation measurements, X-ray and neutron diffraction, neutron time-of-flight and neutron backscattering spectroscopies and finally positive muon spin relaxation spectroscopy. The different facilities visited along this work will be briefly introduced.

## 2.1 Bulk measurements

Bulk experiments such as specific heat and magnetisation measurements are briefly discussed in this section.

### 2.1.1 Specific heat

The specific heat experiments have been conducted at CEA-Grenoble, using a Quantum Design PPMS (Physical Property Measurement System) to perform experiments down to 0.4 K. The temperature of 1.9 K is reached with a first  $^4\text{He}$  cooling equipment. A  $^3\text{He}$  stick can be inserted in the sample space in order to extend the experimental temperature down to 0.4 K. The system is kept adiabatic with a secondary vacuum needed to ensure no heat losses by exchange gas.

The heat capacity characterises the amount of heat to bring to the sample to increase its temperature and it is defined as follows [121]:

$$c_p = \lim_{\delta T \rightarrow 0} \left( \frac{\delta Q_h}{\delta T} \right)_p, \quad (2.1)$$

where  $Q_h$  is a heat input brought to the sample, and the index  $p$  refers to constant pressure. Since the heat capacity is an extensive quantity, one rather works with the specific heat  $C_p$ , being the heat capacity divided by the number of moles. Note that difference between specific heat measured at constant volume ( $C_v$ ) or pressure ( $C_p$ ) is not relevant due to the low compressibility of the studied compounds, i.e.  $C_p - C_v = p \left( \frac{\partial V}{\partial T} \right)_p$  [122].

The PPMS employs the thermal-relaxation technique by measuring the response of the sample after a heat perturbation. In the left panel of Fig. 2.1 is shown the puck used for  $^3\text{He}$  measurements: the sample is placed at the centre of a platform linked by four threads of thermal conductance  $K_1$  to the cryostat. Apiezon N grease ensures a good thermal conductivity between the sample and the platform. Its specific heat temperature dependence is displayed in the left panel of Fig. 2.2. A simplified experimental set up scheme is given in the right panel of Fig. 2.1. We denote  $T_x$ ,  $T_a$  and  $T_0$  the temperatures of respectively the sample, the platform and the cryostat,  $P$  the thermal power applied to the platform and  $c_x$  and  $c_a$  the heat capacity of the sample and the platform. Performing the heat-balance [121] of the platform and sample, we

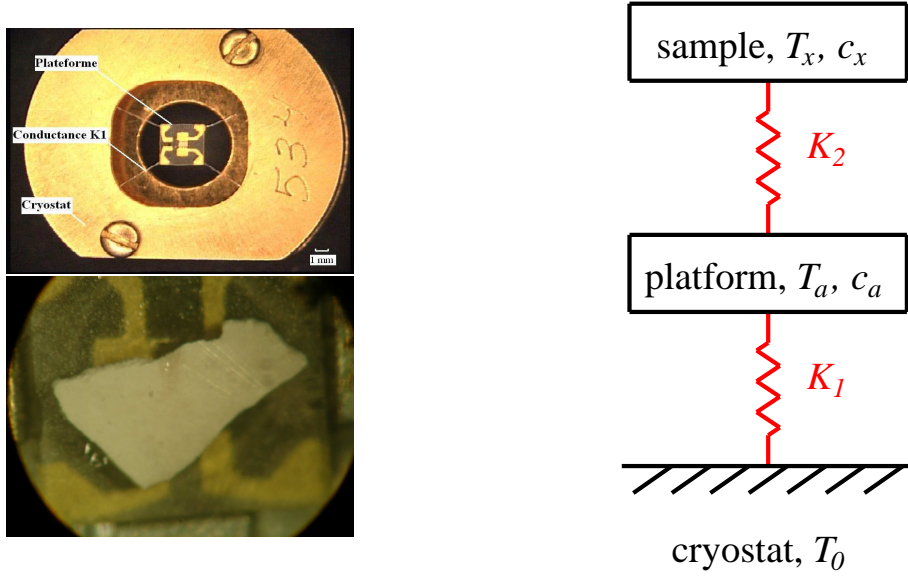


Figure 2.1: Left: On the top panel is shown a picture of the puck used for  $^3\text{He}$  measurements. The sample is placed on the centre of the platform as illustrated in the picture at the bottom. Right: simplified scheme of the PPMS. The heat transfer between the sample and the platform is controlled by a thermal conductance  $K_2$ . The contact between the platform and the cryostat is ensured by four threads of total thermal conductance  $K_1$ .

derive:

$$\begin{cases} P = c_a \frac{dT_a}{dt} + K_2(T_a - T_x) + K_1(T_a - T_0), \\ 0 = c_x \frac{dT_x}{dt} + K_2(T_x - T_a). \end{cases} \quad (2.2)$$

Considering the thermal conduction between the sample and the platform to be important, i.e.  $K_2 \gg K_1$ , see right panel of Fig. 2.1, it results  $T_x \simeq T_a$ . Thus, Eq. 2.2 becomes:

$$P = (c_x + c_a) \frac{dT_x}{dt} + K_1(T_x - T_0). \quad (2.3)$$

A thermal power  $P$  is applied to increase the sample temperature from  $T_0$  to  $T_0 + \Delta T_1$  at a time  $t_f \rightarrow \infty$ . The solution of Eq. 2.3 is then:

$$T_x(t) = T_0 + \Delta T_1 [1 - \exp(-t/\tau_1)], \quad (2.4)$$

where  $\Delta T_1 = P/K_1 \approx 0.01T_0$  and  $\tau_1 = (c_x + c_a)/K_1$  is the relaxation time. Then, cutting the heat power at a time  $t'$ , the sample temperature relaxes down to the temperature set point from  $T_x(t') = T_0 + \Delta T_2$  to  $T_0$ . The solution of Eq. 2.3 becomes:

$$T_x(t) = T_0 + \Delta T_2 \exp(-(t - t')/\tau_1), \quad (2.5)$$

As  $K_1$  is determined by the estimation of  $\Delta T_1$  and  $c_a$  is tabulated, the measure of  $\tau_1$  gives access to the specific heat of our sample. This technique is illustrated in the

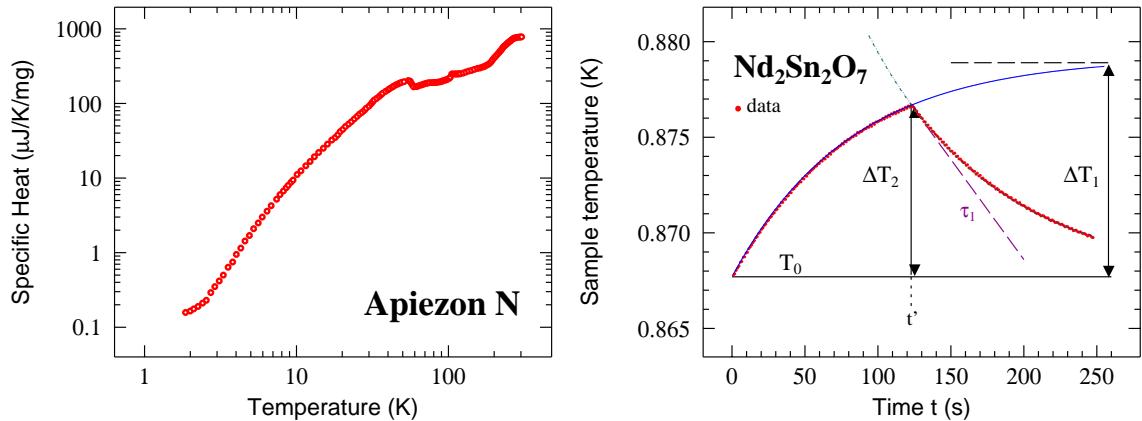


Figure 2.2: Left: Temperature dependence of the Apiezon N specific heat measured by Y. Chapuis [123]. Right: Evolution of the temperature of a  $\text{Nd}_2\text{Sn}_2\text{O}_7$  sample powder to illustrate the relaxation technique. Raw data are displayed by red circles, the full blue line and the green dotted line are a fit using Eq. 2.4 and Eq. 2.5 respectively, the black dashed line is the asymptotic value of Eq. 2.4, the purple dashed-dotted line is the tangent at the origin allowing to determine  $\tau_1$ .

right panel of Fig. 2.2. Practically, it is also checked that the relaxation time between the platform and the cryostat is negligible which is indicative of the goodness of the measurement as it justifies the hypothesis  $K_2 \gg K_1$ .

It has been observed that in some temperature range where the specific heat of the measured sample becomes small, the contribution of the grease should be taken into account. Then, a preliminary measurement of the puck with an appropriate amount of grease is performed. The grease contribution is then interpolated and subtracted from the total specific heat.

### 2.1.2 Magnetometry

Magnetisation experiments have been performed with a Quantum Design MPMS (Magnetic Property Measurement System) at INAC, CEA-Grenoble. This magnetometer gives access to a temperature range from 300 to 2 K thanks to a  $^4\text{He}$  cryostat and a magnetic field up to  $\mu_0 H_{\text{ext}} = 5.5$  T. From this technique is obtained the magnetisation curve  $M = f(H)$  and the bulk magnetic susceptibility defined in the linear approximation (weak magnetic fields) as:

$$\chi = \lim_{H_{\text{ext}} \rightarrow 0} \frac{\partial M}{\partial H_{\text{ext}}} = \frac{M}{H_{\text{ext}}}. \quad (2.6)$$

The MPMS is equipped with a SQUID sensor (Superconducting QUantum Interference Device) and it is illustrated in the left panel of Fig. 2.3 whereas the relevant constituents are displayed in the right panel of Fig. 2.3. The magnetic moment is measured thanks to the extraction method with a precision up to  $1 \times 10^{-11}$  A.m<sup>2</sup>.

A superconducting electromagnet applies a static magnetic field in which the sample is moved. The magnetic flux variation caused by the sample motion induces a current in the three superconducting detection coils configured as a second order gradiometer [124], thus avoiding external magnetic fields perturbations. These detection coils

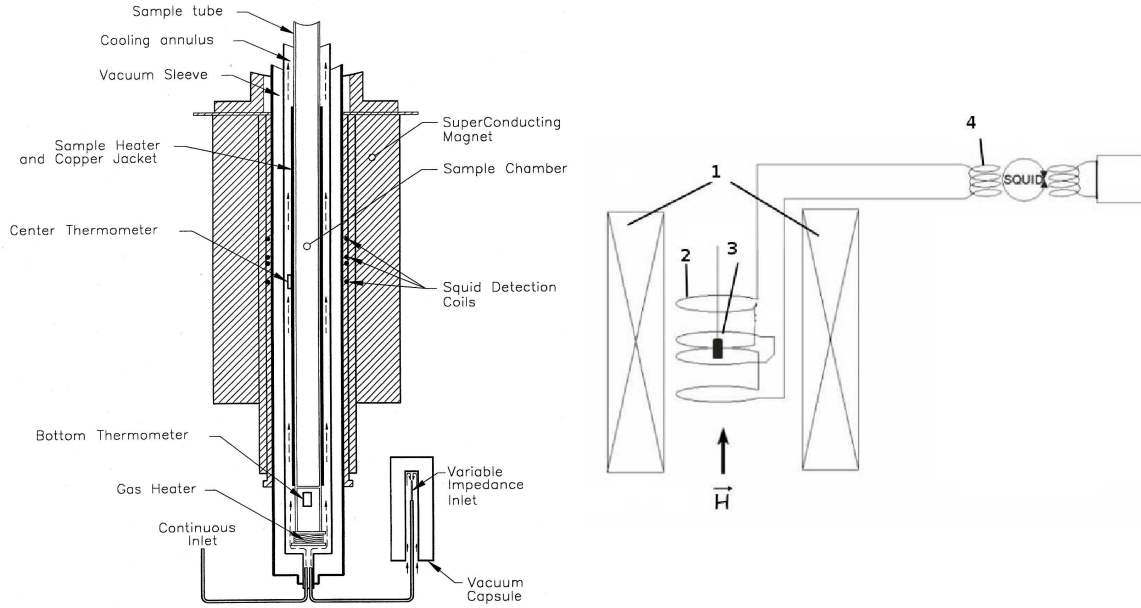


Figure 2.3: *Left: Schematic view of the Quantum Design MPMS [125]. Right: Insight on the relevant constituents involved in the extraction method [126]: (1) Superconducting electromagnet applying a magnetic field  $\mu_0 \mathbf{H}_{\text{ext}}$  at the sample. (2) Superconducting detection coils. (3) Sample moving along the field direction. (4) Input coils and SQUID sensor.*

are connected to the input coil of the SQUID sensor located outside from the sample environment. The sensor is constituted by an annular superconductor with two Josephson junctions inserted in the loop as illustrated in the left panel of Fig. 2.4 and providing a high sensitivity for the detection of magnetic field.

This technique allows us to measure the magnetic susceptibility. As this quantity is measured at small applied magnetic field  $\mu_0 H_{\text{ext}}$  to fulfil the linear approximation, see Eq. 2.6, the real field  $\mu_0 H_{\text{applied}}$  at the sample need to be precisely known, since it differs from the set up value due to the presence of a remanent field of several Oersted in the superconducting magnet. The paramagnet octa-hydrate sulfate of gadolinium ( $\text{Gd}_2(\text{SO}_4)_3 \cdot 8\text{H}_2\text{O}$ ) permits to precisely determine the real field: magnetic interactions are negligible between the spins of the gadolinium  $S = \frac{7}{2}$  as they are magnetically isolated by the  $\text{H}_2\text{O}$  molecules. Through the temperature dependence of its magnetic moment, the real applied field can be measured.

The inverse magnetic susceptibility is plotted in the right panel of Fig. 2.4. We compare preliminary measurements where two different weakly diamagnetic sample holders were used: a cylindrical one in the first case whereas in the second case a flat pellet was introduced in a straw, applying the magnetic field in the pellet plane. In the latter case, the measured magnetic susceptibility is increased since the geometry of our sample reduces the demagnetising field. Therefore, measurements displayed in Chapter ?? are performed with an ellipsoidal pellet.

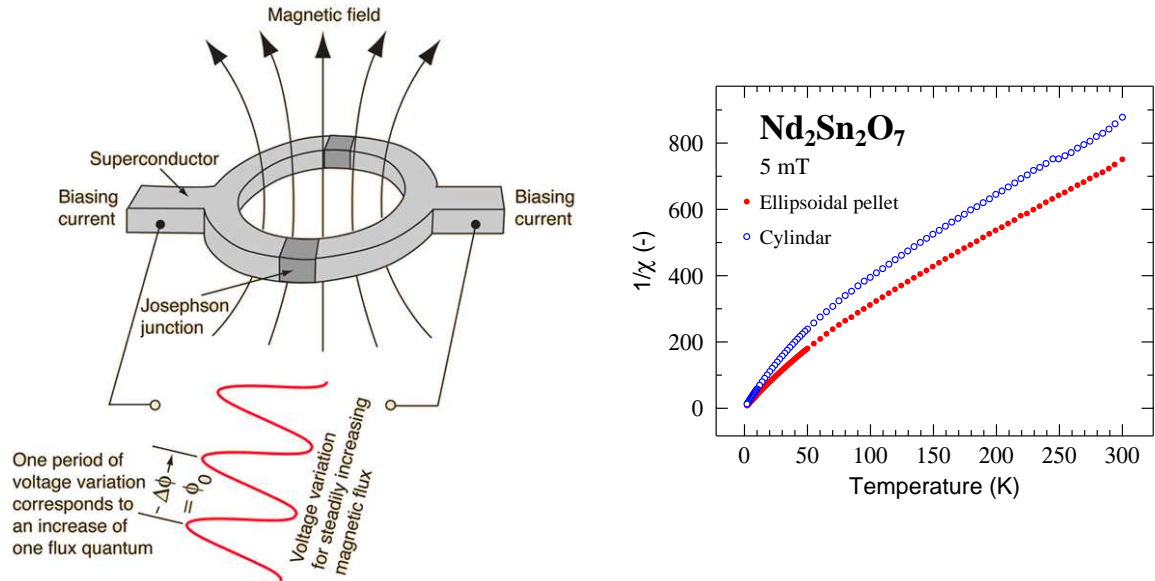


Figure 2.4: *Left: Schematic illustration of the SQUID sensor. A superconducting loop is interrupted by two Josephson junctions. The Josephson effect is the ability to sustain a current with a zero voltage through the tunnelling of Cooper pairs up to the critical current  $I_c$ . To a static magnetic flux, the Josephson junctions current is enslaved to  $I_c$ . The concept is based on the quantisation of the magnetic flux ( $\Phi_0 = \frac{h}{2e}$ ). To a variation of the magnetic flux inside the loop will appear a sinusoidal screening current in the superconducting ring with a period equal to the number of quantum flux changes, and thus a voltage at the Josephson junction with same characteristics as the screening current. Picture taken from Ref. [127]. Right: Inverse of the magnetic susceptibility versus temperature: comparison of a powder filling a cylindrical sample holder and the case where the field is applied in the plane of a flat pellet. In the latter case, the magnetic susceptibility is increased.*

## 2.2 Facilities for microscopic probe measurements

We briefly present the different facilities, illustrated in Fig. 2.5, where are located the different instruments introduced in this chapter.

### 2.2.1 Institut Laue Langevin (ILL), a continuous neutron source

Located at Grenoble, the ILL is a nuclear reactor which provides a high neutron flux. The neutron production is based on the fission of  $^{235}\text{U}$ . A heavy water ( $\text{D}_2\text{O}$ ) moderator at 300 K gives, through inelastic collisions of the neutrons with the nuclei of the moderator, a continuous beam of thermal neutrons with a Maxwellian energy distribution centred at  $\lambda_c = 1.2 \text{ \AA}$  and a flux  $\phi_n = 1.5 \times 10^{15} \text{ n cm}^{-2} \text{ s}^{-1}$  [128]. The diffractometers described here are supplied by these thermal neutrons, see Sec. 2.3.4, whereas the backscattering spectrometer is fed with cold neutrons located in the guide H53, see Sec. 2.5, using a liquid deuterium moderator at 25 K.



Figure 2.5: View of the different facilities encountered during this work: the Institut Laue Langevin (left), ISIS (middle), and the Paul Scherrer Institut (right).

### 2.2.2 ISIS, a muon and neutron pulsed source

ISIS is a neutron spallation and muon source of the Rutherford Appleton laboratory, United Kingdom. To produce neutrons and muons,  $H^-$  ions are accelerated up to 70 MeV in a linear accelerator (Linac) with radiofrequency cavities providing a sinusoidal electric field, and are stripped through an aluminium oxide target to produce protons. Then a continuous beam of protons is injected in the synchrotron. Protons are accelerated up to 800 MeV with radiofrequency cavities where an oscillating field is applied to create two bunches of particles separated by a time of 330 ns. Dipole magnets bend the beam to ensure a circular trajectory in the cyclotron and multipolar magnets focus the beam. Four out of five bunches are propelled to Target Station 1, where the neutron and muon spectrometers of interest are located. About 3 % of the incident flux is dedicated to the production of muons, as explained in Sec. 2.6.2. The remaining protons encounter a tantalum target to produce neutrons ( $\approx 4 \times 10^{14}$  neutrons produced per proton pulse) through a so-called spallation process.

### 2.2.3 A neutron and muon pseudo-continuous source at PSI

The Paul Scherrer Institut, located in Switzerland, owns a neutron spallation and muon source. Three accelerators set up in cascade provide a high energy proton beam up to 590 MeV: a Cockcroft-Walton pre-accelerator (energy up to 870 keV) brings protons in a 4-sector injector cyclotron (energy up to 72 MeV) and then the main cyclotron permits to reach the final energy up to 590 MeV to produce a high intensity beam with bunches separated by a time approximately equal to 20 ns. The beam passes through two pion targets to produce muons for the Swiss Muon Source (S $\mu$ S), see Sec. 2.6.2. Thus, the remaining protons are deviated to the neutron spallation source (SINQ facility) where the incident protons interact with a lead target to provide high energy neutrons that are slowed down in a heavy water moderator. The resulting thermal neutron flux is  $\phi_n \approx \times 10^{14} \text{ n cm}^{-2} \text{ s}^{-1}$  [129].

### 2.2.4 A third generation synchrotron at PSI

Not only a muon and a neutron source, the Paul Scherrer Institut has a third-generation synchrotron, the Swiss Light Source (SLS). A 288 m circumference storage ring produces a very large light spectrum, from infrared to hard X-rays, thanks to an electron beam reaching an energy of 2.4 GeV. The synchrotron light is produced either with bending

magnets resulting in photons with a wide energy spectrum, or with undulators in the straight part of the ring which are composed of a periodic arrangement of permanent magnets, and select the desired wavelength by tuning the magnetic field. A much more intense and narrow beam is achieved compared to the one resulting from the usual bending magnet [129].

## 2.3 Diffraction experiments

Powder diffraction is a well suited technique for the identification of crystalline phases but also for a quantitative analysis of crystallographic structures. A brief introduction to X-ray and neutron diffraction, to the diffractometers, and to the Rietveld method employed to analyse data with the FullProf suite [130] will be presented.

### 2.3.1 Introduction to diffraction

### 2.3.2 Nuclear or charge scattering

Let us consider an X-ray or neutron beam as a plane wave diffracted by a periodical lattice. The incident wavelength  $\lambda$  must be of the same order as the inter-atomic distance. Incident and scattered waves must be in phase to get constructive interferences. This condition of diffraction is described by the Bragg law  $2d_{hkl}\sin\theta = n\lambda$ , where  $d_{hkl} = \frac{2\pi}{k}$  is the interplanar spacing and  $\mathbf{k} = h\mathbf{a}^* + k\mathbf{b}^* + l\mathbf{c}^*$  ( $h, k, l$  integers) is a reciprocal lattice vector,  $\theta$  is the angle of the incident and diffracted beam with respect to the atomic planes, and  $n$  is the order of diffraction. This diffraction condition is illustrated in the left panel of Fig. 2.6. The scattering vector is defined as  $\mathbf{q} = \mathbf{k}_i - \mathbf{k}_f$ , where  $\mathbf{k}_i$  and  $\mathbf{k}_f$  are the incident and final wavevector respectively ( $k_i = k_f = \frac{2\pi}{\lambda}$  in diffraction condition). The Bragg law can be rewritten as  $q = \frac{2\pi n}{d_{hkl}}$ ; the diffraction condition tells that the scattering vector  $\mathbf{q}$  must be a vector of the reciprocal lattice, defining the direction of diffraction. This leads to the well-known Ewald construction, illustrated in the right panel of Fig. 2.6, which is a geometrical representation of the diffraction condition.

The diffracted intensity is proportional to the square modulus of the structure factor  $F_\alpha(\mathbf{q})$  where  $\alpha$  takes the index  $n$  or  $p$  for neutrons or photons, respectively. Photons interact with the electronic cloud of the atoms whereas neutrons interact with the nucleus through the Fermi pseudo-potential:

$$V_F(\mathbf{r}) = \frac{2\pi\hbar^2}{m_n} b_j \delta(\mathbf{r} - \mathbf{r}_j), \quad (2.7)$$

where  $b_j$  is the Fermi length of atom  $j$  and  $m_n$  the neutron mass. Consequently, the atomic form factor for photons is the Fourier transform of the electronic density  $f_j(q)$  whereas for neutrons it is the Fourier transform of the nuclear density taken as a Dirac function in real space, since a nucleus is considered as a point object:

$$\begin{aligned} F_p(\mathbf{q}) &= \sum_{j=1}^N f_j(q) \exp(2i\pi\mathbf{q}\cdot\mathbf{r}_j) \cdot \exp\left(-B_j \frac{\sin^2\theta}{\lambda_j^2}\right), \\ F_n(\mathbf{q}) &= \sum_{j=1}^N b_j \exp(2i\pi\mathbf{q}\cdot\mathbf{r}_j) \exp\left(-B_j \frac{\sin^2\theta}{\lambda_j^2}\right), \end{aligned} \quad (2.8)$$

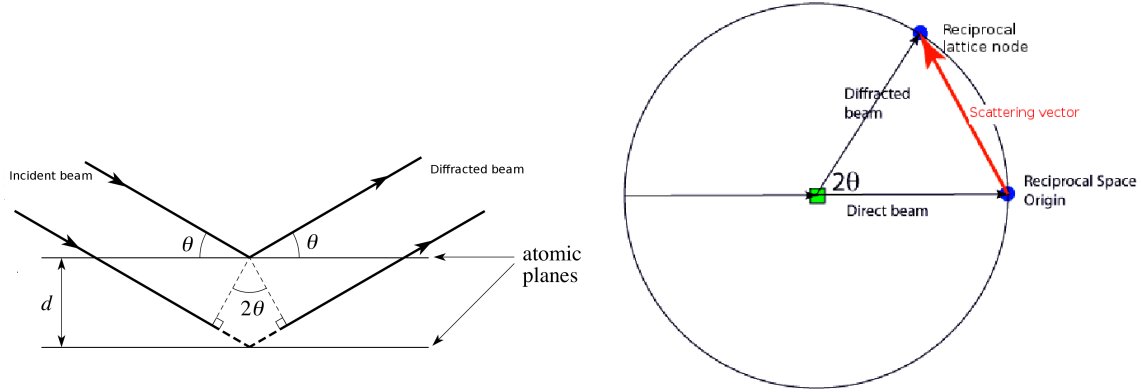


Figure 2.6: Left: Schematic view of the Bragg law. Picture adapted from Ref. [131]. Right: Visualisation of the Ewald sphere with a radius  $2\pi/\lambda$ . The incident beam passes through the sample (green square) reaching the surface of the sphere at the origin of the reciprocal lattice. A reciprocal lattice point must lie on the surface of the Ewald sphere to be in diffraction condition. Picture adapted from Ref. [132].

where the summation runs over the  $N$  atoms of the unit cell,  $\mathbf{r}_j$  is the position of atom  $j$  and  $\exp(-B_j \frac{\sin^2 \theta}{\lambda_i}) = \exp(-W_j(q))$  is the Debye-Waller factor, where  $B_j \propto \langle u_j^2 \rangle$  is the amplitude of an isotropic displacement around the atomic mean position. Ignoring the Debye-Waller factor, the structure factor can be written as the product of two summations, one over the lattice points  $(x_j, y_j, z_j)$  of the primitive cell and the second over the basis of atoms  $r$  attached to a lattice point:

$$F_\alpha(\mathbf{q}) = \left( \sum_j a_{j,\alpha} \exp[2i\pi(hx_j + ky_j + lz_j)] \right) \left( \sum_r \exp[2i\pi(hX_r + kY_r + lZ_r)] \right), \quad (2.9)$$

where  $a_\alpha$  stands for the neutron or X-ray form factor, i.e.  $a_{j,n} = b_j$  and  $a_{j,p} = f_j(q)$ . Now looking at the first factor of the right hand-side of this equation, and considering the face centred Bravais lattice F of interest where the coordinates of the lattice points are  $(0, 0, 0)$ ,  $(\frac{1}{2}, \frac{1}{2}, 0)$ ,  $(0, \frac{1}{2}, \frac{1}{2})$ ,  $(\frac{1}{2}, 0, \frac{1}{2})$ , it results a non vanishing structure factor only if the Miller indexes  $(hkl)$  are of same parity.

The diffracted intensity is proportional to the differential cross section. In the X-ray case, it is written as [133]:

$$\frac{d\sigma}{d\Omega} = n_c \frac{2\pi^3}{v_0} \sum_{\mathbf{k}} \delta(\mathbf{q} - \mathbf{k}) |F_p(\mathbf{q})|^2 P(\theta), \quad (2.10)$$

where  $n_c$  is the number of unit cells,  $v_0$  is the unit cell volume.  $P(\theta) = \frac{1 + \cos^2(2\theta)}{2}$  is the polarisation factor assuming the incident beam is unpolarised, i.e. the electric field is in a plane perpendicular to the incident wavevector. Since the X-ray beam is polarised during the scattering process, the polarisation factor results from the projection of the

two components of the electric field in the direction  $2\theta$  of the scattered beam [134, 135]. In the case of synchrotron radiation, when the incident polarised beam is set up perpendicular to the scattering plane,  $P(\theta) = 1$ . The Dirac term refers to the diffraction condition, i.e. the wavevector transfer must be a vector of the reciprocal lattice.

For neutrons, the Fermi length of an isotope  $j$  will depend on the isotope considered and on the nuclear spin of the latter [136]. To the differential cross section will result a coherent and incoherent contributions, the latter resulting in a background in diffraction experiment. We define:

$$\begin{aligned}\bar{b}_j &= \sum_{\xi} c_{\xi} b_{j,\xi}, \\ \overline{|b_j|^2} &= \sum_{\xi} c_{\xi} |b_{j,\xi}|^2,\end{aligned}\tag{2.11}$$

where  $\xi$  labels an isotope of atom  $j$  with concentration  $c_{\xi}$ . The coherent and incoherent differential cross sections are calculated as:

$$\begin{aligned}\frac{d\sigma_{\text{coh}}(\mathbf{q})}{d\Omega} &= n_c \frac{(2\pi)^3}{v_0} \sum_{\mathbf{k}} \delta(\mathbf{q} - \mathbf{k}) |F'_n(\mathbf{q})|^2, \\ \frac{d\sigma_{\text{inc}}(q)}{d\Omega} &= n_c \sum_j (\overline{|b_j|^2} - |\bar{b}_j|^2) \exp(-W_j(q)),\end{aligned}\tag{2.12}$$

with the so-called unit-cell structure factor:

$$F'_n(\mathbf{q}) = \sum_j \bar{b}_j \exp(i\mathbf{q} \cdot \mathbf{r}_j) \exp(-W_j(q)).\tag{2.13}$$

### 2.3.3 Magnetic scattering

In the case where a compound undergoes a magnetic transition, the periodicity of the magnetic moment resulting from the spin of the unpaired electrons leads to a magnetic structure. This periodicity is described by a magnetic propagation wavevector  $\mathbf{k}_{\text{mag}}$ . The symmetry of the ordered phase is lowered compared to the one of the crystallographic group. Note that even if  $\mathbf{k}_{\text{mag}} = (0, 0, 0)$ , at least the time reversal symmetry is broken. One has to find the symmetry operations leaving  $\mathbf{k}_{\text{mag}}$  invariant in order to constitute a subgroup  $G_k$  whose representation can be decomposed into irreducible representations  $\Gamma_{\nu}$ , where  $\nu$  labels the order of the representation. According to the Landau theory, only one of these representations is selected if the transition is second order, its basis vectors defining the orientation of the magnetic moment [137]. We refer to App. D.1 for more detailed information.

The neutron spin interacts with the magnetic field  $\mathbf{B} = \mu_0 \mathbf{H}$  created by the distribution of unpaired electrons. The potential of interaction is defined as:

$$V_{\text{mag}} = -\boldsymbol{\mu}_n \cdot \mu_0 \mathbf{H},\tag{2.14}$$

where  $\boldsymbol{\mu}_n = -\gamma \mu_N \boldsymbol{\sigma}$  is the magnetic moment of the neutron,  $\gamma = -1.91$ ,  $\mu_N$  is the nuclear Bohr magneton,  $\boldsymbol{\sigma}$  is the neutron spin, and  $\mathbf{H}$  is expressed in  $\text{A.m}^{-1}$ . Within

the dipolar approximation, the amplitude of the magnetic interaction is deduced for unpolarised neutrons as [138, 139]:

$$a_{\text{mag}}(\mathbf{q}) = p f_{\text{mag}}(\mathbf{q}) \boldsymbol{\sigma} \cdot \mathbf{M}_{\perp}(\mathbf{q}), \quad (2.15)$$

where  $2p = |\gamma r_0| = 0.54 \times 10^{-12}$  cm is the magnetic scattering length for a magnetic moment of  $1 \mu_{\text{B}}$  at  $q = 0$ ,  $f_{\text{mag}}(\mathbf{q})$  is the magnetic form factor and  $\mathbf{M}_{\perp}(\mathbf{q}) = \hat{\mathbf{q}} \times (\mathbf{M}(\mathbf{q}) \times \hat{\mathbf{q}})$  (with  $\hat{\mathbf{q}} = \mathbf{q}/q$ ) is the projection of the Fourier transform of the total magnetisation density (orbital and spin contributions) on the plane perpendicular to  $\mathbf{q}$ .

In the case of a periodic magnetic structure with a magnetic propagation wavevector  $\mathbf{k}_{\text{mag}}$ , and considering only one type of magnetic ion, a magnetic moment can be expanded in a Fourier series:

$$\mathbf{m}_j = \sum_{\mathbf{k}_{\text{mag}}} \mathbf{m}^{\mathbf{k}_{\text{mag}}} \exp(-i\mathbf{k}_{\text{mag}} \cdot \mathbf{r}_j), \quad (2.16)$$

Therefore, the elastic magnetic cross section is given by:

$$\frac{d\sigma_{\text{mag}}(\mathbf{q})}{d\Omega} = N_{\text{mag}} \frac{(2\pi)^3}{v_{\text{mag}}} \sum_{\mathbf{k}, \mathbf{k}_{\text{mag}}} \delta(\mathbf{q} - \mathbf{k} - \mathbf{k}_{\text{mag}}) |\mathbf{F}_{\text{mag}}^{\perp}(\mathbf{q})|^2, \quad (2.17)$$

where  $N_{\text{mag}}$  is the number of magnetic cells and  $v_{\text{mag}}$  their volume. The Dirac function refers to the diffraction condition: if the magnetic propagation wavevector  $\mathbf{k}_{\text{mag}} = (0, 0, 0)$ , the magnetic Bragg peaks are at the same positions as the nuclear ones, otherwise satellites peak appear at positions  $\mathbf{q} = \mathbf{k} + \mathbf{k}_{\text{mag}}$ . However, if  $\mathbf{k}_{\text{mag}} \cdot \mathbf{r}_j \neq n\pi$ , Eq. 2.16 is no longer available since the magnetic moment need to remain a real quantity. Therefore, the magnetic propagation vector  $-\mathbf{k}_{\text{mag}}$  has to be taken into account, see for instance Eq. D.7, and consequently satellites peaks are observed at  $\mathbf{q} = \mathbf{k} \pm \mathbf{k}_{\text{mag}}$ . The magnetic structure factor has been introduced as:

$$\mathbf{F}_{\text{mag}}(\mathbf{q}) = p f_{\text{mag}}(\mathbf{q}) \sum_j \mathbf{m}_j \exp(i\mathbf{q} \cdot \mathbf{r}_j) \exp(-W_j(\mathbf{q})), \quad (2.18)$$

where  $\mathbf{F}_{\text{mag}}^{\perp}(\mathbf{q}) = \hat{\mathbf{q}} \times (\mathbf{F}_{\text{mag}}(\mathbf{q}) \times \hat{\mathbf{q}})$ .

### 2.3.4 Powder diffractometers

An overview of the X-ray and neutron powder diffractometers is given here. As the sample is constituted of small randomly oriented crystallites, the main advantage of a powder diffraction experiment is that all the Bragg positions will be observed in the  $2\theta$  position of the detector.

### 2.3.5 X-ray experiments

X-rays experiments were performed in the Bragg-Brentano configuration, see Fig. 2.7, with an Xpert Panalytical Phillips diffractometer at INAC, CEA-Grenoble. A polychromatic X-ray beam is obtained with a copper anode. A nickel filter permits to mainly keep the copper  $K_{\alpha}$  wavelength  $\lambda = 1.5406 \text{ \AA}$ . However a residual small wavelength bandwidth persists taking into account the  $K_{\text{Ni}}$  absorption edge of the nickel

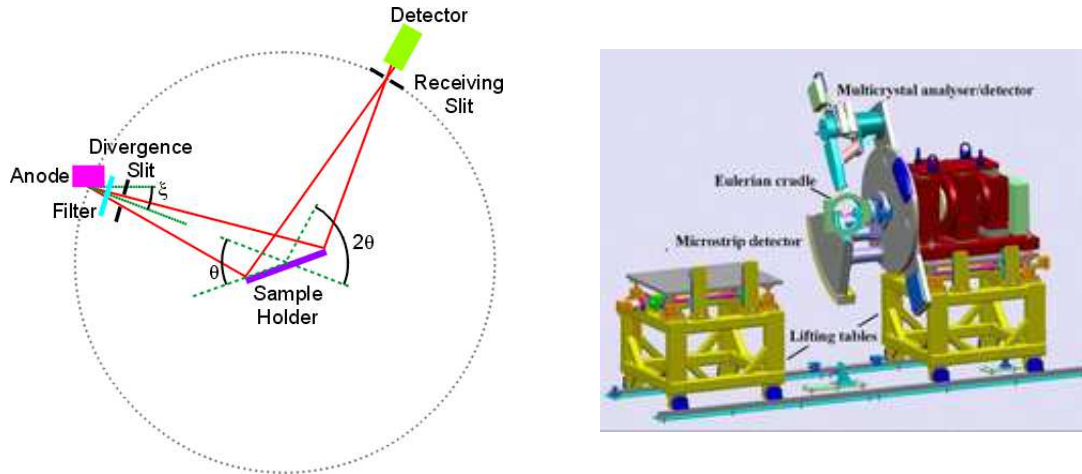


Figure 2.7: Left: illustration of the  $\theta - 2\theta$  geometry. Sample and detector are moved concomitantly to ensure that the detector is always at  $2\theta$  from the sample and the sample surface is always at an angle  $\theta$  from the incident beam. Picture taken from Ref. [141]. Right: schematic view of the high resolution powder diffractometer of the MS beamline in the Debye-Scherrer configuration. Picture taken from Ref. [142]

$\lambda_{K,Ni} = 1.4881 \text{ \AA}$  and do not provide a purely monochromatic beam. This results in a step in the right side of the tail of the Bragg peak precluding a quantitative analysis of the diffracted intensity. The beam is focused with several sets of slits: the first divergence slits with variable size are used to keep constant the irradiated area on the sample and to restrict the beam to the sample size. Determining the size of the receiving slits located in front of the detector is a stake to get better resolution without reducing the diffracted beam intensity. Additional Soller slits limit the axial (vertical) divergence of the beam and increase the resolution, especially at low scattering angles.

Experiments were also conducted using the high resolution powder diffractometer of the Material Science (MS) beamline of SLS which is supplied by photons with an energy raising up to 38 keV, see right panel of Fig. 2.7. It is equipped with a silicon microstrip detector of second generation, MYTHEN II, made of more than 30000 Si-units to cover a total angle from  $2$  to  $120^\circ$  with a maximum resolution of  $3.7 \text{ mdeg}$  [129, 140]. An x-ray beam of wavelength  $\lambda = 0.49646 \text{ \AA}$ , corresponding to an energy  $E = \frac{hc}{\lambda} = 24.98 \text{ keV}$ , was used.

### 2.3.6 Neutron experiments

Neutron powder diffraction experiments were performed at the ILL on the D2B and D1B diffractometers, see Fig. 2.8, and at the PSI on the high resolution powder diffractometer HRPT.

D1B is a two-axis powder diffractometer optimised for high resolution at low  $q$  and high neutron flux ( $\phi_n = 6.5 \times 10^6 \text{ n cm}^{-2} \text{ s}^{-1}$  at the wavelength  $\lambda = 2.52 \text{ \AA}$  thanks to three graphite (002) monochromators). A  $^3\text{He}$  multidetector covers a scattering angle from  $2^\circ \leq 2\theta \leq 80^\circ$ , which can be extended to  $130^\circ$  as the multidetectors can be moved. Angular resolution reaches up to  $\text{FWHM} = 0.2^\circ$  ( $\text{FWHM}$ : full width at half maximum) at small angles. To determine the magnetic structure of our sample deep into the

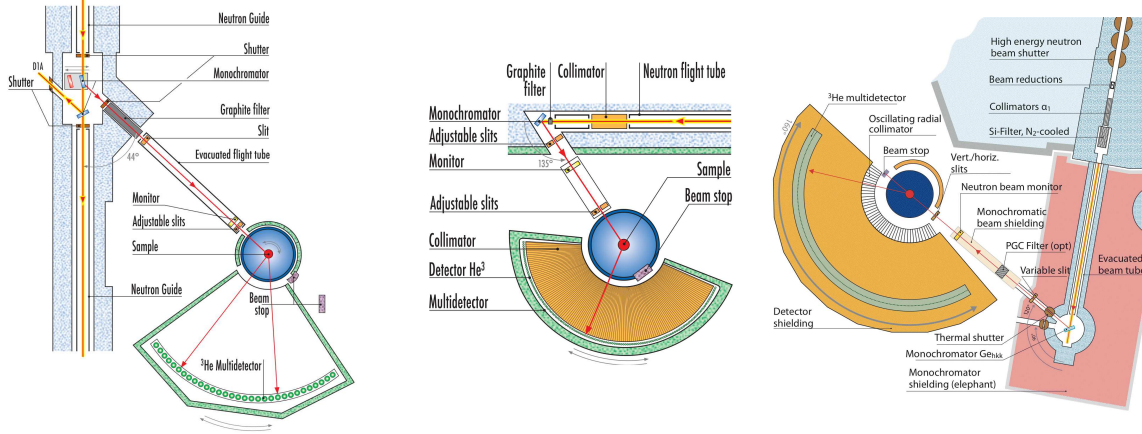


Figure 2.8: Illustration of the D1B (left) and D2B (middle) diffractometers, from Ref. [128], and of HRPT (right), from Ref. [143].

ordered phase (down to 60 mK), we used a  $^3\text{He}$ - $^4\text{He}$  dilution cryostat. As the atomic magnetic form factor decreases with increasing  $q$ , this diffractometer is well suited for the determination of magnetic structures.

D2B is a high resolution two-axis powder diffractometer covering a scattering angle  $5^\circ \leq 2\theta \leq 165^\circ$  thanks to 128  $^3\text{He}$  detectors. A germanium (115) monochromator offers a wavelength  $\lambda = 1.594 \text{ \AA}$  with a neutron flux  $\phi_n = 1 \times 10^6 \text{ n cm}^{-2} \text{ s}^{-1}$  in the high resolution configuration. As a wide angular range is covered with a high neutron flux and high resolution, this diffractometer is well adapted for the determination of a crystal structure and to perform a quantitative analysis of the diffracted intensities.

Additional neutron diffraction experiments have been conducted on HRPT. A germanium (822) monochromator selects a neutron wavelength of  $1.154 \text{ \AA}$  and as the  $^3\text{He}$  detectors cover a scattering angle up to  $165^\circ$  with an angular step of  $0.1^\circ$ , a wider  $q$ -range has been explored compared to the D2B diffractometer. High resolution is achieved for thermal neutrons up to  $\frac{\Delta d}{d} \approx 1 \times 10^{-3}$ .

Note that for the D2B and HRPT diffractometers, an additional oscillating radial collimator reduces the scattering from the sample environment.

### 2.3.7 The Rietveld refinement

Analysis of diffraction data have been performed using the Rietveld method with the FullProf code [130]. The refinement routine minimises the function:

$$\chi^2 = \sum_{i=1}^{N_p} \frac{1}{\sigma_i^2} [y_{o,i} - y_{c,i}(\alpha)]^2, \quad (2.19)$$

where the summation runs over the  $N_p$  experimental points,  $y_{o,i}$  is the observed intensity,  $\sigma_i$  is the standard deviation of  $y_{o,i}$ , and  $y_{c,i}$  is the calculated intensity where  $\alpha = (\alpha_1, \dots, \alpha_n)$  is the parameter set involving the  $n$  free parameters. The calculated intensity is defined as [144]:

$$y_{c,i} = y_{c,0} \sum_{\mathbf{h}} M_{\mathbf{h}} A_{\mathbf{h}} L_{p,\mathbf{h}} I_{\mathbf{h}} Z(\theta_i - \theta_{\mathbf{h}}) + b_{g,i}, \quad (2.20)$$

where  $\mathbf{h}$  labels the Bragg peak positions at the angle  $\theta_{\mathbf{h}}$ ,  $y_{c,0}$  is a scaling factor,  $b_{g,i}$  is the background intensity,  $Z(\theta_i - \theta_{\mathbf{h}})$  is the peak profile function modelling instrumental and sample effects,  $M_{\mathbf{h}}$  is the multiplicity of the reflection  $\mathbf{h}$  and  $A_{\mathbf{h}}$  is the absorption correction. The intensity  $I_{\mathbf{h}}$  is proportional to the differential cross section defined in Eq. 2.10 and in Eq. 2.12 for X-ray and neutrons respectively. The Lorentz factor  $L_{p,\mathbf{h}} = \frac{1}{\sin 2\theta}$  describes the fact that at high angle diffracted intensity is increased as the angular aperture of the Debye Scherrer cone is higher and the intersection between the latter and the Ewald sphere is wider [134, 135].

For an estimate of the analysis goodness, we use three  $R$  factors and  $\chi_{\text{exp}}^2$ . They are defined as follows [145].

$$\left\{ \begin{array}{l} R_p = \frac{\sum_i |y_{o,i} - y_{c,i}|}{\sum_i y_{o,i}}, \quad R_{\text{wp}}^2 = \frac{\sum_i w_i (y_{c,i} - y_{o,i})^2}{\sum_i w_i y_{o,i}^2}, \\ R_{\text{exp}}^2 = \frac{N_p - n}{\sum_i w_i y_{o,i}^2}, \quad \chi_{\text{exp}}^2 = \frac{\sum_i w_i (y_{c,i} - y_{o,i})^2}{N_p - n}. \end{array} \right. \quad (2.21)$$

$R_p$ ,  $R_{\text{wp}}$ , and  $R_{\text{exp}}$  are respectively the profile, weight profile, and expected weight profile factors, and  $w_i = \frac{1}{\sigma_i^2}$  has been introduced for clarity in Eq. 2.21.

Two different profile functions have been utilised in the different diffraction experiments. The pseudo-Voigt function describes the shape of the Bragg peaks as:

$$V_p(x) = \eta L(x) + (1 - \eta)G(x), \quad (2.22)$$

where  $\eta$  is a free mixing parameter which defines the shape of the Bragg peak between the Gaussian ( $G(x)$ ) or Lorentzian ( $L(x)$ ) limits,

$$\begin{aligned} L(x) &= \frac{a_L}{1 + b_L x^2}, \\ G(x) &= a_G \exp(-b_G x^2), \end{aligned} \quad (2.23)$$

with  $a_G = \frac{2\sqrt{\ln 2}}{H_G \sqrt{\pi}}$ ,  $b_G = \frac{4 \ln 2}{H_G^2}$ ,  $a_L = \frac{2}{\pi H_L}$ , and  $b_L = 4H_L^2$ , where  $H_L$  and  $H_G$  are the FWHM (Full Width at Half Maximum) for the Lorentzian and the Gaussian functions, respectively. They are here taken to be equal here and are related to the  $\{U, V, W\}$  half-width free parameters which describe the resolution function of the instrument [144]:

$$H_G^2 = H_L^2 = U^2 \tan^2 \theta + V \tan \theta + W. \quad (2.24)$$

Note that no strain or size effects have been considered.

The Bragg peak shape can alternatively be described by the convolution of a Thompson-Cox-Hastings pseudo-Voigt function [146] with an asymmetric function resulting from the intersection of the diffraction cones with the cylindrical detector [147]. In this case, the Lorentzian and Gaussian functions have different FWHMs,

$$\begin{aligned} H_G^2 &= U \tan^2 \theta + V \tan \theta + W, \\ H_L^2 &= Y / \cos \theta, \end{aligned} \quad (2.25)$$

where  $\{U, V, W, Y\}$  are free parameters and  $Y$  refers to the Lorentzian isotropic size parameter. The mixing parameter  $\eta$  introduced in Eq. 2.22 is no longer a free parameter in this case but it is calculated as a function of  $H_L$  and  $H_G$  [144].

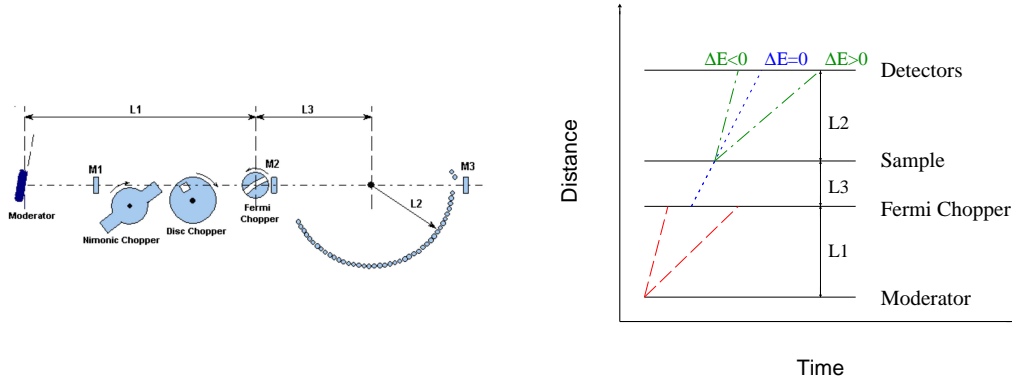


Figure 2.9: Schematic view of the MARI spectrometer [148] (left) and illustration of the neutron path (right) in the time-of-flight technique, explained in the main text. A methane moderator at 100 K thermalises incident high energy neutrons.

## 2.4 Neutron time-of-flight spectroscopy

The time-of-flight (TOF) spectrometer is an instrument well suited to explore excitations since wide energy and momentum transfer ranges are covered. In the direct geometry used here, where the incident energy of the neutron is fixed, the time of flight of the scattered neutron over a known distance is measured to deduce the energy transfer in a given direction. TOF spectrometers are optimal for pulsed source like the ISIS facility, where our experiments have been conducted.

### 2.4.1 The MARI spectrometer

TOF experiments were performed on the MARI spectrometer. A simple scheme of this instrument and the neutron path is given in the left and right panels of Fig. 2.9, respectively. Background coming from high energy neutrons and  $\gamma$  radiation is decreased with a first nematic chopper. The incident energy is selected with a gadolinium Fermi chopper by phasing the neutron transparent curved slits with the neutron pulse, and illustrated by the dotted blue line. The frequency of this rotor raising up to 600 Hz determines the resolution, i.e. the width of the elastic line. The chopper is magnetically suspended to avoid mechanical contact via friction. Several rotor choppers exist allowing us to select incoming energies up to 2 eV. We only use the gadolinium Fermi chopper, allowing to reach an incident energy up to 200 meV. Neutron trajectories from the sample to the detectors are displayed for inelastic (green dash dotted line) or elastic (blue dotted line) processes. To determine precisely the neutron gain or loss of energy and the resolution, the different distances separating the constituents must be precisely known. In the MARI case, we have  $L_1 = 11.05$  m,  $L_2 = 4.02$  m and  $L_3 = 1.689$  m. Low and high angle detector banks, located close to the direct beam and under the sample respectively, are composed of cylindrical  $^3\text{He}$  detectors, covering scattering angles  $3^\circ \leq 2\theta \leq 135^\circ$ . Samples were cooled down to 5 K with a top loading CCR cryostat.

The left panel of Fig. 2.10 illustrates the inelastic scattering process at the sample. An incident neutron of energy  $E_i$  and wavevector  $\mathbf{k}_i$  is scattered in the detector direction  $2\theta$  with a final energy  $E_f$  and wavevector  $\mathbf{k}_f$ . From the momentum conservation

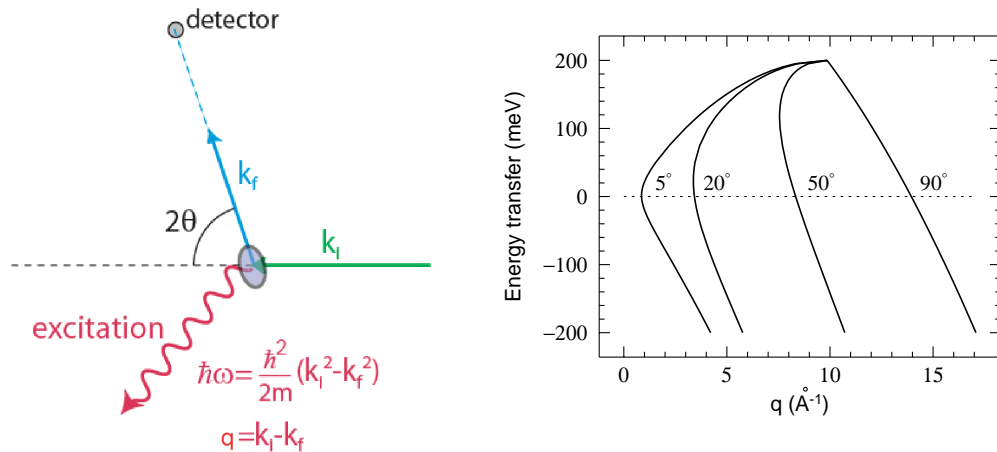


Figure 2.10: Left: Neutron scattering triangle. Right: Illustration of the  $(\mathbf{q}, \hbar\omega)$  space probed by detectors located in the  $2\theta$  directions for neutrons of incident energy  $E_i = 200$  meV in direct geometry.

$\mathbf{q} = \mathbf{k}_i - \mathbf{k}_f$ , we get:

$$q^2 = k_i^2 + k_f^2 - 2k_i k_f \cos(2\theta). \quad (2.26)$$

Using the energy transfer relation  $\hbar\omega = E_i - E_f$ , we get the  $(\mathbf{q}, \hbar\omega)$  space probed by a detector in the direction  $2\theta$ , see right panel of Fig. 2.10:

$$\frac{\hbar^2 q^2}{2m} = 2E_i - \hbar\omega - 2[E_i(E_i - \hbar\omega)]^{\frac{1}{2}} \cos(2\theta). \quad (2.27)$$

## 2.4.2 Energy resolution

The total energy resolution of the spectrometer arises from the convolution of several contributions. The first one originates from the time distribution of neutrons in the pulse. Whereas Gaussian functions are usually introduced to take into account the resolution of spectrometers at a continuous source, they are no longer adequate for a pulsed source where the moderator produces a strongly asymmetric time distribution of the neutrons. The latter distribution has been modelled for a given incident energy  $E_i$  with the convolution of a *slowing down* term described by a  $\chi^2$  distribution function accounting for fast neutrons at short times which are not thermalised and a *storage* term depicted by an exponential function to take into account neutrons emerging after thermalisation [149]. As the distance between the moderator and the Fermi chopper is significant, the initial pulse shape spreads out in time due to the different neutron velocities. As explained above, phasing the Fermi chopper allows to select neutrons with a specific energy and tuning the frequency to determines the wavelength spread. This chopper introduces a second component to the resolution function due to the approximately triangular transmission function which takes into account not only the phase of the Fermi chopper but also the neutron speed and entry angle [150]. An additional component arising from size effects of the sample and detectors geometries has been calculated through Monte Carlo simulations [151]. The efficiency of the detector depends on the neutron speed [152]: the probability of a neutron to be detected at a specific

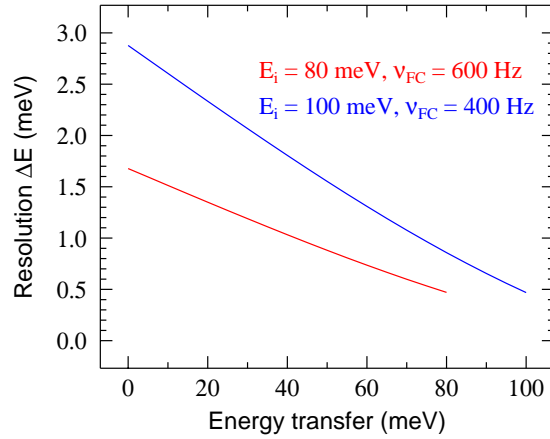


Figure 2.11: Examples of the resolution curves as a function of the transfer energy for two configurations with an incident energy  $E_i = 80$  meV and a Fermi chopper frequency  $\nu_{\text{FC}} = 600$  Hz, and  $E_i = 100$  meV and  $\nu_{\text{FC}} = 400$  Hz.

position within the detector thickness depends on its energy and adds a supplementary broadening in the resolution function.

As explained in Refs. [153, 154], the energy resolution for elastic scattering  $\Delta E$  is calculated as:

$$\frac{\Delta E}{E_i} = 8.7478 \times 10^{-10} \frac{\sqrt{E_i}}{L} \Delta t, \quad (2.28)$$

where  $L$  (in meters) is the total neutron flight path,  $\Delta t$  (in  $\mu\text{s}$ ) is the time width of the pulse at the detector which is the quadratic sum of the aforementioned time dispersion contributions, and  $E_i$  the incident energy (in meV). The total resolution of the MARI spectrometer has been calculated using the MSLICE code [155] supplied by ISIS. Some plots are traced in Fig. 2.11. Note that the resolution is improved as the energy transfer increases.

## 2.5 Neutron backscattering spectroscopy

The backscattering experiments have been performed at the ILL with the IN16 spectrometer characterised by a high energy resolution. This section describes the IN16 spectrometer and discusses the backscattering process and energy resolution considerations.

### 2.5.1 The IN16 spectrometer

The IN16 spectrometer is illustrated in Fig. 2.12. A first graphite (002) deflector scatters a wide wavelength band of neutrons into a focusing neutron guide. A beryllium filter prevents high energy neutrons to enter the spectrometer and a background chopper pulses the neutron beam. In the so-called primary spectrometer, a second rotative deflector, which is composed alternatively of two open segments and two graphite (002) monochromators, deflects the beam towards a spherically curved backscattering monochromator, moved by a Doppler drive at a chosen frequency. Note that the same

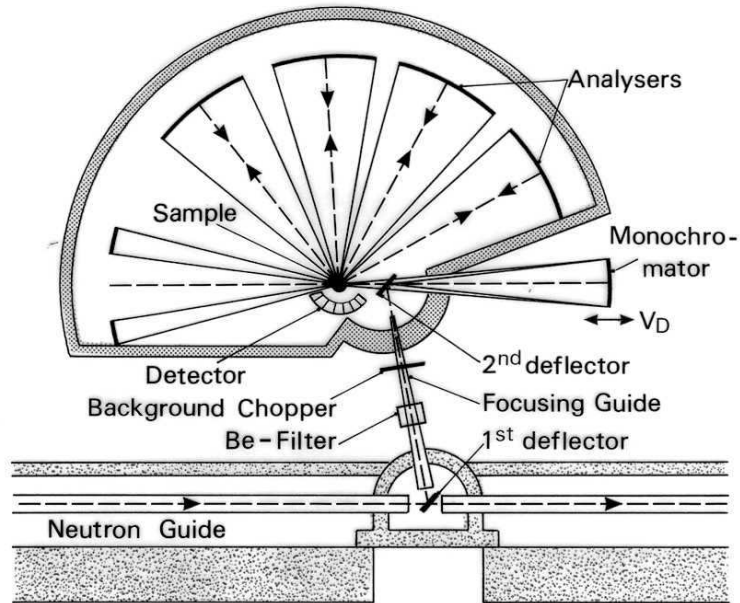


Figure 2.12: Schematic view of the IN16 spectrometer. The basic principle and the role of each constituent is described in the main text. Picture taken from Ref. [156].

material is used for the first deflector and the second rotative deflector allowing to have a backscattered beam parallel to the initial white beam in the neutron guide, simplifying the setup of the spectrometer. Neutrons are backscattered onto the sample located behind the second deflector thanks to the open segments of the rotative deflector, working as a chopper. In the so-called secondary spectrometer, several banks of silicon (111) 140 cm high analysers located at 2 m from the sample and covering an angular range of  $8^\circ \leq \theta \leq 155^\circ$ , select neutrons of an energy of about 2 meV scattered from the sample and reflects these in exact backscattering geometry back through the sample to a set of 320  $^3\text{He}$  detectors placed behind the sample. As the neutron beam being pulsed, neutrons directly scattered by the sample towards detectors are not taken into account since detectors are electronically closed when incident neutrons hit the sample.

### 2.5.2 The backscattering process

The first backscattering process occurs at the Doppler monochromator in the primary spectrometer to select the incident neutron wavelength  $\lambda_i$  with a wavelength spread  $\Delta\lambda$ . The energy resolution is  $\frac{\Delta E}{E} = 2\frac{\Delta\lambda}{\lambda}$ . The aim is to reach the highest energy resolution. By differentiating the Bragg law we get the relation:

$$\frac{\Delta\lambda}{\lambda} = \cot\theta\Delta\theta + \frac{\Delta d}{d}. \quad (2.29)$$

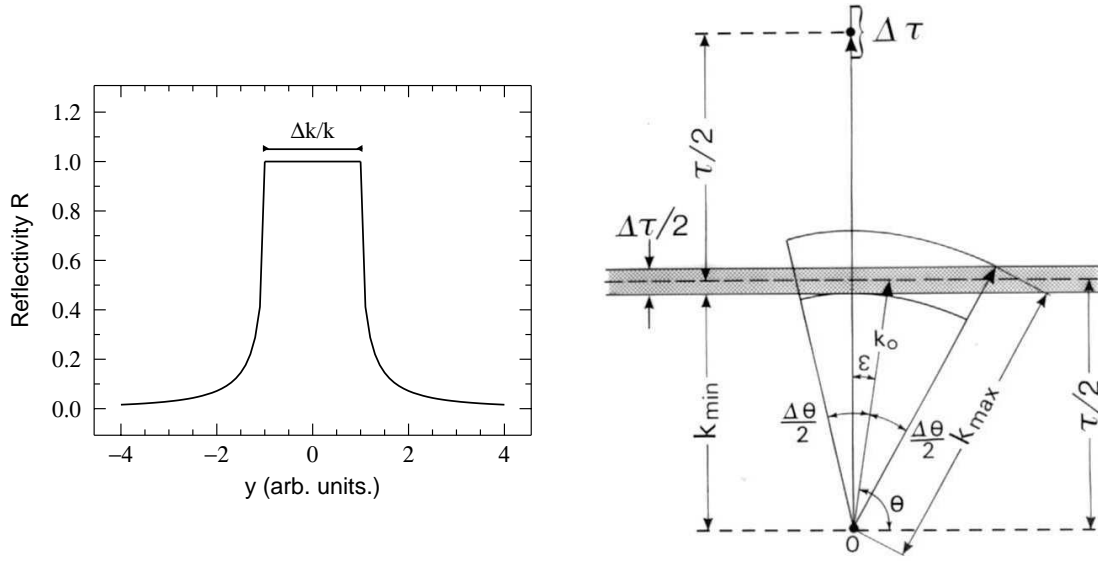


Figure 2.13: *Left: Darwin curve showing the neutron reflection coefficient of the monochromator as a function of an arbitrary parameter  $y$  which could be a variation of  $k$ ,  $\lambda$  or  $\theta$ . Right: Picture taken from Ref. [156] illustrating the nearly backscattering geometry where a small angular deviation of the incident beam is introduced. Here  $\tau$  is a reciprocal lattice vector ( $\tau \equiv k$ ) and  $k_0 \equiv k_i$ .*

In exact backscattering geometry ( $\theta = 90^\circ$ ), the angular term of the right hand side of Eq. 2.29 vanishes. The quantity  $\frac{\Delta d}{d} = \frac{\Delta k}{k}$  can be calculated within the dynamical theory of scattering, where interference effects between the incident and scattered waves are taken into account. In the Bragg case, i.e. where incident waves are reflected, the reflectivity coefficient  $R$  can be calculated [157, 158], see the Darwin curve in the left panel of Fig. 2.13. The so-called Darwin width  $\frac{\Delta k}{k}$  defines the plateau where  $R = 1$ , i.e. the loss of neutron flux is minimised. It is calculated as [159]:

$$\frac{\Delta k}{k} = \frac{16\pi F'_n(\mathbf{k})N}{k^2}, \quad (2.30)$$

where  $N$  is the number density of unit cells and  $F'_n(\mathbf{k})$  is the unit-cell structure factor defined in Eq. 2.13, and calculated at the reciprocal lattice vector  $\mathbf{k}$ . Then, the energy resolution is:

$$\Delta E = \frac{2E\Delta k}{k} = \frac{\hbar^2 4\pi F'_n(\mathbf{k})N}{m_n}, \quad (2.31)$$

where  $E = \frac{\hbar^2(k^2/4)}{2m_n}$ . To ensure a minimised energy resolution, the choice of the material constituting the monochromator is of first importance. For Si (111) crystals, we get  $\frac{\Delta k}{k} = 1.86 \times 10^{-5}$  corresponding to an energy resolution of  $\Delta E = 0.077 \mu\text{eV}$  for  $\lambda = 6.2709 \text{ \AA}$ .

To calculate the true energy resolution, one has to consider also a small divergence of the beam due to a small deviation of the backscattering geometry, i.e.  $\varepsilon = 90^\circ - \theta$  as illustrated in the right panel of Fig. 2.13. This divergence is calculated as the

difference between the minimum and maximum incident  $\mathbf{k}_i$  vectors denoted  $\mathbf{k}_{\min}$  and  $\mathbf{k}_{\max}$ , respectively. Therefore, we derive:

$$k_{\max} = \frac{k/2 + \Delta k/4}{\cos(\frac{\Delta\theta}{2} + \epsilon)}, \quad k_{\min} = \frac{k}{2} - \frac{\Delta k}{4}, \quad \text{and} \quad k_i = \frac{k/2 + \Delta k/4}{\cos(\epsilon)} \approx k/2 + \Delta k/4. \quad (2.32)$$

Assuming that  $\Delta k/(k + \Delta k/2) \approx \Delta k/k$ , we get:

$$\begin{aligned} \frac{\Delta k_i}{k_i} = \frac{k_{\max} - k_{\min}}{k_i} &\approx \frac{1}{\cos(\frac{\Delta\theta}{2} + \epsilon)} - 1 + \frac{\Delta k}{k}, \\ &\approx \frac{1}{2} \left( \frac{\Delta\theta}{2} + \epsilon \right)^2 + \frac{\Delta k}{k}, \end{aligned} \quad (2.33)$$

where the last line is obtained assuming small values of  $\frac{\Delta\theta}{2} + \epsilon$ . Then, the energy resolution is obtained as:

$$\frac{\Delta E}{E} = 2 \frac{\Delta k_i}{k_i} = \left( \frac{\Delta\theta}{2} + \epsilon \right)^2 + 2 \frac{\Delta k}{k}. \quad (2.34)$$

The total energy resolution is then calculated as the convolution of the values of Eq. 2.34 found for the primary and secondary spectrometers.

### 2.5.3 Spectroscopy

To perform spectroscopy measurements, one changes the incident neutron energy. This can be accomplished by changing the lattice parameter via thermal cycling or through the Doppler effect by moving the monochromator at a velocity  $v_D$  parallel to the incident neutron beam as set up on the IN16 spectrometer. The energy change  $\delta E$  of the backscattered neutrons is then linearly dependent of the Doppler velocity  $v_D$ , assuming  $v_D \ll v_i$  [159]:

$$\frac{\delta E}{E} \approx 2 \frac{v_D}{v_i}. \quad (2.35)$$

On IN16, the maximum amplitude of the Doppler velocity is  $2.2 \text{ ms}^{-1}$ . Neutrons of wavelength  $\lambda = 6.2709 \text{ \AA}$  have a velocity  $v_i \approx 631 \text{ ms}^{-1}$ , which results in a maximum energy change of the backscattered neutrons of  $\delta E_{\max} = 14.5 \text{ \mu eV}$ . We recall that the analysers and the Doppler monochromator are identical. Therefore neutrons scattered by the sample will be analysed, i.e. backscattered in the secondary spectrometer, if  $\lambda = 6.2709 \text{ \AA}$ . The velocity profile of the Doppler drive is sinusoidal-like around the mean value  $v_D = 0$ , corresponding to zero energy transfer. Neutrons detected with a velocity different from  $v_i$  will have been inelastically scattered by the sample to fulfil the backscattering condition at the analysers. The variation of the position of the Doppler monochromator is assumed negligible and thus the neutron flight time from the Doppler monochromator to the detector  $t_{\text{MD}}$  is constant. Therefore, the final neutron energy at a time  $t_f$  is deduced from the Doppler velocity recorded at a time  $t_f - t_{\text{MD}}$ .

## 2.6 Muon spectroscopy

A brief introduction on the muon spin relaxation spectroscopy ( $\mu\text{SR}$ ) is presented here. For more detailed information, one has to refer to Ref. [160].

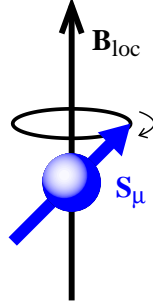


Figure 2.14: Illustration of the muon spin precession around a local magnetic field  $\mathbf{B}_{\text{loc}}$ . Picture taken with kind permission from Ref. [160].

### 2.6.1 Introduction

This technique allows to probe the local magnetic field of a sample. Muon is an elementary particle of mass  $m_\mu = 1.88353 \times 10^{-28} \text{ kg} \approx 200m_e$  where  $m_e$  is the mass of the electron. Here, muons possess a positive electric charge and a lifetime  $\tau_\mu = 2.2 \mu\text{s}$ .

Polarised muons are implanted in the matter and due to their positive electric charge they are localised at an interstitial site. The aim of this technique is to follow the time evolution of the polarisation of these muons in a so-called *time-differential* measurement. As they carry a spin  $S_\mu = \frac{1}{2}$ , muons interact with the local magnetic field  $\mathbf{B}_{\text{loc}}$  of the sample. Thus the spin of the muon undergoes a precession motion around  $\mathbf{B}_{\text{loc}}$ , as pictured in Fig. 2.14, described by the Larmor equation:

$$\frac{d\mathbf{S}_\mu}{dt} = \gamma_\mu \mathbf{S}_\mu \times \mathbf{B}_{\text{loc}}, \quad (2.36)$$

where  $\gamma_\mu = 8.51616 \times 10^8 \text{ rad s}^{-1} \text{ T}^{-1}$  is the muon gyromagnetic ratio.

### 2.6.2 Experimental details

A high energy beam of protons provided by an accelerator hits a graphite target, see Sec. 2.2. Some reactions involved in the collisions of the incident protons  $p$  and neutrons  $n$  and protons of the target are described by the following equations:



where  $\pi$  is a pion, an unstable particle with a lifetime  $\tau_\pi = 26 \text{ ns}$ . This particle decays into a muon  $\mu$  and a muon neutrino  $\nu_\mu$ :

$$\pi^+ \rightarrow \mu^+ + \nu_\mu. \quad (2.38)$$

As we consider a pion at rest, i.e. with zero kinetic energy, the muon and the neutrino are emitted in opposite direction due to momentum conservation. Since the neutrino has a negative helicity — the helicity being defined by the projection of the spin over the momentum — the spin of the muon is antiparallel to its momentum because of

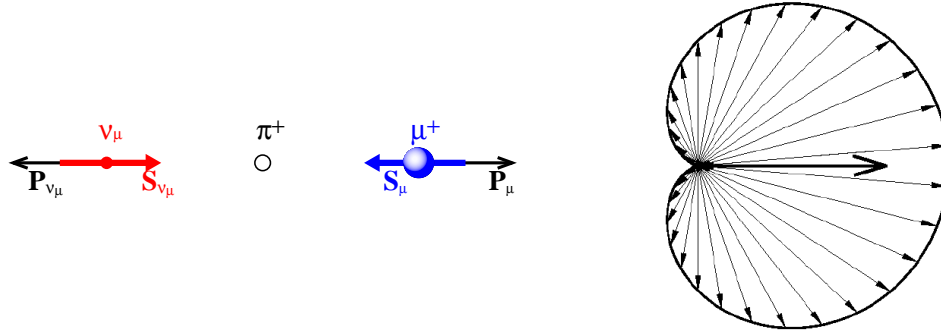


Figure 2.15: *Left: Decay of the pion  $\pi^+$  into a muon  $\mu^+$  and a muon neutrino  $\nu_\mu$ . Right: Probability of the positron emission direction with respect to the muon spin.*

conservation of angular momentum. This is illustrated in the left panel of Fig. 2.15. The decay of the muon follows the reaction:



where  $\nu_e$  and  $\bar{\nu}_\mu$  are respectively the neutrino and antineutrino associated with the positron and the muon. The positron is the particle of interest which is detected by a plastic scintillator to produce a photon which is driven through a light guide to a photomultiplier. As the emitted positrons have a large kinetic energy, up to 52 MeV, they weakly interact with the sample and are weakly absorbed by the surrounding cryostat and vacuum chamber walls.

The key point lies on the direction of the emitted positron, which is correlated to the muon spin orientation as shown in the right panel of Fig. 2.15. This panel illustrates the probability  $W(\theta)$  of the positron to be emitted in a direction making an angle  $\theta$  with the muon spin and calculated as:

$$W(\theta) \propto [1 + a_{as}(\varepsilon) \cos \theta], \quad (2.40)$$

where  $a_{as}$  is an asymmetry parameter varying with the kinetic energy  $\varepsilon$  of the positron as  $(2\varepsilon - 1)/(3 - 2\varepsilon)$ . Counting all the positrons and integrating over the energy range available for the positron give  $\langle a_{as} \rangle = \frac{1}{3}$ .

### 2.6.3 Pseudo-continuous versus pulsed source

The  $S\mu S$  source at PSI is a pseudo-continuous source, see Sec. 2.2.3. A detector is placed in the muon beam close to the sample, and a clock is started when a muon is detected. The clock is stopped when the decay positron is detected to constitute a so-called event. If a second muon is implanted before the positron arising from the first implanted muon is detected, the electronic acquisition system pauses to avoid so-called coincidence. As the detectors do not cover a  $4\pi$  solid angle around the sample, there is a non-negligible probability that the positron arising from the muon decay does not hit the detector. As a result, a timeout of few muon lifetimes is introduced ( $\approx 10 \mu s$ ). In spite of these electronic considerations, the presence of a constant residual background due to the uncertainty to know the muon of origin of the detected positron cannot be avoided.

The ISIS source is a pulsed source described briefly in Sec. 2.2.2. The muon beam has the same time characteristics as the high energy proton beam hitting the graphite target: approximately Gaussian shaped muon pulses are separated by a time of 20 ms and a width of about 100 ns limiting the time resolution of the experiment. Contrary to the  $S\mu S$  source, a bunch of order thousands of muons is implanted in the sample at a time taken at zero. The main advantages lie first that only a few background particles are detected between the muons pulses which permits to characterise the muon spin polarisation function to significantly longer times compared to the  $S\mu S$  source as mentioned above, and thus to characterise slow relaxation process. However, note that an electrostatic deflector has been set up on the  $S\mu S$  line which prevents any additional muons to be implanted in the sample until its predecessor will be detected. This Muons-On-REquest (MORE) concept significantly reduces the background of a pseudo-continuous source without decreasing the intensity [161].

As a result, a pseudo-continuous source provides a high time resolution at short times and allows to observe strongly damped signals but the detection of weak magnetic fields giving a low muon frequency precession and the slow relaxation process are perturbed by the residual background. At the opposite, the latter processes can be evidenced on a pulsed source.

#### 2.6.4 Muon spectrometers

The MuSR spectrometer, see Fig. 2.17, is one of the muon instrument located at ISIS. To cope with the high intensity muons pulse, 32 positron detectors in forward position and 32 positron detectors in backward position surround the sample environment. Only a separator is present on the beam line to remove the background particles arising from the interaction between the proton beam and the graphite target. The muon spin is antiparallel to its momentum. Two possible configurations are available: zero or longitudinal field geometry and transverse field geometry, where the magnetic field is applied parallel or perpendicular to the muon spin, as shown in Fig. 2.16.

The GPS (General Purpose Surface) and LTF (Low Temperature Facility) spectrometers, see Fig. 2.17, have been utilised at the  $S\mu S$ . Their characteristics are summed up in Tab. 2.1. These spectrometers are designed to work also in zero, longitudinal or transverse field. However, in transverse geometry, the magnitude of the applied field is limited since the Lorentz force will deviate the muon beam out of the sample. Therefore, a spin rotator is placed between the muon production target and the spectrometers of interest. Firstly, it is used as a separator to select muons with a certain velocity. The aim is to remove background particles such as positrons arising from the pion decay by deflecting particles with a transverse magnetic field to mainly select muons. In the transverse field geometry, the spin rotator rotates the muon spin by about  $50^\circ$ . Therefore, a component of the muon spin is perpendicular to its momentum. Note that now, we apply the magnetic field parallel to the muon momentum, giving access to higher field magnitude. However, the initial asymmetry detected in the detectors is reduced.

The zero-field compensation process enables to remove the remanent field at the sample by applying hysteresis cycle of 10 mT, complemented with an active compensation device to reach a remanent field lower than  $3 \times 10^{-4}$  mT.

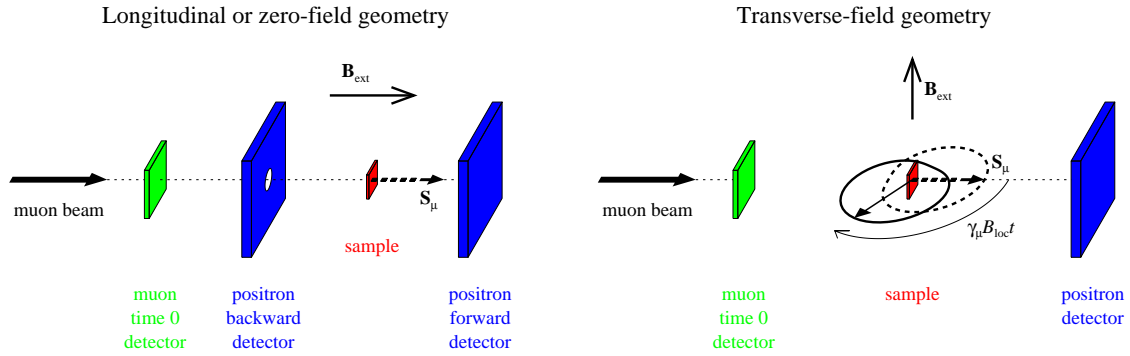


Figure 2.16: *Left: Illustration of the longitudinal (or zero) field geometry where a magnetic field is applied along the direction of the muon spin. Right: Illustration of the transverse geometry where a magnetic field is applied perpendicular to the muon spin. Practically, intensity of transverse magnetic field is low to prevent the deflection of the muon beam before implantation in the sample. Note that for both geometries, the muon spin is antiparallel to its momentum. Pictures taken with kind permission from Ref. [160].*

Spectrometer	Temperature	Maximal longitudinal field	Typical channel time
GPS	1.5-300 K	0.56 T	1 ns
LTF	10 mK-10 K	2.8 T	1 ns
MuSR	40 mK-1000 K	250 mT	16 ns

Table 2.1: *Summary of the characteristics of muon spectrometers of interest. GPS and LTF are respectively equipped with five (Forward, Backward, Up, Down, Right) and four (Forward, Backward, Right and Left) positrons detectors.*

### 2.6.5 Polarisation functions

The positron counts in a detector are modelled as:

$$N(t) = N_0 \exp(-t/\tau_\mu)[1 + a_0 P_\alpha(t)] + a_{bg}, \quad (2.41)$$

where  $N_0$  is the scale of the positron count, the exponential term stands for the finite lifetime of the muon,  $a_0$  is the initial asymmetry, usually of order 0.25 and assumed to be only dependent of the experimental conditions such as the solid angle covered by the detector,  $P_\alpha(t)$  is the time dependent muon polarisation function of interest measured in the  $X, Y, Z$  detector direction, and  $a_{bg}$  is a time-independent background term non negligible in the case of a pseudo-continuous source. In the longitudinal field geometry, only  $P_Z(t)$  is of interest whereas  $P_X(t)$  and  $P_Y(t)$  are accessible in transverse field geometry.

Labelling the forward detector as “+” and the backward one as “-”, then the number of positrons detected in each of one is written as:

$$N_\pm(t) = N_{0,\pm} \exp(-t/\tau_\mu)[1 \pm a_0 P_\alpha(t)] + a_{bg,\pm}. \quad (2.42)$$

Then, assuming that  $a_{bg,\pm} = 0$  and introducing a parameter  $\alpha_d = N_{0,+}/N_{0,-}$  taking into account the difference of efficiency of the detectors, and usually determined applying a weak transverse field, the polarisation function of the muon is then obtained



Figure 2.17: Pictures of the different muon spectrometers of interest in this work: GPS (left), LTF (middle) and MuSR (right).

combining the counts of each detectors as:

$$a_0 P_\alpha(t) = \frac{N_+(t) - \alpha_d N_-(t)}{N_+(t) + \alpha_d N_-(t)}, \quad (2.43)$$

where  $t$  refers to the discretized time channel. In the case of a pseudo-continuous source, a time independent background must be introduced

The basic muons polarisation functions will be introduced. Let us first consider a magnetic sample with a spontaneous local field  $\mathbf{B}_{\text{loc}}$ . If no external magnetic field is applied, muon spins undergo a precession motion around the local field  $\mathbf{B}_{\text{loc}}$  oriented at an angle  $\theta$  with respect to the muon spin. Solving the Larmor equation displayed in Eq. 2.36 leads to:

$$P_Z(t) = \cos^2 \theta + \sin^2 \theta \cos(\omega_\mu t), \quad (2.44)$$

where  $\omega_\mu = \gamma_\mu B_{\text{loc}}$  is the Larmor pulsation. Performing a spatial average of Eq. 2.44 since we are only interested in powder samples, we get:

$$P_Z(t) = \frac{1}{3} + \frac{2}{3} \cos(\omega_\mu t). \quad (2.45)$$

In the paramagnetic case or if the spin fluctuations are sufficiently fast in the ordered state not to keep a constant value of  $B_{\text{loc}}$ , the muon polarisation relaxes through an exchange of energy between the muon spin and the system. The polarisation function of the muon spin is then described by:

$$P_Z(t) = \exp[-(\lambda_Z t)^{\beta_{\text{se}}}], \quad (2.46)$$

where  $\lambda_Z$  is the so-called spin-lattice relaxation rate and  $\beta_{\text{se}} = 1$ . In the case where a continuous distribution of relaxation channels is involved, a stretched exponential function is introduced with  $0 < \beta_{\text{se}} \leq 1$ .

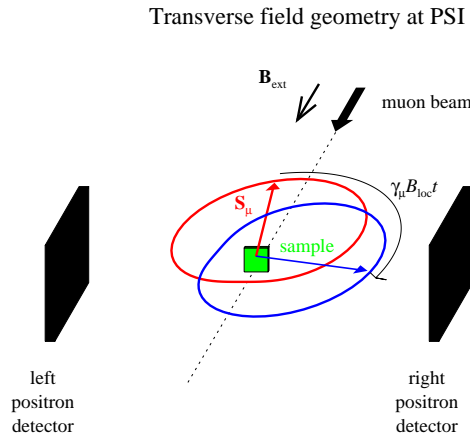


Figure 2.18: Illustration of the transverse geometry used at the LTF spectrometer (PSI). A spin rotator flips the muon spin of about  $\approx 50^\circ$  from its momentum. Note that the initial asymmetry is slightly reduced in this configuration, i.e.  $a_0 \approx 0.22$  compared to the value expected in zero or longitudinal field geometry ( $a_0 \approx 0.25$ ). The magnetic field  $\mathbf{B}_{\text{ext}}$  is applied parallel to the incoming muon beam. Therefore, the muon spin undergoes a precession motion around the local field  $\mathbf{B}_{\text{loc}}$ : the red arrow illustrates the muon spin orientation at the muon implantation time in the sample  $t = 0$  where it is antiparallel and tilted from the muon beam direction. The blue arrow is the muon spin at a time  $t > 0$  with a phase shift  $\gamma_\mu B_{\text{loc}} t$ . The red and blue cardioids represent the probability  $W(\theta)$  of positron emission along the muon spin axis, see Eq. 2.40, at times  $t = 0$  and  $t > 0$ , respectively. The black parallelepipeds are the right and left positron detectors of the muon spectrometer giving access to the transverse muon polarisation function  $a_0 P_X(t)$ .

### 2.6.6 Muon Knight shift measurements

We specify in this section some details about the muon Knight shift technique, used at the  $S\mu S$  (PSI). In order to prevent the deflection of the muon beam out of the sample and apply higher magnetic field, the usual transverse field mode described in Sec. 2.6 is not used here. We rather flip the muon spin  $\mathbf{S}_\mu$  of about  $50^\circ$  from its momentum with a spin rotator and use the transverse-field geometry pictured in Fig. 2.18. The external magnetic field  $\mathbf{B}_{\text{ext}}$  is applied parallel to the muon beam and its direction states the  $Z$  axis of the laboratory frame. The quantity of interest is the TF- $\mu$ SR asymmetry time spectrum  $a_0 P_X^{\text{exp}}(t)$ , where  $P_X^{\text{exp}}(t)$  describes the evolution of the muon polarisation under  $\mathbf{B}_{\text{ext}}$ . The muon polarisation function is described by the sum of two oscillating components: one accounting for the muons implanted in the sample and precessing with a frequency  $\nu_\mu$  around the local field at the muon site  $B_{\text{loc}}$ , and the second for the muons stopped in the sample surroundings, essentially the silver sample holder, which precess around a field close to the external field  $B_{\text{ext}}$  with a frequency  $\nu_{\text{ext}}$ . The normalised muon frequency shift  $K_{\text{exp}}$  is defined as [160]:

$$K_{\text{exp}} = \frac{\mathbf{B}_{\text{ext}} \cdot (\mathbf{B}_{\text{loc}} - \mathbf{B}_{\text{ext}})}{B_{\text{ext}}^2}. \quad (2.47)$$

Usually measurements are performed in a field sufficiently large such as  $|\mathbf{B}_{\text{loc}} - \mathbf{B}_{\text{ext}}|$  is small compared to  $B_{\text{ext}}$ , and Eq. 2.47 becomes:

$$K_{\text{exp}} = \frac{B_{\text{loc}} - B_{\text{ext}}}{B_{\text{ext}}}. \quad (2.48)$$

Note that the aforementioned condition means that  $K_{\text{exp}}$  is a measure of the magnetic response of the system submitted to a magnetic field, i.e. the local magnetic susceptibility at the muon site, along the direction of  $\mathbf{B}_{\text{ext}}$ . Since we have  $\nu_{\mu} = \gamma_{\mu} B_{\text{loc}} / (2\pi)$  and  $\nu_{\text{ext}} = \gamma_{\mu} B_{\text{ext}} / (2\pi)$ , we get:

$$K_{\text{exp}} = \frac{\nu_{\mu} - \nu_{\text{ext}}}{\nu_{\text{ext}}} = \frac{\Delta\nu}{\nu_{\text{ext}}}. \quad (2.49)$$

Since we are dealing with insulators, only the dipolar field  $\mathbf{B}_{\text{dip}}$  arising from the rare earth magnetic moments contributes to the local field at the muon site. The dipolar field at the muon site is calculated as:

$$\mathbf{B}_{\text{dip}} = \frac{g\mu_0\mu_B}{4\pi} \sum_{i=1}^N \frac{\mathbf{J}_i}{r_i^3} - \frac{3(\mathbf{J}_i \cdot \mathbf{r}_i)\mathbf{r}_i}{r_i^5}, \quad (2.50)$$

where  $\mathbf{r}_i$  is the vector linking the muon to the magnetic ion at site  $i$ . Although the dipolar field created by a magnetic moment at a distance  $r$  decreases as  $r^3$ , the number of magnetic moments at this distance increase as  $r^2$ . This statement implies that all the magnetic moments of the sample need to be considered. This dipolar field at the muon site can be decomposed in several contributions [160]:

$$\mathbf{B}_{\text{dip}} = \mathbf{B}'_{\text{dip}} + \mathbf{B}_{\text{Lor}} + \mathbf{B}_{\text{dem}} \quad (2.51)$$

where  $\mathbf{B}'_{\text{dip}}$  is the dipolar field arising from a discrete sum over the magnetic moments located in a so-called Lorentz sphere centered at the muon site and of radius sufficiently large so that the sum convergence is reached. The remaining magnetic dipoles are located outside the Lorentz sphere and can be described in a continuous approach. Therefore, two additional terms to the dipolar field at the muon site contribute: the Lorentz field  $\mathbf{B}_{\text{Lor}}$  and the demagnetising field  $\mathbf{B}_{\text{dem}}$  arising from the magnetic charges located at the surface of the Lorentz sphere and of the sample, respectively. Since the two latter contributions are macroscopic fields, the muon Knight-shift  $K_{\mu}$  is usually described as [160]:

$$K_{\mu} = K_{\text{exp}} - \frac{\mathbf{B}_{\text{ext}} \cdot (\mathbf{B}_{\text{Lor}} + \mathbf{B}_{\text{dem}})}{B_{\text{ext}}^2}. \quad (2.52)$$

Therefore,  $K_{\mu}$  arises only from the dipolar field created by the magnetic moments inside the Lorentz sphere, i.e.  $K_{\mu} = K'_{\text{dip}}$ . Since the Lorentz field arises from magnetic charges located on the surface of the Lorentz sphere, it is easily derived as:

$$\mathbf{B}_{\text{Lor}} = \frac{\mu_0 \mathbf{M}_{\text{Lor}}}{3}, \quad (2.53)$$

where  $\mathbf{M}_{\text{Lor}}$  is the magnetisation per unit of volume inside the Lorentz sphere. Note that we assume that the investigated compound is magnetically saturated and  $\mathbf{M}_{\text{Lor}} = \mathbf{M}$ , where  $\mathbf{M}$  is the bulk magnetisation of the sample. Note that this equality does not hold anymore if magnetisation domains exist. In the case of an ellipsoidal sample, the demagnetising field is uniform and can be derived:

$$\mathbf{B}_{\text{dem}} = -\mu_0 \mathbf{N} \mathbf{M} \quad (2.54)$$

where  $\mathbf{N}$  is a diagonal tensor. Recalling that  $\mathbf{B}_{\text{ext}}$  is collinear to the  $Z$  axis so does the magnetisation in a paramagnetic sample, and combining Eq. 2.53 and Eq. 2.54 in Eq. 2.52 gives us:

$$K_\mu = K'_{\text{dip}} = K_{\text{exp}} - \mu_0 \left( \frac{1}{3} - N^{ZZ} \right) \frac{M}{B_{\text{ext}}}. \quad (2.55)$$

# Chapter 3

## Crystal-electric-field study of the pyrochlore series $R_2M_2O_7$

### Contents

---

<b>3.1</b>	<b>Introduction</b>	<b>69</b>
3.1.1	Rare earth properties	69
3.1.2	The Stevens Hamiltonian	71
3.1.3	Neutron cross section	74
<b>3.2</b>	<b>CEF of the titanate series <math>R_2Ti_2O_7</math></b>	<b>75</b>
3.2.1	Published CEF parameters	75
3.2.2	Proposal of a single CEF solution	75
3.2.3	Analysis of $Tb_2Ti_2O_7$	79
3.2.4	Analysis of $Er_2Ti_2O_7$	81
3.2.5	Analysis of $Ho_2Ti_2O_7$	83
3.2.6	Conclusions	86
<b>3.3</b>	<b>CEF of the stannate series <math>R_2Sn_2O_7</math></b>	<b>88</b>
3.3.1	Published CEF parameters	88
3.3.2	Analysis of $Ho_2Sn_2O_7$	90
3.3.3	Analysis of $Tb_2Sn_2O_7$	94
3.3.4	Analysis of $Er_2Sn_2O_7$	95
3.3.5	Conclusions	98

---

The study of the crystal-electric-field (CEF) acting at the rare earth site is of central importance in the pyrochlore compounds. It fixes the spin symmetry at the rare earth site: Ising, XY, Heisenberg. The prediction of the CEF energy level scheme teaches us if the ground state is well isolated from the excited energy levels as in the spin-ice case, or if we should consider a mixing between the ground state and the low-lying energy level as in  $Tb_2Ti_2O_7$ , see Chapter 5. Finally, the determination of the CEF wavefunctions is necessary to provide a basis for the diagonalisation of the Hamiltonian of interest. We will introduce in this chapter the Stevens Hamiltonian used in this work. Then, using

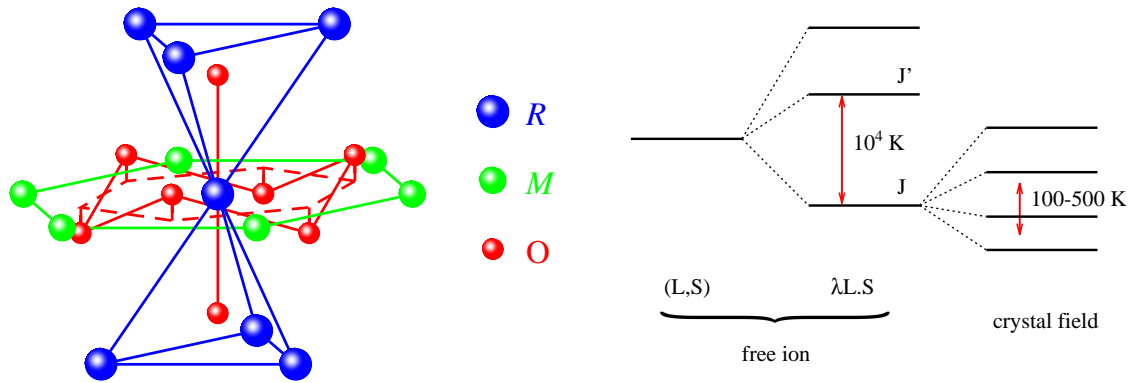


Figure 3.1: *Left: Local environment of a given rare earth ion in the pyrochlore lattice structure. The rare earth atoms are pictured with the largest red spheres, oxygen atoms with the smallest blue spheres, and the atoms  $M = \text{Ti}$  or  $\text{Sn}$  with green intermediate size spheres. Reprinted figure with permission from Ref. [91]. Copyright 2015 by the American Physical Society. Right: Illustration of the ground state multiplet arising from the spin-orbit coupling split by the perturbative CEF Hamiltonian.*

a simple model describing the whole family of the titanate pyrochlore  $R_2\text{Ti}_2\text{O}_7$ , we will compare our results to previous work and finally we will apply the same methodology on the stannate family of chemical formula  $R_2\text{Sn}_2\text{O}_7$  analysing our inelastic neutron scattering measurements.

## 3.1 Introduction

### 3.1.1 Rare earth properties

At the rare earth site, an electric field acts on the magnetic ion. This crystalline field arises from all the electric charges carried by the surroundings ions as illustrated in the left panel of Fig. 3.1. Magnetism in the rare earth compounds arises from the localised  $4f$  electronic shell. The electronic configuration of the ground state of the rare earth ions is of the form  $[\text{Xe}]4f^n5d^16s^2$ . The number  $n$  of electrons in the incomplete  $4f$  electronic shell is given in Tab. 3.1. The degeneracy associated to the ground state of the free ion, characterised by the kinetic energy of the electrons and the electron-electron and nucleus-electron coulombic interactions, is calculated by the number of possibilities to place  $n$  electrons in the incomplete  $4f$  electronic shell, i.e.  $14!/(n!(14-n)!)$ . The Russell-Saunders coupling, which arises from the interaction between the spin and the orbital momentum of the electrons, splits the ground state of the free ion into multiplets.<sup>1</sup> The spin-orbit Hamiltonian takes the following form:

$$\mathcal{H}_{\text{so}} = \lambda_{\text{so}} \mathbf{L} \cdot \mathbf{S}, \quad (3.1)$$

<sup>1</sup>This is valid in the case of the rare earth ions where the interaction between the orbital angular momentum of the  $4f$  electrons is weak. This assumption is not valid anymore for heavier elements for which the  $j-j$  coupling should be considered.

Rare earth	Pr <sup>3+</sup>	Nd <sup>3+</sup>	Gd <sup>3+</sup>	Tb <sup>3+</sup>	Dy <sup>3+</sup>	Ho <sup>3+</sup>	Er <sup>3+</sup>	Tm <sup>3+</sup>	Yb <sup>3+</sup>
$n(4f)$	2	3	7	8	9	10	11	12	13
$S$	1	3/2	7/2	3	5/2	2	3/2	1	1/2
$L$	5	6	0	3	5	6	6	5	3
$J$	4	9/2	7/2	6	15/2	8	15/2	6	7/2
$g_J$	4/5	8/11	2	3/2	4/3	5/4	6/5	7/6	8/7
Ground state	<sup>3</sup> H <sub>4</sub>	<sup>4</sup> I <sub>9/2</sub>	<sup>8</sup> S <sub>7/2</sub>	<sup>7</sup> F <sub>6</sub>	<sup>6</sup> H <sub>15/2</sub>	<sup>5</sup> I <sub>8</sub>	<sup>4</sup> I <sub>15/2</sub>	<sup>3</sup> H <sub>6</sub>	<sup>2</sup> F <sub>7/2</sub>
$\Delta_{so}$ (meV)	266	236	-	294	408	644	802	729	1271
Kramers ion	no	yes	yes	no	yes	no	yes	no	yes

Table 3.1: *Some rare earth properties: the number of electrons in the 4f electronic shell, the total spin  $S$ , orbital momentum  $L$  and total angular momentum  $J$  of the rare earth ions, the Landé factor, the ground state multiplet arising from the spin-orbit coupling, the energy difference between the latter and the first excited term [162], and the Kramers character of the ion of interest are listed in this table. The ground state term is labelled as  $^{2S+1}X_J$  where  $X=(S, P, D, F, G, H, I)$  for  $L=(0, 1, 2, 3, 4, 5, 6)$ .*

where  $\mathbf{L}$  and  $\mathbf{S}$  are the total orbital and spin angular momenta of the rare earth, respectively, and  $\lambda_{so}$  is a constant taking into account the radial part of the electron wavefunction. The matrix form of Eq. 3.1 is diagonal within the basis  $|L, S, J, m_J\rangle$ , where  $\mathbf{J} = \mathbf{L} + \mathbf{S}$  is the total angular momentum and  $-J \leq m_J \leq J$ . All these quantum numbers are determined by Hund's rules,<sup>2</sup> and are gathered in Tab. 3.1 as well as the corresponding denomination of the ground state term, the energy splitting between the ground state and the first excited term, and the Landé factor  $g_J$ . The latter is calculated as:

$$g_J = \frac{1 + J(J + 1) - L(L + 1) + S(S + 1)}{2J(J + 1)}. \quad (3.2)$$

Each multiplet is characterised by a value of  $J$  with a degeneracy equal to  $(2J + 1)$ . The ground state multiplet is defined in Tab. 3.1. The Kramers theorem should be mentioned concerning ions having an odd number of electrons, i.e. for half-integer  $J$  values (Kramers ions): the multiplets arising from the spin-orbit coupling can only be split into at least doubly degenerated states, where the degeneracy can only be lifted by a time-reversal symmetry breaking perturbation such as an external magnetic field. A peculiar feature of the wavefunctions describing these states is that they are time conjugated, i.e. if  $|\Psi^\pm\rangle$  are the wavefunctions of a given doublet state, then  $|\Psi^-\rangle = \hat{\theta}|\Psi^+\rangle$  where  $\hat{\theta}$  is the odd time-reversal operator [163]. On the other side, for non-Kramers ions, i.e. for an even number of electrons, no rule governs the splitting of the multiplets: accidental degenerated states exist and the degeneracy is susceptible to be lifted by any perturbations.

We have introduced above the notion of localised magnetism. The reason lies in the fact that the 4f electronic shell is more internal than the 5s, 5p, 5d and 6s electronic

<sup>2</sup> The three Hund's rules are for a given electronic configuration:

- ① The ground state term is defined with the maximum multiplicity, i.e. the highest value of  $S$ ,
- ② For a given multiplicity, the term with the lowest energy is the one maximising  $L$ ,
- ③ The lowest energy term for atoms with an electronic shell equal or less than half-filled is the one with  $J = |L - S|$  whereas for atoms with an electronic shell more than half-filled,  $J = |L + S|$ .

shells. Besides, the rare earth are usually in the 3+ valence state meaning that two electrons of the 5s shell and one of the 5p shell are missing. Therefore, 5s and 5p electronic shells are involved in the chemical bondings and the 4f electronic shell is shielded by the 5d and 6s external electronic shells: thus, crystal-electric-field effects can be treated as a perturbation of the spin-orbit coupling. The multiplets are split into crystal-electric-field states, e.g.  $(2J + 1)$  states for the ground state multiplet. These successive splittings are illustrated in the right panel of Fig. 3.1 where an order of magnitude of the overall energy splitting is given in units of temperature.

### 3.1.2 The Stevens Hamiltonian

The crystal-electric-field Hamiltonian  $\mathcal{H}_{\text{CEF}}$  can be written in terms of Stevens operators  $O_n^m$  (see App. B):

$$\mathcal{H}_{\text{CEF}} = \sum_{nm} [A_n^m \langle r^n \rangle \Theta_n] O_n^m, \quad (3.3)$$

where  $\Theta_n$  are the Stevens multiplicative factor listed in Tab. B.1,  $\langle r^n \rangle$  are the expectation values of the  $n$ th power distance between the nucleus of the magnetic ion and the 4f electronic shell, listed in Tab. B.2, and the crystal-electric-field parameters  $A_n^m$  are defined by Eq. B.18. We note that the Stevens operators are polynomial functions of  $J_z$  and  $J_{\pm}$ . The aim is to calculate the matrix elements of  $\mathcal{H}_{\text{CEF}}$  within the ground state multiplet defined by the basis  $|L, S, J, m_J\rangle$ , which we will denote  $|m_J\rangle$  in the following since  $L$ ,  $S$ , and  $J$  are fixed values within a multiplet. We assume that the splitting between the ground state and first excited multiplets is sufficiently large not to consider the latter. This hypothesis may not be valid for the lightest rare earths, see  $\Delta_{\text{so}}$  in Tab. 3.1

We need to determine which Stevens operators are involved in the CEF Hamiltonian. First, all matrix elements for operators of order  $n > 2l$  vanish, where  $l$  is the orbital quantum number of the electron (for the 4f electronic shell,  $l = 3$ ) [164]. Besides, the CEF Hamiltonian needs to remain invariant under time reversal symmetry. We focus on the operators  $J_z^n$  involved in the Stevens operator  $O_n^m$ . The time reversal symmetry operator is written within the  $|m_J\rangle$  basis as [163]:

$$\hat{\theta} = \exp(i\pi J_y) K_0, \quad (3.4)$$

where  $K_0$  is the complex conjugation operator acting on a wavefunction of the form  $|\Psi\rangle = \sum_{m_J} \alpha_{m_J} |m_J\rangle$ , where  $\alpha_{m_J}$  are constants, as:

$$K_0 |\Psi\rangle = \sum_{m_J} \alpha_{m_J}^* |m_J\rangle. \quad (3.5)$$

Therefore we calculate the commutator of  $J_z^n$  and  $\hat{\theta}$  within two wavefunctions defining the ground state multiplet  $|m_J\rangle$  and  $|m'_J\rangle$ :

$$\langle m'_J | [J_z^n, \hat{\theta}] | m_J \rangle = \langle m'_J | J_z^n \hat{\theta} - \hat{\theta} J_z^n | m_J \rangle. \quad (3.6)$$

From Ref. [163], the only non-vanishing matrix elements are:

$$\langle -m_J | \exp(i\pi J_y) | m_J \rangle = (-1)^{J-m_J}. \quad (3.7)$$

This leads to:

$$\langle m'_J | [J_z^n, \hat{\theta}] | m_J \rangle = \delta_{m'_J, -m_J} (m_J)^n (-1)^{J-m_J} [(-1)^n - 1]. \quad (3.8)$$

In order to get the CEF Hamiltonian invariant under time reversal symmetry, we need Eq. 3.8 to vanish. This condition is fulfilled only if  $n = 2k$ , where  $k$  is an integer.

We recall that the local point group symmetry at the rare earth site is  $D_{3d}$ . One of the symmetry elements belonging to this group is the  $\frac{2\pi}{3}$  rotation<sup>3</sup> around the  $z$  axis [111] and its associated operator is defined as:

$$R_z \left( \frac{2\pi}{3} \right) = \exp \left( -\frac{2i\pi}{3} J_z \right). \quad (3.9)$$

The CEF Hamiltonian needs to remain invariant under the symmetry operators associated to the local point group. We focus on the operators  $J_{\pm}^m$  involved in the Stevens operators  $O_n^m$ . Therefore, we calculate the commutator of  $J_{\pm}^m$  and the symmetry operator  $R_z \left( \frac{2\pi}{3} \right)$  within the  $|m_J\rangle$  basis:

$$\begin{aligned} \langle m'_J | \left[ J_{\pm}^m, R_z \left( \frac{2\pi}{3} \right) \right] | m_J \rangle &= \langle m'_J | J_{\pm}^m \exp \left( -\frac{2i\pi}{3} J_z \right) - \exp \left( -\frac{2i\pi}{3} J_z \right) J_{\pm}^m | m_J \rangle \\ &= \alpha_{\pm, m} \delta_{m'_J, (m_J \pm m)} \exp \left( -\frac{2i\pi m_J}{3} \right) \left[ 1 - \exp \left( \frac{\mp 2i\pi m}{3} \right) \right], \end{aligned} \quad (3.10)$$

where  $\delta_{a,b}$  is the Kronecker symbol ( $\delta_{a,b} = 1$  if  $a = b$  and 0 otherwise), and the constants  $\alpha_{\pm, m}$  have been introduced such as:

$$\begin{aligned} J_{\pm}^m | m_J \rangle &= \alpha_{\pm, m} | m_J \pm m \rangle, \quad \text{with for instance} \\ J_{\pm} | m_J \rangle &= \sqrt{J(J+1) - m_J(m_J \pm 1)} | m_J \pm 1 \rangle. \end{aligned} \quad (3.11)$$

Therefore, the invariance of the Hamiltonian is preserved, i.e. Eq. 3.10 vanishes, if  $m = 3p$ , where  $p$  is an integer.

In conclusion, we have shown with these geometrical considerations that the CEF Hamiltonian at the rare earth site is written as:<sup>4</sup>

$$\begin{aligned} \mathcal{H}_{\text{CEF}} &= \sum_{nm} [A_n^m \langle r^n \rangle \Theta_n] O_n^m = \sum_{nm} B_n^m O_n^m, \\ &= B_2^0 O_2^0 + B_4^0 O_4^0 + B_4^3 O_4^3 + B_6^0 O_6^0 + B_6^3 O_6^3 + B_6^6 O_6^6, \end{aligned} \quad (3.12)$$

where we have introduced:

$$B_n^m = A_n^m \langle r^n \rangle \Theta_n. \quad (3.13)$$

The useful Stevens operators are expressed as:

<sup>3</sup>Other symmetry elements of this point group are not used here since they are not useful to determine which Stevens operators are needed in the CEF Hamiltonian.

<sup>4</sup>We recall that  $m \leq n$ .

$$\begin{aligned}
O_2^0 &= 3J_z^2 - J(J+1), \\
O_4^0 &= 35J_z^4 - 30J(J+1)J_z^2 + 25J_z^2 - 6J(J+1) + 3J^2(J+1)^2, \\
O_6^0 &= 231J_z^6 - 315J(J+1)J_z^4 + 735J_z^4 + 105J^2(J+1)^2J_z^2 \\
&\quad - 525J(J+1)J_z^2 + 294J_z^2 - 5J^3(J+1)^3 + 40J^2(J+1)^2 \\
&\quad - 60J(J+1), \\
O_6^3 &= \frac{1}{4} \left\{ [11J_z^3 - 3J(J+1)J_z - 59J_z] (J_+^3 + J_-^3) \right. \\
&\quad \left. + (J_+^3 + J_-^3) [11J_z^3 - 3J(J+1)J_z - 59J_z] \right\}, \\
O_4^3 &= \frac{1}{4} [J_z(J_+^3 + J_-^3) + (J_+^3 + J_-^3)J_z], \\
O_6^6 &= \frac{1}{2}(J_+^6 + J_-^6). \tag{3.14}
\end{aligned}$$

Note that in the  $|m_J\rangle$  basis, the Stevens operators  $O_n^0$  are diagonal, and applying operators  $O_n^3$  and  $O_n^6$  on a ket  $|m_J\rangle$ , give us only  $|J, m_J \pm 3\rangle$ , and  $|J, m_J \pm 3\rangle$  and  $|J, m_J \pm 6\rangle$ , respectively. Therefore the matrix representation of the CEF Hamiltonian of dimension  $(2J+1)$  can be ordered in a block form.

From the point charge model introduced in App. B, using Eq. B.18 and expressing the tesseral harmonics  $Z_n^m(\theta_i, \phi_i)$  in Cartesian coordinates,<sup>5</sup> the CEF parameters  $A_n^m$  are derived as:

$$\begin{aligned}
A_2^0 &= -\frac{e}{4\pi\epsilon_0} \left(\frac{1}{4}\right)^2 \left(\frac{5}{\pi}\right) \sum_{i=1}^k \frac{4\pi}{5} q_i \frac{3z_i^2 - R_i^2}{R_i^5}, \\
A_4^0 &= -\frac{e}{4\pi\epsilon_0} \left(\frac{3}{16}\right)^2 \left(\frac{1}{\pi}\right) \sum_{j=i}^k \frac{4\pi}{9} q_i \frac{35z_i^4 - 30z_i^2 R_i^2 + 3R_i^4}{R_i^9}, \\
A_4^3 &= -\frac{e}{4\pi\epsilon_0} \left(\frac{3}{8}\right)^2 \left(\frac{70}{\pi}\right) \sum_{j=i}^k \frac{4\pi}{9} q_i \frac{z_i(x_i^3 - 3x_i y_i^2)}{R_i^9}, \\
A_6^0 &= -\frac{e}{4\pi\epsilon_0} \left(\frac{1}{32}\right)^2 \left(\frac{13}{\pi}\right) \sum_{i=1}^k \frac{4\pi}{13} q_i \frac{231z_i^6 - 315z_i^4 R_i^2 + 105z_i^2 R_i^4 - 5R_i^6}{R_i^{13}}, \\
A_6^3 &= -\frac{e}{4\pi\epsilon_0} \left(\frac{1}{32}\right)^2 \left(\frac{2730}{\pi}\right) \sum_{i=1}^k \frac{4\pi}{13} q_i \frac{(11z_i^3 - 3z_i R_i^2)(x_i^3 - 3x_i y_i^2)}{R_i^{13}}, \\
A_6^6 &= -\frac{e}{4\pi\epsilon_0} \left(\frac{231}{64}\right)^2 \left(\frac{26}{231\pi}\right) \sum_{i=1}^k \frac{4\pi}{13} q_i \frac{x_i^6 - 15x_i^4 y_i^2 + 15x_i^2 y_i^4 - y_i^6}{R_i^{13}}, \tag{3.15}
\end{aligned}$$

<sup>5</sup>The useful tesseral harmonics are tabulated in Tab.IV of Ref. [164].

where  $(x_i, y_i, z_i)$  are the Cartesian coordinates of the  $k$  electric charges located at a distance  $R_i = (x_i^2 + y_i^2 + z_i^2)^{1/2}$  from the magnetic rare earth. Therefore, for isostructural compounds, i.e. belonging to the same family  $R_2M_2O_7$  ( $M = \text{Ti}$  or  $\text{Sn}$ ), a scaling law allows to deduce the CEF parameters for a rare earth  $R'$  from those of a rare earth  $R$  [164]:

$$A_n^m(R') = \frac{a_{\text{lat}}^{n+1}(R)}{a_{\text{lat}}^{n+1}(R')} A_n^m(R) \quad (3.16)$$

where  $a_{\text{lat}}(R)$  is the lattice parameter of the compound  $R_2M_2O_7$ . Note that we have implicitly assumed that the free parameter  $x$ , see Tab. A.1, which governs the position of the oxygen atoms labelled O1, see Tab. A.1, is approximatively constant within the series considered. This is the case of the compounds of interest here, with  $x \approx 1/3$  [165].

Within the framework of ab-initio calculations, the point charge model is clearly not reliable. The exchange charge model (ECM) has been introduced by Malkin *et al.* (see for instance Ref. [166]) to estimate the crystal-electric-field parameters. The latter are calculated from two contributions: the first is the effect of the electric field on  $4f$  electrons arising from a point charge distribution taking into account shielding effects of the external electronic shells. The second contribution takes into account the exchange integrals arising from the overlap of the orbitals of  $4f$  electrons and those of the nearest neighbours. Note that the CEF Hamiltonian is described with the tensor spherical operators  $C_n^m$  rather than the Stevens operators. This is the case for several works in the literature. The two Hamiltonians are equivalent and only differ from a prefactor in the CEF parameters. Relations between the two sets of parameters can be found in Ref. [123]. However, our goal is not to perform ab-initio calculations, and we assume the relation introduced in Eq. 3.16 to be reliable.

### 3.1.3 Neutron cross section

The most common method to determine CEF parameters is to analyse the CEF transitions revealed by inelastic neutron scattering experiments. The neutron partial differential scattering cross section is expressed in the dipole approximation as, see for example Ref. [167]:

$$\frac{d^2\sigma}{d\Omega dE'} = C \frac{k_f}{k_i} S(\mathbf{q}, \omega), \quad (3.17)$$

where  $S(\mathbf{q}, \omega)$  is the scattering function,  $\Omega$  the solid angle,  $k_f/k_i$  the ratio of the momenta of the scattered and incident neutrons and  $C$  a constant. For a polycrystalline sample only the modulus  $q$  of the scattering vector has to be considered. For a set of CEF transitions  $\{i \rightarrow i'\}$  at a constant scattering vector and at temperature  $T$ , we have

$$S(q, \omega) = \frac{I_0}{Z} \sum_{i, i'} \left( \sum_{\alpha=x, y, z} |\langle i | J_\alpha | i' \rangle|^2 \right) \exp[-E_i / (k_B T)] F(E_i - E_{i'} + \hbar\omega), \quad (3.18)$$

where  $Z = \sum_i \exp[-E_i / (k_B T)]$  is the partition function. Here  $I_0$  is a constant,  $|i\rangle$  and  $|i'\rangle$  are eigenvectors of  $\mathcal{H}_{\text{CEF}}$  defined as:

$$|i\rangle = \sum_{m_J=-J}^J \alpha_{m_J} |m_J\rangle. \quad (3.19)$$

Rare earth	Tb <sup>3+</sup>	Dy <sup>3+</sup>	Ho <sup>3+</sup>	Er <sup>3+</sup>	Tm <sup>3+</sup>	Yb <sup>3+</sup>
$a_{\text{lat}}$ (Å)	10.1475(1)	10.1248(1)	10.0986(1)	10.0727(1)	10.0537(2)	10.0204(1)

Table 3.2: List of the lattice parameters  $a_{\text{lat}}$  used in this work for the  $R_2\text{Ti}_2\text{O}_7$  series. Data taken from Ref. [165].

The function  $F(E_i - E_{i'} + \hbar\omega)$  describes the  $i \rightarrow i'$  CEF transition with a neutron energy transfer  $\hbar\omega = E_{i'} - E_i$ . It is taken as the convolution of Gaussian and Lorentzian functions. The Gaussian stands for the resolution of the spectrometer. The Lorentzian function is written as:

$$L_{i,i'}(\hbar\omega + E_i - E_{i'}) = \frac{1}{\pi} \frac{\Gamma_{i,i'}}{\Gamma_{i,i'}^2 + (\hbar\omega - (E_{i'} - E_i))^2} \quad (3.20)$$

where the FWHM  $\Gamma_{i,i'}$  accounts for the lifetime of the  $i'$  CEF energy level during the transition  $i \rightarrow i'$ .

## 3.2 CEF of the titanate series $R_2\text{Ti}_2\text{O}_7$

In this section, after a short review of published CEF parameters, we will present our results of a global analysis leading to a single set of CEF parameters describing the whole  $R_2\text{Ti}_2\text{O}_7$  series. The following sections will focus on the details of the analysis of inelastic neutron scattering spectra for  $\text{Tb}_2\text{Ti}_2\text{O}_7$ ,  $\text{Er}_2\text{Ti}_2\text{O}_7$ , and  $\text{Ho}_2\text{Ti}_2\text{O}_7$ .

### 3.2.1 Published CEF parameters

Many sets of CEF parameters have been proposed in the literature to describe the CEF properties of the titanate series. The most relevant are listed in Tab. 3.3. Mirebeau *et al.* [73] and Rosenkranz *et al.* [168] have derived the CEF parameters analysing inelastic neutron scattering spectra of a polycrystalline sample of  $\text{Tb}_2\text{Ti}_2\text{O}_7$  measured on a triple-axis spectrometer, and of a powder sample of  $\text{Ho}_2\text{Ti}_2\text{O}_7$  measured on a time-of-flight spectrometer, respectively. The corresponding CEF energy levels scheme are shown in the top left and right panels of Fig. 3.2. If computed and experimental CEF energy levels match very well for the investigated compound, some notable discrepancies appear looking at the other titanate compounds of the series: for instance, CEF parameters of Mirebeau *et al.* [73] account very well for  $\text{Tb}_2\text{Ti}_2\text{O}_7$ ; however, inelastic neutron scattering spectra of  $\text{Er}_2\text{Ti}_2\text{O}_7$  and  $\text{Ho}_2\text{Ti}_2\text{O}_7$  cannot be described with this set of parameters. Malkin *et al.* [169] have derived a set of CEF parameters with ab-initio calculations using the ECM model briefly introduced at the end of Sec. 3.1.2. Looking at the bottom left panel of Fig. 3.2, the mismatch between experimental and calculated energy levels does not allow to analyse inelastic neutron scattering spectra of compounds of the titanate series.

### 3.2.2 Proposal of a single CEF solution

Whereas crystal field parameters are determined in the literature for a single compound, we endeavour ourselves here to describe CEF properties of the whole series of the titanate compounds  $R_2\text{Ti}_2\text{O}_7$  with a single set of CEF parameters  $A_n^m$  (related to the  $B_n^m$

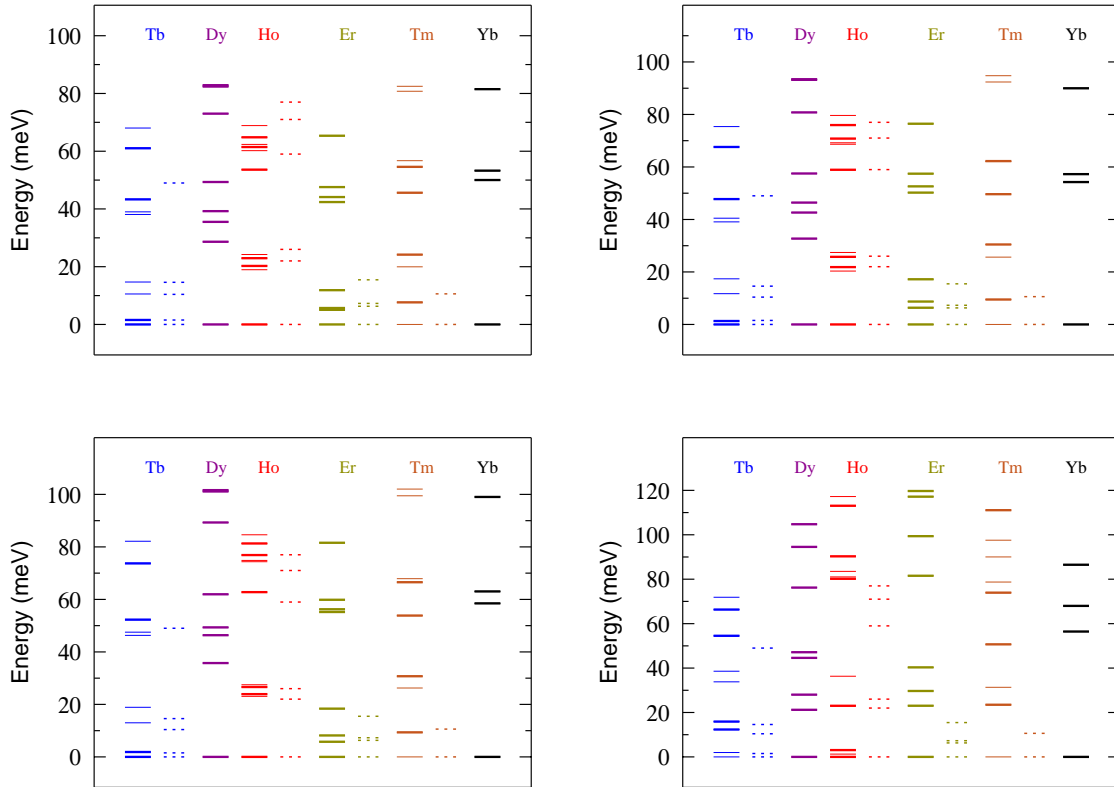


Figure 3.2: Computed CEF energy levels drawn for the  $R$  ions in the  $R_2Ti_2O_7$  pyrochlore series using CEF parameters listed in Tab. 3.3 proposed by Mirebeau *et al.* [73] (top left), Rosenkranz *et al.* [168] (top right), Malkin *et al.* [169] (bottom left), and Hodges *et al.* [83] (bottom right). Solid thin and thick lines stand for singlet and doublet states, respectively. All the theoretical CEF levels have been drawn. They may not be resolved on the figure because of the limited graphical resolution. The calculated energy levels are compared to experimental data extracted from inelastic neutron scattering experiments presented in dashed lines. These data are reproduced from Refs. [73, 170] for  $Tb_2Ti_2O_7$ , Refs. [96, 171] for  $Er_2Ti_2O_7$ , Ref. [168] for  $Ho_2Ti_2O_7$  and Ref. [172] for  $Tm_2Ti_2O_7$ .

parameters through Eq. 3.13) using the scaling law of Eq. 3.16. The lattice parameters  $a_{\text{lat}}$  used in this work are listed in Tab. 3.2. The perturbative CEF Hamiltonian is restrained to the ground state multiplet<sup>6</sup> which allows us to significantly reduce the dimension  $d$  of the matrix elements, i.e.  $d = (2J + 1)$ . The code *CEF* [174] has been developed in order to diagonalise the CEF Hamilton and simultaneously analyse published inelastic neutron scattering spectra of different rare earths with a single set of  $B_n^m$  parameters. The first step of the analysis was to find solutions allowing a match between experimental and calculated energy levels. The interval over which the  $A_n^m$  CEF parameters have been varied is displayed in the last row of Tab. 3.3.

<sup>6</sup>This assumption is valid for the heavier rare earth, but could be debatable, in the case of the lighter rare earth since  $\Delta_{\text{so}}$  becomes of the same order of magnitude as the whole CEF energy splitting, see Tab. 3.1.

$A_n^m$ (meV/ $a_0^n$ )	$A_2^0$	$A_4^0$	$A_4^3$	$A_6^0$	$A_6^3$	$A_6^6$
This work [173]	40.5(1)	24(1)	213(13)	1.03(3)	-17(1)	14(1)
Mirebeau <i>et al.</i> [73]	37	22	184	0.88	-11.2	13.6
Zhang <i>et al.</i> [170]	87	20.3	289	1.55	65.0	110.4
Rosenkranz <i>et al.</i> [168]	45	27	201	0.96	-16.4	17.6
Hodges <i>et al.</i> [83]	51.4	8.1	310	3.1	-20.7	23.8
Malkin <i>et al.</i> [169]	45	27	201	0.96	-16.4	17.6
Interval probed	[0,85]	[-34,50]	[-300,455]	[-3,3]	[-34,34]	[-25,30]

Table 3.3: The  $A_n^m$  parameters obtained from a global fit of the CEF levels determined by inelastic neutron scattering experiments are shown for  $\text{Tb}_2\text{Ti}_2\text{O}_7$  in the second row. The CEF parameters for the other compounds of the series can be obtained from Eq. 3.16. The units for  $A_n^m$  are meV/ $a_0^n$ , where  $a_0$  is the Bohr radius. In the subsequent four rows are listed the  $A_n^m$  parameters derived from the works of Mirebeau *et al.* [73] and Zhang *et al.* [170] on  $\text{Tb}_2\text{Ti}_2\text{O}_7$ , from the work of Rosenkranz *et al.* [168] on  $\text{Ho}_2\text{Ti}_2\text{O}_7$ , and from the work of Hodges *et al.* [83] on  $\text{Yb}_2\text{Ti}_2\text{O}_7$ . For comparison the  $A_n^m$  values inferred from the exchange-charge model are listed in the seventh row [169]. All CEF parameters given here have been rescaled for  $\text{Tb}_2\text{Ti}_2\text{O}_7$  using Eq. 3.16. The last row gives the intervals over which the  $A_n^m$  parameters have been varied in our global analysis.

A peculiar feature of the Hamiltonian given in Eq. 3.12 should be noticed: interchanging the  $A_4^3$  and  $A_6^3$  signs, or equivalently the  $B_4^3$  and  $B_6^3$  signs, has no influence on its eigenvalues as well as on the neutron intensity of the CEF transitions. As a consequence, this enables to reduce the numerical effort by a factor two when scanning the CEF parameters looking for solutions diagonalising  $\mathcal{H}_{\text{CEF}}$ . This can be understood as follows. For the sake of the derivation, the CEF Hamiltonian defined in Eq. 3.12 is denoted here as  $\mathcal{H}_{\text{CEF}}(B_2^0, B_4^0, B_4^3, B_6^0, B_6^3, B_6^6)$ . It can be easily shown that the matrix representation of this Hamiltonian in the Zeeman basis  $\{|m_J = J\rangle, \dots, |m_J = -J\rangle\}$  is the same as that of  $\mathcal{H}_{\text{CEF}}(B_2^0, B_4^0, -B_4^3, B_6^0, -B_6^3, B_6^6)$  in the basis  $\{|m_J = -J\rangle, \dots, |m_J = J\rangle\}$ .<sup>7</sup> Hence the eigenvalues, i.e. the energy levels, are equal. As mentioned in Sec. 3.1.3, we need to consider  $|\langle i|J_\alpha|i'\rangle|^2$  for the neutron intensity, where  $|i\rangle$  and  $|i'\rangle$  are eigenvectors. If  $|i\rangle = \sum_{m_J=-J}^J \alpha_{m_J} |m_J\rangle$  is an eigenvector of the Hamiltonian with the  $B_4^3$  and  $B_6^3$  parameters, the corresponding eigenvector of the second Hamiltonian with  $-B_4^3$  and  $-B_6^3$  is  $|j\rangle = \sum_{m_J=-J}^J \alpha_{m_J} |-m_J\rangle$ . Since  $\langle -m_J|J_\alpha|-m'_J\rangle = p \langle m_J|J_\alpha|m'_J\rangle$  with  $p = 1$  if  $\alpha = x$  and  $p = -1$  if  $\alpha = y$  or  $z$ , the transition intensities associated with the two Hamiltonians are equal.

The advantage of fitting the whole set of available level positions rather than the levels for a single compound is the increase in the number of levels involved. Even for the most favorable case of  $\text{Ho}_2\text{Ti}_2\text{O}_7$  only five levels were experimentally measured. Our global fit for four compounds includes twelve levels. The two highest CEF energy levels of  $\text{Tb}_2\text{Ti}_2\text{O}_7$  revealed by Zhang *et al.* [170] are not included in the analysis since they were not yet published. The second step was to simultaneously analyse the inelastic neutron scattering spectra (details of the analysis are presented in the following section). Within the probed CEF parameters interval, we find a single solution listed in the first

<sup>7</sup>Note the change in the vectors sequence in the two bases

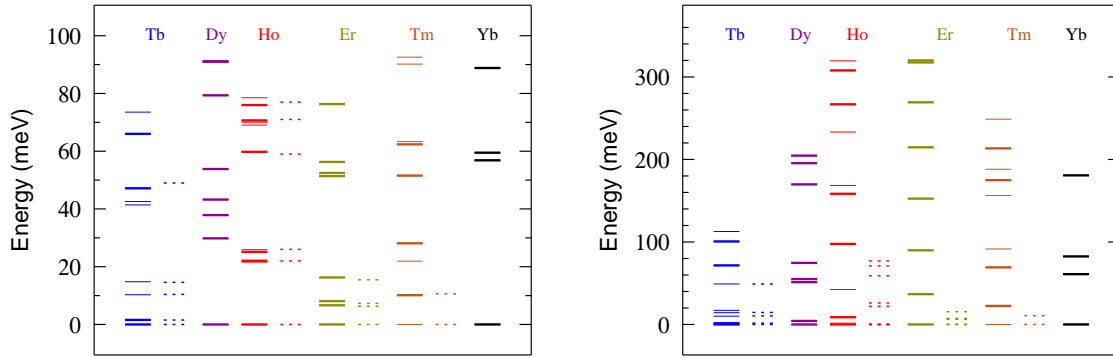


Figure 3.3: Computed CEF energy levels drawn for the  $R$  ions in the  $R_2Ti_2O_7$  pyrochlore series using our CEF parameters listed in the first row of Tab. 3.3 (left) and CEF parameters proposed in Ref. [170] listed in the third row of Tab. 3.3 (right). More details about the description of these panels are given in the caption of Fig. 3.2.

row of Tab. 3.3 leading to a fair description of the experimental data, see for instance the corresponding computed CEF energy levels scheme given in the left panel of Fig. 3.3.

Hodges *et al.* [83] have combined  $^{170}\text{Yb}$  Mössbauer spectroscopy,  $^{172}\text{Yb}$  perturbed angular correlation, magnetisation and susceptibility measurements of  $\text{Yb}_2\text{Ti}_2\text{O}_7$  in order to determine the CEF parameters. These parameters are listed in the fifth row of Tab. 3.3 and the computed CEF energy level scheme is displayed in the bottom right panel of Fig. 3.2 which clearly cannot account for the inelastic neutron scattering data. However, the three excited Kramers doublets of  $\text{Yb}_2\text{Ti}_2\text{O}_7$  are predicted to lie at  $\approx 53$ , 64, and 82 meV. Our set of CEF parameters listed in the first row of Tab. 3.3 leads to energy levels lying at  $\approx 57$ , 59, and 89 meV. These results are supported by the work of Malkin *et al.* [169] where optical measurements on a polycrystalline sample of  $\text{Yb}_2\text{Ti}_2\text{O}_7$  revealed CEF energy levels at 58 and 81 meV. We recall that our model does not take into account the influence of the first excited multiplet which can explain the difference observed between the highest computed energy levels, as it is the case here for  $\text{Yb}_2\text{Ti}_2\text{O}_7$ . On the other hand, Maczka *et al.* [175] performed Raman spectroscopy on  $\text{Dy}_2\text{Ti}_2\text{O}_7$  and evidenced at low temperatures a CEF transition from the ground state to an excited level lying at  $\approx 37.2$  meV. This is consistent with our calculations since we predict an energy level at 37.9 meV.

Concerning  $\text{Tm}_2\text{Ti}_2\text{O}_7$ , CEF excitations are predicted at around 10, 20, 27 and 51 meV; see the left panel of Fig. 3.3. Measurements by Zinkin *et al.* [172], indeed observe a crystal field excitation at around 10 meV in an inelastic neutron scattering spectrum recorded up to 14 meV. However, these authors claim that they looked for other transitions up to a maximum energy of 54 meV, but fail to detect any. Our simulation predicts that the two highest excitations at 27 and 51 meV have a negligible intensity, ( $\approx 6\%$  and  $4\%$  of the intensity of the peak at 10 meV) which certainly explains that they could not be detected. Still the intensity of the transition at 20 meV is predicted to be around 70% of the main peak and it should in principle be visible. A short lifetime of the associated level could smear it out. In the following, we analyse published inelastic neutron scattering spectra for several compounds using, within the

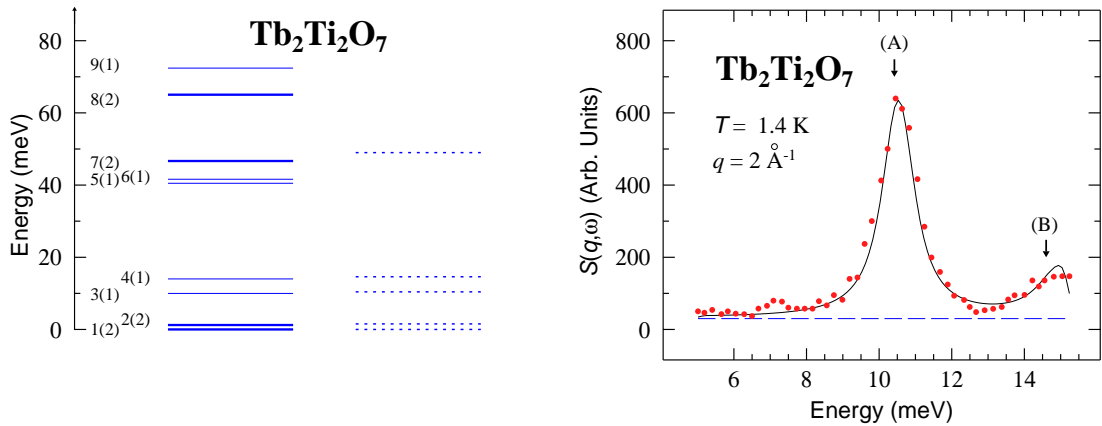


Figure 3.4: Left: Energy levels scheme of  $\text{Tb}_2\text{Ti}_2\text{O}_7$  obtained with our CEF parameters listed in the second row of Tab. 3.3. The different energy levels are labelled by numbers in order to identify the CEF transitions involved in inelastic neutron scattering spectra, see Tab. 3.4 and Tab. 3.5. The numbers in parentheses (1) and (2) correspond to singlet and doublet states, respectively. The dotted lines indicate the experimental CEF transitions revealed by inelastic neutron scattering spectroscopy [73, 170]. Right: Inelastic neutron scattering spectrum recorded on a powder sample of  $\text{Tb}_2\text{Ti}_2\text{O}_7$  at  $T = 1.4$  K and  $q = 2 \text{ \AA}^{-1}$ . Data are extracted from Fig. 5 (left) of Ref. [73]. The blue dashed line is the background contribution taken as a constant value. The black solid line is a fit to the data using our CEF parameters listed in the second row of Tab. 3.3. Black arrows indicate the CEF transitions: they are labelled by letters in order to identify the CEF energy levels, see Tab. 3.4 and left panel of this figure.

errors bars, our CEF parameters listed in the first row of Tab. 3.3.

### 3.2.3 Analysis of $\text{Tb}_2\text{Ti}_2\text{O}_7$

The computed CEF energy level scheme already shown in the left panel of Fig. 3.3 is drawn in the left panel of Fig. 3.4 for  $\text{Tb}_2\text{Ti}_2\text{O}_7$  in order to label the CEF transitions involved in the inelastic neutron scattering spectra of interest. First, we look at data recorded by Mirebeau *et al* [73] on a polycrystalline sample of  $\text{Tb}_2\text{Ti}_2\text{O}_7$ : (i) at  $T = 1.4$  K and  $q = 2 \text{ \AA}^{-1}$ , see the right panel of Fig. 3.4 and Tab. 3.4 for some details of the analysis reporting the linewidths of the Lorentzian functions describing the CEF transitions and their relative intensities, (ii) at  $T = 38$  K and  $q = 2 \text{ \AA}^{-1}$ , see Fig. 3.5 and Tab. 3.5, and (iii) at  $T = 4.1$  K and  $q = 3 \text{ \AA}^{-1}$ , see left panel of Fig. 3.6. The instrumental resolution is taken as a Gaussian function with FWHM equal to 0.25 meV for the right panel of Fig. 3.4 and Fig. 3.5, and to 1.08 meV for the left panel of Fig. 3.6 [73]. Before discussing goodness of the analysis, we should notice that the small peak observed at  $\approx 7$  meV is attributed to two inequivalent  $\text{Tb}^{3+}$  sites [176].

However, we note two issues in the analysis of  $\text{Tb}_2\text{Ti}_2\text{O}_7$ . First, our model predicts that a CEF transition located at 13.3 meV should be visible in the spectrum recorded at  $T = 38$  K, as illustrated in the left panel of Fig. 3.5, corresponding to the transition  $2 \rightarrow 4$  (D) (from the first to the third excited energy level), see left panel of Fig. 3.4, which are not compatible with data recorded by Mirebeau *et al.* [73]. The first excited

Transition ( $a \rightarrow b$ )	1 $\rightarrow$ 3 (A)	1 $\rightarrow$ 4 (B)
Energy (meV)	10.7	14.9
Rel. Int. (arb. units)	6.6	2.1
$\Gamma_{ab}$ (meV)	1.0(1)	1.4(1)

Table 3.4: Results of the analysis of the inelastic neutron scattering spectrum of  $Tb_2Ti_2O_7$  displayed in the right panel of Fig. 3.4. We give the CEF transitions between energy levels labelled ( $a \rightarrow b$ ) as indicated in the left panel of Fig. 3.4, their calculated energy positions, and the linewidths of the Lorentzian functions describing the CEF transitions. Relative intensities are also given.

Transitions ( $a \rightarrow b$ )	1 $\rightarrow$ 3 (A)	1 $\rightarrow$ 4 (B)	2 $\rightarrow$ 3 (C)	2 $\rightarrow$ 4 (D)
Energy (meV)	10.7	14.9	9.1	13.3
Rel. Int. (arb. units)	4.0	1.4	$8.6 \times 10^{-2}$	1.3
Lifetime $\Gamma_{ab}$ (meV)	1.2(F)	1(F)	1(F)	1(F) (left panel)/5(F) (right panel)

Table 3.5: Results of the analysis of the inelastic neutron scattering spectrum of  $Tb_2Ti_2O_7$  displayed in Fig. 3.5. We give the CEF transitions between energy levels labelled ( $a \rightarrow b$ ) as indicated in the left panel of Fig. 3.4, their calculated energy positions, and linewidths of Lorentzian functions describing CEF transitions. The letter (F) means that the variable is fixed to the indicated value. Concerning the CEF transition 2  $\rightarrow$  4 (D), two values of the linewidth are given corresponding to the analysis displayed in the left or right panel of Fig. 3.5.

CEF energy level, labelled (2), is strongly dispersive, as revealed in Refs. [177–179]. Since our model does not take into account the dispersion of the CEF energy level, we could have imagined that at the measured wavevector value the experimental first excited CEF energy level could be shifted and thus the transition 2  $\rightarrow$  4 (D) hidden with an other CEF excitation. However, measurements displayed in Fig. 3.5 have been performed at  $q = 2 \text{ \AA}^{-1}$ , a value at which the first CEF energy level lies at  $\approx 1.6 \text{ meV}$  corresponding to the calculated value. Therefore, the only way to fit the model to the data is to introduce a short lifetime to smear out the transition 2  $\rightarrow$  4 (D), see the right panel of Fig. 3.5 and Tab. 3.5. Note that the CEF parameters proposed in Ref. [73] lead to the same problem.

Furthermore, looking at the inelastic neutron scattering spectrum [73] displayed in the left panel of Fig. 3.6, a supplementary excitation seems to be located at  $\approx 16 \text{ meV}$ . This excitation was better resolved in a recent work [170] where inelastic neutron scattering experiments were performed with a time-of-flight spectrometer on a polycrystalline sample of  $Tb_2Ti_2O_7$ , see right panel of Fig. 3.6. Since these experiments were performed at low temperatures, this excitation would correspond to a transition from the ground state to an excited one located at 16 meV. None of the published CEF parameters can describe this excitation. Therefore, a set of CEF parameters listed in the fourth row of Tab. 3.3 was proposed and allows to describe this excitation, as shown in the right panel of Fig. 3.6. However, the corresponding computed CEF energy levels scheme for the other titanate compounds displayed in the right panel of Fig. 3.3 is clearly incompatible with other inelastic neutron scattering experiments. The nature of this excitation is debatable. From Raman spectroscopy experiments,

Lummen *et al.* [176] identify this excitation to be a CEF transition arising from a second  $\text{Tb}^{3+}$  site: this disorder would arise from structural fluctuations as premises of a Jahn-Teller transition, see Chapter 5. However, this excitation is still observable at high temperature [180] which does not corroborate the explanation proposed in Ref. [176]. Therefore, the origin of this excitation remains unclear: the authors of Ref. [181] propose that this excitation originates from the coupling between an electron and a phonon. A recent paper [182] confirms the presence of this additional excitation with neutron time-of-flight spectroscopy but also fails to include it in a crystal-electric-field analysis. The excitation lying around 70 meV and claimed to be of magnetic origin by the authors of Ref. [170] is shown in Ref. [182] to be of phononic nature. Finally, in both papers, the authors agree to the existence of a crystal-electric-field transition lying at 49 meV, supporting our prediction of a doublet at  $\approx 47$  meV. With high temperature measurements, the authors of Ref. [182] argue that an energy level should lie near 39 meV, also in agreement with our predicted level at  $\approx 40$  meV.

### 3.2.4 Analysis of $\text{Er}_2\text{Ti}_2\text{O}_7$

Champion *et al.* have recorded inelastic neutron scattering spectra for a polycrystalline sample of  $\text{Er}_2\text{Ti}_2\text{O}_7$  at  $T = 1.8$  K, see the right panel of Fig. 3.7. The analysis is performed with our CEF parameters listed in the second row of Tab. 3.3. The refined CEF parameters providing a proper description of the inelastic neutron scattering spectra are given in the second row of Tab. 3.6 and are closely related to the ones listed in

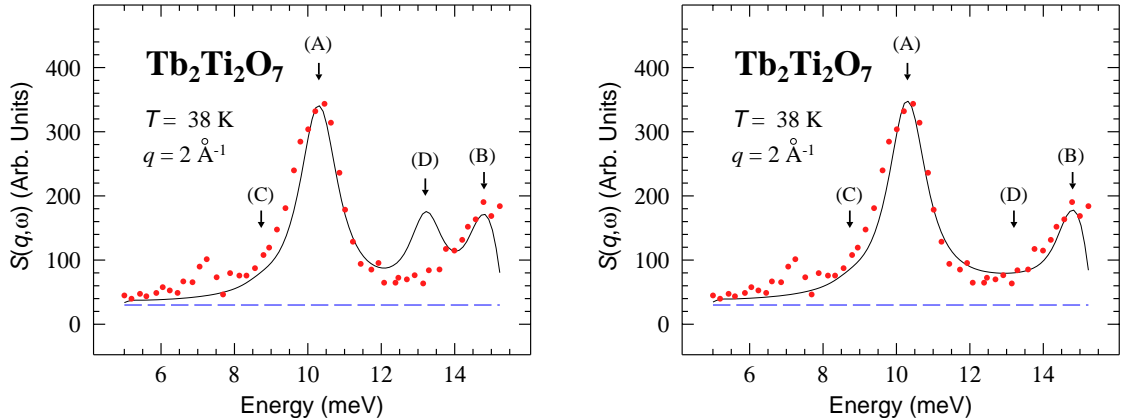


Figure 3.5: Inelastic neutron scattering spectra recorded on a powder sample of  $\text{Tb}_2\text{Ti}_2\text{O}_7$  at  $T = 38$  K and  $q = 2 \text{ \AA}^{-1}$ . Data are extracted from Fig. 5 (right) of Ref. [73]. In both panels, the blue dashed line is the background contribution taken as a constant value. The black solid line is a fit to the data using our CEF parameters listed in the second row of Tab. 3.3. Black arrows indicate the CEF transitions: they are labelled by letters in order to identify the CEF energy levels, see Tab. 3.5 and left panel of Fig. 3.4. The difference between the analysis of the left and right panels lies in the value chosen for the linewidth of the Lorentzian function describing the transition  $2 \rightarrow 4$ . As shown in Tab. 3.5,  $\Gamma_{2 \rightarrow 4} = 5$  meV in the right panel in order to smear out the supplemental CEF transition predicted by our CEF parameters, and evidenced in the left panel of this picture.

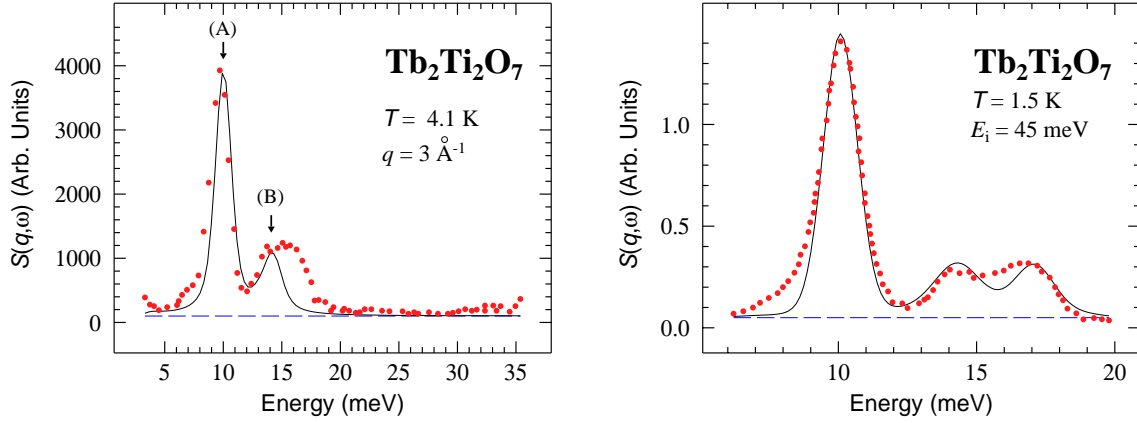


Figure 3.6: *Left: Inelastic neutron scattering spectra recorded on a powder sample of  $Tb_2Ti_2O_7$  at  $T = 4.1$  K and  $q = 3 \text{ \AA}^{-1}$ . Data are extracted from Fig. 7 (right) of Ref. [73]. The black solid line is a fit to the data using our CEF parameters listed in the second row of Tab. 3.3. Black arrows indicate the CEF transitions: they are labelled by letters in order to identify the CEF energy levels, see Tab. 3.4 and left panel of Fig. 3.4. Right: Inelastic neutron scattering spectrum recorded on a polycrystalline sample of  $Tb_2Ti_2O_7$  at  $T = 1.5$  K. The excitation located at 16 meV is better resolved. Data are extracted from the top left panel of Fig. 5 in Ref. [170]. The black solid line is a fit to the data using CEF parameters of Zhang *et al.* [170] listed in the fourth row of Tab. 3.3. In both panels, the blue dashed line is the background contribution taken as a constant value.*

$A_n^m$ (meV/ $a_0^n$ )	$A_2^0$	$A_4^0$	$A_4^3$	$A_6^0$	$A_6^3$	$A_6^6$
$Er_2Ti_2O_7$	40.1(2)	23.6(1)	224(1)	1.078(3)	-16.9(2)	14.4(2)
$Ho_2Ti_2O_7$	40.8(8)	24.2(3)	210(7)	1.07(2)	-16.0(8)	15.4(4)

Table 3.6: *Refined CEF parameters  $A_n^m$  rescaled for  $Tb_2Ti_2O_7$  and used to properly describe inelastic neutron scattering spectra of  $Er_2Ti_2O_7$  (second row), see right panel of Fig. 3.7, and of  $Ho_2Ti_2O_7$  (last row), see Fig. 3.9. These parameters are closely related to those listed in the second row of Tab. 3.3 within the error bars.*

Tab. 3.3 within the errors bars. The corresponding computed CEF energy levels scheme is displayed in the left panel of Fig. 3.7 in order to not only compare computed and experimental CEF energy levels but also in order to label the different energy levels for the identification of the CEF transitions involved in the inelastic neutron scattering spectrum, as reported in Tab. 3.7. The resolution of the instrument is taken as a Gaussian with a FWHM equals to 4% of the energy transfer [183]. Our set of CEF parameters provide a very good analysis of the inelastic neutron scattering spectra revealing transitions from the ground state to the two lowest CEF energy levels located at 6.3 and 7.3 meV. Our model predicts also an energy level evidenced by Shirai [171] at 15.4 meV according to Ref. [184].

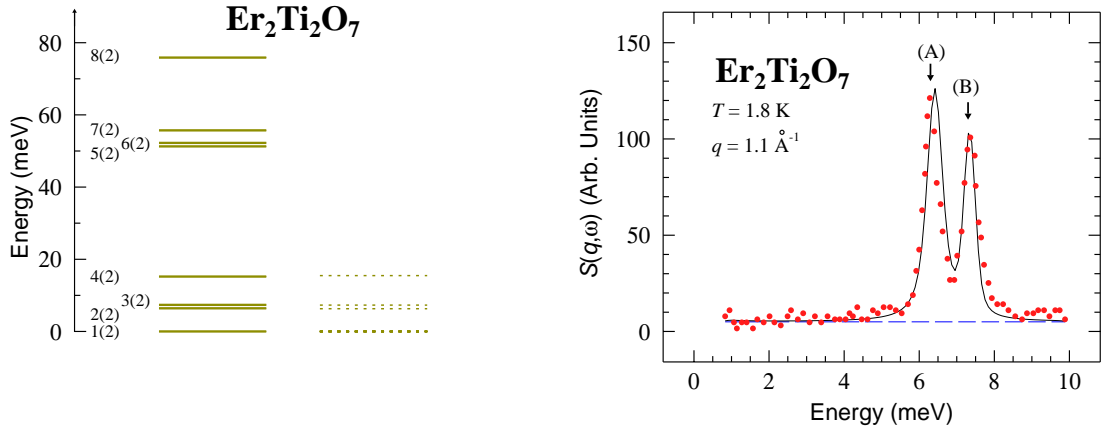


Figure 3.7: Left: Energy levels scheme of  $\text{Er}_2\text{Ti}_2\text{O}_7$  obtained with the CEF parameters listed in the second row of Tab. 3.6. The different energy levels are labelled by numbers in order to identify the CEF transitions involved in the inelastic neutron scattering spectra, see Tab. 3.7. The dotted lines indicate the experimental CEF transitions revealed by inelastic neutron scattering spectroscopy [96]. The highest experimental energy level is listed by Ref. [184] from the PhD dissertation of Shirai [171]. Right: Inelastic neutron scattering spectra recorded on a powder sample of  $\text{Er}_2\text{Ti}_2\text{O}_7$  at  $T = 1.8$  K. Data are extracted from Fig. 3 of Ref [96]. The blue dashed line is the background contribution taken as a constant value. The black solid line is a fit to the data using our CEF parameters listed in the second row of Tab. 3.6. Black arrows indicate the CEF transitions: they are labelled by letters in order to identify the CEF energy levels, see Tab. 3.7 and left panel of this figure.

### 3.2.5 Analysis of $\text{Ho}_2\text{Ti}_2\text{O}_7$

Starting from our CEF parameters listed in Tab. 3.3, we analyse simultaneously two inelastic neutron scattering spectra of  $\text{Ho}_2\text{Ti}_2\text{O}_7$  recorded by Rosenkranz *et al.* [168] at  $T = 10$  K, as shown in Fig. 3.9. The refined CEF parameters are listed in the last row of Tab. 3.6 and correspond within the errors bars to those determined in Tab. 3.3. The instrumental resolution has been determined with a vanadium sample for each incident energy in Ref. [168], but no further information is given. Therefore, we choose a Gaussian function for the instrumental resolution and take a FWHM  $H_G = 1$  and 3 meV for incident energies  $E_i = 35$  and 120 meV, respectively. The linewidths of the Lorentzian functions accounting for CEF transitions are given in the right panel of Fig. 3.8 and Tab. 3.8 for the left and right panels of Fig. 3.9, respectively.

Transition ( $a \rightarrow b$ )	1 $\rightarrow$ 2 (A)	1 $\rightarrow$ 3 (B)
Energy (meV)	6.4	7.3
Rel. Int. (arb. units)	9.9/1.8	6.0/0.11
$\Gamma_{ab}$ (meV)	0.35(4)	0.16(1)

Table 3.7: Results of the analysis of the inelastic neutron scattering spectrum of a polycrystalline sample of  $Er_2Ti_2O_7$  displayed in the right panel of Fig. 3.7. We give the CEF transitions between energy levels labelled (a,b) as indicated in the left panel of Fig. 3.7, their calculated energy positions, and the linewidths of Lorentzian functions describing the CEF transitions. Relative intensities are also given: for a transition involving two doublets, two neutron intensity values are provided.

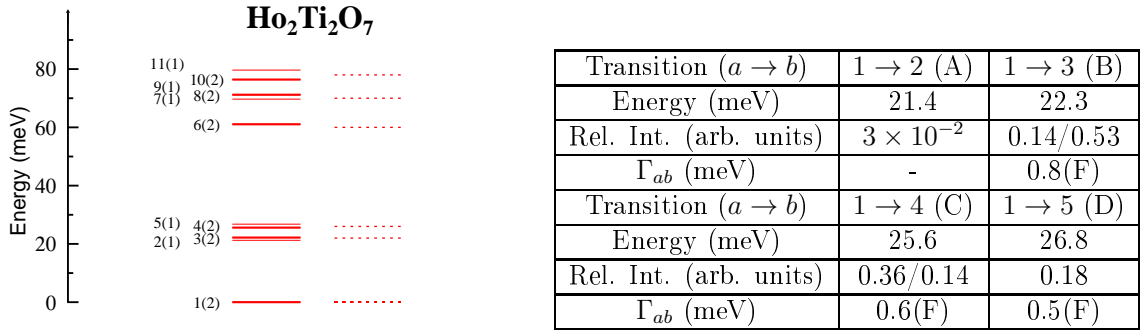


Figure 3.8: Left: Energy levels scheme of  $Ho_2Ti_2O_7$  obtained with the CEF parameters listed in the third row of Tab. 3.6. The different energy levels are labelled by numbers in order to identify the CEF transitions involved in the inelastic neutron scattering spectra, see right panel of this picture and Tab. 3.8. The dotted lines indicate the experimental CEF transitions revealed by inelastic neutron scattering spectroscopy [168]. Right: Results of the analysis of the inelastic neutron scattering spectrum of  $Ho_2Ti_2O_7$  displayed in the left panel of Fig. 3.9. We give the CEF transitions between energy levels labelled (a,b) as indicated in the left panel of this figure, their calculated energy positions, and the linewidths of Lorentzian functions describing the CEF transitions. Relative intensities are also given. The symbol “-” means that no Lorentzian function describes the CEF transition since its relative intensity is negligible compared to other CEF transitions.

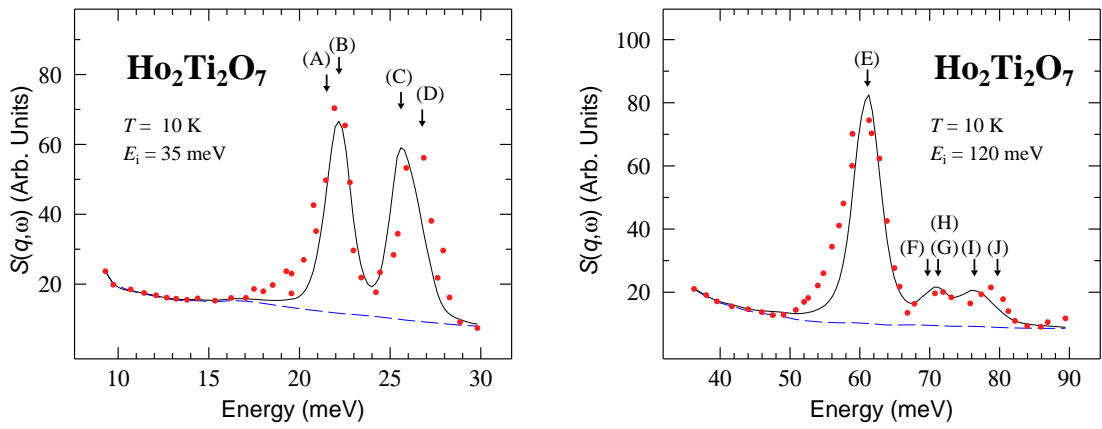


Figure 3.9: Inelastic neutron scattering spectra recorded on a powder sample of  $\text{Ho}_2\text{Ti}_2\text{O}_7$  at  $T = 10$  K and  $E_i = 35$  meV (left) and 120 meV (right). Data are extracted from Fig. 2 of Ref. [168]. The blue dashed line is the background contribution which has been interpolated. The black solid line is a fit to the data using CEF parameters displayed in the last row of Tab. 3.6. Black arrows indicate the CEF transitions: they are labelled by letters in order to identify the CEF transitions, see Fig. 3.8 and Tab. 3.8.

Transition ( $a \rightarrow b$ )	1 $\rightarrow$ 6 (E)	1 $\rightarrow$ 7 (F)	1 $\rightarrow$ 8 (G)
Energy (meV)	61.0	69.7	71.2
Rel. Int. (arb. units)	$1 \times 10^{-4}/4.0$	0.10	$(49/3.8) \times 10^{-3}$
$\Gamma_{ab}$ (meV)	2.5(F)	1.0(F)	-
Transition ( $a \rightarrow b$ )	1 $\rightarrow$ 9 (H)	1 $\rightarrow$ 10 (I)	1 $\rightarrow$ 11 (J)
Energy (meV)	71.2	76.3	79.6
Rel. Int. (arb. units)	0.20	$1.4 \times 10^{-3}/0.77$	$3.6 \times 10^{-2}$
$\Gamma_{ab}$ (meV)	0.7(F)	4.0(F)	-

Table 3.8: Results of the analysis of the inelastic neutron scattering spectrum of  $\text{Ho}_2\text{Ti}_2\text{O}_7$  displayed in the right panel of Fig. 3.9. We give the CEF transitions between energy levels labelled ( $a, b$ ) as indicated in the left panel of Fig. 3.8, their calculated energy positions, and the linewidths of Lorentzian functions describing the CEF transitions. Relative intensities are also given. The symbol “-” means that no Lorentzian function describes the CEF transition since its relative intensity is negligible compared to other CEF transitions.

### 3.2.6 Conclusions

For completeness, we give in Tab. 3.9 the values of the  $B_n^m$  parameters for compounds of interest in the pyrochlore series  $R_2\text{Ti}_2\text{O}_7$  computed with our set of  $A_n^m$  parameters listed in the second row of Tab. 3.3. The corresponding ground state wavefunctions  $\phi_0^\pm$  are also provided in Tab. 3.10. This allows us to calculate the spectroscopic factors along and perpendicular to the local trigonal  $z$  axis,  $g_\parallel$  and  $g_\perp$ , respectively:

$$\begin{aligned} g_\parallel &= 2g_J |\langle \phi_0^\pm | J_z | \phi_0^\pm \rangle|, \\ g_\perp &= g_J |\langle \phi_0^+ | J_+ | \phi_0^- \rangle| = g_J |\langle \phi_0^- | J_- | \phi_0^+ \rangle|. \end{aligned} \quad (3.21)$$

These spectroscopic factors are listed in Tab. 3.11. As expected,  $\text{Er}_2\text{Ti}_2\text{O}_7$  and  $\text{Yb}_2\text{Ti}_2\text{O}_7$  have a strong planar CEF anisotropy and  $\text{Tb}_2\text{Ti}_2\text{O}_7$ ,  $\text{Dy}_2\text{Ti}_2\text{O}_7$  and  $\text{Ho}_2\text{Ti}_2\text{O}_7$  are Ising-like. The  $g_\parallel$  value obtained for  $\text{Yb}_2\text{Ti}_2\text{O}_7$  is intermediate between the experimental values 1.79 and 2.25 of Hodges *et al.* [83] and Cao *et al.* [185], respectively. This is in agreement with the fact that the ratio  $g_\perp/g_\parallel$  is expected to be rather large, i.e.  $g_\perp/g_\parallel \approx 2.4$  [83] compared to our value  $g_\perp/g_\parallel = 2$ . Our  $g_\parallel$  result for  $\text{Tb}_2\text{Ti}_2\text{O}_7$  is consistent with previous estimates [73, 179]. When the ground state is well isolated from the excited ones, we can describe it with an effective spin-1/2. Therefore, we calculate the components of the crystal field magnetic moment along and perpendicular to the trigonal axis [111] such as:

$$\mu_\parallel^{\text{CF}} = \frac{1}{2} g_\parallel \mu_B \quad \text{and} \quad \mu_\perp^{\text{CF}} = \frac{1}{2} g_\perp \mu_B. \quad (3.22)$$

The crystal-electric-field magnetic moment is deduced as:

$$\mu^{\text{CF}} = \sqrt{(\mu_\parallel^{\text{CF}})^2 + (\mu_\perp^{\text{CF}})^2}. \quad (3.23)$$

In the case of the spin-ice compounds, we recover  $\mu^{\text{CF}} \approx 10 \mu_B$  which is consistent with the literature, see Sec. 1.3.

	$B_2^0$	$B_4^0$	$B_4^3$	$B_6^0$	$B_6^3$	$B_6^6$
Tb	-0.34(1)	$4.9(2) \times 10^{-3}$	$4.3(3) \times 10^{-2}$	$-7.9(2) \times 10^{-6}$	$1.30(8) \times 10^{-4}$	$-1.08(8) \times 10^{-4}$
Dy	-0.20(1)	$-2.2(1) \times 10^{-3}$	$-1.9(1) \times 10^{-2}$	$6.6(2) \times 10^{-6}$	$-1.09(6) \times 10^{-4}$	$9.0(6) \times 10^{-5}$
Ho	$-6.8(2) \times 10^{-2}$	$-1.13(5) \times 10^{-3}$	$-1.01(6) \times 10^{-2}$	$-7.4(2) \times 10^{-6}$	$1.23(7) \times 10^{-4}$	$-1.01(7) \times 10^{-4}$
Er	$7.5(2) \times 10^{-2}$	$1.41(6) \times 10^{-3}$	$1.25(8) \times 10^{-2}$	$1.09(3) \times 10^{-5}$	$-1.8(1) \times 10^{-4}$	$1.5(1) \times 10^{-4}$
Tm	0.29(1)	$4.8(2) \times 10^{-3}$	$4.3(3) \times 10^{-2}$	$-2.69(7) \times 10^{-5}$	$4.4(3) \times 10^{-4}$	$-3.7(3) \times 10^{-4}$
Yb	0.87(2)	$-4.8(2) \times 10^{-2}$	-0.43(3)	$6.6(2) \times 10^{-4}$	$-1.09(6) \times 10^{-2}$	$8.9(6) \times 10^{-3}$

Table 3.9: Values of  $B_n^m$  parameters for six compounds of the  $R_2\text{Ti}_2\text{O}_7$  pyrochlore series given in meV.

Tb	$ \phi_0^\pm\rangle = 0.266 \pm 5\rangle \mp 0.133 \pm 2\rangle - 0.129 \mp 1\rangle \mp 0.946 \mp 4\rangle$
Dy	$ \phi_0^\pm\rangle = \mp 0.981 \pm \frac{13}{2}\rangle - 0.190 \pm \frac{9}{2}\rangle \pm 0.022 \pm \frac{3}{2}\rangle + 0.037 \mp \frac{3}{2}\rangle \mp 0.005 \mp \frac{9}{2}\rangle \pm 0.001 \mp \frac{13}{2}\rangle$
Ho	$ \phi_0^\pm\rangle = -0.979 \pm 8\rangle \pm 0.190 \pm 5\rangle - 0.014 \pm 2\rangle \pm 0.070 \mp 1\rangle - 0.031 \mp 4\rangle \pm 0.005 \mp 7\rangle$
Er	$ \phi_0^\pm\rangle = \mp 0.471 \pm \frac{13}{2}\rangle - 0.421 \pm \frac{7}{2}\rangle \pm 0.569 \pm \frac{1}{2}\rangle + 0.240 \mp \frac{5}{2}\rangle \mp 0.469 \mp \frac{11}{2}\rangle$
Tm	$ \phi_0\rangle = 0.148 6\rangle - 0.691 3\rangle - 0.691 -3\rangle - 0.148 -6\rangle$
Yb	$ \phi_0^\pm\rangle = 0.374 \pm \frac{7}{2}\rangle \pm 0.923 \pm \frac{1}{2}\rangle - 0.093 \mp \frac{5}{2}\rangle$

Table 3.10: Ground-state wavefunctions for six compounds of the  $R_2\text{Ti}_2\text{O}_7$  pyrochlore series.

The CEF parameter  $A_2^0$  can be deduced from the measurement of the nuclear quadrupole splitting  $\Delta_Q$  arising from the electric-field gradient in a gadolinium compound from  $^{155}\text{Gd}$  Mössbauer spectroscopy. From Refs. [117, 186],  $\Delta_Q = 1.62 \times 10^{-3}$  meV in  $\text{Gd}_2\text{Ti}_2\text{O}_7$ . Since the quadrupole moment of the excited Mössbauer state of  $^{155}\text{Gd}$  is negligible ( $Q_{\text{ex}} = 0.18$  barns [187]) compared to the ground state ( $Q_{\text{gs}} = 1.27$  barns [160]), we only consider the splitting of the latter. The nuclear spin of the ground state is  $I = \frac{3}{2}$  yielding two doublets  $|\pm \frac{3}{2}\rangle$  and  $|\pm \frac{1}{2}\rangle$ . From the point symmetry at the rare earth site,  $V_{zz}$  is the principal component of the electric-field gradient tensor and the asymmetry parameter vanishes. Therefore, the quadrupolar Hamiltonian is written as:

$$\mathcal{H}_Q = \frac{eQ_{\text{gs}}V_{zz}}{4I(2I-1)}[3I_z^2 - I(I+1)]. \quad (3.24)$$

Since this Hamiltonian is diagonal, we directly determine the nuclear quadrupolar splitting between the two aforementioned Zeeman states  $\Delta_Q = -eQ_{\text{gs}}V_{zz}/2$ . Besides, the CEF parameter  $A_2^0$  is commonly related to  $V_{zz}$  through the relation [188]:

$$V_{zz} = -\frac{4A_2^0}{e} \frac{1 - \gamma_\infty}{1 - \sigma_2}, \quad (3.25)$$

where  $\gamma_\infty = -61$  and  $\sigma_2 = 0.67$  are Sternheimer and screening coefficients [189]. Using

	Tb	Dy	Ho	Er	Yb
$g_{\parallel}$	9.6	19.6	19.6	2.1	2.04
$g_{\perp}$	0	0	0	7.7	4.09

Table 3.11: Spectroscopic factors  $g_{\parallel}$  and  $g_{\perp}$  for the ground state doublets of five compounds of the  $R_2\text{Ti}_2\text{O}_7$  series using  $A_n^m$  parameters listed in the second row of Tab. 3.3. For  $\text{Tm}_2\text{Ti}_2\text{O}_7$  the thulium ion has a singlet ground state and therefore  $g_{\parallel} = g_{\perp} = 0$ .

this formula, we compute  $A_2^0 = 95 \text{ meV}/a_0^2$  for  $\text{Gd}_2\text{Ti}_2\text{O}_7$ . From the scaling law given in Eq. 3.16, we then get  $A_2^0 = 97 \text{ meV}/a_0^2$  for  $\text{Tb}_2\text{Ti}_2\text{O}_7$ . This is 2.4 larger than the value listed in the second row of Tab. 3.3. We do not have a reliable explanation accounting for such a difference between our calculations and the value inferred from Mössbauer experiment. We have tested if this large  $A_2^0$  could provide a description of the inelastic neutron scattering data probing a relatively wide range of  $A_4^m$  and  $A_6^m$  without finding any solution.

To conclude, we have introduced a simple methodology using a scaling law for a reliable determination of the rare-earth crystal-field parameters for a series of isostructural rare-earth compounds. This requires the availability of inelastic CEF neutron scattering data for a sufficiently large number of compounds of the series. We have found a single set of CEF parameters within the interval probed, see last row of Tab. 3.3, which enables us to calculate CEF energy levels close to the experimental ones revealed by inelastic neutron scattering spectroscopy, at least at low energy. Not only energy levels are calculated, starting from the proposed CEF parameters we are also able to describe intensities of inelastic neutron scattering spectra which depend on the wavefunctions. This suggests that we have at least reached a reasonable phenomenological model for the low-energy local properties of the  $R_2\text{Ti}_2\text{O}_7$  series. However, we have made the strong approximation to only consider the splitting of the ground state multiplet. The perturbation of the first excited multiplet might not be negligible, especially for the lightest rare earth ions, see Tab. 3.1. This could explain the mismatch of the highest computed and experimental energy level of  $\text{Tb}_2\text{Ti}_2\text{O}_7$  for instance.

In the next section, we intend to apply the same methodology in order to find a single set of CEF parameters describing the pyrochlore series  $R_2\text{Sn}_2\text{O}_7$ .

### 3.3 CEF of the stannate series $R_2\text{Sn}_2\text{O}_7$

In order to determine the CEF parameters of the pyrochlore stannate series  $R_2\text{Sn}_2\text{O}_7$ , we have performed measurements at the time-of-flight spectrometer MARI (ISIS facility), see Sec. 2.4, on three different polycrystalline samples:  $\text{Ho}_2\text{Sn}_2\text{O}_7$ ,  $\text{Tb}_2\text{Sn}_2\text{O}_7$ , and  $\text{Nd}_2\text{Sn}_2\text{O}_7$ . An amount of about 20 g of powder sample was rolled in an aluminium foil and placed in an annular sample holder. Data were corrected for absorption effects as explained in App. C. Inelastic neutron scattering spectra are analysed following the methodology introduced in Sec. 3.1.3. The resolution of the spectrometer is approximated as a Gaussian function with a FWHM calculated as a function of the energy transfer, as explained in Sec. 2.4, for each configuration of the experiment depending on the incident energy  $E_i$  and on the Fermi chopper frequency  $\nu_{\text{FC}}$ .

#### 3.3.1 Published CEF parameters

Several sets of CEF parameters have been published in the literature. Some of the most relevant are listed in Tab. 3.12: measurements on powder samples of  $\text{Tb}_2\text{Sn}_2\text{O}_7$  have been conducted by Mirebeau *et al.* [73] at a triple-axis spectrometer and by Zhang *et al.* [170] at a neutron time-of-flight instrument. Guitteny *et al.* [104] measured at a triple-axis spectrometer a powder sample of  $\text{Er}_2\text{Sn}_2\text{O}_7$ . Their data are fully consistent with those recorded previously by Sarte *et al.* [105]. The computed CEF energy levels

	$A_2^0$	$A_4^0$	$A_4^3$	$A_6^0$	$A_6^3$	$A_6^6$
This work	53.2(1.4)	22.4(4)	-155(9)	0.84(2)	13.4(6)	17.7(3)
Mirebeau <i>et al.</i> [73]	23.8	17.1	128.9	-0.34	-5.292	15.5
Zhang <i>et al.</i> [170]	23.6	17.3	13	-0.37	-8.17	15.1
Guitteny <i>et al.</i> [104]	38.9	24.7	-146.3	0.79	14.3	16.0
Interval probed	[0,85.9]	[-43,43]	[0,344]	[-1.7,1.7]	[-43,43]	[-43,43]

Table 3.12: The  $A_n^m$  parameters deduced from the analysis of the inelastic neutron scattering spectra of a polycrystalline sample of  $\text{Ho}_2\text{Sn}_2\text{O}_7$  are listed in the second row. The units for  $A_n^m$  are  $\text{meV}/a_0^n$ , where  $a_0$  is the atomic unit. In the subsequent three rows are listed the  $A_n^m$  parameters derived from the works of Mirebeau *et al.* [73] and Zhang *et al.* [170] on  $\text{Tb}_2\text{Sn}_2\text{O}_7$ , and from the work of Guitteny *et al.* [104] on  $\text{Er}_2\text{Sn}_2\text{O}_7$ . All CEF parameters given here have been rescaled for  $\text{Tb}_2\text{Sn}_2\text{O}_7$  using Eq. 3.16. The last row gives the intervals over which the  $A_n^m$  parameters have been varied in the global fit.

scheme for some compounds of the stannate series using CEF parameters of Mirebeau *et al.* [73] and Zhang *et al.* [170] are displayed in the left and right panels of Fig. 3.10, respectively. Notable discrepancies are evidenced between calculated and experimental CEF energy levels, except for  $\text{Tb}_2\text{Sn}_2\text{O}_7$  which is the investigated compound in those references. In Fig. 3.11, the CEF energy levels scheme is computed using CEF parameters proposed by Guitteny *et al.* [104] and deduced from the analysis of inelastic neutron scattering spectra of  $\text{Er}_2\text{Sn}_2\text{O}_7$ . If the correspondence between calculated and experimental CEF energy levels is roughly acceptable, we cannot analyse inelastic neutron scattering spectra of  $\text{Ho}_2\text{Sn}_2\text{O}_7$  and  $\text{Tb}_2\text{Sn}_2\text{O}_7$ .

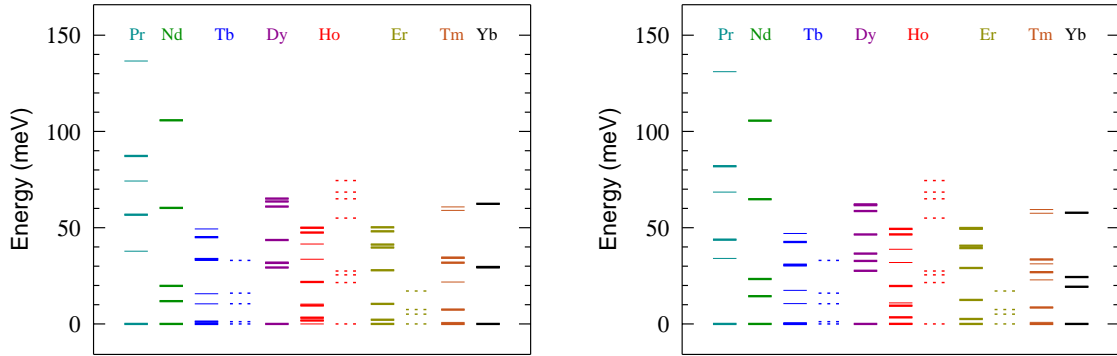


Figure 3.10: Computed CEF energy levels drawn for the  $R$  ions in the  $R_2\text{Sn}_2\text{O}_7$  pyrochlore series using CEF parameters listed in Tab. 3.12 proposed by Mirebeau *et al.* [73] (left panel) and Zhang *et al.* [170] (right panel). Solid thin and thick lines stand for singlet and doublet states, respectively. All the theoretical CEF levels have been drawn. They may not be resolved on the figure because of the limited graphical resolution. The calculated energy levels are compared to experimental data extracted from inelastic neutron scattering experiments presented in dashed lines. Data for  $\text{Er}_2\text{Sn}_2\text{O}_7$  are reproduced from Refs. [104, 105], and data for  $\text{Ho}_2\text{Sn}_2\text{O}_7$  and  $\text{Tb}_2\text{Sn}_2\text{O}_7$  are extracted from our neutron time-of-flight experiments.

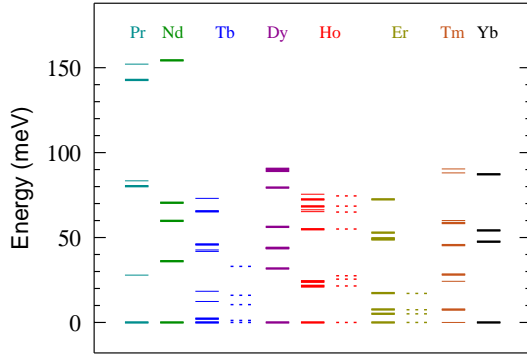


Figure 3.11: *Computed CEF energy levels drawn for the  $R$  ions in the  $R_2Sn_2O_7$  pyrochlore series using CEF parameters listed in Tab. 3.12 proposed by Guitteny et al. [104]. More details about the description of this panel are given in the caption of Fig. 3.10.*

Rare earth	Tb <sup>3+</sup>	Dy <sup>3+</sup>	Ho <sup>3+</sup>	Er <sup>3+</sup>	Tm <sup>3+</sup>	Yb <sup>3+</sup>
$a_{\text{lat}}$ (Å)	10.4235(2)	10.3979(3)	10.3726(2)	10.3504(1)	10.3262(2)	10.3046(1)

Table 3.13: *List of the lattice parameters  $a_{\text{lat}}$  used in this work for the  $R_2Sn_2O_7$  series. Data taken from Ref. [190].*

### 3.3.2 Analysis of $Ho_2Sn_2O_7$

We apply the same methodology introduced in the foregoing section. We will see in the following that the scaling law given by Eq. 3.16 is still satisfactory in order to describe inelastic neutron scattering spectra of different compounds of the stannate series. Useful lattice parameters are listed in Tab. 3.13. However, we have to note that a global fit including energy levels of three compounds, i.e.  $Er_2Sn_2O_7$ ,  $Ho_2Sn_2O_7$  and  $Tb_2Sn_2O_7$  is not fully conclusive. We only extract solutions allowing to analyse inelastic neutron scattering spectra of a subset of aforementioned compounds, namely two out of the three compounds. Nevertheless, we present here a set of CEF parameters listed in the second row of Tab. 3.12 which gives a good correspondence between calculated and experimental CEF energy levels, see the left panel of Fig. 3.12. This set of CEF parameters has been used to analyse simultaneously inelastic neutron scattering spectra of a polycrystalline sample of  $Ho_2Sn_2O_7$  and we will see in the following that the CEF parameters allowing to describe spectra of  $Er_2Sn_2O_7$  and  $Tb_2Sn_2O_7$  only differs from the initial ones by three error bars at worst.

The set of CEF parameters proposed in the second row of Tab. 3.12 allows to describe the CEF excitations of  $Ho_2Sn_2O_7$ . The corresponding CEF energy level scheme for this compound is shown in the right panel of Fig. 3.12. Not only the comparison between computed and experimental CEF energy levels is displayed, we also label the different energy levels in order to identify the CEF transitions involved in the analysis. With neutron time-of-flight experiments performed at low temperatures, we reveal energy levels lying at 21.5 and 25.5 meV, which are consistent with published data of Ref. [21], but also at 27.5, 55, 65, 68.5, and 74.5 meV. An inelastic neutron scattering intensity map of  $Ho_2Sn_2O_7$  recorded at  $T = 5$  K and showing the energy transfer versus the wavevector  $q$  is displayed in the left panel of Fig. 3.13 in order to evidence the low lying CEF energy levels. Integrations of these data over several wavevector ranges are shown in the right panel of the same figure. The following methodology, applied to all our recorded inelastic neutron scattering spectra, allows to determine the phononic or

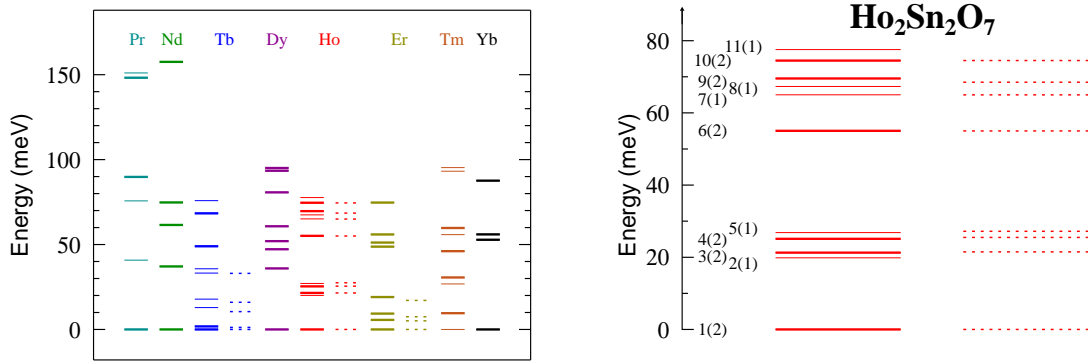


Figure 3.12: Left: Computed CEF energy levels drawn for the  $R$  ions in the  $R_2\text{Sn}_2\text{O}_7$  pyrochlore series using our CEF parameters listed in the second row of Tab. 3.12 and comparison with experimental values extracted from inelastic neutron scattering measurements. More details about the description of this panel are given in the caption of Fig. 3.10. Right: Zoom over  $\text{Ho}_2\text{Sn}_2\text{O}_7$ . The different energy levels are labelled by numbers in order to identify the CEF transitions involved in inelastic neutron scattering spectra, see Tab. 3.14 and Tab. 3.15. The numbers in parentheses (1) and (2) correspond to a singlet and doublet states, respectively. The dotted lines indicate the experimental CEF transitions revealed by inelastic neutron scattering spectroscopy.

electronic nature of the observed excitations: since the magnetic form factor decreases when  $q$  increases whereas the phonon intensity grows as  $q^2$ , we can conclude that the two excitations revealed at 10 meV and 17 meV are attributed to phonons, whereas those at 21.5, 25.5, and 27.5 are ascribed to CEF transitions. Integration of these data over the wavevector range  $0.26 \leq q \leq 4 \text{ \AA}^{-1}$  is shown in Fig. 3.14. Our set of CEF parameters accounts very well for this spectrum. Some details of this analysis are summed up in Tab. 3.14 such as the CEF transitions involved, their relative intensities and the linewidths of the Lorentzian function needed to properly describe the peak shapes.

An inelastic neutron scattering intensity map of  $\text{Ho}_2\text{Sn}_2\text{O}_7$  recorded at  $T = 5 \text{ K}$  and displayed in the left panel of Fig. 3.15 reveals the highest CEF energy levels observed during the experiment. The right panel of Fig. 3.15 shows the analysis of these

Transition ( $a \rightarrow b$ )	$1 \rightarrow 2$ (A)	$1 \rightarrow 3$ (B)	$1 \rightarrow 4$ (C)	$1 \rightarrow 5$ (D)
Energy (meV)	20.1	21.5	25.4	27.1
Rel. Int. (arb. units)	0.13	0.76/0.27	0.55/0.38	0.23
$\Gamma_{ab}$ (meV)	1.0(F)	0.25(2)	0.30(2)	0.20(3)

Table 3.14: Results of the analysis of the inelastic neutron scattering spectrum of  $\text{Ho}_2\text{Sn}_2\text{O}_7$  displayed in Fig. 3.14. We give the CEF transitions between energy levels labelled ( $a, b$ ) as indicated in the right panel of Fig. 3.12, their calculated energy positions, and linewidths of Lorentzian functions describing CEF transitions. The letter (F) means that the variable is fixed to the indicated value. Relative intensities are also given.

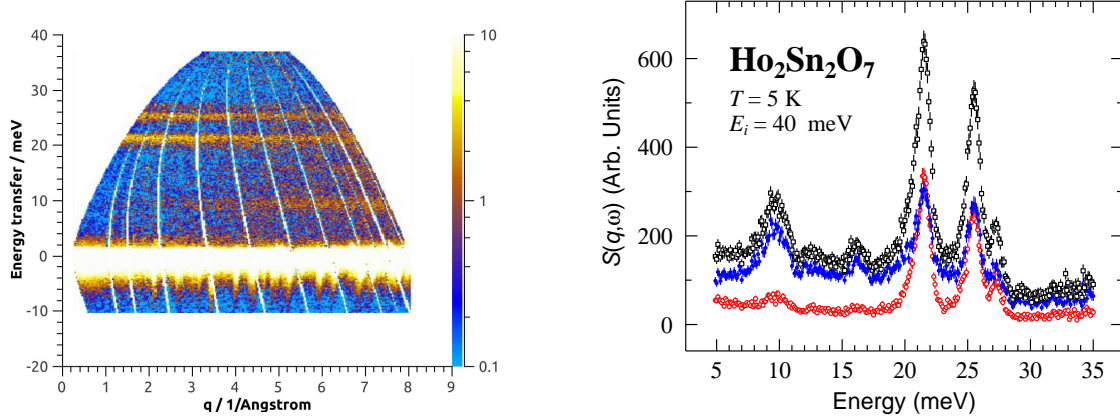


Figure 3.13: Left: Inelastic neutron scattering spectrum of  $\text{Ho}_2\text{Sn}_2\text{O}_7$  recorded at  $T = 5$  K,  $E_i = 40$  meV and  $\nu_{\text{FC}} = 300$  Hz. Right: Integrations of these data over  $0.26 \leq q \leq 4 \text{ \AA}^{-1}$  (red empty circles),  $4 \leq q \leq 8.1 \text{ \AA}^{-1}$  (blue full circles) and  $0.26 \leq q \leq 8.1 \text{ \AA}^{-1}$  (black empty squares) in order to determine the nature of the observed transitions.

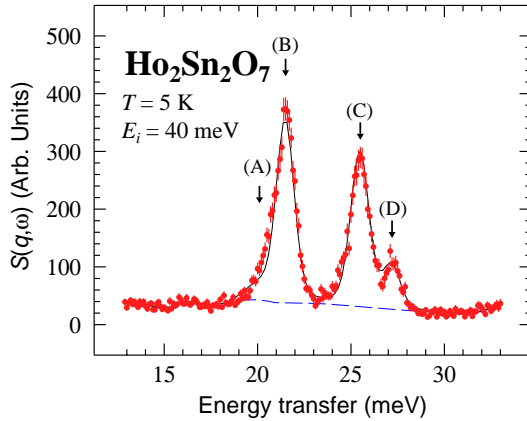


Figure 3.14: Integration of the data displayed in the left panel of Fig. 3.13 over the wavevector range  $0.26 \leq q \leq 4 \text{ \AA}^{-1}$ . The black solid line is a fit to the data using CEF parameters displayed in the second row of Tab. 3.12. Black arrows indicate the CEF transitions: they are labelled by letters in order to identify the CEF energy levels, see Tab. 3.14 and right panel of Fig. 3.12.

Transition ( $a \rightarrow b$ )	$1 \rightarrow 6$ (E)	$1 \rightarrow 7$ (F)	$1 \rightarrow 8$ (G)	$1 \rightarrow 10$ (H)
Energy (meV)	55.1	65.1	67.5	74.6
Rel. Int. (arb. units)	$3.4 \times 10^{-4}/4.2$	0.18	0.11	$3.0 \times 10^{-3}/0.30$
$\Gamma_{ab}$ (meV)	0.50(2)	0.1(F)	0.1(F)	0.1(F)

Table 3.15: Results of the analysis of the inelastic neutron scattering spectrum of  $\text{Ho}_2\text{Sn}_2\text{O}_7$  displayed in the right panel of Fig. 3.15. We give the CEF transitions between energy levels labelled ( $a, b$ ) as indicated in the right panel of Fig. 3.12, their calculated energy positions and linewidths of Lorentzian functions describing CEF transitions. The letter (F) means that the variable is fixed to the indicated value: indeed most of the Lorentzian linewidths were fixed to arbitrary values since the calculated energy resolution function dominates the width of the inelastic CEF transitions. Note that the linewidths of the Lorentzian functions describing CEF labelled (A), (B), (C), (D) have been blocked to 0.2 meV in this spectrum. Relative intensities are also given to show whether or not a CEF transition is observed in the inelastic neutron scattering spectrum.

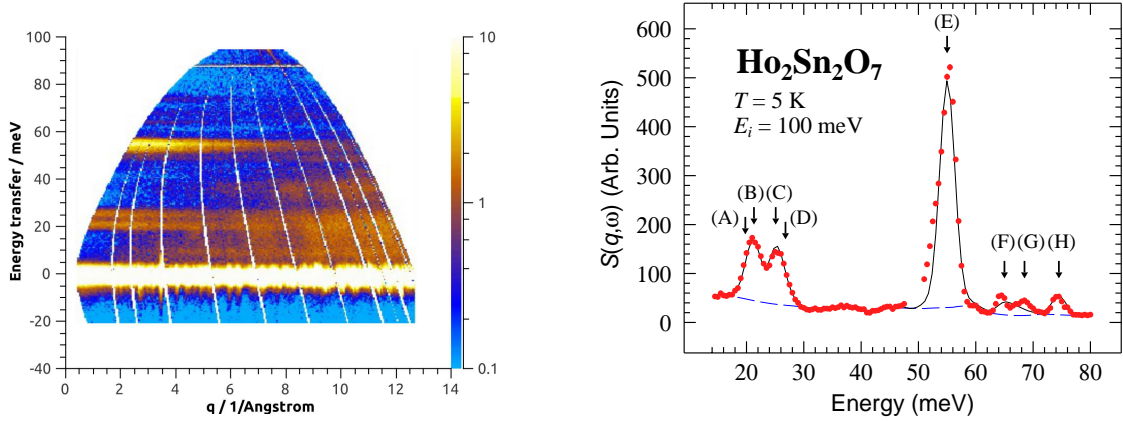


Figure 3.15: *Left: Inelastic neutron scattering spectrum of a polycrystalline sample of  $\text{Ho}_2\text{Sn}_2\text{O}_7$  recorded at  $T = 5$  K,  $E_i = 100$  meV and a Fermi chopper frequency  $\nu_{\text{FC}} = 400$  Hz. Right: Integration over the wavevector range  $0.42 \leq q \leq 6 \text{ \AA}^{-1}$ . The black solid line is a fit to the data using CEF parameters displayed in the second row of Tab. 3.12. Black arrows indicate the CEF transitions: they are labelled by letters in order to identify the CEF energy levels, see Tab. 3.15 and right panel of Fig. 3.12.*

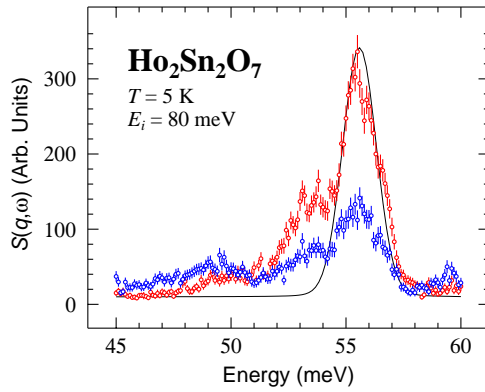


Figure 3.16: *Zoom over the excitation lying at 55 meV extracted from an inelastic neutron scattering spectrum of  $\text{Ho}_2\text{Sn}_2\text{O}_7$  recorded at  $T = 5$  K,  $E_i = 80$  meV and  $\nu_{\text{FC}} = 600$  Hz. Integrations over two wavevector ranges are shown,  $0 \leq q \leq 5 \text{ \AA}^{-1}$  (red symbols) and  $7 \leq q \leq 12 \text{ \AA}^{-1}$  (blue symbols), in order to characterise the phononic or electronic nature of the observed excitations. The black solid line is a fit to the data recorded over  $0 \leq q \leq 5 \text{ \AA}^{-1}$  using CEF parameters listed in the second row of Tab. 3.12.*

data integrated over the wavevector range  $0.42 \leq q \leq 6 \text{ \AA}^{-1}$  using our set of CEF parameters. Details of the analysis are gathered in Tab. 3.15. However, focusing on the CEF transition lying at 55 meV, a second CEF transition is located at  $\approx 53$  meV, as illustrated in Fig. 3.16. The nature of the transition seems to be electronic since its intensity decreases with  $q$ . Note that our CEF model does not predict any transition at this specific energy.

$A_n^m$ (meV/ $a_0^n$ )	$A_2^0$	$A_4^0$	$A_4^3$	$A_6^0$	$A_6^3$	$A_6^6$
$Tb_2Sn_2O_7$	50.0(2.0)	21.2(8)	-159(7)	1.01(7)	14.4(2.0)	17.5(5)

Table 3.16: CEF parameters  $A_n^m$  deduced from the analysis of the inelastic neutron scattering spectra of  $Tb_2Sn_2O_7$  and given in units of meV/ $a_0^n$ , where  $a_0$  is the atomic unit.

Transition ( $a \rightarrow b$ )	$1 \rightarrow 2$ (A)	$1 \rightarrow 3$ (B)
Energy (meV)	1.2	10.6
Rel. Int. (arb. units)	7.0	3.6
$\Gamma_{ab}$ (meV)	0.60(2)	1.00(7)

Table 3.17: Results of the analysis of the inelastic neutron scattering spectrum of  $Tb_2Sn_2O_7$  displayed in the right panel of Fig. 3.18. We give the CEF transitions between energy levels labelled ( $a, b$ ) as indicated in Fig. 3.17, their calculated energy positions, and linewidths of Lorentzian functions describing CEF transitions. Relative intensities are also given.

### 3.3.3 Analysis of $Tb_2Sn_2O_7$

Starting from the CEF parameters listed in the second row of Tab. 3.12, we analyse inelastic neutron scattering spectra of a polycrystalline sample of  $Tb_2Sn_2O_7$ . A new set of CEF parameters is listed in Tab. 3.16, close to the initial one, and the corresponding computed CEF energy level scheme for this compound is displayed in Fig. 3.17 in order to compare with experimental data and identify the different observed CEF transitions. Our measurements are consistent with those of Refs. [73, 170].

An inelastic neutron scattering intensity map of  $Tb_2Sn_2O_7$  recorded at  $T = 5$  K is shown in the left panel of Fig. 3.18, revealing CEF transitions lying at 1.2 and 10.5 meV. In the right panel of the same figure, data are integrated over the wavevector range  $0.16 \leq q \leq 2 \text{ \AA}^{-1}$  and analysed using CEF parameters listed in Tab. 3.16. Some details of the analysis are gathered in Tab. 3.17.

In the left panel of Fig. 3.19, we show an inelastic neutron scattering intensity map of  $Tb_2Sn_2O_7$ , recorded at  $T = 5$  K, exhibiting the highest CEF transitions that we have accessed during the experiment, revealing excitations lying approximately at 10.5, 15

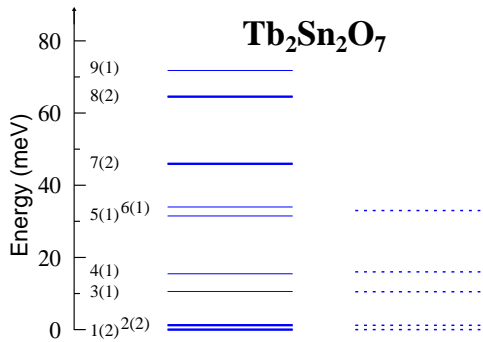


Figure 3.17: Energy levels scheme of  $Tb_2Sn_2O_7$  obtained with the CEF parameters listed in Tab. 3.16. The different energy levels are labelled by numbers in order to identify the CEF transitions involved in the inelastic neutron scattering spectra, see Tab. 3.17 and Tab. 3.18. The numbers in parentheses (1) and (2) correspond to a singlet and doublet states, respectively. The dotted lines indicate the experimental CEF transitions revealed by inelastic neutron scattering spectroscopy.

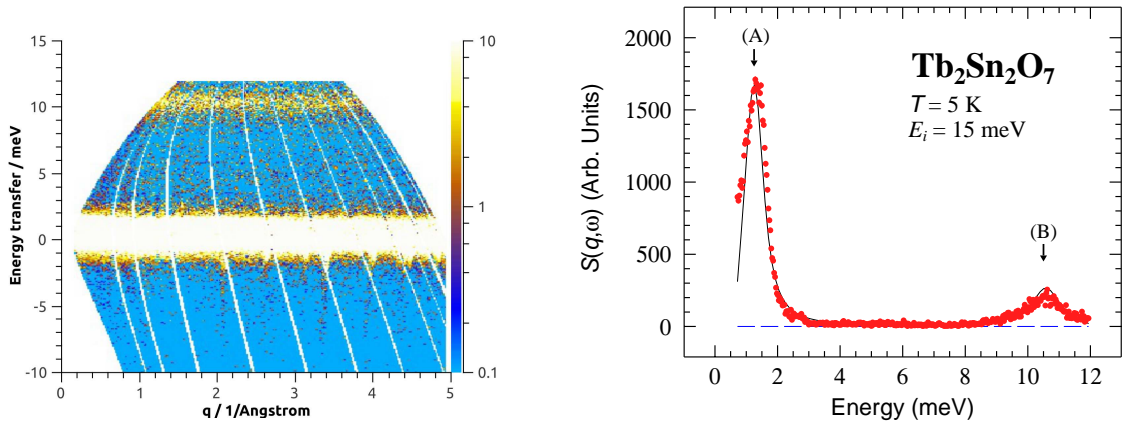


Figure 3.18: *Left: Inelastic neutron scattering spectrum of a polycrystalline sample of  $\text{Tb}_2\text{Sn}_2\text{O}_7$  recorded at  $T = 5$  K,  $E_i = 15$  meV and a Fermi chopper frequency  $\nu_{\text{FC}} = 300$  Hz. Right: Integration of these data over the wavevector range  $0.16 \leq q \leq 2 \text{ \AA}^{-1}$ . The black solid line is a fit to the data using CEF parameters displayed in Tab. 3.16. Black arrows indicate the CEF transitions: they are labelled by letters in order to identify the CEF energy levels, see Tab. 3.17 and Fig. 3.17.*

and 33 meV. In the right panel of Fig. 3.19, data are integrated over the wavevector range  $0.32 \leq q \leq 4 \text{ \AA}^{-1}$  and analysed using the set of CEF parameters listed in Tab. 3.16. Some details of the analysis are given in Tab. 3.18. Except for the highest excitation located at 33 meV, our set of CEF parameters accounts very well for the data.

### 3.3.4 Analysis of $\text{Er}_2\text{Sn}_2\text{O}_7$

In the following, we intend to analyse inelastic neutron scattering spectra recorded by Guitteny *et al.* [104] on a polycrystalline sample of  $\text{Er}_2\text{Sn}_2\text{O}_7$  at the 4F2 triple-axis spectrometer located at the Léon Brillouin laboratory (LLB, Saclay). Starting from the CEF parameters given in the second row of Tab. 3.12, we successfully analyse a spectrum recorded at  $T = 1.5$  K, see left panel of Fig. 3.21 using the CEF parameters listed in Tab. 3.19, which are relatively close to the initial ones. The corresponding CEF energy levels scheme for this compound is shown in Fig. 3.20 in order to not only compare experimental and computed CEF energy levels but also to label the different energy levels for the identification of the involved CEF transition. Details of the analysis are gathered in Tab. 3.20. A simulation/comparison of data recorded at  $T = 100$  K is displayed in the right panel of Fig. 3.21, and additional information is provided in Tab. 3.21.

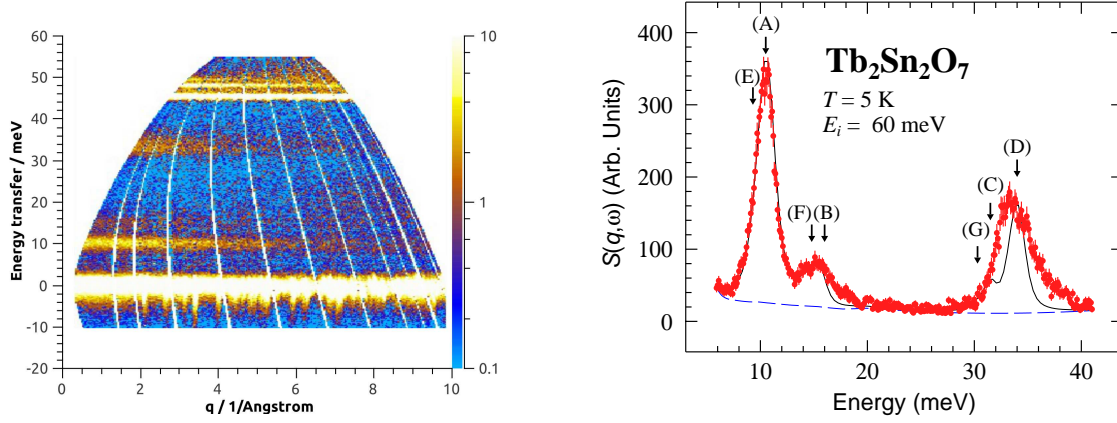


Figure 3.19: Left: Inelastic neutron scattering spectrum of  $Tb_2Sn_2O_7$  recorded at  $T = 5$  K,  $E_i = 60$  meV and  $\nu_{FC} = 600$  Hz. Right: Integration over the wavevector range  $0.32 \leq q \leq 4 \text{ \AA}^{-1}$ . The black solid line is a fit to the data using CEF parameters displayed in Tab. 3.16. Black arrows indicate the CEF transitions: they are labelled by letters in order to identify the CEF energy levels, see Tab. 3.18 and Fig. 3.17.

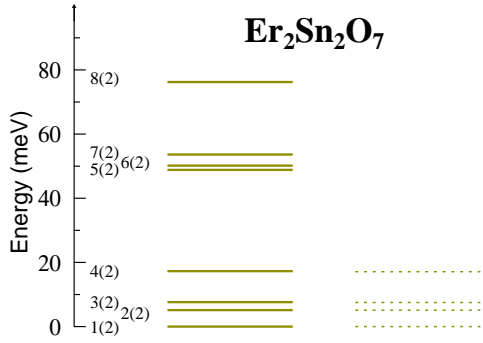


Figure 3.20: Energy levels scheme of  $Er_2Sn_2O_7$  obtained with the CEF parameters listed in Tab. 3.19. The different energy levels are labelled by numbers in order to identify the CEF transitions, see Tab. 3.20 and Tab. 3.21. The dotted lines indicate the experimental CEF transitions revealed by inelastic neutron scattering spectroscopy [104, 105].

Transition ( $a \rightarrow b$ )	$1 \rightarrow 3$ (A)	$1 \rightarrow 4$ (B)	$1 \rightarrow 5$ (C)	$1 \rightarrow 6$ (D)
Energy (meV)	10.6	15.5	31.5	34.0
Rel. Int. (arb. units)	3.7	0.3	0.18	1.5
$\Gamma_{ab}$ (meV)	1.2(F)	0.5(F)	0.5(F)	1.0(F)
Transition ( $a \rightarrow b$ )	$2 \rightarrow 3$ (E)	$2 \rightarrow 4$ (F)	$2 \rightarrow 5$ (G)	$2 \rightarrow 6$ (H)
Energy (meV)	9.4	14.3	30.3	32.8
Rel. Int. (arb. units)	0.13	0.24	0.13	$4.9 \times 10^{-2}$
$\Gamma_{ab}$ (meV)	0.1(F)	0.9(F)	0.5(F)	-

Table 3.18: Results of the analysis of the inelastic neutron scattering spectrum of  $Tb_2Sn_2O_7$  displayed in the right panel of Fig. 3.19. We give the CEF transitions between energy levels labelled ( $a, b$ ) as indicated in Fig. 3.17, their calculated energy positions, and linewidths of Lorentzian functions describing CEF transitions. The symbol “-” means that no Lorentzian function describes the CEF transition since its relative intensity is negligible compared to other CEF transitions. Relative intensities are also given.

$A_n^m$ (meV/ $a_0^n$ )	$A_2^0$	$A_4^0$	$A_4^3$	$A_6^0$	$A_6^3$	$A_6^6$
$\text{Er}_2\text{Sn}_2\text{O}_7$	52.1(1.5)	24.6(3)	-180(4)	0.89(1)	14.6(5)	15.9(4)

Table 3.19: CEF parameters  $A_n^m$  rescaled for  $\text{Tb}_2\text{Sn}_2\text{O}_7$  and deduced from the analysis of the inelastic neutron scattering spectrum of  $\text{Er}_2\text{Sn}_2\text{O}_7$  recorded at  $T = 1.5$  K, see left panel of Fig. 3.21.

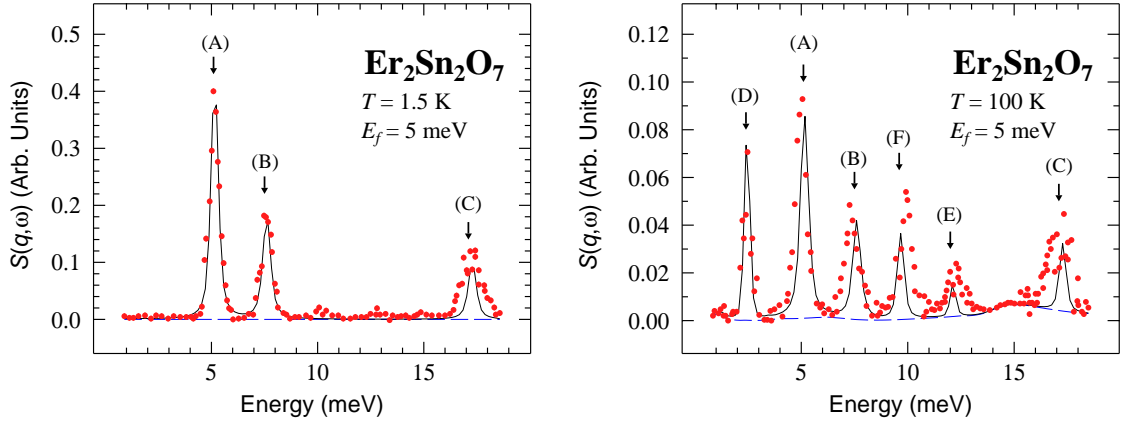


Figure 3.21: Inelastic neutron scattering spectra of  $\text{Er}_2\text{Sn}_2\text{O}_7$  recorded at  $T = 1.5$  K (left) and 100 K (right). Data are reproduced from Fig. 3 of Ref. [104]. The black solid line is a fit to the data (left) or a simulation and comparison to the data (right) using CEF parameters displayed in Tab. 3.19. Black arrows indicate the CEF transitions: see Fig. 3.20, and Tab. 3.20 and Tab. 3.21 for the left and right panels, respectively.

Transition ( $a \rightarrow b$ )	1 $\rightarrow$ 2 (A)	1 $\rightarrow$ 3 (B)	1 $\rightarrow$ 4 (C)
Energy (meV)	5.2	7.6	17.3
Rel. Int. (arb. units)	2.16/10.5	0.66/5.4	$3.6 \times 10^{-3}$ /3.3
$\Gamma_{ab}$ (meV)	0.25(F)	0.3(F)	0.3(F)

Table 3.20: Results of the analysis of the inelastic neutron scattering spectrum of  $\text{Er}_2\text{Sn}_2\text{O}_7$  displayed in the left panel of Fig. 3.21. We give the CEF transitions between energy levels labelled ( $a, b$ ) as indicated in Fig. 3.20, their calculated energy positions and linewidths of Lorentzian functions describing CEF transitions. Relative intensities are also given.

Transition ( $a \rightarrow b$ )	1 $\rightarrow$ 2 (A)	1 $\rightarrow$ 3 (B)	1 $\rightarrow$ 4 (C)
Energy (meV)	5.2	7.6	17.3
Rel. Int. (arb. units)	1.0/5.0	0.3/2.5	$1.7 \times 10^{-3}$ /1.6
$\Gamma_{ab}$ (meV)	0.2(F)	0.5(F)	0.4(F)
Transition ( $a \rightarrow b$ )	2 $\rightarrow$ 3 (D)	2 $\rightarrow$ 4 (E)	3 $\rightarrow$ 4 (F)
Energy (meV)	2.4	12.1	9.7
Rel. Int. (arb. units)	0.7/2.6	$2.4 \times 10^{-2}$ /0.5	$1.8 \times 10^{-2}$ /2.0
$\Gamma_{ab}$ (meV)	0.1(F)	0.1(F)	0.2(F)

Table 3.21: Results of the simulation of the inelastic neutron scattering spectrum of  $\text{Er}_2\text{Sn}_2\text{O}_7$  displayed in the right panel of Fig. 3.21. We give the CEF transitions between energy levels labelled ( $a, b$ ) as indicated in Fig. 3.20.

$A_n^m$ (meV/ $a_0^n$ )	$A_2^0$	$A_4^0$	$A_4^3$	$A_6^0$	$A_6^3$	$A_6^6$
$\text{Ho}_2\text{Sn}_2\text{O}_7$	53.2(1.4)	22.4(4)	-155(9)	0.84(2)	13.4(6)	17.7(3)
$\text{Tb}_2\text{Sn}_2\text{O}_7$	50.0(2.0)	21.2(8)	-159(7)	1.01(7)	14.4(2.0)	17.5(5)
$\text{Er}_2\text{Sn}_2\text{O}_7$	52.1(1.5)	24.6(3)	-180(4)	0.89(1)	14.6(5)	15.9(4)

Table 3.22: Summary of the CEF parameters  $A_n^m$  rescaled for  $\text{Tb}_2\text{Sn}_2\text{O}_7$  and deduced from the analysis of the inelastic neutron scattering spectra of  $\text{Ho}_2\text{Sn}_2\text{O}_7$  (second row),  $\text{Tb}_2\text{Sn}_2\text{O}_7$  (third row), and  $\text{Er}_2\text{Sn}_2\text{O}_7$  (last row).

Tb	$ \phi_0^\pm\rangle = \pm 0.895 \pm 5\rangle + 0.224 \pm 2\rangle + 0.000 \mp 1\rangle + 0.386 \mp 4\rangle$
Dy	$ \phi_0^\pm\rangle = \pm 0.988 \pm \frac{15}{2}\rangle - 0.144 \pm \frac{9}{2}\rangle \mp 0.041 \pm \frac{3}{2}\rangle + 0.030 \mp \frac{3}{2}\rangle \pm 0.006 \mp \frac{9}{2}\rangle - 0.004 \mp \frac{15}{2}\rangle$
Ho	$ \phi_0^\pm\rangle = 0.981 \pm 8\rangle \pm 0.156 \pm 5\rangle + 0.074 \pm 2\rangle \pm 0.073 \mp 1\rangle + 0.053 \mp 4\rangle \pm 0.007 \mp 7\rangle$
Er	$ \phi_0^\pm\rangle = \mp 0.392 \pm \frac{13}{2}\rangle + 0.431 \pm \frac{7}{2}\rangle \pm 0.566 \pm \frac{1}{2}\rangle - 0.266 \mp \frac{5}{2}\rangle \mp 0.520 \mp \frac{11}{2}\rangle$
Tm	$ \phi_0\rangle = 0.108 6\rangle + 0.699 3\rangle + 0.699 -3\rangle - 0.108 -6\rangle$
Yb	$ \phi_0^\pm\rangle = -0.269 \pm \frac{7}{2}\rangle \pm 0.960 \pm \frac{1}{2}\rangle + 0.074 \mp \frac{5}{2}\rangle$

Table 3.23: Ground-state wavefunctions for six compounds of the  $R_2\text{Sn}_2\text{O}_7$  pyrochlore series computed with the CEF parameters listed in the second row of Tab. 3.12 except for  $\text{Tb}_2\text{Sn}_2\text{O}_7$  and  $\text{Er}_2\text{Sn}_2\text{O}_7$  computed with those listed in Tab. 3.16 and Tab. 3.19, respectively. Note that we do not include  $\text{Nd}_2\text{Sn}_2\text{O}_7$  and  $\text{Pr}_2\text{Sn}_2\text{O}_7$ .

### 3.3.5 Conclusions

To conclude, from a global fit including energy levels of the three aforementioned compounds, we find a set of CEF parameters describing inelastic neutron scattering spectra of  $\text{Ho}_2\text{Sn}_2\text{O}_7$ . This constitutes a good starting point for the analysis of  $\text{Tb}_2\text{Sn}_2\text{O}_7$  and  $\text{Er}_2\text{Sn}_2\text{O}_7$  since the refined CEF parameters for each compound do not differ very much from the initial ones, as summed up in Tab. 3.22.

For completeness, we give the ground state wavefunctions and the spectroscopic  $g$  factors, computed using Eqs. 3.21, of several compounds of the  $R_2\text{Sn}_2\text{O}_7$  series in Tab. 3.23 and Tab. 3.24, respectively. We find a similar anisotropy between titanate and stannate compounds since we recover a strong Ising anisotropy for the spin-ice compound  $\text{Ho}_2\text{Sn}_2\text{O}_7$  and  $\text{Dy}_2\text{Sn}_2\text{O}_7$  and a crystal field magnetic moment of order of  $10 \mu_B$ . The XY anisotropy of  $\text{Yb}_2\text{Sn}_2\text{O}_7$  is stronger than found in  $\text{Yb}_2\text{Ti}_2\text{O}_7$  ( $r = g_\perp/g_\parallel \approx 2.7$  and  $2$  for the stannate and titanate compound, respectively), and the spectroscopic factors are consistent with those deduced from Mössbauer spectroscopy, i.e.  $g_\parallel = 1.1$  and  $g_\perp = 4.2$  [92]. Finally, we find that  $\text{Er}_2\text{Sn}_2\text{O}_7$  ( $r \approx 19.3$ ) has a stronger planar anisotropy than  $\text{Er}_2\text{Ti}_2\text{O}_7$  ( $r \approx 3.7$ ).

Similarly to the titanate series, we use the nuclear quadrupole splitting  $\Delta_Q = 1.15 \times 10^{-3}$  meV measured by  $^{155}\text{Gd}$  Mössbauer spectroscopy in  $\text{Gd}_2\text{Sn}_2\text{O}_7$  [117] to deduce  $A_2^0 = 67.7$  meV/ $a_0^2$ . Using the scaling law given in Eq. 3.16 with  $a_{\text{lat}} = 10.4644$  Å for  $\text{Gd}_2\text{Sn}_2\text{O}_7$ , we then get  $A_2^0 = 68.2$  meV/ $a_0^2$  rescaled for  $\text{Tb}_2\text{Sn}_2\text{O}_7$ . This  $A_2^0$  value is still larger than the result of our model, although the discrepancy is smaller than in the titanate case. This value is included in the range of explored CEF parameters given in the last row of Tab. 3.12 and does not provide any solution.

Finally, note that inelastic neutron scattering spectra of the pyrochlore compound  $\text{Nd}_2\text{Sn}_2\text{O}_7$  were not discussed in this section. We fail to include it in a global analysis. As for the pyrochlore compound  $\text{Pr}_2\text{Sn}_2\text{O}_7$  [69], the effect of the first excited multiplet

	Tb	Dy	Ho	Er	Yb
$g_{\parallel}$	10.5	19.7	19.5	0.4	1.6
$g_{\perp}$	0	0	0	7.7	4.3

Table 3.24: Spectroscopic factors  $g_{\parallel}$  and  $g_{\perp}$  for the ground state doublets of five compounds of the  $R_2\text{Sn}_2\text{O}_7$  series using  $A_n^m$  parameters listed in the second row of Tab. 3.12 except for  $\text{Tb}_2\text{Sn}_2\text{O}_7$  and  $\text{Er}_2\text{Sn}_2\text{O}_7$  computed with those listed in Tab. 3.16 and Tab. 3.19, respectively. Note that we do not include  $\text{Nd}_2\text{Sn}_2\text{O}_7$  and  $\text{Pr}_2\text{Sn}_2\text{O}_7$  since the hypothesis consisting of neglecting the effect of the first excited multiplets is not valid anymore. For  $\text{Tm}_2\text{Sn}_2\text{O}_7$  the thulium ion has a singlet ground state and therefore  $g_{\parallel} = g_{\perp} = 0$ .

cannot be neglected and should be considered to correctly analyse inelastic neutron scattering spectra, see for instance Ref. [69], resulting in a  $J$ -mixing of the ground state wavefunctions.

# Chapter 4

## Experimental study of $\text{Nd}_2\text{Sn}_2\text{O}_7$

### Contents

---

<b>4.1</b>	<b>Introduction</b>	<b>101</b>
<b>4.2</b>	<b>Powder synthesis</b>	<b>101</b>
<b>4.3</b>	<b>Crystal structure analysis</b>	<b>102</b>
<b>4.4</b>	<b>Neutron time-of-flight spectroscopy</b>	<b>103</b>
<b>4.5</b>	<b>Bulk measurements</b>	<b>104</b>
4.5.1	Specific heat	104
4.5.2	Magnetisation	107
<b>4.6</b>	<b>Determination of the magnetic structure</b>	<b>110</b>
<b>4.7</b>	<b>Neutron backscattering measurements</b>	<b>114</b>
4.7.1	Spin Hamiltonian for $^{143}\text{Nd}$	114
4.7.2	Incoherent scattering cross-section	115
4.7.3	Magnetic scattering cross-section	116
4.7.4	Data analysis	117
<b>4.8</b>	<b><math>\mu\text{SR}</math> spectroscopy</b>	<b>120</b>
4.8.1	Evidence of long-range order	121
4.8.2	Persistence of spin dynamics	125
4.8.3	$\lambda_Z$ behaviour in the paramagnetic phase	127
4.8.4	Anomalously slow paramagnetic fluctuations	130
<b>4.9</b>	<b>Conclusions</b>	<b>132</b>

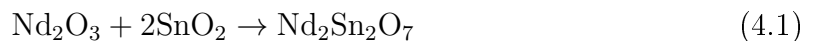
---

## 4.1 Introduction

Whereas most of the pyrochlore compounds have been extensively studied, the ground state of  $\text{Nd}_2\text{Sn}_2\text{O}_7$  is still unknown. Since the neodymium possesses a total angular momentum  $J = 9/2$ , it is classified as a Kramers ion. The sign of the Stevens multiplicative factor  $\Theta_2$ , see Tab. B.1, teaches us about the Ising character of the magnetic moment. Blöte *et al.* [82] have studied this compound with specific heat measurements and evidenced a second-order magnetic transition at  $T_c = 0.91$  K. On the other hand, Bondah-Jagalu and Bramwell [110] revealed with magnetic susceptibility measurements the antiferromagnetic nature of the exchange interactions. The combination of these features has not been encountered yet in the pyrochlore series of interest. Therefore, looking for new magnetic ground states, we have performed a full characterisation of this compound with a wide panel of techniques. Hence, we report in this chapter our study of the pyrochlore compound  $\text{Nd}_2\text{Sn}_2\text{O}_7$  with specific heat, magnetisation, neutron and X-ray diffraction, inelastic neutron scattering and  $\mu\text{SR}$  measurements.

## 4.2 Powder synthesis

Powder samples of  $\text{Nd}_2\text{Sn}_2\text{O}_7$  were synthesised by C. Marin from CEA-Grenoble and by A. Forget from CEA-Saclay. We briefly discuss the procedure of C. Marin to get powder sample of  $\text{Nd}_2\text{Sn}_2\text{O}_7$ . A stoichiometric mixture of oxides  $\text{Nd}_2\text{O}_3$  (quality 4N7, i.e. 99.997 % pure) and  $\text{SnO}_2$  (quality 5N, i.e. 99.999 % pure) were carefully weighed and ground with acetone in an agate mortar in order to get an homogeneous mixture. A heat treatment under air atmosphere in an alumina crucible (chemically inert at heat treatment temperatures) ensures a solid phase diffusion according to the reaction:



To get a single phase polycrystalline sample, successive heat treatments (2 days at  $900^\circ\text{C}$ , 2 days at  $1150^\circ\text{C}$ , and 4 days at  $1300^\circ\text{C}$ ) were intersperse with grindings. At Saclay, the temperature for the heat treatment reaches  $1400^\circ\text{C}$ , which constitutes the main difference compared to the method displayed here.

X-ray diffraction measurements were performed at CEA-Grenoble, as described in Sec. 2.3.5, to check the quality of our samples. Powder samples were placed with a small amount of grease on an almost transparent Pyrex plate, which gives a very low diffuse scattering at small angles. The single phase character of our samples was evidenced since only traces of  $\text{Nd}_2\text{O}_3$  and  $\text{SnO}_2$  in the sample from Saclay and  $\text{SnO}_2$  in the sample from Grenoble were detected.

Note that single crystals cannot be synthesised by vertical crystal growth with an image furnace since the  $\text{SnO}_2$  oxide is very volatile and evaporates at high temperature. We could imagine to get small crystals in a closed airtight crucible, withstanding to the fusion temperature of the oxides of interest, in an atmosphere saturated with  $\text{SnO}_2$ .

Results displayed in this chapter were acquired with Saclay's sample, except for the neutron time-of-flight measurements.

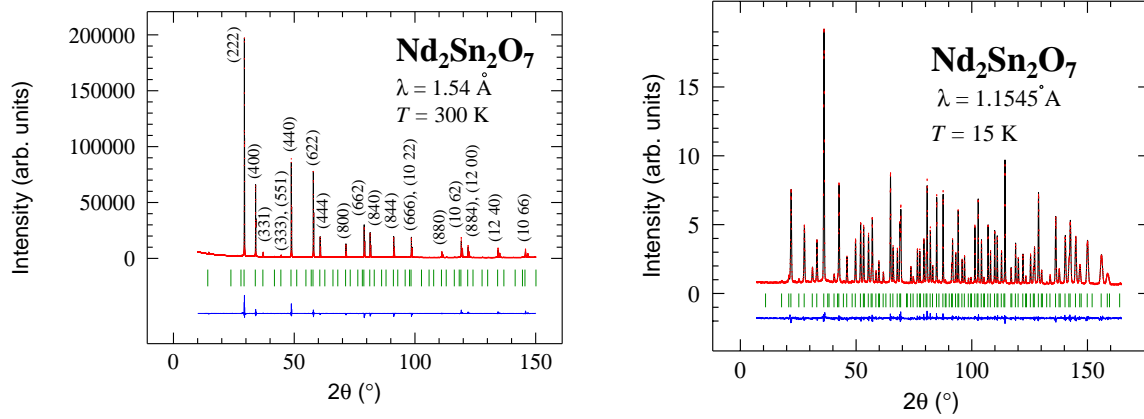


Figure 4.1: *Left: X-ray diffraction pattern of  $\text{Nd}_2\text{Sn}_2\text{O}_7$  recorded at room temperature. At large scattering angle, the peaks are twinned, resulting from the presence of the  $\text{Cu } K_{\alpha 1}$  and  $K_{\alpha 2}$  radiations in the incident beam. Right: Neutron diffraction diagram of  $\text{Nd}_2\text{Sn}_2\text{O}_7$  recorded at  $T = 15 \text{ K}$  with a neutron wavelength of  $\lambda = 1.1545 \text{ \AA}$ . For both panels, the solid line is the result of a Rietveld analysis using the FullProf code and the blue solid line at the bottom gives the difference between the data and the model. The vertical markers indicate the positions of the Bragg peaks.*

### 4.3 Crystal structure analysis

An X-ray pattern recorded at room temperature is shown in the left panel of Fig. 4.1. Our compound crystallises in the  $\text{Fd}\bar{3}\text{m}$  face centered cubic space group. The description of its primitive cell is summed up in Tab. A.1. A Rietveld analysis is performed with the FullProf suite [130], as detailed in Sec. 2.3.7, using a pseudo-Voigt function, see Eq. 2.22. Here, the occupation of the different sites was fixed to their nominal values. The lattice parameter and the position  $x$  of oxygen atom O1 are gathered in Tab.4.1.

Type	Diffractometer	Temperature (K)	$a_{\text{lat}}$ (Å)	$x$	$R_p$	$R_{\text{wp}}$	$R_{\text{exp}}$	$\chi^2$
X-ray	Xpert Panalytical	300	10.5744(1)	0.3274(3)	10.8	11.8	1.28	84
Neutrons	D2B	300	10.5679(3)	0.33250(8)	11.5	10.5	4.51	5.1
Neutrons	HRPT	15	10.5586(6)	0.33259(8)	7.28	7.22	4.90	2.2

Table 4.1: *Lattice parameter  $a_{\text{lat}}$  and position  $x$  of oxygen atom O1 determined by X-ray and neutron diffraction.  $R$ -factors are listed as indicators of the analysis goodness, see Sec. 2.3.7. Note that the difficulty to modelise the distribution of wavelength in the X-ray beam induces slightly different values from those determined by neutron diffraction. A slight reduction of the lattice parameter deduced from HRPT measurements arises from the lattice contraction since measurements were performed at  $T = 15 \text{ K}$ . Results are in good agreement with Ref. [190].*

However, as mentioned in Sec. 2.3.5, the X-ray beam is not fully monochromatic which forbids a deeper analysis of the data. Neutron diffraction experiments were also performed at the D2B diffractometer of Institut Laue Langevin and at the high resolution diffractometer HRPT of the SINQ neutron source at the Paul Scherrer Institute (Sec. 2.3.6). A Rietveld analysis of data recorded on HRPT at  $T = 15 \text{ K}$  is displayed on the right panel of Fig. 4.1. The shape of a Bragg peak was modelled with a Thompson-

Atom	$U_{11}(\times 10^{-3})$	$U_{22}(\times 10^{-3})$	$U_{33}$	$U_{12}(\times 10^{-4})$	$U_{13}$	$U_{23}(\times 10^{-3})$
Nd	0.17(2)	E( $U_{11}$ )	E( $U_{11}$ )	-0.2(2)	E( $U_{12}$ )	E( $U_{12}$ )
Sn	0.25(2)	E( $U_{11}$ )	E( $U_{11}$ )	-0.5(2)	E( $U_{12}$ )	E( $U_{12}$ )
O1	0.64(3)	0.58(2)	E( $U_{22}$ )	0(F)	0(F)	-0.18(3)
O2	0.69(2)	E( $U_{11}$ )	E( $U_{11}$ )	0(F)	0(F)	0(F)

Table 4.2: The displacement parameters  $U_{ij}$  in  $\text{\AA}^2$  units deduced from the analysis of the neutron diffraction pattern recorded at  $T = 15$  K for  $\text{Nd}_2\text{Sn}_2\text{O}_7$ . The occupations of the different sites have been released as explained in the main text. When we write 0(F) the parameter was fixed to zero during the fit. E( $U_{ij}$ ) means that the parameter was taken equal to  $U_{ij}$ .

Cox-Hastings pseudo-Voigt function, see Sec. 2.3.7. The Debye-Waller factors were expressed in terms of the symmetry-allowed anisotropic displacement parameters  $U_{\alpha\beta}$ , listed in Tab. 4.2. In a second step we analysed our data in search for a deviation of the nominal stoichiometry of our sample. We have considered the possibility of stuffing, i.e. a fraction of the Nd atom sitting at the Sn site or reciprocally. This leads to the chemical formula  $\text{Nd}_{2+y}\text{Sn}_{2-y}\text{O}_{7+\delta}$ . Since there are two crystallographically non equivalent oxygen sites, a stoichiometric compound is actually more explicitly named as  $\text{Nd}_2\text{Sn}_2(\text{O1})_6(\text{O2})$  where O1 and O2 are the two oxygen sites [191]. For our investigation of the non-stoichiometry of our sample we need to decide where to locate the excess/lack of oxygen. We have tried three models:

- Model 1:  $\text{Nd}_{2+y}\text{Sn}_{2-y}(\text{O1})_6(\text{O2})_{1+\delta}$ ,
- Model 2:  $\text{Nd}_{2+y}\text{Sn}_{2-y}(\text{O1})_{6+\delta}(\text{O2})$ ,
- Model 3:  $\text{Nd}_{2+y}\text{Sn}_{2-y}(\text{O1})_{6+\frac{6\delta}{7}}(\text{O2})_{1+\frac{\delta}{7}}$ .

Electric charge conservation enforces  $y = -\frac{\delta}{2}$ . Within the errors bars, these three models provide equivalent fits to the data with the following values  $y = 0.013$  (7) and  $\delta = -0.006$  (3). These are extremely small deviations from stoichiometry and we can assume our sample to be stoichiometric thereafter.

## 4.4 Neutron time-of-flight spectroscopy

In order to determine the crystal-electric-field energy levels scheme of  $\text{Nd}_2\text{Sn}_2\text{O}_7$ , we report measurements performed at the MARI spectrometer, see Sec. 2.4 for technical details. We display in the left panels of Fig. 4.2 and Fig. 4.3 the whole  $(\mathbf{q}, \hbar\omega)$  space probed at  $T = 5$  K. Spectra in the right panels result from an integration over a selected low- $q$  range to avoid the phonon contribution, since the magnetic form factor decreases when  $q$  increases whereas the phonons intensity grows as  $q^2$ . Furthermore, data have been corrected for absorption effects as explained in App. C. Since neodymium is a Kramers ion ( $J = \frac{9}{2}$ ), we expect five doublets. All the energy levels are resolved: four excited doublets lie at 26, 38.5, 39.8 and 110 meV. Therefore, the ground state doublet is well isolated from the excited ones.

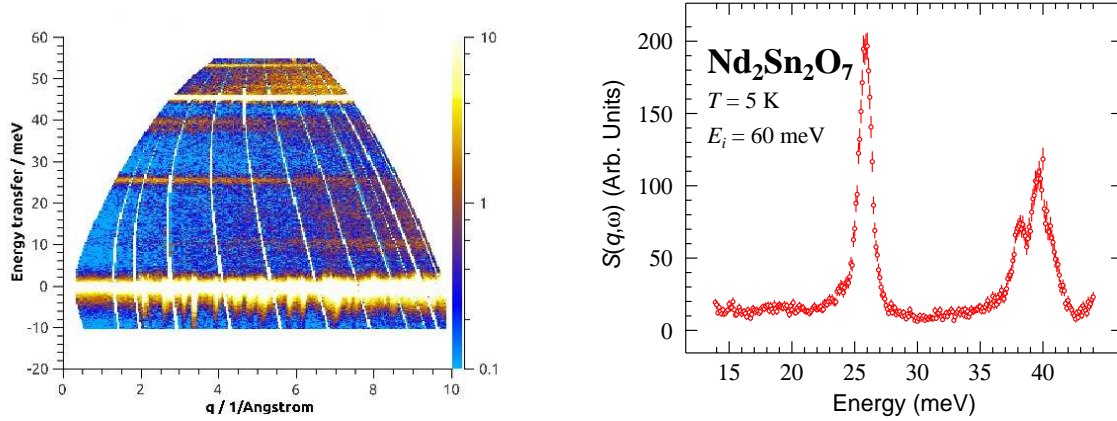


Figure 4.2: *Left: Inelastic neutron scattering spectrum of a  $\text{Nd}_2\text{Sn}_2\text{O}_7$  powder sample recorded at  $T = 5$  K with an incident energy  $E_i = 60$  meV and a Fermi chopper frequency  $\nu_{\text{FC}} = 600$  Hz. Right: Integration of the data on the left over wavevector range  $0.32 \leq q \leq 4.02 \text{ \AA}^{-1}$ . Crystal-electric-field energy levels are observed at 26, 38.5 and 39.8 meV.*

## 4.5 Bulk measurements

Specific heat and magnetisation measurements reported here were performed at CEA-Grenoble. One refers to Sec. 2.1.1 and Sec. 2.1.2 for more details on the technical aspects of the PPMS and the MPMS, respectively.

### 4.5.1 Specific heat

The heat capacity measurements are displayed in Fig. 4.4, in good agreement with those performed by Blöte *et al.* [82]. A  $\lambda$ -type peak occurs at  $T_c \approx 0.91$  K, consistent with a second order phase transition. This goes in line with the peak in the magnetic susceptibility previously observed [33]. There is no broad hump above  $T_c$ , as sometimes found for geometrically frustrated magnetic materials and interpreted as the signature of short-range correlations [192]. To describe the low temperature behaviour of the specific heat, we assume gapless excitations described by a linear dispersion law in a three-dimensional system, similarly to the contribution of antiferromagnetic magnons to the specific heat [193]:

$$\omega(q) = v_{\text{ex}}q, \quad (4.2)$$

where  $v_{\text{ex}}$  accounts for the excitation velocity and we have assumed an isotropic  $q$  dependence of the dispersion law. We can write the density of states  $g(\omega)d\omega = \frac{1}{(2\pi)^3}4\pi q^2\left(\frac{dq}{d\omega}\right)d\omega$ . Therefore, the energy associated to these excitations is written as:

$$\begin{aligned} E_{\text{ex}} &= \int_0^\infty \hbar\omega g(\omega) n_{\text{P}} \left( \frac{\hbar\omega}{k_{\text{B}}T} \right) d\omega, \\ &= \int_0^\infty \hbar\omega \frac{1}{2\pi^2} \left( \frac{\omega}{v_{\text{ex}}} \right)^2 \frac{1}{v_{\text{ex}}} n_{\text{P}} \left( \frac{\hbar\omega}{k_{\text{B}}T} \right) d\omega, \end{aligned} \quad (4.3)$$

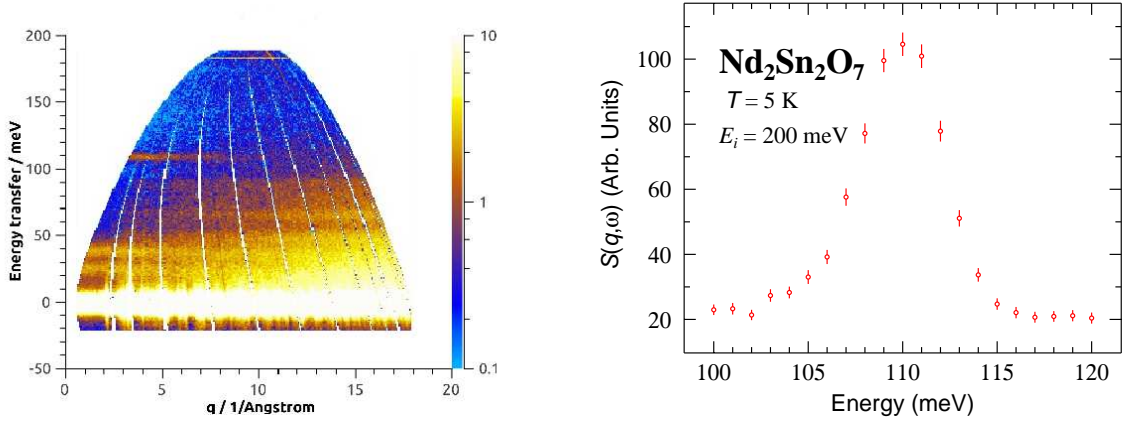


Figure 4.3: *Left: Inelastic neutron scattering spectrum of a  $\text{Nd}_2\text{Sn}_2\text{O}_7$  powder sample recorded at  $T = 5$  K with an incident energy  $E_i = 200$  meV and a Fermi chopper frequency  $\nu_{\text{FC}} = 400$  Hz. Right: Integration of the data on the left over wavevector range  $0.59 \leq q \leq 7 \text{ \AA}^{-1}$ . This configuration allows to detect the highest energy level lying at 110 meV.*

where  $n_{\text{P}}\left(\frac{\hbar\omega}{k_{\text{B}}T}\right)$  is the Planck distribution function, assuming here these excitations are described by bosons, analogously to the magnons:

$$n_{\text{P}}\left(\frac{\hbar\omega}{k_{\text{B}}T}\right) = \frac{1}{\exp\left(\frac{\hbar\omega}{k_{\text{B}}T}\right) - 1}. \quad (4.4)$$

Note that this function is the particular case of the Bose-Einstein function with the chemical potential  $\mu = 0$ . With  $x = \frac{\hbar\omega}{k_{\text{B}}T}$ , Eq. 4.3 becomes:

$$E_{\text{ex}} = \frac{1}{2\pi^2}(k_{\text{B}}T)^4 \left(\frac{1}{\hbar v_{\text{ex}}}\right)^3 \int_0^{\infty} \frac{x^3}{\exp(x) - 1} dx. \quad (4.5)$$

Since [194]:

$$\int_0^{\infty} \frac{x^3}{\exp(x) - 1} dx = \Gamma(4)\xi(4) = \frac{\pi^4}{15}, \quad (4.6)$$

where  $\Gamma$  is the well-known Gamma function and  $\xi$  the Riemann zeta function. We get the  $T^3$  dependence of these magnon-like excitations to the specific heat:

$$C_{\text{ex}} = \frac{dE_{\text{ex}}}{dT} = N \frac{2\pi^2}{30} \frac{k_{\text{B}}^4}{\hbar^3 v_{\text{ex}}^3} T^3 = \mathcal{B}T^3, \quad (4.7)$$

where  $N$  is the number of magnetic atoms, i.e.  $N = \mathcal{N}_{\text{A}} \frac{a_{\text{lat}}^3}{8}$ . This law accounts well for the data at low temperatures with  $\mathcal{B} = 11.0(7) \text{ JK}^{-4} \text{ mol}^{-1}$ . Therefore, from  $\mathcal{B} = \frac{\pi^2}{120} \mathcal{N}_{\text{A}} \frac{k_{\text{B}}^4 a_{\text{lat}}^3}{\hbar^3 v_{\text{ex}}^3}$ , we infer an excitation velocity  $v_{\text{ex}} = 55(1) \text{ ms}^{-1}$  in line with the value found for  $\text{Er}_2\text{Ti}_2\text{O}_7$  [195].

The uprise of the specific heat above  $\approx 10$  K is attributed to the contribution of the phonons. Indeed, as the first excited crystal-electric-field (CEF) doublet lies at 26 meV above the ground-state doublet, see Sec. 4.4, no CEF contribution to the specific heat

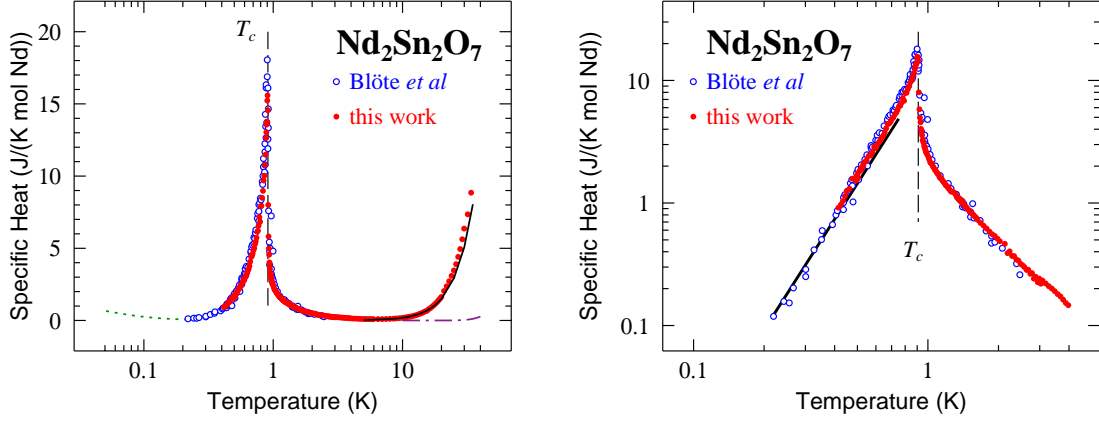


Figure 4.4: Left: Temperature dependence of the specific heat of a  $\text{Nd}_2\text{Sn}_2\text{O}_7$  powder sample. The black solid, the purple dashed-dotted and the green dotted lines are the phonons, crystal-electric-field and nuclear contributions to the specific heat, respectively. For both panels, the transition temperature is indicated by a vertical black dashed line. Our data are displayed with full red circles whereas those of Ref. [82] are reproduced with open blue circles. Right: Zoom over the lowest temperatures with a double logarithmic scale. The black solid line is a fit of Eq. 4.7 to the data.

is expected in the displayed temperature range. The electronic specific heat variation provides us with a measure of the degeneracy of the ground state through the entropy. Recalling that the electronic entropy variation  $\Delta S_{\text{el}}(T_1, T_2)$  between temperatures  $T_1$  and  $T_2$  is given by the well known formula

$$\Delta S_{\text{el}}(T_1, T_2) = \int_{T_1}^{T_2} \frac{C_{\text{el}}}{T} dT, \quad (4.8)$$

we obtain  $\Delta S_{\text{el}}(T_1 = 0.2 \text{ K}, T)$  as shown in the left panel of Fig. 4.5. Assuming the Debye model to be valid, the lattice contribution  $C_{\text{ph}}$  to the specific heat has been subtracted from  $C_{\text{p}}$  in the temperature range  $5 \leq T \leq 20 \text{ K}$  to obtain  $C_{\text{el}}$  following a  $T^3$  law [193]:

$$C_{\text{ph}} = \frac{12\pi^4}{5} N k_{\text{B}} \left( \frac{T}{\Theta_{\text{D}}} \right)^3, \quad (4.9)$$

We infer the Debye temperature  $\Theta_{\text{D}} = 385(2) \text{ K}$ . We have also determined the nuclear contribution  $C_{\text{nuc}}$  to the low temperature specific heat which should also be subtracted. It originates from the nuclear splitting arising from a Zeeman interaction between the nuclear spin and the hyperfine field  $B_{\text{hyp}}$  created by the unpaired electrons, and a quadrupolar interaction which is negligible, see Sec. 4.7. Note that two isotopes, labelled by the index  $i$ ,  $^{143}\text{Nd}$  and  $^{145}\text{Nd}$ , with the same nuclear spin  $I = \frac{7}{2}$ , need to be taken into account since they have a different gyromagnetic ratio  $\gamma_i$ . Therefore,  $(2I + 1)$  energy levels are equally separated by  $\Delta_{\text{N},i} = \hbar\gamma_i B_{\text{hyp}}$  where  $B_{\text{hyp}}$  is inferred from neutron backscattering spectroscopy, see Sec. 4.7. Thus, the nuclear contribution to the specific heat is derived as:

$$C_{\text{nuc}} = \frac{d}{dT} \left\{ \sum_i \frac{p_i}{Z_i} \sum_{E_i} E_i \exp[-E_i/(k_{\text{B}}T)] \right\}, \quad (4.10)$$

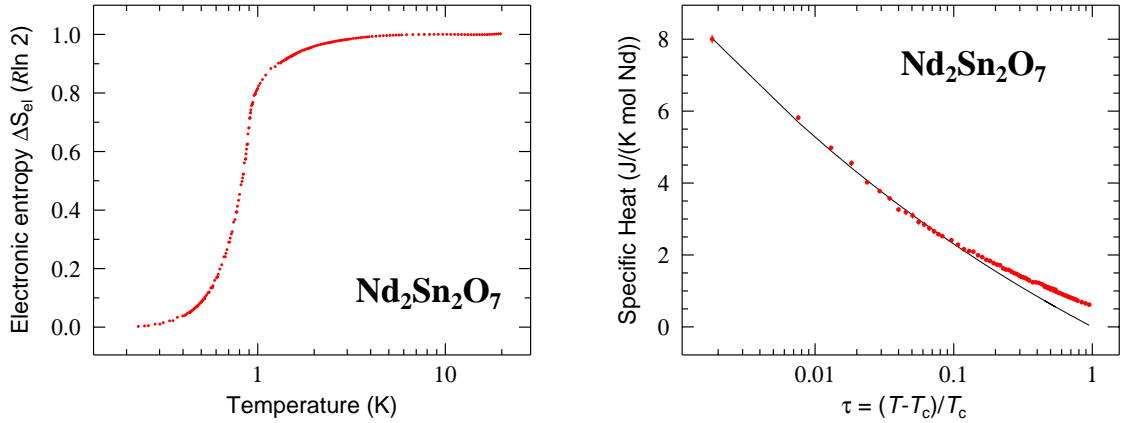


Figure 4.5: Left: Temperature dependence of the variation of the electronic entropy  $\Delta S_{\text{el}}$ . The data are plotted in units of  $R \ln 2$  where  $R$  is the ideal gas constant. Right: Specific heat plotted versus the reduced temperature  $\tau = \frac{T-T_c}{T_c}$  in the paramagnetic regime. The black solid line is a fit to the data as explained in the main text.

where  $E_i = n\hbar\gamma_i B_{\text{hyp}}$  ( $0 \leq n \leq 2I$ ) refers to the energy levels of the nuclear spin of isotope  $i$  with relative abundance  $p_i$  and  $Z_i$  denotes the partition function. We compute a value of  $C_{\text{nuc}} = 0.06$  J/(K mol Nd) for the nuclear specific heat at 0.25 K. Since  $C_{\text{nuc}}$  decreases as  $T^{-2}$  in the high-temperature limit which applies in the temperature range of interest here, we can safely neglect it.

The left panel of Fig. 4.5 indicates that well above the transition temperature the entropy per mole of Nd is  $R \ln 2$ , a value expected when only the ground state doublet is populated. The electronic entropy decreases to zero deep in the ordered magnetic phase. Therefore, no macroscopic degeneracy is present contrary to the spin-ice pyrochlore characterised by a non vanishing entropy at zero temperature, see Sec. 1.3.1.

In the right panel of Fig. 4.5 is displayed the specific heat versus the reduced temperature  $\tau = (T - T_c)/T_c$  in the paramagnetic phase in order to investigate the critical regime. According to Refs. [196, 197], we expect to observe the power-law critical behaviour:

$$C_{\text{el}}(T) = \frac{C_{\text{sh}}}{\alpha_c} \left[ \left( \frac{T - T_c}{T_c} \right)^{-\alpha_c} - 1 \right], \quad (4.11)$$

where  $C_{\text{sh}}$  is a constant and  $\alpha_c$  a critical exponent expected to be equal to 0.110,  $-0.015$  and  $-0.134$  for three-dimensional Ising, XY and Heisenberg magnets, respectively [198]. The fit displayed in the right panel of Fig. 4.5 corresponds to the three dimensional Ising case ( $\alpha_c = 0.110$ ). We found  $C_{\text{sh}} = 0.88(2)$  J K $^{-1}$  mol $^{-1}$  and  $T_c = 0.913(1)$  K. The critical regime is observed up to  $\tau \approx 0.1$ . In the case of  $\alpha_c = -0.015$  and  $-0.134$ , acceptable fits lead to  $T_c = 0.917(1)$  and  $0.926(1)$  K, respectively, such that we cannot determine with certainty the spin symmetry with this analysis.

## 4.5.2 Magnetisation

As explained in Sec. 2.1.2, a sample pellet close to an ellipsoidal shape is introduced in a weak diamagnetic sample holder. The external field is applied along a major axis of the ellipsoid. This geometry reduces the demagnetising field. According to Eq. 2.6,

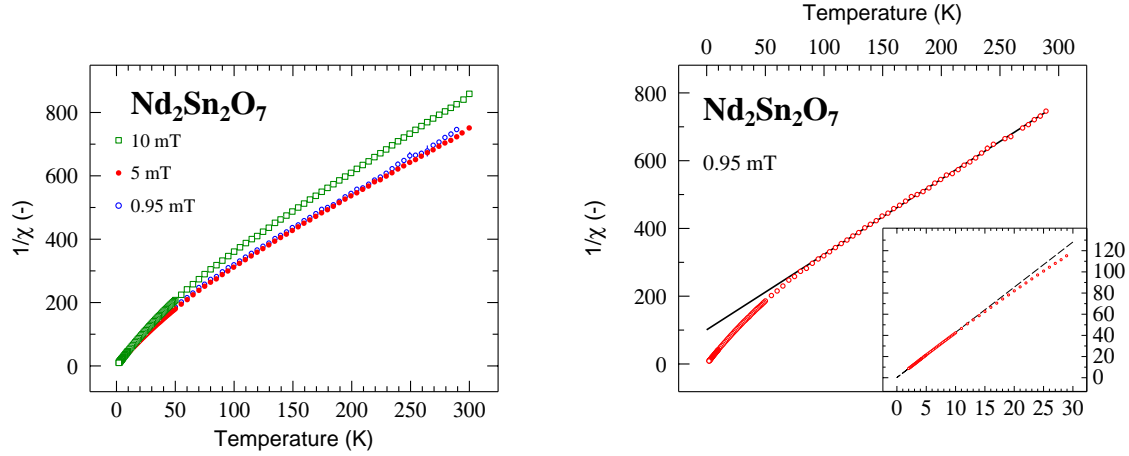


Figure 4.6: Left: Inverse of the magnetic susceptibility at 0.95, 5, and 10 mT: evidence of the field invariance below 5 mT. Right: Temperature dependence of the inverse of the magnetic susceptibility  $1/\chi$  measured in a field of 0.95 mT. The insert displays the low temperatures data. In the two panels, the solid lines are results of fits as explained in the main text.

determining the weak field limit, i.e.  $M \propto H_{\text{applied}}$ ,<sup>1</sup> is of first importance to extract the intrinsic magnetic susceptibility. In the left panel of Fig. 4.6, we compare measurements for  $\mu_0 H_{\text{applied}} = 0.95, 5,$  and  $10$  mT. The field invariance of the magnetic susceptibility is then no longer verified for magnetic fields higher than 5 mT. However, we must note that measurements at very low magnetic fields could be more influenced by the presence of magnetic impurities than at higher magnetic fields, explaining the field dependence of the magnetic susceptibility recorded at  $\mu_0 H_{\text{applied}} = 5$  and  $10$  mT.

In the right panel of Fig. 4.6 is displayed the inverse of the static susceptibility  $1/\chi$  measured in a field of 0.95 mT. In the temperature range  $150 \leq T \leq 290$  K  $\chi$  follows a Curie-Weiss law, i.e.  $\chi = C/(T - \theta_{\text{CW}})$ , with a Curie-Weiss temperature  $\theta_{\text{CW}} = -46.3$  (1.9) K and a paramagnetic moment  $m_{\text{pm}} = g_J \mu_B \sqrt{J(J+1)} = 3.57$  (4)  $\mu_B$  comparable with the value  $m_{\text{pm}} = 3.62 \mu_B$  for a free  $\text{Nd}^{3+}$  ion. As shown in the insert, assuming  $\chi$  to follow a Curie-Weiss law for  $5 \leq T \leq 15$  K we get  $\theta_{\text{CW}} = -0.32$  (1) K, indicating a weak net antiferromagnetic exchange interaction and  $m_{\text{pm}} = 2.63$  (3)  $\mu_B$ , in very good agreement with results of Ref. [110]. As the first excited crystal-field doublet is located at  $\approx 26$  meV above the Kramers doublet ground-state of  $\text{Nd}^{3+}$ , an effective spin  $S' = 1/2$  model is justified for the ion description at low temperatures. We deduce a spectroscopic factor  $g_{\text{eff}} = m_{\text{pm}}/(\sqrt{S'(S'+1)}\mu_B) = 3.04$  (3). Assuming the  $\text{Nd}^{3+}$  magnetic moments to interact through nearest-neighbour Heisenberg interaction, the exchange integral  $\mathcal{I}$  can be computed as [199]:

$$\frac{\mathcal{I}}{k_B} = \frac{3|\theta_{\text{CW}}|}{z_{\text{nn}}S'(S'+1)} = 0.213(7) \text{ K}, \quad (4.12)$$

where  $z_{\text{nn}} = 6$  is the number of nearest neighbour  $\text{Nd}^{3+}$  ions to a given  $\text{Nd}^{3+}$  ion. The field dependence of the magnetisation in the paramagnetic phase is displayed in Fig. 4.7. In the paramagnetic regime, i.e. in a system without any magnetic interactions,

<sup>1</sup>We refer to Sec. 2.1.2 for the definition of the real applied field  $H_{\text{applied}}$  at the sample

Temperature (K)	2	5	10	25	100
$m_{\text{sat}}(\mu_{\text{B}})$	1.17(3)	1.35(5)	1.4(1)	1.4(1)	1.6(1)

Table 4.3: Saturation value of the magnetic moment resulting from the analysis of the magnetisation curves using Eq. 4.14 for several temperatures.

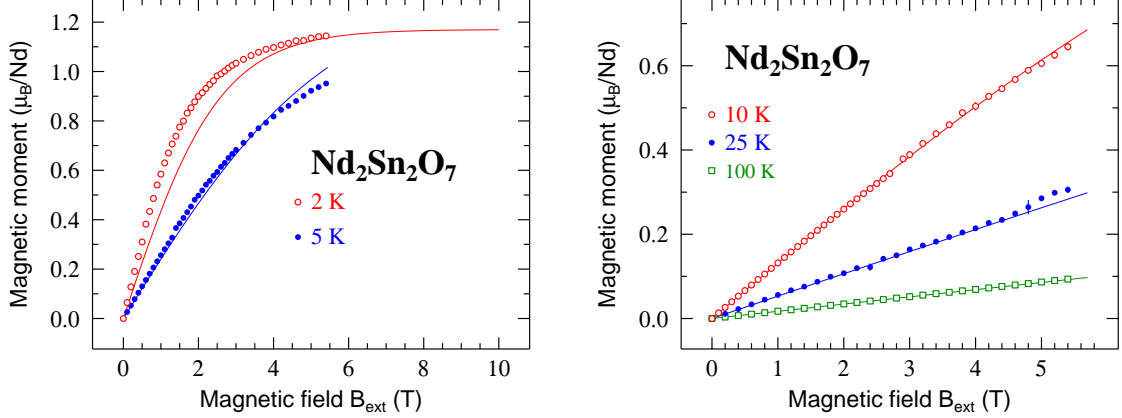


Figure 4.7: Field dependence of the magnetic moment in the paramagnetic phase at 2 and 5 K (left) and at 10, 25 and 100 K (right). Solid lines are fits of Eq. 4.14 to the data.

the ground state multiplet arising from the spin-orbit coupling is split in  $(2J + 1)$  energy levels by Zeeman effect. Therefore, the field dependence of the magnetic moment follows [199]:

$$m = g_J J \mu_{\text{B}} B_J(x), \quad \text{and} \quad x = \frac{g_J J \mu_{\text{B}} B_{\text{ext}}}{k_{\text{B}} T} \quad (4.13)$$

where  $m_{\text{sat}} = g_J J \mu_{\text{B}}$  is the saturation value of the paramagnetic moment and  $B_J(x)$  is the Brillouin function. This model is only valid for equally distributed energy levels, which is not the case here looking at the crystal-electric-field energy levels, see Sec. 4.4. However, the ground state energy level is well isolated from the excited ones and we can tentatively describe it with an effective spin  $S' = \frac{1}{2}$ . Therefore, Eq. 4.13 becomes for a two energy levels system:

$$m = m_{\text{sat}} \tanh(x), \quad \text{and} \quad x = \frac{m_{\text{sat}} B_{\text{ext}}}{k_{\text{B}} T}. \quad (4.14)$$

In Fig. 4.7, magnetisation curves are displayed for several temperature. Solid lines are fits of Eq. 4.14 to the data. Results are summed up in Tab. 4.3.

Note that the saturation values of the magnetic moment are far below the value of the paramagnetic moment deduced from the analysis of the inverse magnetic susceptibility in the low temperature region, i.e.  $m_{\text{pm}} = 2.63(3) \mu_{\text{B}}$ . However, as previously mentioned, this model is valid in a system without any magnetic interactions. As we will see in the following sections, strong magnetic correlations are at play since spin dynamics is much slower than expected.

## 4.6 Determination of the magnetic structure

We performed magnetic powder neutron diffraction measurements at the D1B diffractometer located at ILL, see Sec. 2.3.6, to determine the magnetic structure of  $\text{Nd}_2\text{Sn}_2\text{O}_7$ . A magnetic diffraction diagram recorded at 60 mK is presented in the left panel of Fig. 4.8. It was recorded with neutrons of wavelength  $2.524 \text{ \AA}$  using a cylindrical copper sample container. Experimental data nearby  $2\theta = 74.4^\circ$  and  $88.5^\circ$  are not shown because they are strongly influenced by neutrons scattered from the container. Data recorded in the paramagnetic phase at 1.2 K were subtracted to only exhibit the magnetic signal. The presence of Bragg reflections implies that a long-range structure of the  $\text{Nd}^{3+}$  magnetic moments is established. The reflections only occurring at the nuclear Bragg peak positions, the magnetic propagation vector of the structure is  $\mathbf{k}_{\text{mag}} = (0, 0, 0)$ . Among all the symmetry allowed operations, those leaving  $\mathbf{k}_{\text{mag}}$  invariant constitute the little group  $G_k$ , the representation of which can be decomposed in terms of irreducible representations (IR)  $\Gamma_\nu^{(\mu)}$  where  $\nu$  labels the different representations of dimension  $\mu$ . For the Nd atomic Wyckoff site  $16d$  of symmetry  $\bar{3}m$  in the cubic space group  $Fd\bar{3}m$  in which  $\text{Nd}_2\text{Sn}_2\text{O}_7$  crystallises:

$$\Gamma(G_k) = 1\Gamma_3^{(1)} + 1\Gamma_5^{(2)} + 1\Gamma_7^{(3)} + 2\Gamma_9^{(3)}. \quad (4.15)$$

The  $\Gamma_3$ ,  $\Gamma_5$ ,  $\Gamma_7$ , and  $\Gamma_9$  representations are one-, two-, three-, and three-dimensional IR respectively. More details are given in App. D.1. We perform a Rietveld refinement, see Sec. 2.3.7, with the FullProf suite [130]. The peak shapes are described with a pseudo-Voigt function (Eq. 2.22). The results of the Rietveld analysis are summed up in Tab. 4.4. The symmetry of the magnetic phase is described by the  $\Gamma_3$  irreducible representation with a basis vector  $\Psi_{1,j}$  tabulated in Tab. D.1. It corresponds to the noncoplanar all-in-all-out magnetic moment arrangement pictured in the right panel of Fig. 4.8: corner-sharing tetrahedra possess alternatively four spins pointing into the direction of the center of the tetrahedron and four spins pointing out. Not only the Rietveld refinement predicts the  $\Gamma_3$  IR, we have analytically shown in App. D.3 that only this IR can provide a proper description of our data. This structure should not give

IR	$R_p$	$R_{\text{wp}}$	$R_{\text{exp}}$	$\chi^2$	IR	$R_p$	$R_{\text{wp}}$	$R_{\text{exp}}$	$\chi^2$
$\Gamma_3, \Psi_{1,j}$	16.5	7.46	4.64	2.59	$\Gamma_9, \Psi_{7,j}$	80.3	80.3	4.65	298
$\Gamma_5, \Psi_{2,j}$	81.3	79.6	4.65	292	$\Gamma_9, \Psi_{8,j}$	106	95.8	4.65	423
$\Gamma_5, \Psi_{3,j}$	81.4	79.6	4.65	292	$\Gamma_9, \Psi_{9,j}$	80.3	80.3	4.65	298
$\Gamma_7, \Psi_{4,j}$	97.2	91.5	4.65	386	$\Gamma_9, \Psi_{10,j}$	106	95.8	4.65	423
$\Gamma_7, \Psi_{5,j}$	97.2	91.5	4.65	386	$\Gamma_9, \Psi_{11,j}$	80.3	80.3	4.65	298
$\Gamma_7, \Psi_{6,j}$	97.2	91.5	4.65	386	$\Gamma_9, \Psi_{12,j}$	106	95.8	4.65	423

Table 4.4: Indicators of the goodness of the analysis using basis vectors of each possible IR. See Sec. 2.3.7 for a definition of the  $R$ -factors. Basis vectors  $\Psi_{i,j}$  are tabulated in Tab. D.1. The selected IR used to performed the analysis of magnetic neutron diffraction patterns is highlighted in red. Note that for a given IR of dimension  $d > 1$ , we should use a linear combination of the basis vectors. However, such a combination of the resulting calculated intensity cannot describe the data.

rise to a structural distortion, consistently with the second order nature of the magnetic

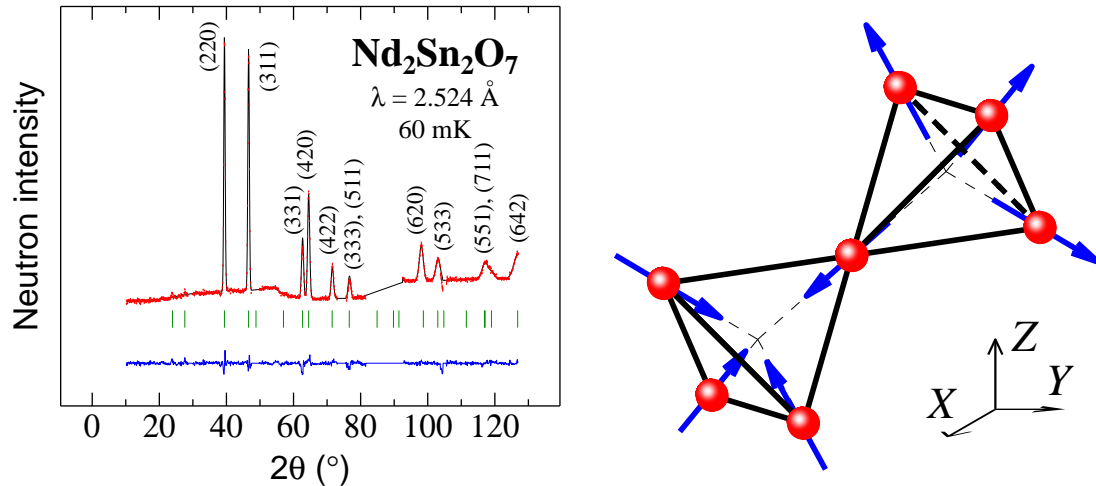


Figure 4.8: *Left: Powder magnetic neutron diffraction diagram versus the scattering angle  $2\theta$  resulting from the difference between 60 mK and 1.2 K data sets. The black line results from a Rietveld refinement assuming an all-in-all-out magnetic structure. The positions of the magnetic reflections are indicated by the green vertical markers. The difference between the experimental data and the refinement is shown by the blue bottom line. Right: Illustration of the all-in-all-out magnetic structure. The  $(X, Y, Z)$  frame refers to the cubic axis. The spheres represent the  $\text{Nd}^{3+}$  ions and the arrows their magnetic moments oriented along the local trigonal  $\langle 111 \rangle$  axes of the cubic crystal structure. Two corner-sharing tetrahedra are shown, one with the magnetic moments pointing inwards and an adjacent tetrahedron with moments pointing outwards.*

phase transition, since this structure belongs to the symmetric  $A_g$  group [200]. This is understood physically because the magnetic moments are oriented along the trigonal axes of the cubic crystal structure.

The left panel of Fig. 4.9 presents  $m_{\text{sp}}(T)$  resulting from the Rietveld analysis. The spontaneous magnetic moment for  $T \rightarrow 0$  is  $m_{\text{sp}}(0) = 1.708(3) \mu_B$ . In the right panel of Fig. 4.9, is displayed the analysis of  $m_{\text{sp}}(T)$  close to the transition using the equation:

$$m_{\text{sp}}(T) = m_{\text{sp}}(0) \left( \frac{|T - T_c|}{T_c} \right)^{\beta_c}. \quad (4.16)$$

We find  $\beta_c = 0.28(2)$  and  $T_c = 0.916(6)$  K. The exponent  $\beta_c$  is smaller than for any three-dimensional magnetic system, i.e.  $\beta_c = 0.325(2)$ ,  $0.346(2)$ , and  $0.365(3)$  for Ising, XY, and Heisenberg systems, respectively [201]. This may not be totally surprising since we did not approach  $T_c$  close enough to probe the critical regime.

As introduced in Sec. 4.5.1, we assume excitations to be responsible for the decay of the magnetic moment in the ordered phase, similarly to antiferromagnetic magnons. Although our system consists of four non collinear sublattices, let us consider for simplicity an Heisenberg collinear antiferromagnetic system which can be described in the most simple case by two interlaced sublattices  $d_1$  and  $d_2$ , see Sec. E.2, where all the spins of one sublattice point in the same direction, the spins of the second sublattice being in the opposite direction. Note that for an ion belonging to sublattice  $d_1$ , all its nearest neighbour belong to sublattice  $d_2$ , and reciprocally. In the following, we focus

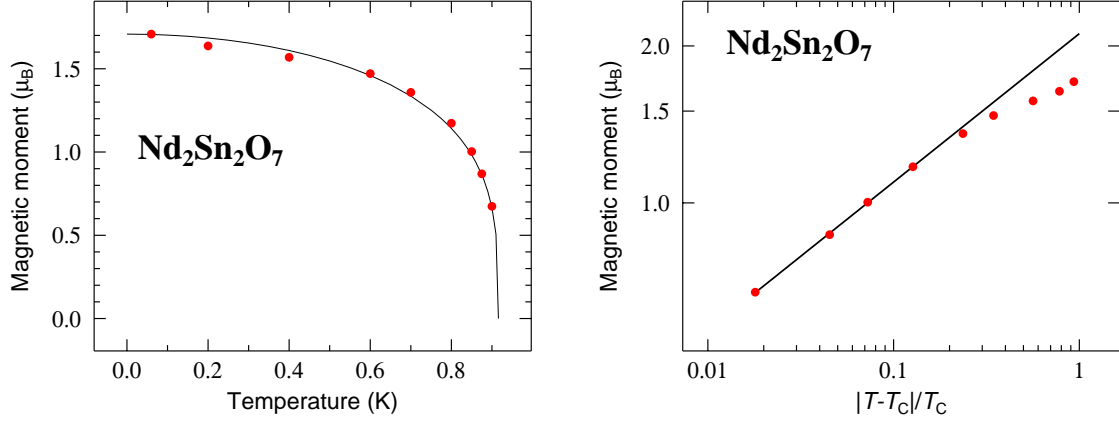


Figure 4.9: *Left: Temperature dependence of the spontaneous magnetic moment  $m_{\text{sp}}(T)$ . Note that error bars are smaller than the symbols. The solid line is a fit of Eq. 4.32 to the data. Right: Magnetic moment versus the reduced temperature in the critical regime in order to determine the critical exponent  $\beta_c$ .*

on sublattice  $d_1$ . The  $z$  component of spin  $J$  located at site  $i$  is defined as, see Eq. E.41:

$$J_i^Z = a_i^\dagger a_i - J, \quad (4.17)$$

where  $a^\dagger$  and  $a$  are the boson creation and annihilation operators. Using Eq. E.42, we perform the following space Fourier transform:

$$J_i^Z = \frac{1}{n_c} \sum_{\mathbf{q}\mathbf{q}'} a_{\mathbf{q}'}^\dagger a_{\mathbf{q}} \exp[i(\mathbf{q} - \mathbf{q}') \cdot \mathbf{i}] - J, \quad (4.18)$$

where  $n_c$  is the number of unit cells,  $\mathbf{i}$  is the vector linking the magnetic ion at site  $i$  to the origin of the sublattice.

$$\begin{aligned} J^Z &= \sum_i J_i^Z = \frac{1}{n_c} \sum_{\mathbf{q}\mathbf{q}'} a_{\mathbf{q}'}^\dagger a_{\mathbf{q}} \sum_{\mathbf{i}} \exp[i(\mathbf{q} - \mathbf{q}') \cdot \mathbf{i}] - NJ, \\ &= \sum_{\mathbf{q}} a_{\mathbf{q}}^\dagger a_{\mathbf{q}} - NJ, \end{aligned} \quad (4.19)$$

where  $N$  is the number of magnetic ions in the sublattice. We have used the following relation:

$$\sum_{\mathbf{i}} \exp[i(\mathbf{q} - \mathbf{q}') \cdot \mathbf{i}] = n_c \delta(\mathbf{q} - \mathbf{q}'). \quad (4.20)$$

Then introducing the Bogoliubov transformation, see Eq. E.43, we derive:

$$J^Z = \sum_{\mathbf{q}} u_{\mathbf{q}}^2 \alpha_{\mathbf{q}}^\dagger \alpha_{\mathbf{q}} + v_{\mathbf{q}}^2 \beta_{\mathbf{q}} \beta_{\mathbf{q}}^\dagger + u_{\mathbf{q}} v_{\mathbf{q}} (\alpha_{\mathbf{q}}^\dagger \beta_{\mathbf{q}}^\dagger + \beta_{\mathbf{q}} \alpha_{\mathbf{q}}) - NJ. \quad (4.21)$$

Since  $\beta_{\mathbf{q}}$  commutes with  $\alpha_{\mathbf{q}}$ , recalling that  $\alpha_{\mathbf{q}}^\dagger \beta_{\mathbf{q}}^\dagger + \alpha_{\mathbf{q}} \beta_{\mathbf{q}} = 0$ , see Sec. E.2, and using the usual commutation rules for boson operators, see Eq. E.44, we obtain:

$$J^Z = \sum_{\mathbf{q}} u_{\mathbf{q}}^2 \alpha_{\mathbf{q}}^\dagger \alpha_{\mathbf{q}} + v_{\mathbf{q}}^2 (1 + \beta_{\mathbf{q}}^\dagger \beta_{\mathbf{q}}) - NJ. \quad (4.22)$$

We recall that  $\langle \alpha_{\mathbf{q}}^\dagger \alpha_{\mathbf{q}} \rangle = \langle \beta_{\mathbf{q}}^\dagger \beta_{\mathbf{q}} \rangle = n_{\text{P}} \left( \frac{\hbar \omega_{\mathbf{q}}}{k_{\text{B}} T} \right)$  where  $\langle \dots \rangle$  denotes the thermal average and  $n_{\text{P}}(x)$  is the Planck distribution function, see Eq. 4.4. Note that  $\lim_{T \rightarrow 0} n_{\text{P}} \left( \frac{\hbar \omega_{\mathbf{q}}}{k_{\text{B}} T} \right) = 0$ . Therefore the temperature dependence of the sublattice magnetisation is:

$$-\langle J^z \rangle_{T=0} + \langle J^z \rangle_T = \sum_{\mathbf{q}} n_{\text{P}} \left( \frac{\hbar \omega_{\mathbf{q}}}{k_{\text{B}} T} \right) (u_{\mathbf{q}}^2 + v_{\mathbf{q}}^2). \quad (4.23)$$

In App. E.2.2, we have introduced a function  $x_{\mathbf{q}}$  such as:

$$u_{\mathbf{q}} = \cosh(x_{\mathbf{q}}) \quad \text{and} \quad v_{\mathbf{q}} = \sinh(x_{\mathbf{q}}), \quad (4.24)$$

since from the Bogoliubov transformation, we have  $u_{\mathbf{q}}^2 - v_{\mathbf{q}}^2 = 1$ . Consequently, we get:

$$-\langle J^z \rangle_{T=0} + \langle J^z \rangle_T = \sum_{\mathbf{q}} n_{\text{P}} \left( \frac{\hbar \omega_{\mathbf{q}}}{k_{\text{B}} T} \right) \cosh(2x_{\mathbf{q}}). \quad (4.25)$$

Using the relation  $\cosh(x) = [1 - \tanh(x)]^{-\frac{1}{2}}$ , combined with Eq. E.51 where we have assumed the gap of the excitations to be extremely small, i.e.  $\tanh(2x_{\mathbf{q}}) = -\gamma_{\mathbf{q}}$ , leads to:

$$-\langle J^z \rangle_{T=0} + \langle J^z \rangle_T = \sum_{\mathbf{q}} n_{\text{P}} \left( \frac{\hbar \omega_{\mathbf{q}}}{k_{\text{B}} T} \right) (1 - \gamma_{\mathbf{q}}^2)^{-\frac{1}{2}} \quad (4.26)$$

Once again, neglecting the energy gap  $\Delta$  in Eq. E.48 give:

$$\hbar \omega_{\mathbf{q}} = \hbar \omega_{\text{ex}} \sqrt{1 - \gamma_{\mathbf{q}}^2} \quad (4.27)$$

Finally, we get the temperature variation of the magnetic moment as:

$$m_{\text{sp}}(0) - m_{\text{sp}}(T) = g \mu_{\text{B}} (-\langle J^z \rangle_{T=0} + \langle J^z \rangle_T) = \int n_{\text{P}} \left( \frac{\hbar \omega_{\mathbf{q}}}{k_{\text{B}} T} \right) \frac{\omega_{\text{ex}}}{\omega_{\mathbf{q}}} \frac{d^3 \mathbf{q}}{(2\pi^3)}, \quad (4.28)$$

where we have assumed the excitation energy  $\hbar \omega_{\mathbf{q}}$  to only depend on the modulus of  $\mathbf{q}$ . Introducing  $x = \frac{\hbar \omega_{\mathbf{q}}}{k_{\text{B}} T}$ , and using a dispersion law valid at small  $q$ , see Eq. E.50 with  $\Delta = 0$ , Eq. 4.28 becomes:

$$\Delta m_{\text{sp}}(T) = m_{\text{sp}}(0) - m_{\text{sp}}(T) = \frac{\sqrt{2}}{4\pi^2} \frac{g \mu_{\text{B}}}{D_{\text{AF}}^2} (k_{\text{B}} T)^2 \int_0^\infty \frac{x}{\exp(x) - 1} dx, \quad (4.29)$$

where we have introduced  $D_{\text{AF}} = \sqrt{2} \hbar \omega_{\text{ex}} = 2\sqrt{2} \mathcal{I} z_{\text{nn}} J$  and  $\mathcal{I}$  the exchange integral between the  $z_{\text{nn}}$  nearest neighbours. Following Ref. [194],

$$\int_0^\infty \frac{x}{\exp(x) - 1} dx = \Gamma(2) \xi(2) = \frac{\pi^2}{3}. \quad (4.30)$$

Therefore we have evidenced the  $T^2$  variation of the magnetic moment in the case of spin-waves like excitations with a negligible energy gap:

$$m_{\text{sp}}(T) = m_{\text{sp}}(0) \left[ 1 - \frac{\sqrt{2}}{12} \frac{g \mu_{\text{B}}}{D_{\text{AF}}^2 m_{\text{sp}}(0)} (k_{\text{B}} T)^2 \right] \quad (4.31)$$

Fitting Eq. 4.31 to the data displayed in the left panel of Fig. 4.9 in a temperature range up to 0.8 K allows us to determine  $D_{\text{AF}}/k_{\text{B}} = 0.70(1)$  K and the exchange integral  $\mathcal{I}/k_{\text{B}} = 0.083(1)$  K,<sup>2</sup> using an effective spin-1/2 and  $g_{\text{eff}} = 2.97$ , previously determined in Sec. 4.5.2. Consequently, the solid line in the left panel of Fig. 4.9 is the result of the fit with the phenomenological formula:

$$m_{\text{sp}}(T) = m_{\text{sp}}(0) [1 - (T/T_c)^{\alpha_c}]^{\beta_c}, \quad (4.32)$$

where  $\alpha_c = 2$ . It encompasses the critical behavior near  $T_c$  and the quadratic decay of the magnetic moment at low temperatures.

## 4.7 Neutron backscattering measurements

For an independent estimate of  $m_{\text{sp}}(0)$  and to gather information on spin dynamics we performed neutron backscattering measurements at the IN16 spectrometer of ILL, see Sec. 2.5. Neutrons interact with the unpaired electrons and the nuclei of matter. As far as electrons are concerned we expect magnetic scattering from the unfilled shell of the  $\text{Nd}^{3+}$  ions. Since we only consider data outside the  $\text{Nd}_2\text{Sn}_2\text{O}_7$  Bragg scattering positions, only incoherent scattering processes are relevant for the nuclear contribution to the signal. In the following we will therefore describe the spin Hamiltonian of the neodymium nuclei, examine the nuclear and magnetic scattering cross-sections and finally, we will report our data analysis.

### 4.7.1 Spin Hamiltonian for $^{143}\text{Nd}$

The only chemical element entering the composition of  $\text{Nd}_2\text{Sn}_2\text{O}_7$  with a notable incoherent scattering cross-section is Nd. Among the natural Nd isotopes two of them are to be considered:  $^{143}\text{Nd}$  and  $^{145}\text{Nd}$  of abundance 12.2% and 8.3% and incoherent scattering cross-sections 55 (7) and 5 (5) barns, respectively. The spin of both isotopes is  $I = 7/2$ . Due to the presence of several isotopes, isotope-incoherent as well as spin-incoherent cross-sections must be considered. We will write below the differential cross-sections associated with the two processes. Before, we examine the scattering intensity related to the  $^{143}\text{Nd}$  spin, neglecting  $^{145}\text{Nd}$  due to its relatively small cross-section.

The  $^{143}\text{Nd}$  isotope is characterised by a quadrupolar moment  $Q = -0.630$  barn and a gyromagnetic ratio  $\gamma_{143} = -14.57 \times 10^6 \text{ rad s}^{-1} \text{ T}^{-1}$  [202]. The spin Hamiltonian relevant for the  $^{143}\text{Nd}$  nucleus is the sum of two terms: one accounts for the Zeeman interaction between the nuclear spin and the magnetic hyperfine field  $B_{\text{hyp}}$ , and the other for the quadrupolar interaction between the nuclear charge density and the electric field gradient at the nucleus created by the surrounding electronic shell and the neighbouring ions. We write for the Zeeman Hamiltonian,

$$\mathcal{H}_Z = -\hbar\omega_Z I_z \quad \text{with} \quad \omega_Z = \gamma_{143} B_{\text{hyp}}, \quad (4.33)$$

where the index  $z$  refers to the  $\langle 111 \rangle$  local axis at the  $\text{Nd}^{3+}$  site. The hyperfine splitting  $\hbar\omega_Z$  is related to the  $\text{Nd}^{3+}$  magnetic moment  $m_{\text{sp}}$  through the relation  $\hbar\omega_Z = m_{\text{sp}} \mathcal{A}_{\text{hyp}}^{143}$

---

<sup>2</sup>Note that this exchange constant differs from the value inferred from the Curie-Weiss analysis of the magnetic susceptibility at low temperatures, and listed in Eq. 4.12.

where the hyperfine constant of isotope  $^{143}\text{Nd}$ ,  $\mathcal{A}_{\text{hyp}}^{143} = 20.9$  (3) mT has been accurately measured by electron spin resonance measurements [203]. The point symmetry at the rare earth site dictates that the local  $\langle 111 \rangle$  axis belongs to the eigen basis of electric field gradient tensor and that  $V_{zz}$  is the principal component of this tensor which in addition has a zero asymmetry parameter. Therefore the quadrupole Hamiltonian is written as:

$$\mathcal{H}_Q = \hbar\omega_Q(3I_z^2 - I^2) \quad \text{and} \quad \hbar\omega_Q = \frac{eQV_{zz}}{4I(2I-1)} \quad (4.34)$$

This means that  $\mathcal{H}$  is diagonal and the eigenvectors are the Zeeman functions  $|m\rangle$  associated with the eigenvalues  $E_m$ ,  $\mathcal{H}|m\rangle = E_m|m\rangle$ , with  $-I \leq m \leq I$ .

We estimate now the intensity of these two interactions. The analysis displayed below leads to  $\hbar\omega_Z = 2.027$  (7)  $\mu\text{eV}$ . Since  $\text{Nd}_2\text{Sn}_2\text{O}_7$  is an insulator,  $V_{zz}$  is the sum of two terms:

$$V_{zz} = V_{zz}^{4f} + V_{zz}^{\text{lat}}, \quad (4.35)$$

where the first and second term accounts for the  $4f$ -electron and lattice contributions, respectively. Estimates of these quantities to  $V_{zz}$  are  $V_{zz}^{4f} = 1.0 \times 10^{22} \text{ V m}^{-2}$  and  $V_{zz}^{\text{lat}} = -1.0 \times 10^{22} \text{ V m}^{-2}$ , which lead to a vanishing electric field gradient at the nucleus. Still, we note that a value  $V_{zz} = 10^{22} \text{ V m}^{-2}$  for the total electric field gradient would lead to  $\hbar\omega_Q = -7.5 \times 10^{-3} \mu\text{eV}$ , a value two orders of magnitude less than the Zeeman interaction. Consistently, fitting the model to the neutron backscattering data with  $\hbar\omega_Q$  as a free parameter also leads to a negligible value of this parameter.

### 4.7.2 Incoherent scattering cross-section

As stated earlier, the double differential incoherent scattering cross-section is the sum of the spin-incoherent and isotope-incoherent contributions,

$$\left( \frac{d^2\sigma}{d\Omega dE} \right)_{\text{inc}} = \frac{k_f}{k_i} [\sigma_{\text{spin}}^{\text{Nd}} S_{\text{spin}}(\mathbf{q}, \hbar\omega) + \sigma_{\text{iso}}^{\text{Nd}} S_{\text{iso}}(\mathbf{q}, \hbar\omega)], \quad (4.36)$$

where  $\mathbf{k}_i$  and  $\mathbf{k}_f$  are the incident and scattered neutron wavevectors. The transfer of energy being extremely small we can safely set  $k_i = k_f$ . In the magnetically ordered phase, i.e. for a finite hyperfine field, following Ref. [204], we write the spin-incoherent scattering function,

$$\begin{aligned} S_{\text{spin}}(\mathbf{q}, \hbar\omega) &= \frac{N_{\text{Nd}} \exp(-2W(\mathbf{q}))}{4\pi I(I+1)} \frac{1}{Z} \\ &\times \sum_{m=-I}^I e^{-E_m/k_B T} \left[ \frac{1}{2} [I(I+1) - m(m+1)] \delta(\hbar\omega - (E_{m+1} - E_m)) \right. \\ &\left. + \frac{1}{2} [I(I+1) - m(m-1)] \delta(\hbar\omega + (E_m - E_{m-1})) + m^2 \delta(\hbar\omega) \right], \end{aligned} \quad (4.37)$$

where  $Z$  is the partition function:

$$Z = \sum_{m=-I}^I \exp(-E_m/k_B T). \quad (4.38)$$

$N_{Nd}$  is the total number of  $^{143}Nd$  nuclei in the sample, and  $\exp(-2W(\mathbf{q}))$  is the Debye-Waller factor. As discussed above, we can safely neglect the quadrupolar interaction and set  $|E_{m\pm 1} - E_m| = |\hbar\omega_Z|$ ,  $\forall m$ . In order to accommodate the small observed broadening of the inelastic peaks due to a finite lifetime of the nuclear levels, the Dirac delta functions in Eq. 4.37 are replaced by Lorentzian functions centered at  $\pm\hbar\omega_Z$  or 0,

$$L(\hbar\omega \pm \hbar\omega_Z) = \frac{1}{\pi} \frac{\Gamma_Z}{(\hbar\omega \pm \hbar\omega_Z)^2 + \Gamma_Z^2}, \quad (4.39)$$

where  $\Gamma_Z$  is the half-width at half-maximum, which corresponds to the inverse lifetime of the nuclear level. For simplicity, we assume that the lifetime is identical for all the levels.

In the paramagnetic phase,  $B_{hyp}$  is zero and the nuclear levels are degenerate. It is straightforward to check that Eq. 4.37 becomes

$$S_{spin}(\mathbf{q}, \hbar\omega) = \frac{N_{Nd} \exp(-2W(\mathbf{q}))}{4\pi} \delta(\hbar\omega) \quad (4.40)$$

which is the expected expression for the spin-incoherent scattering function.

The isotope-incoherent scattering function is written as

$$S_{iso}(\mathbf{q}, \hbar\omega) = \frac{N_{Nd} \exp(-2W(\mathbf{q}))}{4\pi} \delta(\hbar\omega), \quad (4.41)$$

a relation which naturally holds both in the paramagnetic and ordered phases.

The values of the  $\sigma_{spin}^{Nd}$  and  $\sigma_{iso}^{Nd}$  cross-sections are evaluated from Ref. [136]. We have  $\sigma_{spin}^{Nd} = 6.8$  barns and  $\sigma_{iso}^{Nd} = 1.8$  barns. At the temperature of our experiments the Debye-Waller factor is close to 1 and was set to this value in the fitting procedure.

### 4.7.3 Magnetic scattering cross-section

The double differential cross-section for inelastic magnetic scattering is expressed as

$$\left( \frac{d^2\sigma}{d\Omega dE} \right)_{mag} = \frac{k_f}{k_i} (\gamma r_0)^2 S_{mag}(\mathbf{q}, \hbar\omega), \quad (4.42)$$

where again  $k_f/k_i \approx 1$ ,  $|\gamma r_0| = -0.54 \times 10^{-12}$  cm is the magnetic scattering length<sup>3</sup>, and  $S_{mag}(\mathbf{q}, \hbar\omega)$  the inelastic magnetic scattering function. From Refs. [205, 206], assuming an isotropic dynamic susceptibility and performing a spatial average for a powder sample:

$$S_{mag}(\mathbf{q}, \hbar\omega) = \frac{2}{3} \left[ \frac{1}{2} g_J f_{mag}(q) \right]^2 N_{Nd} e^{-2W(q)} \frac{1}{1 - \exp\left(-\frac{\hbar\omega}{k_B T}\right)} \chi''(q, \hbar\omega), \quad (4.43)$$

where  $g_J$  is the Landé factor ( $g = 8/11$  for  $Nd^{3+}$ ), and  $\chi''(q, \hbar\omega)$  stands for the imaginary part of  $\chi(q, \hbar\omega)$ . This quantity is taken as

$$\chi''(q, \hbar\omega) = \frac{\hbar\omega}{\pi} \frac{\chi'(q) \Gamma_q}{(\hbar\omega)^2 + \Gamma_q^2}, \quad (4.44)$$

with  $\chi'(q)$  being the  $q$ -dependent static susceptibility and  $\Gamma_q$  the quasielastic Lorentzian linewidth. Again the Debye-Waller factor was set equal to 1.

---

<sup>3</sup> $|\gamma r_0| = 2p$  according to Eq. 2.15.

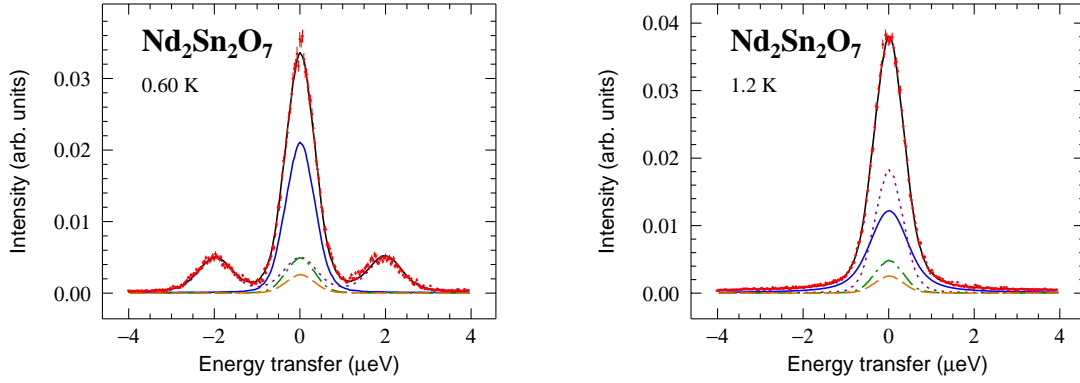


Figure 4.10: Backscattering spectra recorded at 0.60 K (left) and 1.2 K (right). The black full line is a fit of Eq. 4.45 to the data. The blue full, green dashed-dotted, purple dotted and orange dashed lines are respectively the magnetic, isotope incoherent, spin incoherent and sample environment incoherent scattering contributions to the signal.

#### 4.7.4 Data analysis

The code *BS\_fit* [207] was developed to analyse data from backscattering experiments. The measurements were performed for a range of wavevectors  $0.38 < q < 1.95 \text{ \AA}^{-1}$  excluding the region between  $1.60$  and  $1.725 \text{ \AA}^{-1}$  which corresponds to the (220)  $\text{Nd}_2\text{Sn}_2\text{O}_7$  Bragg peak. For the quantitative analysis of the spectra we express the total cross-section. Taking into account the instrumental resolution  $R(\hbar\omega)$  measured with a vanadium specimen of the same geometry as the  $\text{Nd}_2\text{Sn}_2\text{O}_7$  sample, we have:

$$I(q, \hbar\omega) = I_0 R(\hbar\omega) \otimes \left[ \left( \frac{d^2\sigma}{d\Omega dE} \right)_{\text{mag}} + \left( \frac{d^2\sigma}{d\Omega dE} \right)_{\text{inc}} + \left( \frac{d^2\sigma}{d\Omega dE} \right)_{\text{se}} \right] + I_{\text{bg}}, \quad (4.45)$$

where the symbol  $\otimes$  stands for the convolution product,  $I_0$  is a proportionality constant and  $I_{\text{bg}}$  is a small background contribution. The first two terms in the brackets are described by Eq. 4.42 and Eq. 4.36, respectively. The last term in the brackets is the contribution to the measured intensity arising from the sample environment, i.e. essentially the sample container, the inner calorimeter and the cryostat windows. The last two, aluminium made, have a negligible cross-section. The cross-section associated with the Cu sample holder is incoherent and is written as:

$$\left( \frac{d^2\sigma}{d\Omega dE} \right)_{\text{se}} = \frac{k_f}{k_i} \left[ \frac{N_{\text{Cu}}}{4\pi} \sigma_{\text{inc}}^{\text{Cu}} \delta(\hbar\omega) \right], \quad (4.46)$$

where  $N_{\text{Cu}}$  is the number of Cu nuclei in the sample holder part impinged by the neutron beam and  $\sigma_{\text{inc}}^{\text{Cu}}$  the Cu incoherent scattering cross-section. From the sample mass, we estimate  $\sigma_{\text{inc}}^{\text{Cu}} N_{\text{Cu}} / (\sigma_{\text{spin}}^{\text{Nd}} + \sigma_{\text{iso}}^{\text{Nd}}) N_{\text{Nd}} \approx 11\%$ . This ratio allowed us to link the amplitude of the sample environment contribution in Eq. 4.45 to that of the  $^{143}\text{Nd}$  nuclei. To finish with the quantitative analysis, a small energy offset of the spectrometer, of order  $0.03 \text{ \mu eV}$ , was an additional fitting parameter not appearing in Eq. 4.45 for the sake of simplicity. Fig. 4.10 displays examples of data recorded in the ordered and paramagnetic phases, together with the result of fits according to Eq. 4.45.

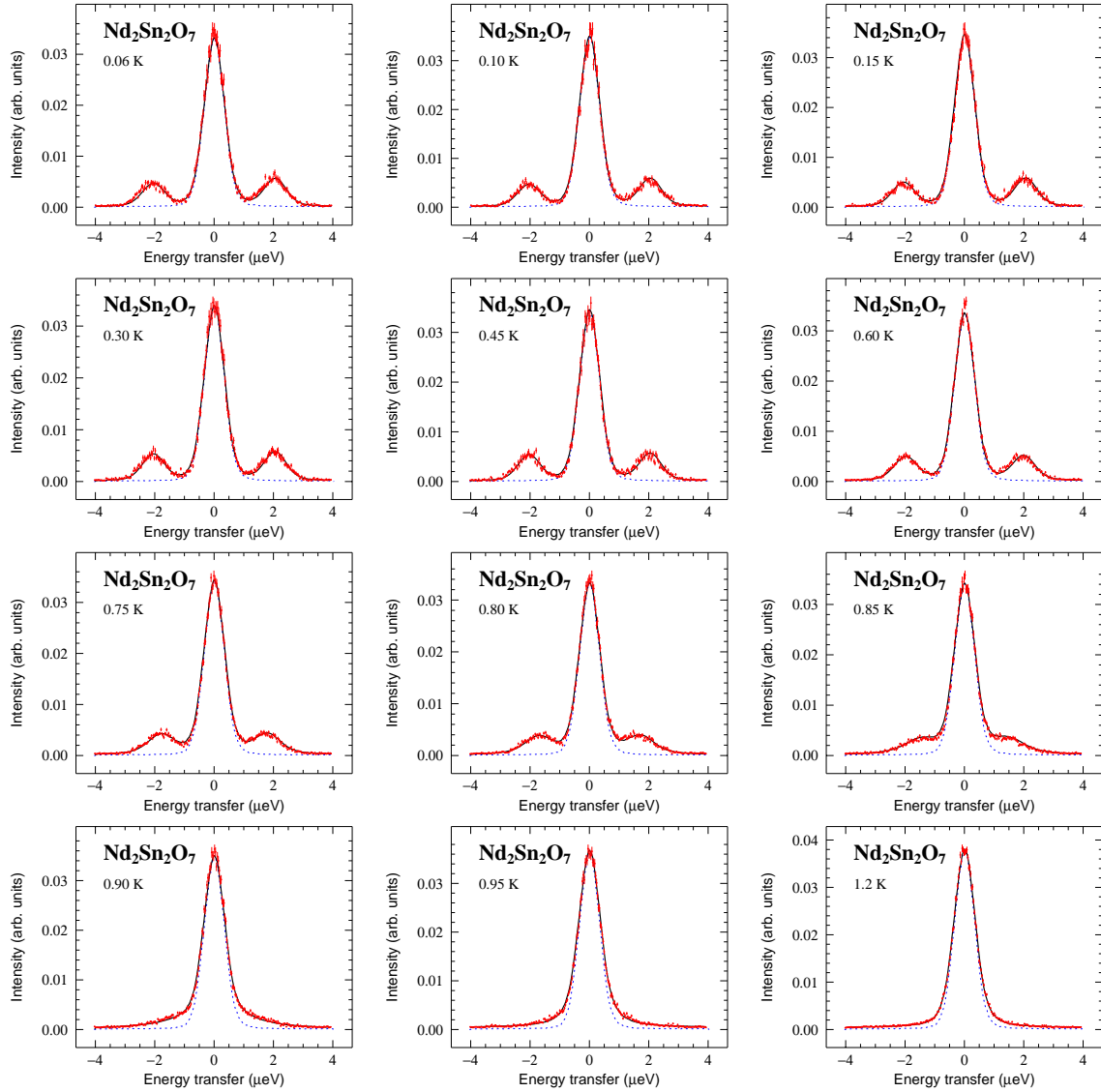


Figure 4.11: Neutron backscattering spectra recorded at selected temperatures in a  $\pm 4 \mu\text{eV}$  energy window and integrated over all the available wavevectors outside the Bragg peak region. While at 1.2 K, i.e. in the paramagnetic phase, the neutron intensity is only observed near zero energy, for  $T < T_c$  inelastic incoherent scattering from the  $^{143}\text{Nd}$  nuclei is detected. The black solid lines correspond to fits as explained in the main text, with the instrument resolution displayed by the blue dotted lines taken into account.

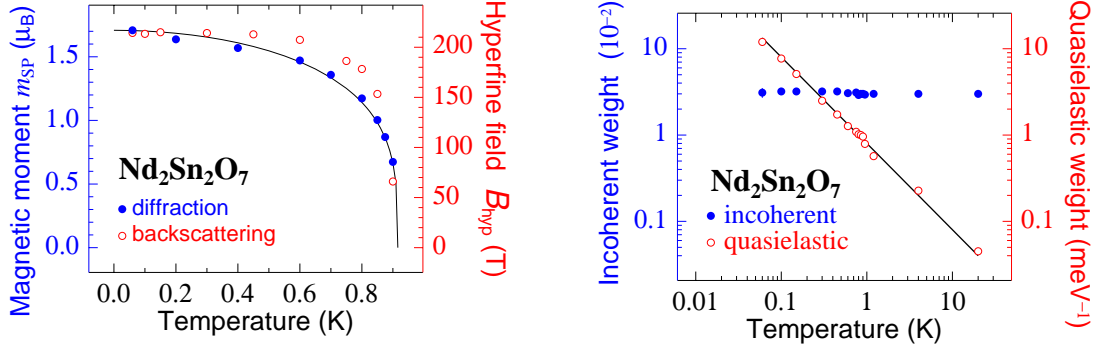


Figure 4.12: *Left: Temperature dependence of the spontaneous magnetic moment  $m_{\text{sp}}(T)$  derived from the diffraction measurements and of the hyperfine field  $B_{\text{hyp}}(T)$  obtained from the analysis of the backscattering spectra. Note that error bars are smaller than the symbols. The black solid line is a fit as explained in Sec. 4.6. Right: Temperature dependence of the weighing factors  $A_{\text{inc}}$  and  $A_{\text{mag}}$  for the incoherent nuclear and quasielastic magnetic intensities. The black solid line follows a Curie-Weiss law.*

Apart from a weak evolution of the quasielastic width in the paramagnetic phase which will be discussed below, the spectra are essentially independent of the wavevector in the available range  $0.38 - 1.95 \text{ \AA}^{-1}$ , excluding the wavevector region around the (220) Bragg peak at  $1.69 \text{ \AA}^{-1}$ . Therefore the data shown in Fig. 4.10 and Fig. 4.11 are integrated over this range. We present in Fig. 4.11 the different backscattering spectra recorded at several temperatures in order to exhibit the nuclear splitting progressively vanishing as the temperature increases. Since the magnetic moment is proportional to the nuclear splitting  $\hbar\omega_Z$ , we extract the temperature dependence of the hyperfine field  $B_{\text{hyp}}(T)$ , see left panel of Fig. 4.12. The splitting  $\hbar\omega_Z(T \rightarrow 0) = 2.027(7) \text{ \mu eV}$  corresponds to  $m_{\text{sp}}(0) = \hbar\omega_Z(0)/\mathcal{A}_{\text{hyp}}^{143} = 1.68(3) \text{ \mu}_B$ , consistent with the one found with neutron diffraction experiments, see Sec. 4.6. Since the diffraction, which measures a volume average [208], and the local probe determinations of  $m_{\text{sp}}(0)$  are in agreement, no phase segregation occurs in our sample. Surprisingly,  $B_{\text{hyp}}(T)$  does not track  $m_{\text{sp}}(T)$  when approaching  $T_c$ . Although this difference calls for a more detailed interpretation, it could be understandable that the two techniques lead to different values of  $m_{\text{sp}}(T)$ . It may originate from the difference in the time scales at which the two techniques probe the system under study. However, the explanation does not go in the right way since the interaction time between the neutron and the system is around  $10^{-12} \text{ s}$  for diffraction and  $10^{-9} \text{ s}$  for backscattering. Therefore, if the local field was fluctuating with a characteristic time comprised between the typical time scale of the two techniques, the magnetic moment inferred from backscattering measurements will be lowered compared to the one deduced from magnetic diffraction experiments. An alternative explanation may lie from differences in the temperature dependences of the  $4f$  and other electronic shell magnetic moments. While diffraction essentially probes the  $4f$  shell magnetic moment since the magnetic form factor of the delocalised  $5d$  electronic shell vanishes extremely rapidly with increasing  $Q$ , the latter electronic shell contributes to  $B_{\text{hyp}}(T)$ . In this case,  $m_{\text{sp}}(0)$  inferred from the two techniques would be different.

In addition to the incoherent nuclear contribution, a quasielastic magnetic signal

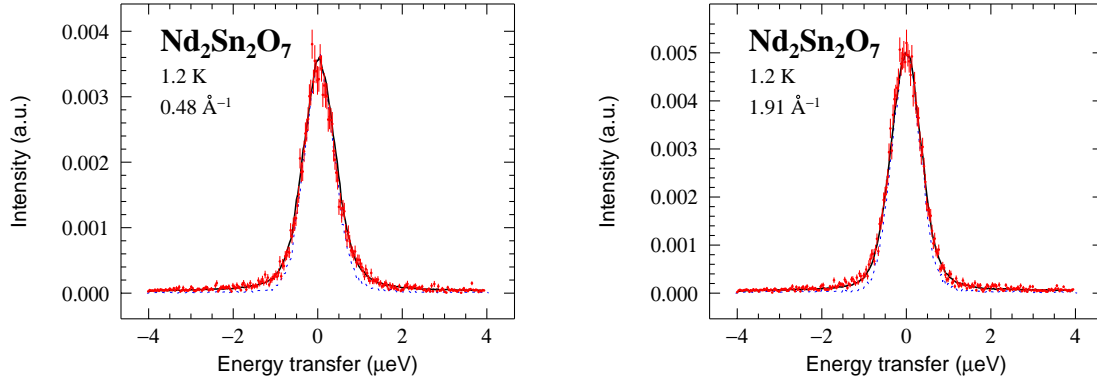


Figure 4.13: *Backscattering spectra recorded at 1.2 K for a wavevector range  $0.37 \leq q \leq 0.59 \text{ \AA}^{-1}$  centered around  $0.48 \text{ \AA}^{-1}$  (left) and for a wavevector range  $1.87 \leq q \leq 1.95 \text{ \AA}^{-1}$  centered around  $1.91 \text{ \AA}^{-1}$  (right). The full line is a fit to the data as explained in the main text and the dotted line corresponds to the resolution of the spectrometer.*

arising from the  $\text{Nd}^{3+}$  electrons is observed in neutron backscattering. Note that the internal calibration provided by the  $^{143}\text{Nd}$  incoherent nuclear scattering gives a measure of the magnetic contribution, i.e. the susceptibility, in absolute value. Therefore, we define the weight of the nuclear contribution  $A_{\text{inc}}$  and of the magnetic scattering  $A_{\text{mag}}$  as:

$$A_{\text{inc}} = I_0 N_{\text{Nd}}, \quad \text{and} \quad A_{\text{mag}} = \frac{2}{3} I_0 N_{\text{Nd}} \left[ \frac{1}{2} g J f_{\text{mag}}(q) \right]^2 \chi'(q). \quad (4.47)$$

Fitting the incoherent and quasielastic contributions to the data, see Sec. 4.7.2 and Sec. 4.7.3, we find  $A_{\text{inc}}$  to be temperature independent within experimental uncertainties, and  $A_{\text{mag}}$  decreasing as the inverse temperature, as illustrated in the right panel of Fig. 4.12. The result of the fit gives  $\chi'(q) = C/(k_{\text{B}}T)$  with  $C = 26(1)$ , i.e.  $\chi'(q)$  follows a Curie law in the investigated wavevector range.

As already mentioned, no notable  $q$  dependence was noticed for the spectra recorded in the magnetically ordered phase. In the paramagnetic phase, we observed a small broadening of the spectra at small wavevectors. It can be seen from a comparison of the spectra displayed in Fig. 4.13. The wavevector dependence of the quasielastic half-width at half-maximum  $\Gamma_q$  measured at 1.2 K is plotted in Fig. 4.14. A linear fit yields a fair description:  $\Gamma_q = \Gamma_0 + a_q q$  with  $\Gamma_0 = 0.271(9) \text{ \mu eV}$  and  $a_q = -0.070(2) \text{ \mu eV \AA}$ . To  $\Gamma_0$  is associated a fluctuation time  $\tau_0 = \hbar/\Gamma_0 = 2.43(8) \times 10^{-9} \text{ s}$ . This value is relatively large for a temperature outside the critical regime. We would have expected a value in the range of  $\hbar/(k_{\text{B}}|\theta_{\text{CW}}|) = 2.4(1) \times 10^{-11} \text{ s}$ , where we take the  $\theta_{\text{CW}}$  value derived from the  $\chi(T)$  fit at low temperatures. Even slower paramagnetic fluctuations are revealed by the  $\mu\text{SR}$  study discussed in Sec. 4.8.

## 4.8 $\mu\text{SR}$ spectroscopy

To get further information on the system,  $\mu\text{SR}$  measurements were performed at the MuSR spectrometer of the ISIS pulsed muon source (Rutherford Appleton Laboratory, United Kingdom) and at the GPS and LTF spectrometers of the Swiss Muon Source (Paul Scherrer Institute, Switzerland), see Sec. 2.6. First, we will discuss the signature

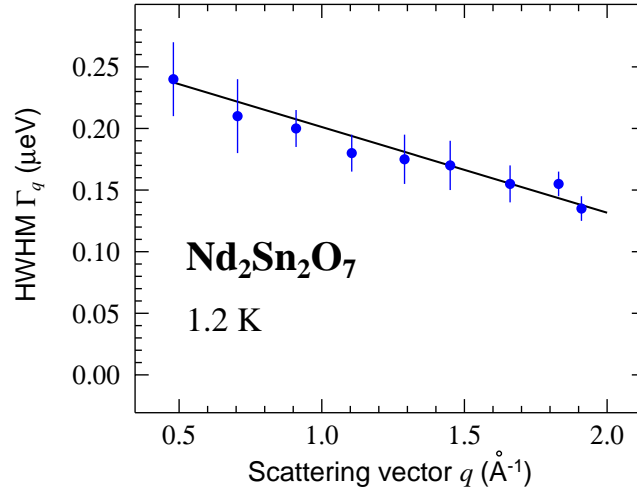


Figure 4.14: Wavevector dependence of the quasielastic half-width at half-maximum (HWHM)  $\Gamma_q$  of the magnetic scattering in the paramagnetic phase at 1.2 K. The solid black line is a fit as explained in the main text.

of a long-range order. Then, persistence of spin dynamics in the ordered phase and anomalously slow spin dynamics in the paramagnetic regime will be evidenced.

#### 4.8.1 Evidence of long-range order

A  $\mu$ SR asymmetry spectrum recorded deep into the ordered phase is displayed in the left panel of Fig. 4.15. The inset evidences the presence of spontaneous oscillations, i.e. in the absence of external magnetic field, up to  $T \leq 0.65$  K  $\approx 0.7 T_c$  which reflect the Larmor precession of the muon spin around a local magnetic field  $B_{\text{loc}}$ . This is a signature of a magnetic long-range order. Although a spontaneous muon spin precession is expected and often observed in the ordered phase of magnets as for  $\text{Gd}_2M_2\text{O}_7$  with  $M = \text{Sn}$  or  $\text{Ti}$  [112, 116], it is not present for  $\text{Tb}_2\text{Sn}_2\text{O}_7$  [75, 77],  $\text{Er}_2\text{Ti}_2\text{O}_7$  [2, 102], and  $\text{Yb}_2\text{Sn}_2\text{O}_7$  [92, 94]. In Fig. 4.16 is compared the case of  $\text{Nd}_2\text{Sn}_2\text{O}_7$  (left panel) and  $\text{Tb}_2\text{Sn}_2\text{O}_7$  (right panel) which both exhibit magnetic Bragg peaks ( $\mathbf{k}_{\text{mag}} = (0, 0, 0)$ ) as a signature of a long-range order, see magnetic neutron diffraction pattern in the insets. However, whereas spontaneous oscillations are observed in the neodymium case, only an exponential-like relaxation of the muon spin polarisation is evidenced in the case of  $\text{Tb}_2\text{Sn}_2\text{O}_7$ . In the latter case, the absence of spontaneous oscillations was explained with the dynamical nature of the local field, jumping from a configuration to another. A fluctuation time  $\tau_c = 8 \times 10^{-11}$  s was inferred, consistent with the observation of magnetic Bragg peaks with neutron diffraction since the magnetic structure is probed with a time scale  $\Delta t \approx 10^{-12}$  s.

The measured asymmetry is  $a_0 P_Z^{\text{exp}}(t)$  where  $a_0$  is an experimental parameter and  $P_Z^{\text{exp}}(t)$  the muon polarization function which reflects the physics of the compound under study [160]:

$$a_0 P_Z^{\text{exp}}(t) = a_s P_Z(t) + a_{\text{bg}}, \quad (4.48)$$

where the first term accounts for muons probing the sample and the time-independent second term reflects muons implanted in the sample surroundings, essentially in the

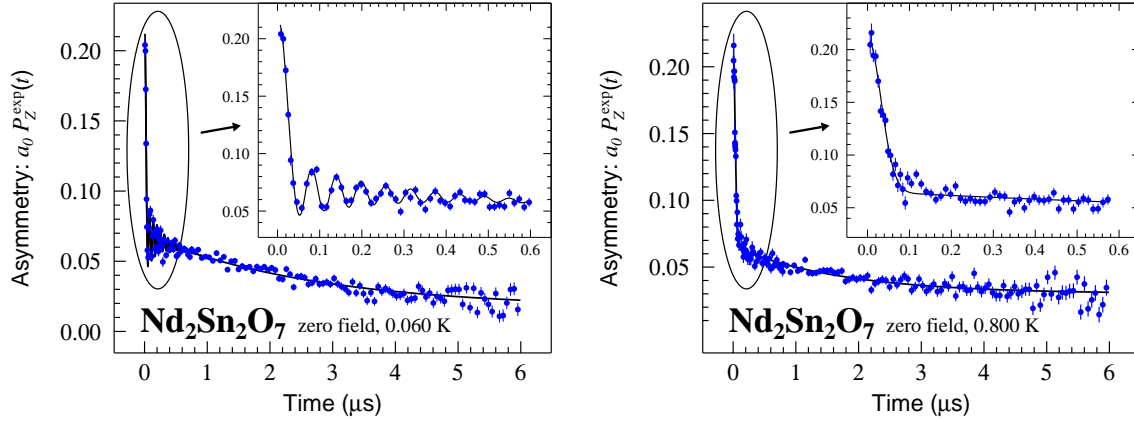


Figure 4.15:  $\mu\text{SR}$  spectra recorded for a powder sample of  $\text{Nd}_2\text{Sn}_2\text{O}_7$  at the LTF spectrometer (PSI) in zero field deep into the ordered phase at  $T = 0.06$  K (left) and at  $T = 0.800$  K (right). The insets focus on the short time details in order to evidence the presence of spontaneous oscillations or not. The black solid lines are fits as explained in the main text.

silver backing plate. Spectra up to 0.65 K were well fitted with the effective following function:

$$\begin{aligned} a_s P_Z(t) &= a_1 P_{\perp,1}(t) + a_2 P_{\perp,2}(t) + a_3 \exp(-\lambda_Z t) \\ &= a_1 \exp(-\lambda_X t) \cos(\gamma_\mu B_{\text{loc}} t + \varphi) + a_2 \exp(-\gamma_\mu^2 \Delta_X^2 t^2 / 2) + a_3 \exp(-\lambda_Z t). \end{aligned} \quad (4.49)$$

The first two terms, labelled  $P_{\perp,i}$ , refer to the component of  $P_Z(t)$  perpendicular to the local field  $B_{\text{loc}}$ . Introducing two functions can be understood as the existence of two muon sites (1, 2) probing a different field distribution. However, this equation remains a purely phenomenologic description since the muon site is not precisely known. The summation of their amplitude accounts for about 2/3 of the total amplitude. The third component of amplitude  $a_3 \simeq a_s/3$  is ascribed to the spin-lattice relaxation channel, and will be discussed in Sec. 4.8.2.

Let us focus on the components of  $P_Z(t)$  perpendicular to the local field  $B_{\text{loc}}$ . Considering an isotropic, static, Gaussian field distribution, we can easily derive the corresponding static polarisation function [160]:

$$P_{\perp}^{\text{stat}}(t) = \exp\left(-\frac{\gamma_\mu^2 \Delta_G^2 t^2}{2}\right) \cos(\gamma_\mu B_{\text{loc}} t), \quad (4.50)$$

where  $\Delta_G^2$  is the variance of the Gaussian field distribution. However, usually the field distribution is not static and assuming dynamics with a single magnetic correlation time  $\tau_c = 1/\nu_c$ , the polarisation function is described by the Abragam function within the weak collision model [160]:

$$P_{\perp}(t) = \exp\left\{-\frac{\gamma_\mu^2 \Delta_G^2}{\nu_c^2} [\exp(-\nu_c t) - 1 + \nu_c t]\right\} \cos(\gamma_\mu B_{\text{loc}} t). \quad (4.51)$$

In the so-called motional narrowing limit, i.e.  $\nu_c \gg \gamma_\mu \Delta_G$ , we retrieve the first term of the right-hand side of Eq. 4.49:

$$P_{\perp,1}(t) = \exp(-\lambda_X t) \cos(\omega_\mu t), \quad (4.52)$$

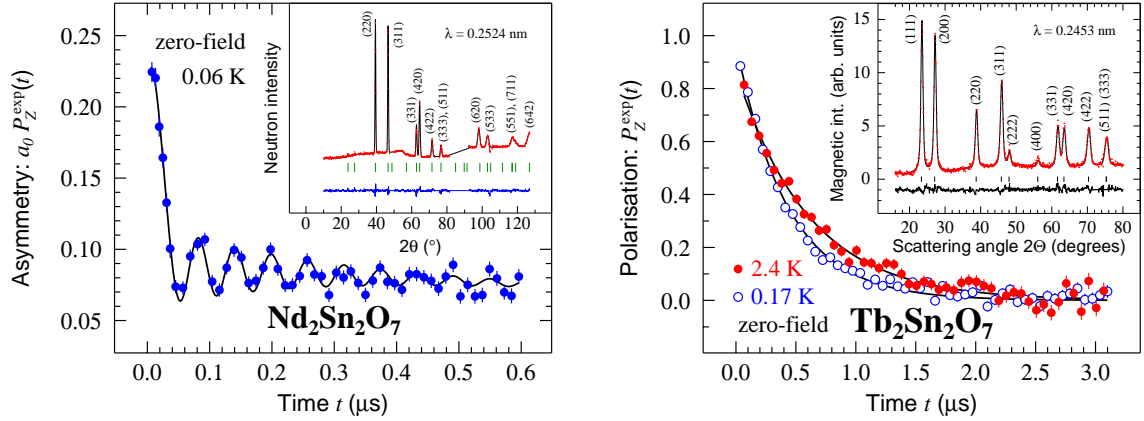


Figure 4.16: Comparison of  $\mu$ SR spectra of  $\text{Nd}_2\text{Sn}_2\text{O}_7$  (left) and  $\text{Tb}_2\text{Sn}_2\text{O}_7$  (right) recorded in the ordered phase. The two compounds exhibit magnetic Bragg peaks with  $\mathbf{k}_{\text{mag}} = (0, 0, 0)$  (see insets). However, spontaneous oscillations are resolved for  $\text{Nd}_2\text{Sn}_2\text{O}_7$  whereas only an exponential relaxation of the muon spin polarisation is observed for  $\text{Tb}_2\text{Sn}_2\text{O}_7$ . Right panel is adapted from Ref. [75].

where the damping rate is  $\lambda_X = \gamma_\mu^2 \Delta_G^2 \tau_c$  and  $\omega_\mu = \gamma_\mu B_{\text{loc}}$ . By analogy with NMR (nuclear magnetic resonance), the transverse relaxation rate  $\lambda_X$  is also called spin-spin relaxation rate since the surrounding spins at the origin of the field distribution and their dynamics lead to a spread in muon frequencies. We have found  $\lambda_X \approx 45 \mu\text{s}^{-1}$  at low temperatures. The cosine function describes the Larmor precession of the muon spin around this local field. The observation of these oscillations implies that the magnitude of the field  $B_{\text{loc}}$  at muon site (1) is sufficiently large relative to the field distribution width.

On the other hand, in the case of  $\nu_c \ll \gamma_\mu \Delta_G$ , Eq. 4.51 becomes:

$$\begin{aligned}
 P_{1,2}(t) &= \exp\left(-\frac{\gamma_\mu^2 \Delta_G^2 t^2}{2}\right) \cos(\omega_\mu t), \\
 &= \exp\left(-\frac{\gamma_\mu^2 \Delta_G^2 t^2}{2}\right),
 \end{aligned} \tag{4.53}$$

where the second line is obtained considering the field distribution of the local field at the muon site (2) to be sufficiently large to not resolve any spontaneous oscillations, i.e.  $\Delta_G \gg \omega_\mu / \gamma_\mu$ . Hence, we recognise the second term of the right-hand side of Eq. 4.49 with  $\Delta_X = \Delta_G$ . This second component is necessary in order to describe the fast depolarisation of  $a_0 P_Z^{\text{exp}}(t)$  at short times. The temperature dependence of  $\Delta_X$  and  $B_{\text{loc}}$  are displayed in the left and right panels of Fig. 4.17, respectively, together with the temperature dependence of the magnetic moment inferred from magnetic diffraction. We found  $B_{\text{loc}}(T \rightarrow 0) = 127.5(1.3)$  mT and  $\Delta_X(T \rightarrow 0) = 84.7(6.6)$  mT. Since these quantities arise from the spin distribution at the muon site, this is not surprising that they follow the same temperature behaviour as the magnetic moment.

For completeness, oscillations are not resolved for  $T \geq 0.65$  K, as shown in the right panel of Fig. 4.15. This is probably due to the broadening of the field distribution arising from sample inhomogeneities and dynamical effects. Therefore, spectra are analysed

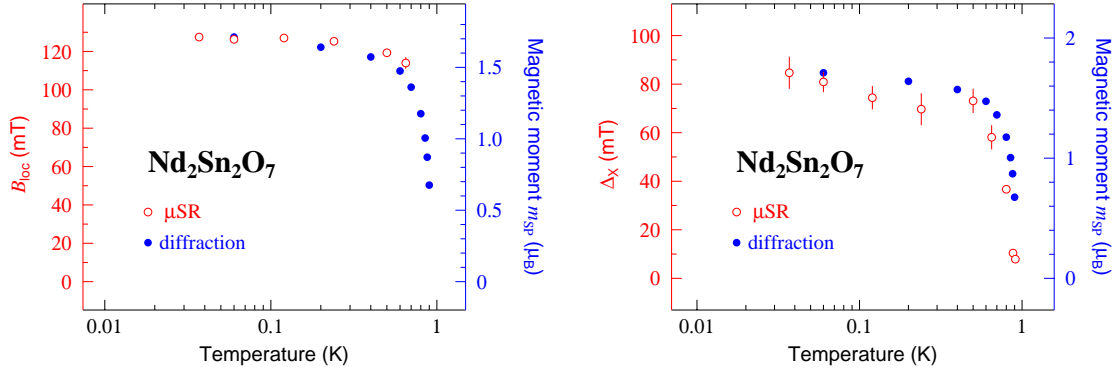


Figure 4.17: Temperature dependence of the local field inferred from the oscillations frequency at muon site 1 (left) and of the variance of the field distribution  $\Delta_X$  (right). The temperature variation of the magnetic moment inferred from magnetic diffraction is displayed by full blue circles.

with the following function:

$$a_s P_Z(t) = a_X \exp(-\gamma_\mu^2 \Delta_X^2 t^2 / 2) + a_3 \exp(-\lambda_Z t), \quad (4.54)$$

where  $a_X = \frac{2}{3} a_S$ .

Note that a phase  $\varphi \approx -135^\circ$  has been introduced in the cosine function of Eq. 4.49. The magnetic collinear structures are usually associated with a single value of  $B_{\text{loc}}$ , proportional to the magnetic moment and no phase shift should be introduced. However, an incommensurate modulation of the amplitude of the field could introduce a shift of the oscillations, as it is the case for instance for incommensurate magnetic structure. In Ref. [160], a generalised field distribution has been developed to control the phase shift  $\varphi$ . Note that it was pointed out that such a field distribution is not necessarily a signature of an incommensurate magnetic structure, which would be incompatible with the collinear all-in-all-out structure evidenced in Sec. 4.6. In our case, the following field distribution leads to  $\varphi = -\frac{3\pi}{4}$ :

$$D_c(B_{\text{loc}}) = \frac{[1 - (B_{\text{loc}}/B_{\text{max}})^2]^{1/2}}{\pi^{1/2} \Gamma(1/2) B_{\text{max}}}, \quad (4.55)$$

where  $B_{\text{loc}}$  is modulated between  $-B_{\text{max}} \leq B_{\text{loc}} \leq B_{\text{max}}$ . This possible field distribution is illustrated in Fig. 4.18. This will lead to the polarisation function:

$$a_s P_Z(t) = a_1 \left( \frac{2}{\gamma_\mu B_{\text{max}} t} \right) J_1(\gamma_\mu B_{\text{max}} t) + a_2 \exp(-\lambda_Z t), \quad (4.56)$$

where  $J_1$  is a Bessel function of the first kind. Note that for  $t \gg 1/(\gamma_\mu B_{\text{max}})$ , the latter function can be expanded such as:

$$J_1(\gamma_\mu B_{\text{max}} t) \approx \sqrt{\frac{2}{\pi \gamma_\mu B_{\text{max}} t}} \cos\left(\gamma_\mu B_{\text{max}} t - \frac{3\pi}{4}\right), \quad (4.57)$$

and we recover the phase shift  $\varphi = -\frac{3\pi}{4}$  introduced above. More information is needed to understand the field distribution leading to the observed muon spin polarisation

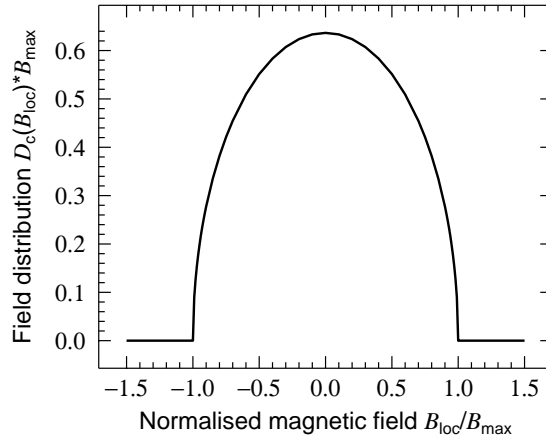


Figure 4.18: *Illustration of the possible field distribution at the muon site (1), depicted by Eq. 4.55.*

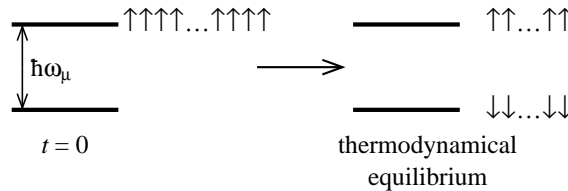


Figure 4.19: *Illustration of the Zeeman splitting of the two muon spin states. From a fully polarised state, the system relaxes towards an equilibrium state where the two muon states are equally populated. Reproduced with kind permission from Ref. [160].*

function. It is important to keep in mind that Eq. 4.49 is a phenomenological equation to analyse at best our data, since introducing two muon sites probing two different field distributions is purely speculative and just accounts well spectra in the ordered phase. The next step would be to calculate the actual muon site and simulate the field distribution created by our magnetic structure to derive a true polarisation function, since no usual ones derived from standard field distributions could describe our spectra. Due to the positive electric charge, the muon should be located in a site close to an oxygen atom.

### 4.8.2 Persistence of spin dynamics

We will focus here on the third term of Eq. 4.49. The spin-lattice relaxation rate  $\lambda_Z$  arises from exchange energy between the muon spin and the system. The spin muon state is a two-level system (up and down) with a Zeeman splitting of  $\hbar\omega_\mu = \hbar\gamma_\mu B_{\text{loc}} \approx 70$  neV where  $B_{\text{loc}} = 127.5$  mT at 37 mK. At thermodynamical equilibrium the two states are equally populated as shown in Fig. 4.19 and  $\lambda_Z$  illustrates the relaxation from the initial polarised muon state to this equilibrium. This is a direct probe of the spin dynamics in the system. The temperature dependence of the spin-lattice relaxation rate is displayed in Fig. 4.20, in zero field and 50 mT longitudinal field. At  $T \ll T_c$  we would expect  $\lambda_Z$  to vanish, see App. E.2. Nevertheless, a temperature independent

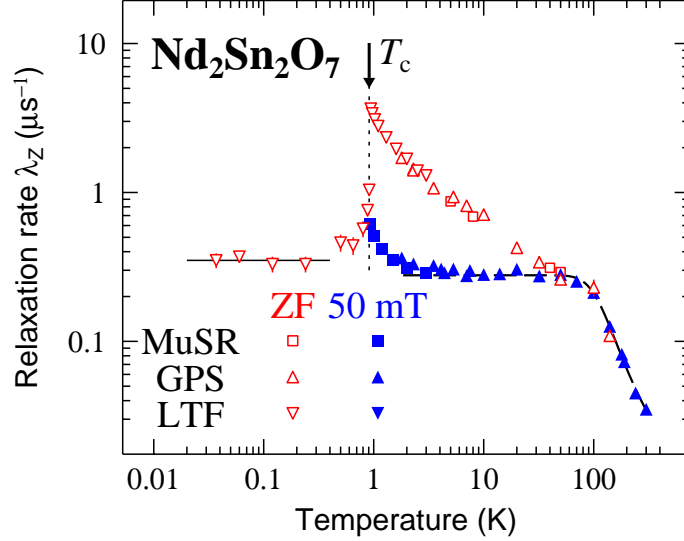


Figure 4.20: Temperature dependence of the spin lattice relaxation rate  $\lambda_Z$  in zero field (empty symbols) and for  $B_{\text{ext}} = 50 \text{ mT}$  (full symbols). The data have been recorded at different spectrometers as indicated in the figure. The  $T_c$  value is shown as a dotted line and the full line emphasises the temperature independent zero-field  $\lambda_Z$  at low temperatures. The dashed line is a fit of Eq. 4.72 to the data, illustrating an Orbach relaxation mechanism, see Fig. 4.21, and involving the third excited crystal-electric-field energy level lying at 39.8 meV.

plateau is observed in the ordered phase. Since the muon energy  $\hbar\omega_\mu \approx 70 \text{ neV}$  for  $\text{Nd}_2\text{Sn}_2\text{O}_7$  is much lower than any energy gap expected for excitations in the ordered phase, a single excitation cannot be at the origin of the muon spin relaxation process. Therefore, this relaxation is described by a Raman process, i.e. a two excitation scattering, see Fig. E.1. In App. E.2, we have derived the expression of the spin lattice relaxation rate for the case of ferromagnetic and antiferromagnetic magnons, see Eq. E.39 and Eq. E.54, respectively. We have shown that these conventional excitations in the ordered phase cannot be at the origin of a temperature independent behaviour of  $\lambda_Z$ . For the description of the excitations at the origin of this plateau, we generalise Eq. E.54:

$$\lambda_Z = \mathcal{C} \int_{\Delta}^{\infty} n\left(\frac{E}{k_B T}\right) \left[ n\left(\frac{E}{k_B T}\right) \pm 1 \right] g_m^2(E) dE, \quad (4.58)$$

where  $\mathcal{C}$  is a temperature independent constant involving the coupling tensor between the muon spin and the spins of the systems. Whereas the excitations are bosonic (+) or fermionic (-), we introduce  $n(x)$  the Bose-Einstein or Fermi-Dirac distribution functions, respectively. We recall that:

$$\begin{aligned} n_{\text{BE}}\left(\frac{E}{k_B T}\right) &= \frac{1}{\exp\left(\frac{E-\mu}{k_B T}\right) - 1}, \\ n_{\text{FD}}\left(\frac{E}{k_B T}\right) &= \frac{1}{\exp\left(\frac{E-E_F}{k_B T}\right) + 1}, \end{aligned} \quad (4.59)$$

where  $E_F$  and  $\mu$  accounts for the energy Fermi level and the chemical potential of bosons, respectively. Note that in the case of magnons or photons the chemical potential  $\mu = 0$  since we do not need to limit the number of bosons. To these excitations are associated a magnetic density of states  $g_m(E)$  and an energy gap  $\Delta$ . To get  $\lambda_Z$  temperature independent, we need  $g_m(E) = bE^{-1/2}$  and  $(\Delta - E_F)$  or  $(\Delta - \mu)$  proportional to temperature, i.e. equal to  $ak_B T$ , where  $a$  and  $b$  are finite constants. For the bosonic case, within the approximation  $(E - \mu) \ll k_B T$ , we derive [112]:

$$\lambda_Z = \frac{Cb^2}{a^2}. \quad (4.60)$$

The inverse square root form for  $g_m(E)$  needs to be verified only at low energy. Expressing  $g_m(E)$  in terms of the spin correlation function  $\langle \mathbf{J}(\mathbf{q}, t) \mathbf{J}(-\mathbf{q}, 0) \rangle$  we obtain in the case where a single energy mode is available for a given  $\mathbf{q}$  wavevector:

$$g_m(E) = \sum_{\mathbf{q}} \int_{-\infty}^{\infty} \frac{\langle \mathbf{J}(\mathbf{q}, t) \cdot \mathbf{J}(-\mathbf{q}, 0) \rangle}{\langle \mathbf{J}(\mathbf{q}, 0) \cdot \mathbf{J}(-\mathbf{q}, 0) \rangle} \exp\left(\frac{iEt}{\hbar}\right) \frac{dt}{2\pi\hbar}. \quad (4.61)$$

The sum runs over the first Brillouin zone vectors. We recall that:

$$\langle \mathbf{J}(\mathbf{q}, t) \cdot \mathbf{J}(-\mathbf{q}, 0) \rangle = \sum_i \exp(-i\mathbf{q} \cdot \mathbf{i}) \langle \mathbf{J}_0(t) \cdot \mathbf{J}_i(0) \rangle, \quad (4.62)$$

where  $\mathbf{J}_i$  and  $\mathbf{J}_0$  are the spins at the lattice point  $i$  and at the origin of the lattice, respectively. Since muons probe the very low energy spin excitations it is justified to consider the correlation function at long times. In this limit it is governed by a diffusion equation for a Heisenberg Hamiltonian system, [209–211]:

$$\langle \mathbf{J}_0(t) \cdot \mathbf{J}_i(0) \rangle \propto 1/(D_{\text{diff}}|t|)^{d/2} \quad (4.63)$$

where  $d$  is the dimensionality of the spin system and  $D_{\text{diff}}$  a diffusion coefficient. We calculate the following Fourier transform:

$$\int_{-\infty}^{\infty} \exp(i\omega t) \frac{1}{\sqrt{t}} dt = \sqrt{\frac{2\pi}{\omega}} = \sqrt{\frac{2\pi\hbar}{E}}. \quad (4.64)$$

It follows that for a magnetic density of states  $g_m(E) \propto E^{-\frac{1}{2}}$  corresponds unidimensional spin correlations ( $d = 1$ ), at the origin of the observation of a temperature independent behaviour of  $\lambda_Z$ . We tentatively associate the low energy unidimensional excitations inferred from the temperature independent relaxation rate to loop spin structures. An illustration for a possible spin loop structure running on an hexagonal plaquette is displayed in the left panel of Fig. 4.21. This reminds the introduction of flippable plaquette to describe the quantum spin-ice state, see Sec. 1.4.

### 4.8.3 $\lambda_Z$ behaviour in the paramagnetic phase

In the case of a static isotropic Gaussian field distribution with a variance  $\Delta_G^2$ , the longitudinal polarisation function is described by the well-known Kubo-Toyabe function [160]:

$$P_Z^{\text{stat}}(t) = \frac{1}{3} + \frac{2}{3}(1 - \gamma_\mu^2 \Delta_G^2 t^2) \exp\left(-\frac{\gamma_\mu^2 \Delta_G^2 t^2}{2}\right) \quad (4.65)$$

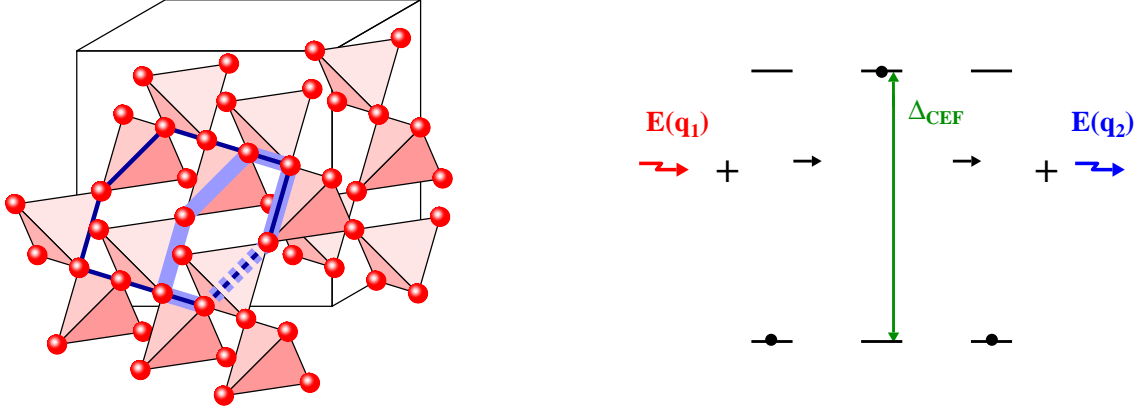


Figure 4.21: Left: Rare-earth ion lattice in the pyrochlore  $R_2M_2O_7$ . The thicker light blue (thinner dark blue) bold line represents a 6 (10)-site loop accounting for 1-dimensional excitation possibly responsible for the non vanishing spin-lattice relaxation rate at low temperatures. Reprinted figure with permission from Ref. [212]. Copyright 2015 by the American Physical Society. Right: Illustration of the Orbach relaxation mechanism resulting from the magnetoelastic coupling between the rare earth ion and two real phonons and involving an excited crystal-electric-field energy level. A magnetic ion lies in the doublet ground state defined by two wavefunctions  $|\Psi_+^0\rangle$  and  $|\Psi_-^0\rangle$ . Direct transitions are forbidden between these wavefunctions of the Kramers doublet, i.e.  $\langle\Psi_\pm^0|J_\pm|\Psi_\pm^0\rangle = 0$ . Therefore, a phonon of energy  $E(q_1)$  is absorbed, exciting the magnetic ion in an excited CEF state, located here at  $\Delta_{\text{CEF}} = 38.9$  meV, see Sec. 4.4. Emitting a phonon of energy  $E(q_2) = E(q_1)$ , the magnetic ion relaxes to the ground state. Therefore, the relaxation process of the magnetic ion from the state  $|\Psi_+^0\rangle$  to  $|\Psi_-^0\rangle$  involves a flip of the muon spin. Since both the muon spin states and the crystal-electric-field ground state are not split by Zeeman effect (in the paramagnetic regime), the relaxation of the muon spin is a zero energy process. Picture adapted from Ref. [160].

In the extreme motional narrowing limit, we derive:

$$P_Z(t) = \exp(-\lambda_Z t), \quad (4.66)$$

where  $\lambda_Z = 2\gamma_\mu^2 \Delta_G^2 \tau_c$ . In the case where a continuous distribution of relaxation channels is involved, the stretched exponential function needs to be introduced:

$$P_Z(t) = \exp[-(\lambda_Z t)^{\beta_{\text{se}}}], \quad (4.67)$$

where  $0 < \beta_{\text{se}} \leq 1$ . Above  $T_c$ , spectra are well accounted with Eq. 4.67 with here  $0.7 \leq \beta_{\text{se}} \leq 1$ . We refer to Sec. 4.8.4 for a discussion on the field behaviour of  $\lambda_Z$ . In zero field  $\lambda_Z(T)$  displays a pronounced maximum at  $T_c$ . This reflects the slowing down of the critical fluctuations at the approach of a second-order magnetic phase transition. We now focus our attention on the behaviour of  $\lambda_Z$  above the magnetic transition. The general expression of  $\lambda_Z$  is given by Eq. E.16. Thanks to the fluctuation-dissipation theorem, paramagnetic fluctuations described by the symmetrised spin correlation function  $\Lambda^{\alpha\beta}(\mathbf{q}, \omega)$ , see Eq. E.14, are related to the generalised susceptibility  $\chi^{\alpha\beta}(\mathbf{q}, \omega)$  [213]:

$$\Lambda^{\alpha\beta}(\mathbf{q}, \omega) = \frac{\hbar v_c}{\mu_0 g^2 \mu_B^2} \coth\left(\frac{\hbar\omega}{k_B T}\right) \mathcal{I}m\{\chi^{\alpha\beta}(\mathbf{q}, \omega)\}$$

$$= \frac{2k_{\text{B}}T v_c \mathcal{I}m\{\chi^{\alpha\beta}(\mathbf{q}, \omega)\}}{\mu_0 g^2 \mu_{\text{B}}^2 \omega} \quad (4.68)$$

where the second line has been obtained in the limit  $\hbar\omega \ll k_{\text{B}}T$ , valid since the Zeeman splitting of the two spin muon states is  $\hbar\omega_{\mu} = 0$  in zero field experiments, i.e. only zero energy transfers are probed by the spin-lattice relaxation rate. Following the definition introduced for the imaginary part of the generalised susceptibility ( $\mathcal{I}m\{\chi^{\alpha\beta}(\mathbf{q}, \omega)\} = \chi''(\mathbf{q}, \omega)$ ), see Eq. 4.44, and assuming the susceptibility to be isotropic, the spin correlation tensor becomes scalar, i.e.  $\Lambda^{\alpha\beta}(\mathbf{q}, \omega) = \Lambda(\mathbf{q}, \omega)\delta_{\alpha,\beta}$ :

$$\Lambda(\mathbf{q}, \omega) = \frac{2v_c}{\mu_0 g^2 \mu_{\text{B}}^2} k_{\text{B}}T \chi'(\mathbf{q}) \frac{\Gamma_q}{\omega^2 + \Gamma_q^2}, \quad (4.69)$$

where  $\Gamma_q$  is the linewidth of a Lorentzian function describing the quasielastic excitations, i.e. the spin correlation function decreases exponentially. Since  $\lambda_Z$  probes here zero energy excitations, Eq. 4.69 becomes:

$$\Lambda(\mathbf{q}, \omega = 0) = \frac{2v_c}{\mu_0 g^2 \mu_{\text{B}}^2} k_{\text{B}}T \frac{\chi'(\mathbf{q})}{\Gamma_q} \quad (4.70)$$

In the paramagnetic regime at high temperature, the susceptibility is expected not to depend on  $\mathbf{q}$ , i.e.  $\chi'(\mathbf{q}) = \chi'$ , since the thermal energy is much higher than the exchange energy [213]. Within this approximation, only the spin autocorrelation function is probed, i.e.  $\Gamma_q = \Gamma$  and it is also temperature independent meaning that the characteristic time of the spin correlations is temperature independent. Therefore Eq. E.16 simplifies as:

$$\lambda_Z = \frac{\mathcal{D}}{2} \frac{2v_c}{\mu_0 g^2 \mu_{\text{B}}^2} \frac{k_{\text{B}}T}{\Gamma} \chi' \int_{v_{\text{c}}} \sum_{\beta,\gamma} \mathcal{A}^{\beta\gamma}(\mathbf{q}) \frac{d^3\mathbf{q}}{(2\pi^3)} \quad (4.71)$$

Since the susceptibility is expected to follow a Curie-Weiss law, the spin lattice relaxation rate should be found temperature independent, as it is the case for the gallium garnet compound  $\text{Yb}_3\text{Ga}_5\text{O}_{12}$  [192]. A temperature independent behaviour of the spin lattice relaxation rate appears when applying a small magnetic field  $B_{\text{ext}} = 50$  mT in the range  $2 \leq T \leq 100$  K, see Fig. 4.20. However, no plateau is evidenced in zero field measurements. This is due to the development of spin correlations in the low temperature region of the paramagnetic regime which unexpectedly extends up to about 30 K, i.e.  $\approx 30 T_{\text{c}}$ . The strong dependence of the relaxation rate on  $B_{\text{ext}}$  will be discussed in the next section.

An Orbach local relaxation mechanism [192] could be at the origin of an inflexion point located at  $\approx 100$  K, i.e. the relaxation of the magnetic moments through a real two-phonons process with an excited crystal-electric-field as intermediate state as explained and illustrated in the right panel of Fig. 4.21. Following Ref. [192], data are described by the following equation:

$$\lambda_Z^{-1} = A + B_{\text{me}} \exp\left[\frac{-\Delta_{\text{CEF}}}{k_{\text{B}}T}\right], \quad (4.72)$$

where  $\Delta_{\text{CEF}} = 39.8$  meV is the energy splitting between the ground state and the third excited crystal-electric-field energy level<sup>4</sup> revealed in Sec. 4.4,  $A$  is the saturation

<sup>4</sup>Analysis using other CEF energy levels leads to a worse  $\chi^2$ .

value of  $\lambda_Z^{-1}$  expected at low temperatures in the paramagnetic regime, and  $B_{me}$  refers to the strength of the spin-lattice interaction. We find  $B_{me} = 118(6) \mu\text{s}$  and  $A^{-1} = 0.28(1) \mu\text{s}^{-1}$ , which is the plateau value inferred from longitudinal field measurements.

#### 4.8.4 Anomalously slow paramagnetic fluctuations

In order to evaluate the characteristic time of the magnetic fluctuations in the paramagnetic phase, experiments in longitudinal field geometry are performed. Within the approximation that the applied magnetic field has no influence on the system, in the extreme motional narrowing limit, i.e.  $\nu_c \gg \gamma_\mu \Delta_G$  where  $\nu_c$  is the characteristic spin fluctuations rate and  $\Delta_G^2$  the variance of the Gaussian field distribution at the muon site, the spin-lattice relaxation rate is given by the Redfield formula [214]:

$$\begin{aligned} \lambda_Z(\omega_\mu = \gamma_\mu B_{\text{ext}}) &= \frac{2\gamma_\mu^2 \Delta_G^2 \nu_c}{\omega_\mu^2 + \nu_c^2}, \\ \Leftrightarrow \frac{\lambda_Z(\omega_\mu = \gamma_\mu B_{\text{ext}})}{\Delta_G^2} &= \frac{2\nu_c}{B_{\text{ext}}^2 + \left(\frac{\nu_c}{\gamma_\mu}\right)^2}. \end{aligned} \quad (4.73)$$

Spectra recorded in the paramagnetic phase in zero or longitudinal field geometry were analysed with the stretched exponential function introduced in Eq. 4.67. The results of the fits at  $B_{\text{ext}} = 50 \text{ mT}$  are displayed in Fig. 4.20. From backscattering experiments, we have found a fluctuation time  $\tau_0 \approx 2 \times 10^{-9} \text{ s}$ . Following the second line of Eq. 4.73, the field dependence of the spin-lattice relaxation rate  $\lambda_Z(B_{\text{ext}})$  is expected to be a Lorentzian function with a half width at half maximum (HWHM)  $\nu_0/\gamma_\mu$  at 1.2 K, as displayed in Fig. 4.22. Therefore, the expected value of  $\lambda_Z^{\text{exp}}$  at low field should be very close to the zero-field value. Surprisingly, this small magnetic field of 50 mT strongly modifies the response of the system. Its influence extends up to about 30 K, i.e.  $\approx 30 T_c$ . Because of this strong  $B_{\text{ext}}$  dependence of  $\lambda_Z$  at low field for  $2 < T < 30 \text{ K}$ , we infer the presence of spin fluctuations with a correlation time  $\tau_c$  in the 100 ns range. The field dependence of the spin-lattice relaxation rate  $\lambda_Z$  has been performed for several temperatures, see Fig. 4.23. Data were analysed using the first line of Eq. 4.73 with an additional constant  $\lambda_{Z,0}$  and the results are summed up in Tab. 4.5. They confirmed the 100 ns time scale of the paramagnetic fluctuations introduced above. In

T (K)	$\tau_c$ ( $\mu\text{s}$ )	$\Delta_G$ (mT)	$\lambda_{Z,0}$ ( $\mu\text{s}^{-1}$ )
2	0.32(3)	1.64(41)	0.211(20)
2.3	0.28(4)	1.72(14)	0.321(28)
5	0.3(5)	1.12(9)	0.197(8)
20	0.12(2)	1.03(11)	0.190(12)

Table 4.5: Results of the analysis of the field dependence of  $\lambda_Z$ . The correlation time  $\tau_c = 1/\nu_c$ , the variance of the field distribution  $\Delta_G^2$  and  $\lambda_{Z,0}$  are reported here.

the inset of the left panel of Fig. 4.23 is shown a possible maximum around 0.002 mT. We should expect a slowing down of the spin fluctuations as the field increases, and

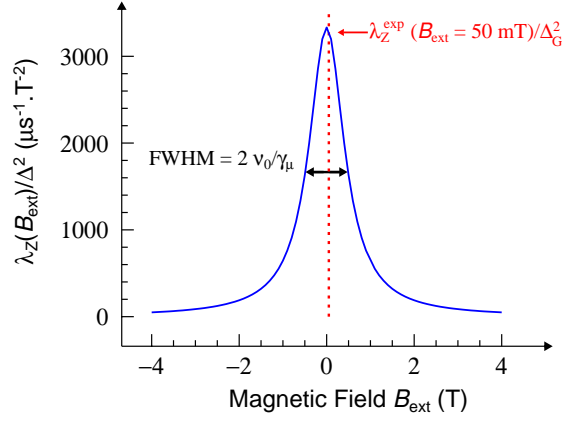


Figure 4.22: Field dependence of the spin-lattice relaxation rate at 1.2 K modelled with a Lorentzian function with a HWHM of  $\nu_0/\gamma_\mu = 0.49$  T expected from backscattering measurements where a fluctuation time  $\tau_0 \approx 2.4 \times 10^{-9}$  s has been inferred. Therefore, as shown by the red dotted line, the influence of a small magnetic field, i.e.  $B_{\text{ext}} = 50$  mT should not influence the value of  $\lambda_Z$ . This is not the case experimentally, referring to Fig. 4.20.

therefore a decrease of  $\lambda_Z$ . A low-field maximum has already been reported for instance in  $\text{Tb}_2\text{Sn}_2\text{O}_7$  [75] and  $\text{Tb}_2\text{Ti}_2\text{O}_7$  [215], but also in the spinel compound—the magnetic ions form the same lattice of corner-sharing tetrahedra as in the pyrochlore compounds —  $\text{CdHo}_2\text{S}_4$  [212], the gallium garnet compound  $\text{Yb}_3\text{Ga}_5\text{O}_{12}$  [192] or the Kagome antiferromagnet  $\text{Nd}_3\text{Ga}_5\text{SiO}_{14}$  [216]. An avoided level-crossing resonance might be at play [217]. However, this maximum was neglected in the analysis with a Lorentzian function. Above 0.2 T, a slight increase is observed associated with crystal-electric-field effect (not shown).

Hence, the zero-field fluctuations probed by  $\mu$ SR are characterised by  $\tau_c$  much larger than the time estimated from our quasielastic neutron scattering data, i.e.  $\tau_0$ .  $\text{Nd}_2\text{Sn}_2\text{O}_7$  is not a unique example of this feature [85]. In fact, a wide range of correlation times

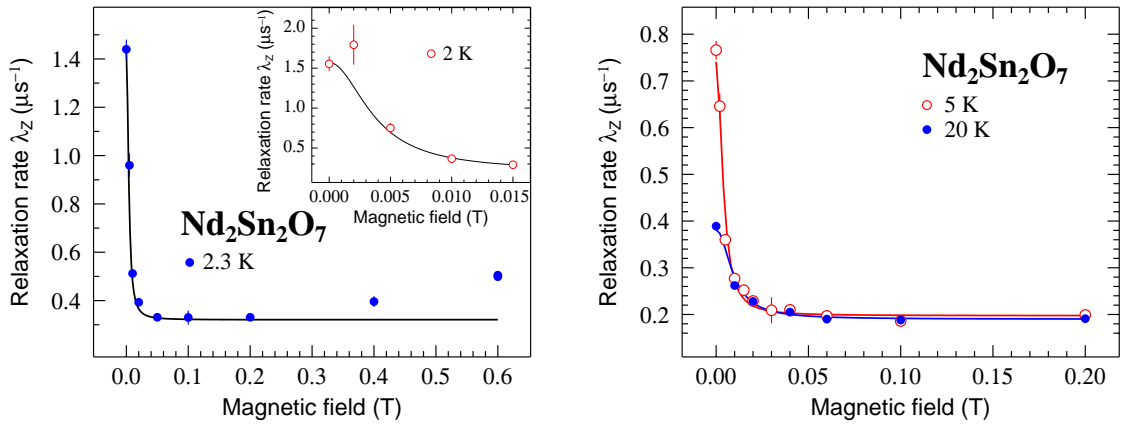


Figure 4.23: Field dependence of  $\lambda_Z$  at 2 and 2.3 K (left) and 5 and 20 K (right). Solid lines are fits following Eq. 4.73 with an additional constant  $\lambda_{Z,0}$ .

seems to be a signature of geometrically frustrated magnetic materials.

## 4.9 Conclusions

$\text{Nd}_2\text{Sn}_2\text{O}_7$  crystallises in the  $\text{Fd}\bar{3}m$  crystallographic structure. It belongs to the geometrically frustrated magnetic family of the pyrochlore compounds where the frustrated lattice consists of magnetic ions sitting on a corner-shared tetrahedra network. No deviation of the stoichiometry has been shown by high resolution neutron diffraction attesting the good quality of our sample.  $\text{Nd}_2\text{Sn}_2\text{O}_7$  exhibits a second order magnetic phase transition at  $T_c = 0.91$  K. Neutron time-of-flight measurements have revealed an isolated Kramers ground state doublet. No residual entropy was found at low temperatures, contrary to the spin-ice compound family. The study of magnetic susceptibility allows to extract a Curie-Weiss temperature much larger than the transition temperature, which is not surprising in frustrated magnets, and predominant antiferromagnetic interactions at play between the rare-earth ions. A long-range order has been evidenced with the presence of spontaneous oscillations by zero-field  $\mu\text{SR}$  measurements and magnetic neutron diffraction experiments reveal an all-in-all-out magnetic structure with a spontaneous magnetic moment at low temperatures  $m_{\text{SP}}(T \rightarrow 0) \approx 1.7 \mu_{\text{B}}$ . From neutron backscattering measurements, we confirm the value of the spontaneous magnetic moment at low temperatures as a proof of the absence of phase segregation in the sample, but its temperature variation does not track the one inferred from magnetic diffraction. No reliable interpretation can explain this difference yet. The time range probed by this technique does not allow to exhibit the presence of spin dynamics in the ordered phase whereas a spin correlation time  $\tau_0 \approx 10^{-9}$  s is found in the paramagnetic phase. With  $\mu\text{SR}$  experiments, a strong influence of a small longitudinal applied magnetic field  $B_{\text{ext}} = 50$  mT on the temperature variation of the spin-lattice relaxation rate  $\lambda_Z$  was not expected and is a signature of magnetic fluctuations with a correlation time of order 100 ns in the paramagnetic phase. Interestingly, the persistence of spin dynamics in the ordered phase as evidenced by the temperature independent plateau in zero-field measurements was ascribed to 1-dimensional spin fluctuations. The  $T^3$  dependence of the specific heat at low temperatures and the  $T^2$  decrease of the magnetic moment in the ordered phase supports the existence of antiferromagnetic spin wave-like excitations. These results do not go in line with a purely Ising system and could be understood with the existence of anisotropic exchange interactions, as it has been introduced in the exchange Hamiltonian describing the quantum spin-ice, see Eq. 1.12. Therefore, it can be pictured that quantum fluctuations of the Ising spin lead to the existence of a transverse spin coupling term. This hypothesis should be resolved with the full characterisation of the crystal-electric-field Hamiltonian. The determination of the ground state wavefunctions will determine the type of Kramers ions we are dealing with.

# Chapter 5

## Insights into $\text{Tb}_2\text{Ti}_2\text{O}_7$

### Contents

---

<b>5.1</b>	<b>Introduction</b>	<b>133</b>
<b>5.2</b>	<b><math>\text{Tb}_2\text{Ti}_2\text{O}_7</math>: a Jahn-Teller transition?</b>	<b>136</b>
5.2.1	Context	136
5.2.2	X-ray synchrotron radiation measurements	139
<b>5.3</b>	<b><math>\text{Tb}_2\text{Ti}_2\text{O}_7</math>: a quantum spin-ice realisation?</b>	<b>140</b>
5.3.1	The exchange Hamiltonian	140
5.3.2	Prediction of a magnetisation plateau	145
5.3.3	$\mu\text{SR}$ frequency shift measurements	148
<b>5.4</b>	<b>Conclusions</b>	<b>152</b>

---

$\text{Tb}_2\text{Ti}_2\text{O}_7$  is one of the most extensively studied pyrochlore compound since its magnetic ground state arouses questions: is it a realisation of a quantum spin-ice or does a Jahn-Teller transition occur at low temperatures? After an introduction on previous experimental and theoretical results, we will report X-ray synchrotron radiation diffraction and  $\mu\text{SR}$  measurements.

### 5.1 Introduction

The pyrochlore titanate  $\text{Tb}_2\text{Ti}_2\text{O}_7$  has been one of the most intriguing compounds over the past few years. A Curie-Weiss law describes the bulk susceptibility down to 50 K with a Curie-Weiss temperature  $\theta_{\text{CW}} = -19$  K indicative of strong antiferromagnetic interactions and a  $\text{Tb}^{3+}$  magnetic moment of  $9.6 \mu_{\text{B}}$  [109, 179]. The analysis of the crystal-electric-field transitions measured by inelastic neutron scattering shows that this compound is characterised by Ising spins, i.e. they are oriented along the trigonal axis  $\langle 111 \rangle$ , and the first excited energy level is a doublet located at  $\approx 1.5$  meV from the ground state doublet, see Chapter 3. Usual Ising pyrochlore models introduced in Chapter 1 cannot account for the paramagnetic diffuse scattering at  $T = 9$  K [218]. No long-range magnetic order was evidenced by  $\mu\text{SR}$  spectroscopy down to  $T = 50$  mK [219], in agreement with previous measurements [178, 220], or neutron diffraction also down to

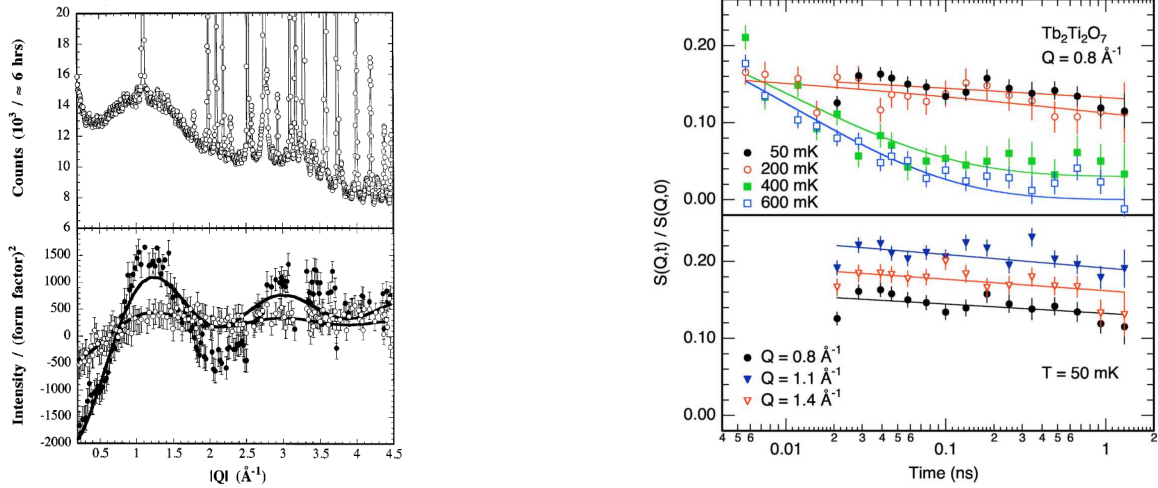


Figure 5.1: *Left: Neutron diffraction pattern recorded at  $T = 2.5$  K (top) and neutron diffraction patterns at  $T = 2.5$  K (closed symbols) and 50 K (open symbols) where data recorded deep into the paramagnetic state at 100 K (bottom) were subtracted: sinusoidal-like neutron diffuse scattering is exhibited. Reprinted figure with permission from Ref. [178]. Copyright 2015 by the American Physical Society. Right: Normalised intermediate scattering function measured by neutron spin echo experiments on a powder sample of  $Tb_2Ti_2O_7$ . Reprinted figure with permission from Ref. [221]. Copyright 2015 by the American Physical Society.*

$T = 50$  mK [221]. Powder neutron diffraction data recorded at  $T = 2.5$  K evidence diffuse magnetic scattering attributed to liquid-like spin correlations restricted to a single tetrahedron [178] as shown in the left panel of Fig. 5.1. Neutron scattering experiments on a single crystal of  $Tb_2Ti_2O_7$  reveal strong anisotropic diffuse scattering below 100 K and down to 50 mK in the (hhl) scattering plane, which contains the following high symmetry directions for a cubic system:  $\langle 001 \rangle$ ,  $\langle hh0 \rangle$ , and  $\langle hhh \rangle$  [222]; a diffuse scattering map recorded at  $T = 9$  K is displayed in the left panel of Fig. 5.8, which will be discussed later. The observed magnetic diffuse scattering covers a broad region in reciprocal space, with a very high intensity at the reciprocal point (0,0,2). Hence, the spin correlation length was deduced to be much smaller than the unit cell lattice parameter and assumed restricted to a single tetrahedra [221, 222]. Therefore the name *cooperative paramagnet* was coined, since spin correlations start to develop at high temperature and persist down to the lowest ones. Since then, the spin dynamics of  $Tb_2Ti_2O_7$  was investigated, firstly by neutron spin echo revealing a slowing down of the spin fluctuations in the nanosecond time range [221] in a temperature range  $400 \leq T \leq 600$  mK, see right panel of Fig. 5.1. At lower temperatures, a fraction of roughly 10% of the total magnetic moments is frozen. The neutron spin echo results are consistent with  $\mu$ SR spectroscopy measurements [178, 219, 220]. Weak longitudinal-field  $\mu$ SR experiments have been performed on a crystal of  $Tb_2Ti_2O_7$  in Ref. [219]: contrary to the work of Refs. [178, 220], the spectra were analysed with an exponential-power function, see Eq. 4.67. The temperature dependence of the spin-lattice relaxation rate  $\lambda_Z$  and of the exponent  $\beta_{se}$  is displayed in Fig 5.2. An increase of  $\lambda_Z$  is found in the temperature range  $1 \leq T \leq 10$  K, which illustrates a significant slowing down of the spin fluctuations. The

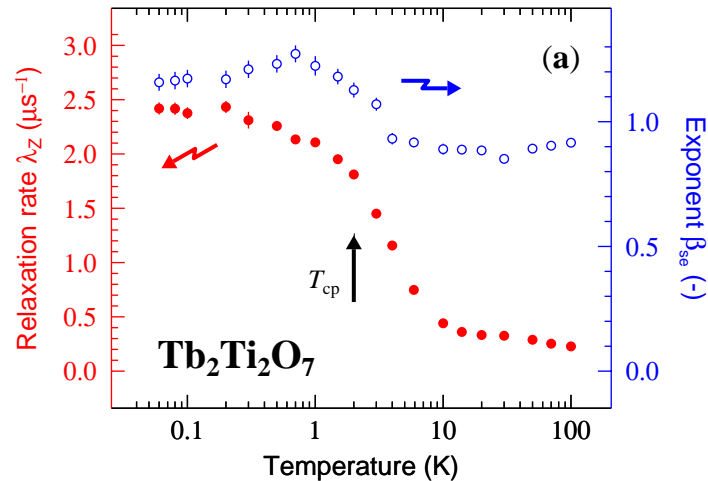


Figure 5.2: Investigation of the spin dynamics in  $Tb_2Ti_2O_7$  with 13 mT longitudinal field  $\mu$ SR measurements: temperature dependence of the spin-lattice relaxation rate  $\lambda_Z$  and the exponent  $\beta_{se}$ . A slowing down of the spin fluctuations is evidenced as the system enters in a paramagnetic state characterised by strong spin correlations. Reprinted figure with permission from Ref. [219]. Copyright 2015 by the American Physical Society.

temperature  $T_{cp} \approx 2$  K is indicated by a black arrow in order to point out that the compound enters a strongly correlated paramagnetic state. An increase of the exponent  $\beta_{se}$  is also evidenced in the same temperature range, which can be interpreted as an additional proof of the progressive slowing down of the spin fluctuations: indeed, in the motional narrowing limit, i.e. if the spin dynamics is sufficiently fast, spectra are usually described with an exponential function ( $\beta_{se} = 1$ ) whereas a value of  $\beta_{se} = 2$  means that the local field at the muon site is static. Finally, the temperature independent plateau of  $\lambda_Z$  is indicative of persistent spin fluctuations.

Independently, this spin freezing has also been evidenced with neutron scattering experiments on a triple axis spectrometer, where a reduction of the quasielastic linewidth occurs for  $T \leq T_{cp}$  [219, 223] near the specific  $q$ -value (0,0,2) where previous neutron scattering experiments found strong magnetic diffuse scattering [222]. The temperature dependence of the magnetisation shows an irreversibility between zero-field and field cooling below  $\approx 200$  mK [109, 224, 225], indicative of a spin freezing. A peak is revealed in the real part of the a.c. susceptibility at  $T \approx 0.2$  K [225, 226]. The analysis of the frequency dependence of this maximum cannot be performed with usual relations characteristic of a spin-glass transition [225, 227]. Therefore, this maximum was associated with a glassy behaviour rather than a spin-glass transition. The analysis of the dissipative part of the susceptibility show two distinct frequency regimes: at low frequency, a peak occurs at the same temperature as the one observed for the real part of the susceptibility. However, in the high frequency regime, the dissipative part of the susceptibility vanishes at temperatures larger than 4 K, which is higher than the freezing temperature  $T_{cp}$ : this behaviour is ascribed to the existence of very slow spin dynamics. To conclude, spins correlations start to develop at  $T = 50$  K. A wide panels of techniques evidence a slowing down of the spin fluctuations at a freezing temperature  $T_{cp} \approx 2$  K. Looking at the time scales probed by neutron scattering ( $\approx 10^{-11}$  s),

neutron spin echo ( $\approx 10^{-9}$  s),  $\mu$ SR ( $\approx 10^{-8}$  s) and a.c. susceptibility ( $\approx 10^{-2}$  s) experiments, a broad range of spin correlation times are involved which is a common feature of frustrated magnets.

The challenge of the past few years was to determine the ground state of  $Tb_2Ti_2O_7$  and thus explain the lack of magnetic ordering. Two proposals have been recently discussed: the compound would be an experimental realisation of the quantum spin-ice state, see Sec. 1.4, and the second suggests a Jahn-Teller like structural distortion at low temperatures. Therefore in the following, we will discuss the two aforementioned proposals.

## 5.2 $Tb_2Ti_2O_7$ : a Jahn-Teller transition?

### 5.2.1 Context

With the purpose to explain the lack of magnetic long-range order in  $Tb_2Ti_2O_7$ , Chappuis *et al.* [228] firstly suggest from the analysis of the variation in the magnetic entropy that the ground state doublet is split, a reasonable hypothesis since terbium is a non-Kramers ion. This assumption could support the existence of a structural distortion at low temperatures. The left panel of Fig 5.3 displays the temperature dependence of the specific heat  $C_p$ , whereas the inset shows the electronic specific heat, after subtraction of the nuclear and phonons contributions to  $C_p$ . An anomalous minimum is clearly evidenced at  $T_t \approx 0.15$  K. The right panel of Fig. 5.3 displays the temperature dependence of the entropy derived from the electronic specific heat. The overall variation of the electronic entropy variation  $\Delta S_{\text{elec}} = R \ln(4)$  is not consistent with the predictions of the crystal-electric-field energy levels scheme of Ref. [73] and Chapter 3 for instance, since the electronic entropy should saturate at  $R \ln(2)$  at low temperatures, see Fig. 3 in Ref. [228]. A splitting  $\delta_{\text{CEF}} \approx 2$  K of the low-lying crystal-electric-field energy levels needs to be introduced to describe the magnetic entropy, as illustrated by the black dashed line. The lifting of the degeneracy of the ground state has been interpreted as a signature of a structural distortion, ruled by the perturbative Hamiltonian  $\mathcal{H}_{\text{per}} = -\mathcal{D}_t J_Z^2$ , where  $Z$  refers to a cubic axis and  $\mathcal{D}_t \approx 0.27$  K scales the strength of the distortion [228]. The latter value is consistent with the one introduced in Ref. [229] in order to describe the quasielastic signal in inelastic neutron scattering measurements as a CEF excitation lying at  $\approx 2$  K, and resulting from the splitting of the ground state. The latter results were strongly debated in Ref. [230], claiming that the quasielastic signal does not originate from a splitting of the ground state. They also argue that the lack of entropy resulting from the simulation of an unsplit ground state doublet could be compensated by the introduction of spins correlations. This idea is supported by the strong decrease of the elastic constants with temperature [231, 232], as illustrated in the left panel of Fig. 5.4. Therefore, a Jahn-Teller transition driven by magnetoelastic effects has been suggested.

Additional transverse field  $\mu$ SR measurements report the temperature dependence of the normalised muon spin frequency shift  $\Delta\nu/\nu_{\text{ext}}$ , where  $\Delta\nu = \nu_\mu - \nu_{\text{ext}}$ ,  $\nu_\mu$  is the frequency of the muon spin precession around the local field at the muon site  $\mathbf{B}_{\text{loc}}$ , and  $2\pi\nu_{\text{ext}} = \gamma_\mu B_{\text{ext}}$ , with  $\mathbf{B}_{\text{ext}}$  being the transverse field applied along the [110] direction. More details on this technique are given in Sec. 2.6.6. The temperature

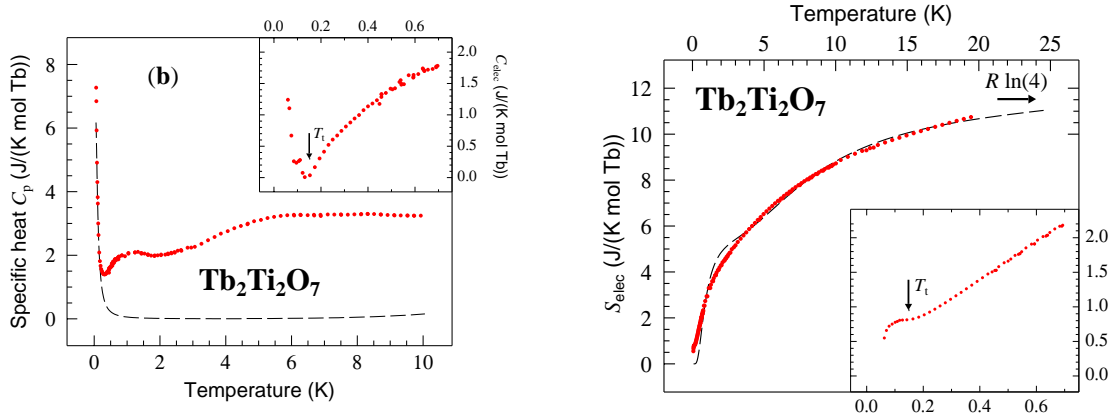


Figure 5.3: Left: Temperature dependence of the specific heat for a  $Tb_2Ti_2O_7$  crystal. The inset displays a zoom over the lowest temperatures in order to show the unusual upturn of the electronic specific heat, after subtraction of the nuclear and phonons contributions to  $C_p$ . Therefore this behaviour is ascribed to additional degrees of freedom. Right: Temperature dependence of the entropy of electronic origin  $S_{elec}$ . The black dashed line is a prediction following the crystal-electric-field energy scheme described in the main text. The inset shows the low temperatures part of the magnetic entropy. A plateau is exhibited at  $T_t$ , to be connected with the uprise of the specific heat below  $T_t$ . Reprinted figures with permission from Ref. [219]. Copyright 2015 by the American Physical Society.

dependence of the normalised frequency shift is shown in the right panel of Fig. 5.4. The frequency shift is negative and decreases with temperature from 10 K down to the lowest temperatures, which is consistent with an increase of the mean value of the local field at the muon site. However, an extremum is evidenced at  $T_t = 0.15$  K, as a signature of an exotic transition. In the inset of Fig. 5.4 an irreversibility between field cooling and zero-field cooling is shown, meaning the system enters a glassy state. Moreover, the significant value of  $\lambda_Z$  at low temperatures, see Fig. 5.2, is not consistent with a spin-glass transition, supporting the results of a.c. susceptibility presented in Sec. 5.1.

Looking for such a structural transition, high resolution X-ray diffraction has been performed by Ruff *et al.* [233] on a single crystal of  $Tb_2Ti_2O_7$ . As illustrated in the left panel of Fig. 5.5, they found a broadening of the Bragg peaks from 20 K down to 0.3 K, interpreted as the development of spatial correlations. The temperature dependence of the inverse correlation lengths are displayed in the right panel of Fig. 5.5. Furthermore, as illustrated in the right panel of Fig 5.6, an anomaly in the temperature dependence of the lattice parameter occurs around  $T \approx 15$  K: the latter does not follow the usual lattice contraction as the temperature is decreased. The authors of Ref. [233] claim that below  $T \approx 20$  K, the system develops spatial correlations as a signature of a Jahn-Teller transition occurring at lower unreachable temperatures. On the other hand, X-ray powder diffraction on a polycrystalline sample of  $Tb_2Ti_2O_7$  [234] shows no anomalous negative lattice expansion [234], and does not support the conclusions of Ruff *et al.* [233].

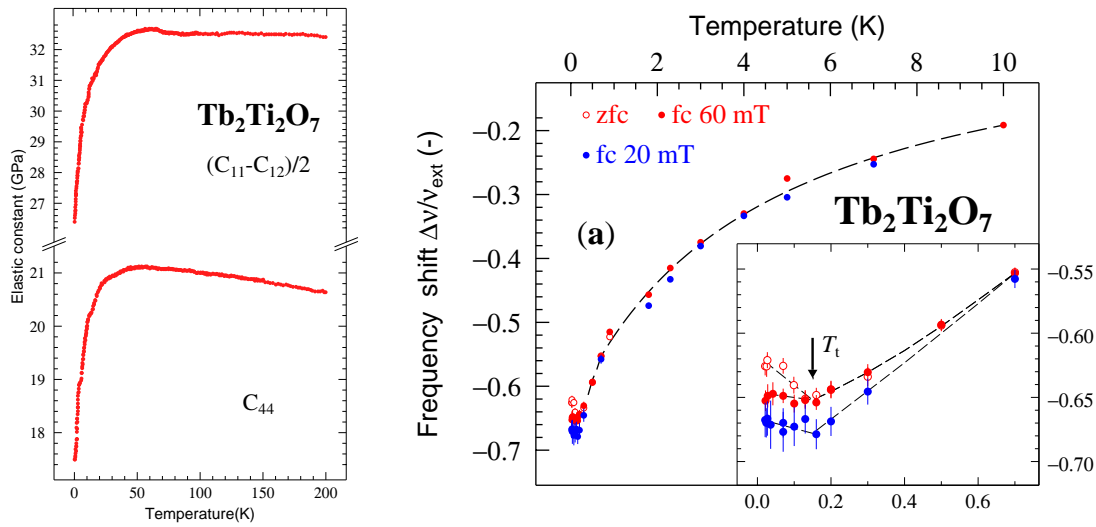


Figure 5.4: Left: Temperature dependence of the elastic constants of  $Tb_2Ti_2O_7$ . Data reproduced from Ref. [232]. Right: Temperature dependence of the normalised  $\mu$ SR frequency shift  $\Delta\nu/\nu_{ext}$  recorded for two applied magnetic fields along the  $[110]$  direction. An exotic transition is exhibited at  $T_t \approx 0.15$  K, which could be a signature of a structural transition. The inset focuses on the lowest temperatures to exhibit an irreversibility between zero and field cooling, characteristic of a glassy behaviour. Reprinted figure with permission from Ref. [219]. Copyright 2015 by the American Physical Society.

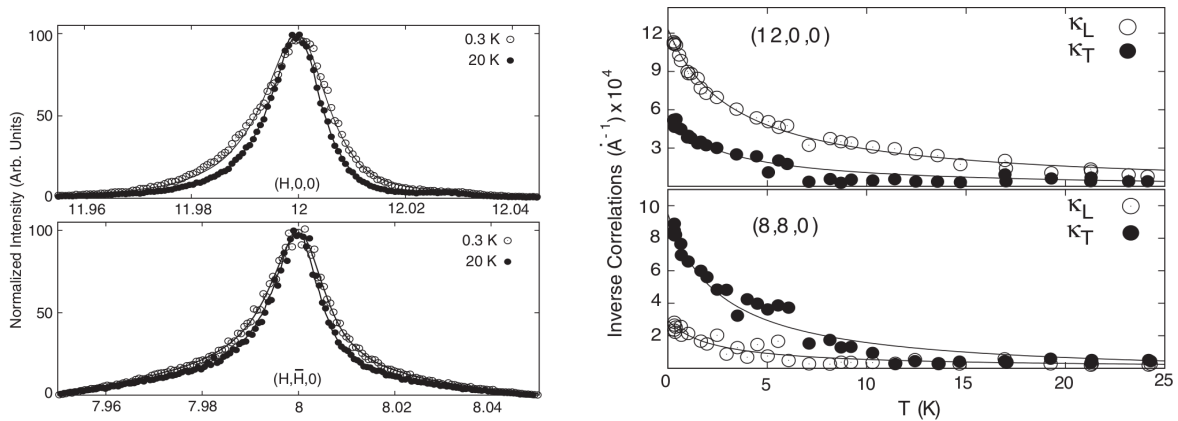


Figure 5.5: Left: Bragg peaks of a crystal of  $Tb_2Ti_2O_7$  recorded on a four-circle X-ray diffractometer for  $T = 0.3$  and 20 K. The broadening of the Bragg peaks located at  $(12, 0, 0)$  (top) and  $(8, 8, 0)$  (bottom) is highlighted. Right: Temperature dependence of the longitudinal and transverse parts of the inverse spatial correlation lengths deduced from the broadening of the  $(12, 0, 0)$  and  $(8, 8, 0)$  Bragg peaks. Reprinted figures with permission from Ref. [233]. Copyright 2015 by the American Physical Society.

### 5.2.2 X-ray synchrotron radiation measurements

In order to corroborate or refute the results provided in Refs. [233, 234], we performed X-ray synchrotron radiation measurements at the high resolution powder diffractometer of the Material Science beamline (MS) at the Swiss Light Source of PSI, see Sec. 2.2.4. An X-ray beam of wavelength  $\lambda = 0.49646 \text{ \AA}$  was used, where the flux was maximum [140]. For this experiment, we used a sample of  $Tb_2Ti_2O_7$  denoted "C" in Refs. [123, 225, 228]. Details of the synthesis of this crystal can be found in Ref. [123, 228]. A crushed fragment of the  $Tb_2Ti_2O_7$  crystal and  $\simeq 18 \text{ wt.}\%$  of silicon powder was mixed and ground to obtain a homogeneous mixture. The presence of silicon helps in reducing the  $Tb_2Ti_2O_7$  sample X-ray absorption. The specimen was loaded into a 0.3 mm diameter glass capillary. The data were taken from room temperature down to 4 K. A synchrotron X-ray diffraction pattern recorded at  $T = 6 \text{ K}$  is displayed in the left panel of Fig. 5.6. Data were analysed with the FullProf code [130] and Bragg peak shapes of both silicon and  $Tb_2Ti_2O_7$  were described by a Thompson-Cox-Hastings pseudo-Voigt function, see Sec. 2.3.7. Note that an additional free parameter was introduced and the second line of Eq 2.25 becomes:

$$H_L^2 = X \tan \theta + Y / \cos \theta, \quad (5.1)$$

where  $H_L$  is the FWHM of the Lorentzian function, and  $X$  and  $Y$  refer to isotropic strain and size parameters, respectively. Note that the geometry of our sample holder lead to a strong absorption in the center of the capillary. This gives a strong asymmetry to the Bragg peaks at small angles, which consequently were analysed using two identical phases for both the silicon and  $Tb_2Ti_2O_7$  compounds, introducing opposite offset perpendicular to the beam. Furthermore, isotropic Debye-Waller factors have been used.

Results of the analysis of a spectrum recorded at 4 K are displayed in Tab. 5.1. We have investigated the temperature dependence of the lattice parameter looking for the emergence of a Jahn-Teller like transition. The relative change of the lattice parameter as a function of the temperature is shown in the right panel of Fig. 5.6. We define:

$$\frac{\Delta a_{\text{lat}}}{a_{\text{lat}}} = \frac{a_{\text{lat}}(T) - a_{\text{lat}}(T = 20 \text{ K})}{a_{\text{lat}}(T = 20 \text{ K})}, \quad (5.2)$$

where  $a_{\text{lat}}(T = 20 \text{ K}) = 10.13681(7) \text{ \AA}$ . The compound shows the expected smooth thermal contraction as it is cooled down with a plateau below  $\approx 25 \text{ K}$  to  $a_{\text{lat}} \simeq 10.1368 \text{ \AA}$ . This goes in line with the work of Goto *et al.* [234] and does not follow the uprise of  $\frac{\Delta a_{\text{lat}}}{a_{\text{lat}}}$  put forward in Ref. [233]. Data of Ruff *et al.* [233] predict  $\frac{\Delta a_{\text{lat}}}{a_{\text{lat}}} \approx 0.4 \times 10^{-4}$  at  $T = 4 \text{ K}$ . Therefore, the lattice parameter would be at this temperature  $a_{\text{lat}} = 10.13700 \text{ \AA}$ . We performed a Rietveld refinement using this value (see Tab. 5.1) that shows that the goodness of the analysis decreased when fixing the lattice parameter to this value.

This experiment was especially designed to study the Bragg peak profiles. In Ref. [233], a broadening of the Bragg peak is claimed to appear at 20 K, which increases with temperature decreasing down to 300 mK, see Fig. 5.5. This was interpreted as a precursor of a structural transition. In Fig. 5.7, we compare the profiles of the (8, 8, 0) (left panel) and (12, 0, 0) (right panel) Bragg peaks recorded at 20 and 4 K, where clearly no broadening is shown. The full width at half maximum (FWHM) of the Bragg peaks is of the order of  $9 \times 10^{-3}$  in reciprocal units, to be compared with the Bragg peaks

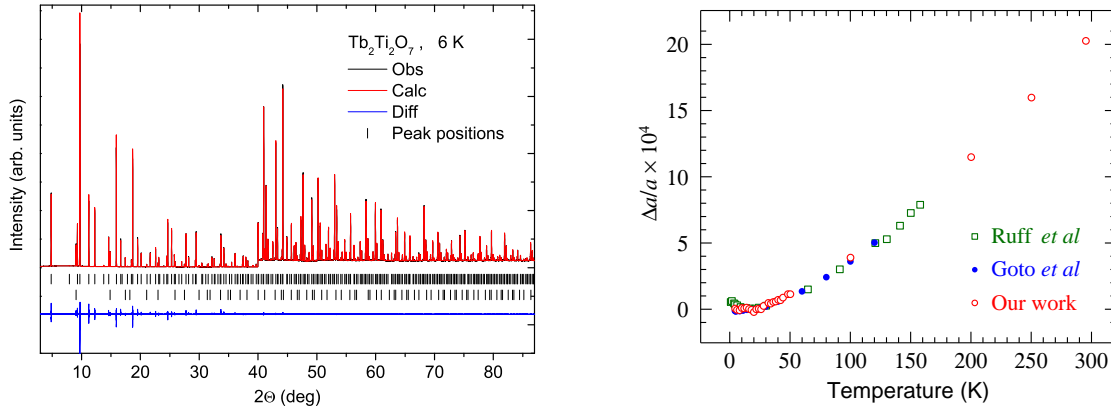


Figure 5.6: *Left: Synchrotron X-ray powder diffraction pattern of  $Tb_2Ti_2O_7$  recorded at  $T = 6$  K with a photon energy of 25 keV. The red solid line is the result of a Rietveld analysis using FullProf and the blue solid line at the bottom gives the difference between the data and the model. Ticks below the graph show the calculated peak positions for  $Tb_2Ti_2O_7$  and Si (upper and lower rows respectively). The intensities beyond  $2\theta = 40^\circ$  have been enlarged by a factor of 10 in order to illustrate the quality of the refinement at higher angles. Picture reproduced from Ref. [235] with kind permission of IOP Publishing. Right: Relative change in the lattice parameter  $a_{\text{lat}}$  as a function of temperature. The green squares refer to data obtained by Ruff *et al.* [233] on a crystal of  $Tb_2Ti_2O_7$  recorded on a four-circle diffractometer X-ray diffractometer. The blue full circles are data from Goto *et al.* [234] recorded on a polycrystalline sample of  $Tb_2Ti_2O_7$  with a X-ray powder diffractometer. Finally, our data are displayed by red open circles.*

displayed in Fig. 5.5, having a FWHM  $\approx 0.02$  in the same units. Therefore, we can conclude that no broadening of the Bragg peaks is visible down to 4 K. Therefore, since the instrumental resolution is better in our case rather than in Ref. [233], the response of the samples used in Ref. [233] and here is different. Consequently, no clear experimental evidence can be brought to the existence or not of a Jahn-Teller transition.

### 5.3 $Tb_2Ti_2O_7$ : a quantum spin-ice realisation?

Some recent theoretical works have been developed to describe the ground state of  $Tb_2Ti_2O_7$ , and they conclude that this compound is a quantum spin-ice, see Sec. 1.4. First, we will present the exchange Hamiltonian introduced by S. Curnoe [58, 237]. Then following these works, a magnetisation plateau has been put forward as a signature of spin-ice correlations, similarly to the classical spin-ice. Finally, we will discuss experimental results on the existence or not of this peculiar feature.

#### 5.3.1 The exchange Hamiltonian

Since the simple Ising model with antiferromagnetic isotropic interactions and the dipolar spin-ice model both fail to describe the diffuse magnetic scattering in the paramagnetic phase [218], we present here some pieces of the work of Curnoe [237], where an

T (K)	$a_{\text{lat}}$ (Å)	$x$	$R_p$	$R_{\text{wp}}$	$R_{\text{exp}}$	$\chi^2$
4	10.13688(5)	0.32777(9)	8.53	8.66	2.61	11.0
4	10.13700(F)	0.32779(12)	10.6	12.0	2.61	21.1
295	10.15735(10)	0.32720(11)	10.2	10.6	4.76	5.0

Table 5.1: Lattice parameter  $a_{\text{lat}}$  and position  $x$  of the oxygen atom O1 determined by synchrotron X-ray diffraction at  $T = 4$  and 295 K.  $R$ -factors are listed as indicators of the quality of the fit, see Sec. 2.3.7. The second line refers to a Rietveld analysis with the lattice parameter  $a_{\text{lat}}$  fixed to the value expected from the anomalous lattice expansion evidenced in Ref. [233]. This value is not consistent with a good quality of the refinement. Note that the value of  $a_{\text{lat}}$  is slightly larger than the one usually found in the literature. Recently it was reported that  $a_{\text{lat}} = 10.15529(1)$  Å [236].

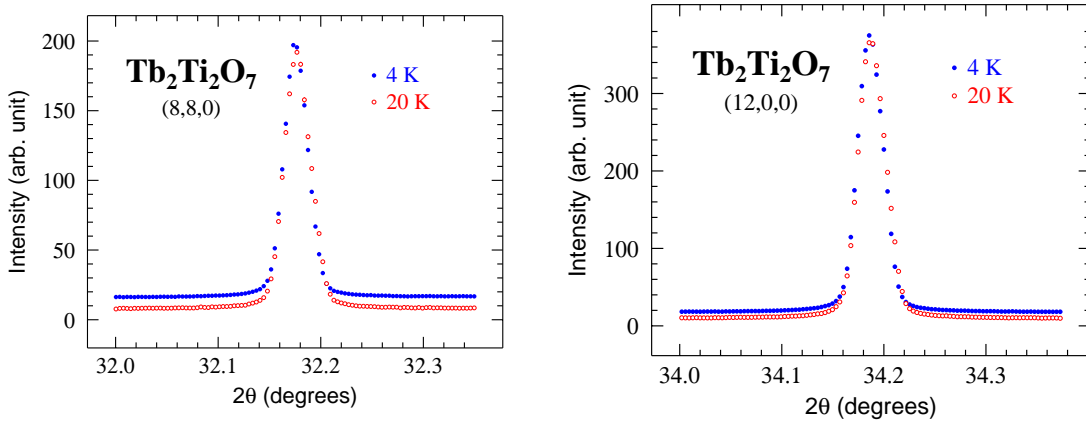


Figure 5.7: Comparison of the  $(8, 8, 0)$  and  $(12, 0, 0)$  X-ray Bragg peak profiles measured at 20 and 4 K for our  $Tb_2Ti_2O_7$  powder sample. The full width at half maximum of the Bragg peak is  $9 \times 10^{-3}$  in reciprocal lattice units. Pictures reproduced from Ref. [235] with kind permission of IOP Publishing.

effective spin-1/2 anisotropic exchange Hamiltonian has been developed, similar to the one introduced in Eq. 1.12:

$$\mathcal{H}_{\text{ex}} = \mathcal{J}_1 X_1 + \mathcal{J}_2 X_2 + \mathcal{J}_3 X_3 + \mathcal{J}_4 X_4, \quad (5.3)$$

where  $\mathcal{J}_i$  are four independent anisotropic exchange interaction constants and  $X_i$  are the exchange terms which are invariants under space group symmetries:

$$\begin{aligned}
X_1 &= -\frac{1}{3} \sum_{\langle i,j \rangle} J_{iz} J_{jz}, \\
X_2 &= -\frac{\sqrt{2}}{3} \sum_{\langle i,j \rangle} [\Lambda_{ij} (J_{iz} J_{j+} + J_{jz} J_{i+}) \\
&\quad + \Lambda_{ij}^* (J_{iz} J_{j-} + J_{jz} J_{i-})], \\
X_3 &= \frac{1}{3} \sum_{\langle i,j \rangle} (\Lambda_{ij}^* J_{i+} J_{j+} + \Lambda_{ij} J_{i-} J_{j-}), \\
X_4 &= -\frac{1}{6} \sum_{\langle i,j \rangle} (J_{i+} J_{j-} + J_{j+} J_{i-}), \quad (5.4)
\end{aligned}$$

where  $\Lambda_{12} = \Lambda_{34} = 1$ ,  $\Lambda_{13} = \Lambda_{24} = \exp(\frac{2i\pi}{3})$  and  $\Lambda_{14} = \Lambda_{23} = \exp(\frac{4i\pi}{3})$ . Note that for  $X_2, X_3, X_4 = 0$ , we recover the classical Ising case where all spins are pointing into or out of the center of the tetrahedron ( $\mathcal{J}_1 > 0$ ), or the spin-ice case with the two-in/two-out spin configuration ( $\mathcal{J}_1 < 0$ ). The subscript  $z$  stands for the local [111] axis and  $x, y$  have been chosen to define an orthonormal basis. The single tetrahedron approximation is adopted here so that the summation over  $\langle i, j \rangle$  in Eq. 5.4 is restricted to the four magnetic sites of a tetrahedron.

In order to understand the ground state of  $Tb_2Ti_2O_7$ , four coupling constants need to be determined. This was successfully done for the case of  $Yb_2Ti_2O_7$  by analysing the spin-wave dispersion in a magnetic field [60] and for  $Er_2Ti_2O_7$  using the same methodology [17] as well as analysing the diffuse scattering intensity [195]. In these examples, the ground state doublet was described with an effective spin-1/2.

In the case of  $Tb_2Ti_2O_7$ , the total angular momentum is  $J = 6$ . Since the ground state is not well isolated from the first excited crystal-electric-field energy level, the ground state wavefunctions can no longer be  $\pm\frac{1}{2}$  but those introduced in Sec. 3.2. Following the notations of Ref. [237], the exchange Hamiltonian for  $Tb_2Ti_2O_7$  is described by coupling constants labelled  $\mathcal{I}_i$  rather than  $\mathcal{J}_i$ , the latter notations kept for the effective spin-1/2 case:

$$\mathcal{H}_{\text{ex}}^{\text{Tb}} = \mathcal{I}_1 X_1 + \mathcal{I}_2 X_2 + \mathcal{I}_3 X_3 + \mathcal{I}_4 X_4. \quad (5.5)$$

Since we focus on a single tetrahedron, and since only two states are available for a magnetic ion with a ground state doublet, it results  $2^4 = 16$  collective states. They are commonly written as [58, 238]:

$$|\pm\pm\pm\pm\rangle_\alpha \equiv |\pm\rangle_1 \otimes |\pm\rangle_2 \otimes |\pm\rangle_3 \otimes |\pm\rangle_4, \quad (5.6)$$

where  $\alpha \equiv 1/2$ , Tb denotes whether we are using effective spin-1/2 or the whole wavefunctions to describe the ground state, and the indices (1,2,3,4) label the tetrahedron magnetic sites. An important property has been pointed out in Ref. [58]: the decomposition in terms of irreducible representations of the symmetry group of a tetrahedron in the pyrochlore lattice is the same using tetrahedron states defined by the effective spin-1/2 or the ground state wavefunctions of  $Tb_2Ti_2O_7$ . This property holds for the kind of non-Kramers ions involved here as it requires the Zeeman ket  $|1/2\rangle$  to appear in the ground state wavefunctions. Therefore a map between the states  $|\pm\pm\pm\pm\rangle_{>1/2}$  and  $|\pm\pm\pm\pm\rangle_{\text{Tb}}$  can be established. Using the ground state wave functions  $|\pm\rangle$  determined in Sec. 3.2, the matrix elements for  $J_\pm$  vanish and therefore, comparing the matrix elements of  $\mathcal{H}_{\text{ex}}^{\text{Tb}}$  and  $\mathcal{H}_{\text{ex}}$  leads to:

$$\mathcal{J}_1 = 4\mathcal{I}_1 j_1^2, \quad \text{where } j_1 = \langle +|J_z|+\rangle \quad \text{and} \quad \mathcal{J}_{2,3,4} = 0. \quad (5.7)$$

This corresponds to the classical spin-ice case or the all-in-all-out case if  $\mathcal{I}_1 < 0$  or  $\mathcal{I}_1 > 0$ , respectively: none of these two states are acceptable for  $Tb_2Ti_2O_7$ . However, contrary to the spin-ice compounds, the ground state is not well isolated and an excited crystal-electric-field energy level lies at  $\Delta \approx 1.5$  meV, see Sec. 3.2. Therefore, using wavefunctions of the ground state ( $|\pm\rangle$ ) and first excited ones ( $|\uparrow\downarrow\rangle$ ), S. Curnoe [237] calculates the following matrix elements:

$$j_1 = \langle +|J_z|+\rangle = -3.21, \quad j_3 = \langle \uparrow|J_z|+\rangle = -2.37,$$

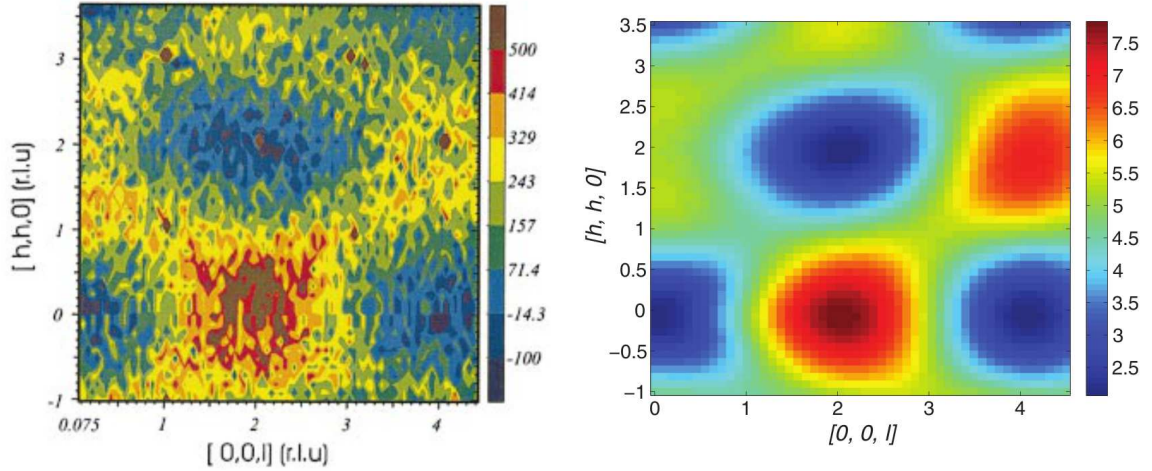


Figure 5.8: *Left: Diffuse scattering map recorded in the (hhl) plane at  $T = 9$  K for  $Tb_2Ti_2O_7$ . Data at 100 K have been subtracted in order to only show diffuse magnetic scattering. Reprinted figure with permission from Ref. [222]. Copyright 2015 by the American Physical Society. Right: the corresponding calculated diffuse scattering map. Reprinted figure with permission from Ref. [237]. Copyright 2015 by the American Physical Society.*

$$j_2 = \langle \uparrow | J_z | \uparrow \rangle = 4.05, \quad t = \langle \uparrow | J_+ | - \rangle = 4.72. \quad (5.8)$$

Note that the relative importance of the matrix element  $t$  is indicative of the significant admixture of the first crystal-electric-field level to the ground state. Consequently, four states need to be considered per magnetic ion site, leading to 256 states per tetrahedron. The exchange Hamiltonian  $\mathcal{H}_{\text{ex}}^{\text{Tb}}$  is treated as a perturbation of the Stevens Hamiltonian  $\mathcal{H}_{\text{CEF}}$  introduced in Sec. 3.1. Therefore an effective Hamiltonian  $\mathcal{H}_{\text{eff}}^{\text{Tb}}$  is inferred restricted to the crystal-electric-field ground state. The resulting exchange matrices found using perturbation theory take the same form as the ones from the 1/2-spin model. Consequently, a map between the 16 lowest energy eigenstates of  $\mathcal{H}_{\text{eff}}^{\text{Tb}}$  and the 16 tetrahedron states of  $\mathcal{H}_{\text{ex}}$  is established. Analysing the diffuse scattering maps for  $Tb_2Ti_2O_7$  provides the exchange constants  $\mathcal{I}_i$  involved in  $\mathcal{H}_{\text{eff}}^{\text{Tb}}$  (and  $\mathcal{H}_{\text{ex}}^{\text{Tb}}$ ). Using the map established between  $\mathcal{H}_{\text{eff}}^{\text{Tb}}$  and  $\mathcal{H}_{\text{ex}}$ , and the matrix elements calculated in Eq. 5.8, lead to the exchange constants involved in the spin-1/2 model. Consequently, due to the property of the wavefunctions of this kind of non-Kramers ion, the problem can be mapped onto an effective spin-1/2 Hamiltonian.

The diffuse scattering map in the (hhl) plane recorded at  $T = 9$  K by Gardner *et al.* [222] is displayed in the left panel of Fig. 5.8. In the right panel of the same figure is the corresponding calculated diffuse scattering [237], in good agreement with experimental data. The deduced exchange coupling constants given in Kelvin units for the spin-1/2 model in the single tetrahedron approximation are:

$$\begin{aligned} \mathcal{J}_1 &= -10.2, & \mathcal{J}_2 &= -0.4, \\ \mathcal{J}_3 &= 0.2, & \mathcal{J}_4 &= 0.6. \end{aligned} \quad (5.9)$$

Note that in the single tetrahedron approximation, half of the exchange paths are omitted: the pyrochlore lattice can be decomposed into two tetrahedra networks A and

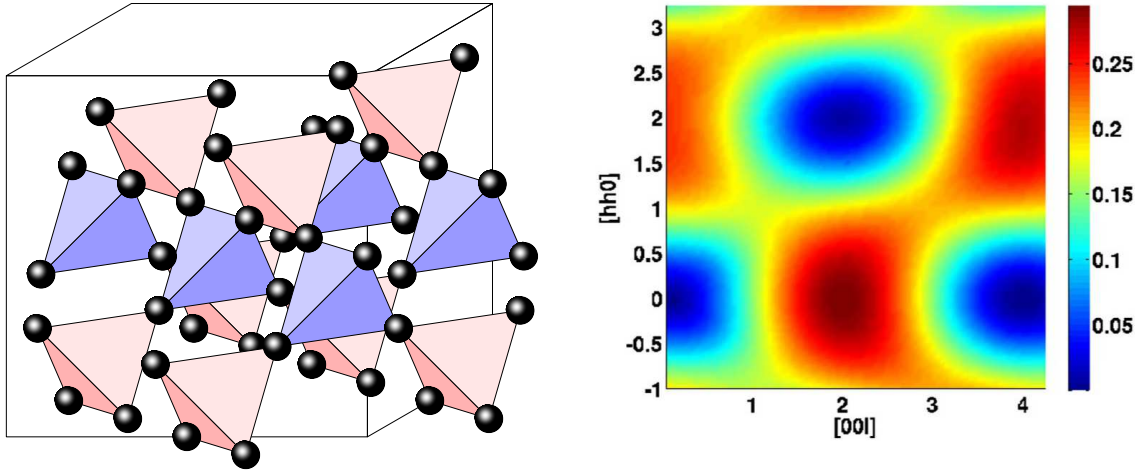


Figure 5.9: Left: Illustration of the pyrochlore lattice where the existence of two different network of tetrahedra is highlighted. The network labelled A (red tetrahedra) can be rotated by  $\frac{\pi}{2}$  along a cubic axis to recover the network labelled B (blue tetrahedra). Reprinted figure with permission from Ref. [2]. Copyright 2015 by the American Physical Society. Right: Calculated diffuse scattering map at  $T = 9$  K to be compared with the experimental data displayed in the left panel of Fig. 5.8. Reprinted figure with permission from Ref. [239]. Copyright 2015 by the American Physical Society.

B differing from their orientation (a rotation of  $\frac{\pi}{2}$  along a fourfold cubic axis transform a tetrahedra of network A into a tetrahedra of network B) as illustrated in Fig.5.9. A magnetic ion belongs to one tetrahedron of network A and one tetrahedron of network B. Therefore, to compensate for the missing exchange paths, it is a fair approximation to divide the exchange coupling constants in Eq. 5.9 by a factor two. To conclude,  $Tb_2Ti_2O_7$  can be described by an effective spin-1/2 model revealing a spin-ice configuration ( $\mathcal{J}_1 < 0$ ). The existence of small transverse coupling terms are revealed that lift the degeneracy associated with the classical spin-ice state. These transverse terms are at the origin of quantum spin fluctuations, contrary to the classical spin-ice where flips of the Ising spins only arise from thermal fluctuations. To compare with the effective spin-1/2 nearest-neighbour exchange Hamiltonian introduced in Ref. [65] and discussed in Sec. 1.4, the following equations relate the exchange couplings given in Kelvin units in the two Hamiltonians as:

$$\begin{aligned} \mathcal{I}_{zz} &= -\frac{1}{6}\mathcal{J}_1 = 1.7, & \mathcal{I}_{z\pm} &= \frac{1}{3\sqrt{2}}\mathcal{J}_2 = -0.094, \\ \mathcal{I}_{\pm\pm} &= \frac{1}{6}\mathcal{J}_3 = 0.033, & \mathcal{I}_{\pm} &= \frac{1}{12}\mathcal{J}_4 = 0.05. \end{aligned} \quad (5.10)$$

For non-Kramers ion, Lee *et al.* [66] have predicted a phase diagram by mean-field theory at zero temperature as illustrated in Fig 5.10. With the exchange parameters listed in Eq. 5.10, the quantum spin-ice phase is predicted for  $Tb_2Ti_2O_7$ .

Note that early work succeeded in describing the spin correlations in the paramagnetic phase at  $T = 9$  K. In Ref. [240], isotropic exchange and dipolar interactions were taken into account within the two first crystal-electric field doublets. However, this model predict the all-in/all-out magnetic ordering at  $T_c = 1.8$  K. For completeness,

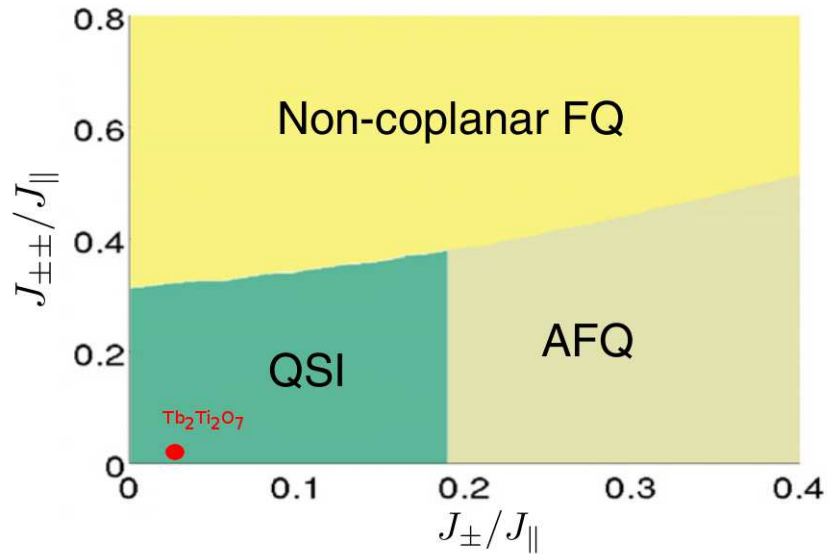


Figure 5.10: Zero-temperature phase diagram for non-Kramers ions predicted in Ref. [66]. Here  $J_{\parallel} \equiv \mathcal{I}_{zz}$ ,  $J_{z\pm} \equiv \mathcal{I}_{z\pm}$ ,  $J_{\pm} \equiv \mathcal{I}_{\pm}$ , and  $J_{\pm\pm} \equiv \mathcal{I}_{\pm\pm}$ . Note that  $J_{z\pm}$  is taken to be zero. The red sphere roughly indicates the position of  $Tb_2Ti_2O_7$  in the quantum spin-ice phase, using the parameters of Eq. 5.10. Picture modified from Ref. [55].

a work very similar to the one of Curnoe [237] has been developed in Ref. [239], and lead to the same conclusions. The calculated diffuse scattering intensity at  $T = 9$  K is displayed in the right panel of Fig. 5.9, also in good agreement with experimental data shown in the left panel of Fig. 5.8.

Experimental proofs of a spin-ice configuration have been brought out by Fennell *et al.* [241] using polarised neutrons at  $T = 50$  mK: pinch points have been observed in the “non-spin flip” channel corresponding to the Ising contribution of the spin to the neutron scattering intensity. These pinch points are characteristic of algebraic dipolar correlations, and usually observable in classical spin-ice compounds, see Sec. 1.3. Therefore, two-in-two-out spin configurations are at play in  $Tb_2Ti_2O_7$ . Besides, anisotropic exchange interactions slightly moving the spins out of the [111] direction exist. These transverse components have been evidenced in the “spin-flip” channel, also with algebraic correlations leading to pinch points at the Brillouin zone center and characterised by a “two-up/two-down” spin configuration. These observations have recently been confirmed in Refs. [242, 243].

### 5.3.2 Prediction of a magnetisation plateau

An interesting property of the spin-ice compounds has been established in Refs. [13, 244], which predicts the presence of a plateau in the field dependence of the magnetisation when a magnetic field is applied in the [111] direction. To understand this property, the pyrochlore lattice can be seen as a superposition of triangular and Kagome planes when we are looking along the [111] direction, see the left panel of Fig. 5.11. Let us consider a tetrahedron: the magnetisation plateau corresponds to the alignment of one

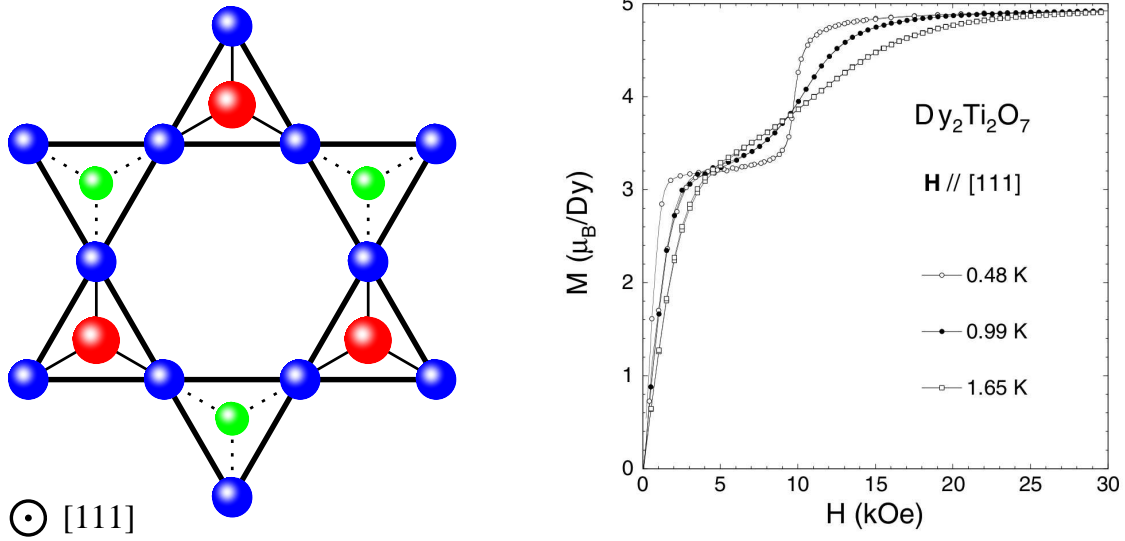


Figure 5.11: *Left: Projection of the network of corner-sharing tetrahedra along the [111] axis in order to evidence the succession of triangular and Kagome planes. Spheres of same colour represents magnetic ions belonging to the same plane. Right: Field dependence of the magnetisation for the classical spin-ice  $Dy_2Ti_2O_7$  exhibiting a distinct plateau at low temperatures. Copyright IOP Publishing. Reproduced from Ref. [245] by permission of IOP Publishing. All rights reserved.*

of the Ising spins in the direction of the applied magnetic field. Since this spin can be viewed as belonging to a triangular plane perpendicular to the [111] direction, the three remaining spins of the tetrahedron belong to a Kagome plane. They fulfil the ice rule with two spins pointing into and two spins pointing out of the center of the tetrahedron. Therefore, the degrees of freedom live in the Kagome planes, defining the so-called "Kagome ice" state. This leads to a low temperatures residual entropy that is lower than the one found in zero-field. As the field increases, the ice-rule constraint is broken and the system chooses a configuration where the magnetisation is saturated, i.e. three spins pointing into and one pointing out of the center of the tetrahedron, or conversely. This property has been experimentally verified in the case of the classical spin-ice compound  $Dy_2Ti_2O_7$  [245, 246], see the right panel of Fig. 5.11.

As explained in Sec. 5.3.1,  $Tb_2Ti_2O_7$  could be a realisation of a quantum spin-ice, i.e. an ice rule spin configuration with the existence of transverse exchange coupling terms. Therefore, similarly to the classical spin-ice, the observation of a plateau in the field dependence of the magnetisation when a magnetic field is applied along the [111] direction would provide an experimental evidence of "two-in/two-out" spin correlations restricted to a single tetrahedron [247]. Consequently, using the crystal-electric-field parameters for  $Ho_2Ti_2O_7$  [168] and rescaled for  $Tb_2Ti_2O_7$ , the wavefunctions of the crystal-electric-field states are calculated to define a basis where the Hamiltonian of interest is diagonalised. The latter takes into account the Zeeman interaction due to the applied magnetic field, antiferromagnetic isotropic exchange (coupling  $\mathcal{I}$ ) and dipolar interactions. Calculations were restricted to a single tetrahedron (ITA approximation). The calculated magnetisation curves are shown in the left panel of Fig. 5.12. An

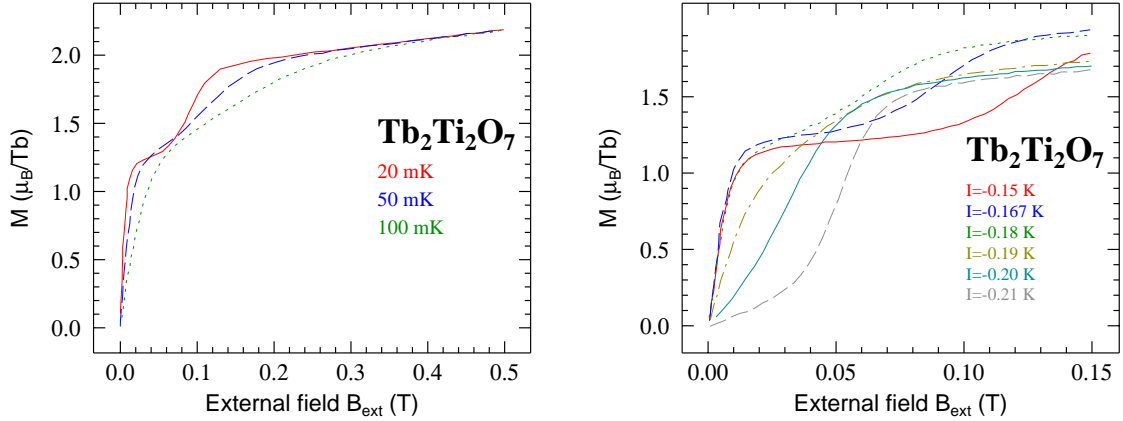


Figure 5.12: *Left: Calculated field dependence of the magnetisation of  $Tb_2Ti_2O_7$  in the single tetrahedron approximation (ITA) when  $\mathbf{B}_{\text{ext}}$  is applied along the trigonal axis  $[111]$  for several temperature  $T = 20, 50,$  and  $100$  mK. Right: Same quantity at  $T = 20$  mK for several values of the exchange integral  $\mathcal{I}$ . Data reproduced from Ref. [247].*

inflection point is predicted for  $T = 50$  mK whereas at  $T = 20$  mK a magnetisation plateau should appear. In the right panel of Fig. 5.12, the magnetisation plateau at  $T = 20$  mK is shown as a function of the applied field for different values of the antiferromagnetic exchange coupling constant. The Curie-Weiss temperature in the paramagnetic regime is  $\theta_{\text{CW}} = -0.19$  K. To deduce an isotropic exchange constant between nearest neighbours, the crystal-electric-field contribution has been subtracted of to give  $\theta_{\text{CW}}^{\text{ex}} = -0.14$  K, which corresponds to  $\mathcal{I} = -0.167$  K [240]. Note that a lower value of the exchange coupling constant,  $\mathcal{I} = -0.083$  K [73], has been put forward from the analysis of the field dependence of the magnetisation and the temperature dependence of the magnetic susceptibility at high temperatures, i.e. neglecting spin correlations. Nevertheless, a magnetisation plateau is expected for values  $|\mathcal{I}| \leq |\mathcal{I}_c| = 0.187$  K [247]. As for the classical spin-ice case, the interpretation of this magnetisation plateau is attributed to the transition from the two-in/two-out Ising spin configuration in a single tetrahedron to a saturated state with a "three-in-one-out" spin configuration.

These predictions have generated a lot of experimental studies searching for the magnetisation plateau as a signature of spin-ice like spin correlations. Magnetisation measurements have been performed by Lhotel *et al.* [225] and are reported in the left panel of Fig. 5.13 for a single crystal of  $Tb_2Ti_2O_7$ . The magnetic field was applied in the  $[111]$  direction in the plane of a disk geometry to minimise demagnetisation effects. No evidence of a magnetisation plateau is found down to 57 mK for a magnetic field up to 8 T (not shown). Curves recorded at 57 mK and 100 mK (not shown) are very similar, which is not predicted in Ref. [247] (see the left panel of Fig. 5.12). However, since anisotropic exchange is established, the isotropic exchange coupling  $\mathcal{I}$  used in the left panel of Fig. 5.12 to calculate the magnetisation curve could be larger, and according to the right panel of Fig. 5.12, the predicted magnetisation plateau is expected at lower temperatures. These experimental results are confirmed by the work of Legl *et al.* [224], where a vibrating-coil magnetometer was used in order to measure the magnetisation down to 43 mK in applied magnetic field along  $[111]$  up to 5 T. Further a.c. magnetic

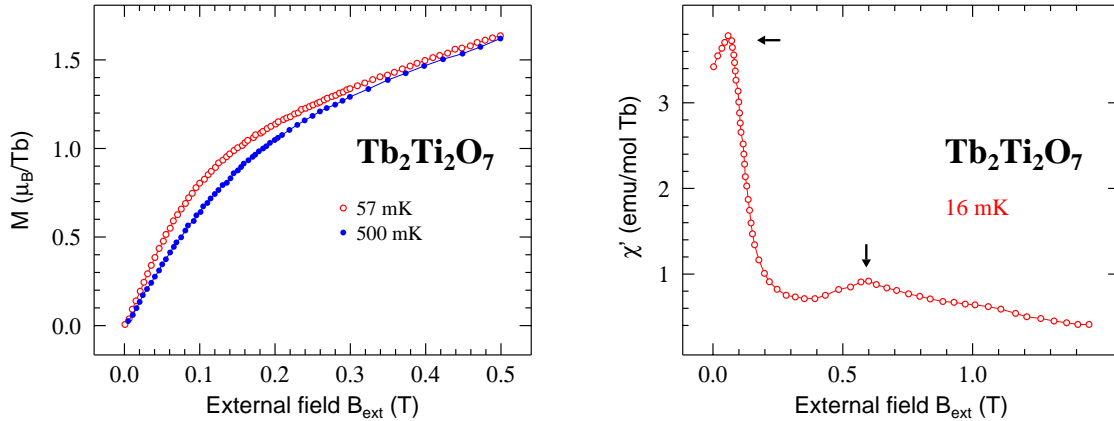


Figure 5.13: *Left:* Field dependence of the magnetisation of a crystal of  $Tb_2Ti_2O_7$  with a magnetic field applied along the  $[111]$  direction at  $T = 57$  mK (open red circles) and 500 mK (full blue circles). Data reproduced from Lhotel *et al.* [225]. *Right:* Field dependence of the real part of the susceptibility for a crystal of  $Tb_2Ti_2O_7$  with a magnetic field applied along the  $[111]$  direction at  $T = 16$  mK. The black arrows locate the two peaks in  $\mu_0 dM/dB_{\text{ext}}$  that delimit the weak magnetisation plateau. Data reproduced from Yin *et al.* [226].

susceptibility measurements have been performed by Yin *et al.* [226] on a single crystal of  $Tb_2Ti_2O_7$  with  $\mathbf{B}_{\text{ext}}$  parallel to the three-fold axis  $[111]$ . The field dependence of the real part of the susceptibility measured at  $T = 16$  mK with an a.c. field amplitude of 0.94 mT is displayed in the right panel of Fig. 5.13. This quantity is a measure of  $\mu_0 dM/dB_{\text{ext}}$ : the two black arrows indicate an inflection point in the magnetisation curve and therefore the field range delimited by these arrows is ascribed to the predicted magnetisation plateau. However, this data should be integrated over  $B_{\text{ext}}$  to give a more significant insight onto the magnetisation curve, see Sec. 5.3.3.

### 5.3.3 $\mu$ SR frequency shift measurements

In this section, we report transverse-field  $\mu$ SR measurements performed at the LTF spectrometer of the  $S\mu$ S (PSI) in the temperature range  $20 \leq T \leq 500$  mK. We refer to Sec. 2.6.6 for technical details. On a silver disc is deposited a mosaic of crystal plates whose normal axis is a  $[111]$  axis: their thickness is about 1/3 mm and their lateral size is up to 6 mm. The external magnetic field  $\mathbf{B}_{\text{ext}}$  is applied parallel to the muon beam which is along one of the threefold  $\langle 111 \rangle$  axis of the crystal. Fig. 5.14 shows a  $\mu$ SR spectrum recorded at  $T = 20$  mK with a magnetic field  $B_{\text{ext}} = 800$  mT. We recall that the muon polarisation function is described by the sum of two oscillating components: one accounting for the muons implanted in the sample and precessing around the local field at the muon site  $B_{\text{loc}}$ , and the second for the muons stopped in the sample surroundings, essentially the silver sample holder, which precess around a field close to the external field. Therefore the data are described by the following function:

$$a_0 P_X^{\text{exp}}(t) = a_1 \exp(-\lambda_{X,1}t) \cos(2\pi\nu_1 t + \varphi) + a_2 \exp(-\lambda_{X,2}t) \cos(2\pi\nu_2 t + \varphi). \quad (5.11)$$

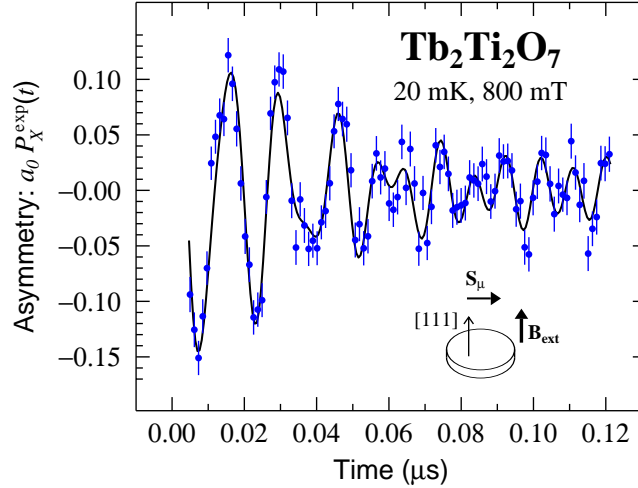


Figure 5.14: A typical transverse-field  $\mu$ SR asymmetry time spectrum recorded at  $T = 20$  mK for a mosaic of  $Tb_2Ti_2O_7$  crystals with  $\mathbf{B}_{\text{ext}}$  applied along a three-fold axis and  $B_{\text{ext}} = 800$  mT. The black solid line is a fit of Eq. 5.11 to the data. Picture reproduced from Ref. [235] with kind permission of IOP Publishing.

The transverse relaxation rates  $\lambda_{X,1}$  and  $\lambda_{X,2}$  illustrate the damping of the oscillations and reflect the spread of muon frequencies arising from the field distribution, as already explained in Sec. 4.8. The analysis of the measured spectrum gives  $a_1 = 0.192(13)$  and  $a_2 = 0.028(2)$ . These initial asymmetries are found to be constant when varying the magnetic field. Note that only  $\approx 13\%$  of the incoming muons are stopped in the surroundings of the sample with  $\nu_2 = 108.46(1)$  MHz. This value is very close to the precession frequency  $\nu_{\text{ext}} = \gamma_{\mu} B_{\text{ext}} / (2\pi) = 108.43$  MHz expected for muons subject to a field of  $B_{\text{ext}} = 800$  mT.

The purpose of this experiment was not to focus on the muon frequency  $\nu_1$  but on the normalised muon frequency shift  $K_{\text{exp}} = (\nu_1 - \nu_{\text{ext}}) / \nu_{\text{ext}}$ , introduced in Sec. 2.6.6. The field dependence of this quantity is displayed in Fig. 5.15 at  $T = 20$  and 500 mK. Below  $B_{\text{ext}} \approx 0.6$  T, an extra contribution to  $K_{\text{exp}}$  appears for data recorded at  $T = 20$  mK, compared to data recorded at 500 mK. This goes in line with the first magnetisation curves recorded in Ref. [225] and displayed in the left panel of Fig. 5.13.

Note that the corrections of the demagnetising field are complicated in our case since the sample is not a pure ellipsoid, leading to an inhomogeneous demagnetisation field. Consequently, we refrain to do it for our data. However, we recall the definition of the frequency shift introduced in Sec. 2.6.6, see Eq. 2.48:

$$K_{\text{exp}} = K_{\mu} + \mu_0 \alpha_D \frac{M}{B_{\text{ext}}}, \quad (5.12)$$

where  $\alpha_D$  is a constant,  $M$  is the magnetisation, and  $K_{\mu} = K'_{\text{dip}}$  is the muon Knight shift that arises only from the dipolar field created by the magnetic moments inside the Lorentz sphere. This field can be defined in terms of a field dipole tensor  $D_{\mathbf{r}_i}^{\alpha\beta}$  associated with site  $\mathbf{r}_i$  [160]:

$$B_{\text{dip}}^{\alpha} = \frac{\mu_0}{4\pi} \frac{1}{v_{\text{Tb}}} \sum_{\beta} \sum_{i=1}^{N_L} D_{\mathbf{r}_i}^{\alpha\beta} m_i^{\beta}, \quad (5.13)$$

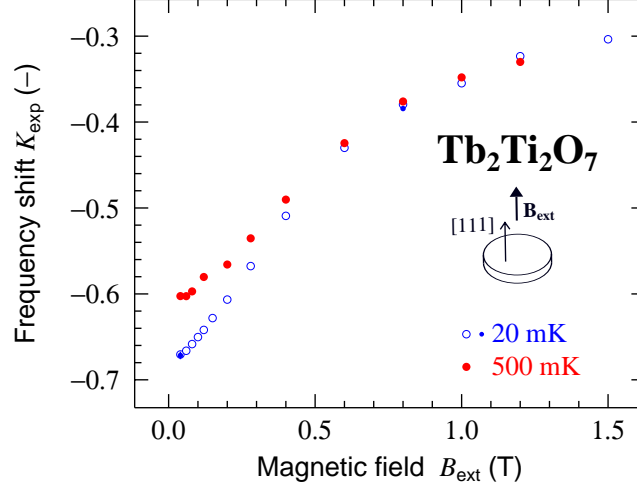


Figure 5.15: *Field dependence of the normalised muon frequency shift  $K_{\text{exp}}$  recorded at  $T = 20$  and  $500$  mK. The errors bars are smaller than the symbols. The data at  $T = 20$  mK shown by open blue circles have been measured after zero-field cooling in increasing  $B_{\text{ext}}$  up to  $1.5$  T. Further data (close blue circles) recorded after decreasing  $B_{\text{ext}}$  from  $800$  to  $40$  mT show no hysteresis. This is in contrast to the temperature dependence of  $K_{\text{exp}}$  measured at  $60$  mT after zero-field and field cooling, see inset of the right panel of Fig. 5.4. Data at  $T = 500$  mK shown by red circles have been recorded after heating the sample from  $T = 20$  mK and  $B_{\text{ext}} = 40$  mT to  $T = 500$  mK, after which the field was gradually increased up to  $1.5$  T. Picture reproduced from Ref. [235] with kind permission of IOP Publishing.*

where the sum runs over the  $N_L$  magnetic moments inside the Lorentz sphere,  $v_{\text{Tb}}$  is the volume per terbium ion<sup>1</sup> and:

$$D_{\mathbf{r}_i}^{\alpha\beta} = v_{\text{Tb}} \left( -\frac{\delta_{\alpha,\beta}}{r_i^3} + \frac{3r_i^\alpha r_i^\beta}{r_i^5} \right). \quad (5.14)$$

The muon Knight shift can be expressed as:

$$K_\mu = K'_{\text{dip}} = \frac{\mathbf{B}_{\text{ext}} \cdot \mathbf{B}'_{\text{dip}}}{B_{\text{ext}}^2}. \quad (5.15)$$

With our assumption,<sup>1</sup>  $m_i^\beta = v_{\text{Tb}} M^\beta$ , where  $M^\beta$  is the  $\beta$  component of the total magnetisation  $M$  per unit volume. In the paramagnetic regime,  $M^\beta = M \delta_{\beta,Z}$ , where the magnetic field is applied along the Z axis. We derive:

$$K_\mu = K'_{\text{dip}} = \frac{\mu_0}{4\pi} \left( \sum_{i=1}^{N_L} D_{\mathbf{r}_i}^{ZZ} \right) \frac{M}{B_{\text{ext}}}, \quad (5.16)$$

Therefore, combining Eq. 5.12 and Eq. 5.16, the frequency shift can be written as:

$$K_{\text{exp}} = \mu_0 \left[ \alpha_D + \frac{1}{4\pi} \left( \sum_{i=1}^{N_L} D_{\mathbf{r}_i}^{ZZ} \right) \right] \frac{M}{B_{\text{ext}}}. \quad (5.17)$$

<sup>1</sup>Note that we assume all the terbium ions to be magnetically equivalent, i.e. we consider only one type of magnetic ion per magnetic unit cell. Therefore, we adopt formula valid for Bravais lattices.

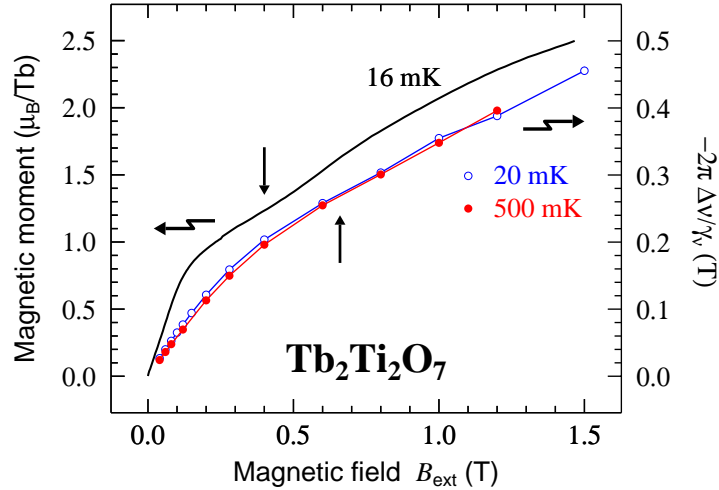


Figure 5.16: Open circles and bullets: product  $-B_{\text{ext}}K_{\text{exp}} = -2\pi\Delta\nu/\gamma_{\mu}$  deduced from the 20 and 500 mK data displayed in Fig. 5.15, versus  $B_{\text{ext}}$ . The experimental points are linked by segments. Solid line: field dependence of the terbium magnetic moment measured at 16 mK for  $\mathbf{B}_{\text{ext}}$  applied along a [111] crystal direction. As explained in the main text, the latter curve is computed from the data published by Yin *et al* [226]. Picture reproduced from Ref. [235] with kind permission of IOP Publishing.

Consequently, recalling that  $K_{\text{exp}} < 0$  here, we expect the product  $-K_{\text{exp}}B_{\text{ext}}$  to be proportional to  $M$ . This quantity is displayed in Fig. 5.16. As discussed in Sec. 5.3.2, if there was a definitive plateau in the magnetisation, the product would be field independent in a finite field range. This is not observed. However, as indicated by the up-arrow, a weak inflection point is present for the 20 mK data at  $B_{\text{ext}} \simeq 0.66$  T. It has disappeared at 500 mK. Yin *et al.* [226] have performed a.c. magnetic susceptibility measurements on a crystal of  $Tb_2Ti_2O_7$  with the external field applied along [111]. The real part of the susceptibility, outside the linear regime, is expressed as:

$$\chi'_{\text{ac}} = \mu_0 \frac{dM}{dB_{\text{ext}}}, \quad (5.18)$$

and therefore the magnetic moment (see the black solid line in Fig. 5.16), is deduced by field integration of the data displayed in the right panel of Fig. 5.13 as:

$$m = \int_0^{B_{\text{max}}} \frac{v_{\text{Tb}}}{\mu_0} \chi'_{\text{ac}} dB_{\text{ext}}, \quad (5.19)$$

where  $B_{\text{max}} = 1.5$  T. The black down arrow indicates an inflection point located at  $B_{\text{ext}} = 0.4$  T. Note that the data were corrected from demagnetising effects according to Ref. [248]. However, the real part of the susceptibility is plotted versus the external field. Following the note 35 of Ref. [226], the internal field at  $B_{\text{ext}} = 0.59$  T, i.e. the second maximum in the curve of the magnetisation derivative, is  $B_{\text{int}} = 0.53$  T, i.e. a relatively small shift of 60 mT. The geometry of our experiments gives rise to a much more important demagnetising field. As we found an inflexion point at 0.66 T while it is found at  $\approx 0.4$  T in Ref. [226], we assume a demagnetising field of  $\approx 0.3$  T so that the inflection point of our data and those of Ref. [226] would coincide. Therefore, our  $\mu$ SR

measurements and a.c. susceptibility measurements of Ref. [226] reveal an inflection point located in terms of the internal field at  $B_{\text{int}} \approx 0.3$  T. However, this result cannot allow us to draw a definitive conclusion whether the magnetisation plateau exists or not.

## 5.4 Conclusions

The pyrochlore compound  $Tb_2Ti_2O_7$  fails to order down to the lowest temperatures despite a significant Curie-Weiss constant. Spin correlations restricted over a single tetrahedron exist deep in the paramagnetic regime. On cooling the sample, a slowing down of the fluctuations was revealed by a large panel of techniques covering an extended time range (neutron scattering, neutron spin echo,  $\mu$ SR and a.c. susceptibility measurements), suggesting that the compound would enter a cooperative paramagnetic (or spin-liquid) state at roughly  $T_{\text{cp}} = 2$  K.

Two different ground states were proposed. One is that  $Tb_2Ti_2O_7$  would be an experimental realisation of a quantum spin-ice. Pinch points evidenced by polarised neutron scattering are a proof of algebraic spins correlations, characteristic of a spin-ice configuration. An anisotropic exchange Hamiltonian, considering an admixture of the ground state and the first excited crystal-electric-field level, and within the approximation of non-interacting tetrahedra, leads to the prediction of Ising spins constrained to satisfy the ice rule, with the existence of small transverse spin interaction terms lifting the degeneracy expected in a classical spin-ice, i.e. the quantum spin-ice state. This model accounts very well for the diffuse neutron scattering in the paramagnetic regime. A magnetisation plateau has been predicted when a magnetic field is applied along the [111] direction, similarly to what is predicted and observed in the case of the classical spin-ice state. However, neither a.c. susceptibility nor transverse field  $\mu$ SR measurements were able to confirm this prediction. Only a weak inflection point in the field dependence of the magnetisation is found at  $\approx 0.3$  T. The model uses an isotropic nearest-neighbour exchange constant although the pyrochlore compounds are found to interact strongly anisotropically. As suggested in Ref. [225], increasing the mean value of the exchange constant might decrease the temperature at which the magnetisation plateau is expected.

A second proposal is the existence of a low-temperature tetragonal distortion along the cubic axis, as suggested by specific heat and inelastic neutron scattering measurements. An anomaly in the frequency shift of the muon spin precession revealed by transverse  $\mu$ SR experiments and in the specific heat occurs at  $T_t \approx 0.15$  K. The compound enters a glassy state, as confirmed by d.c. and a.c. susceptibility measurements. However, the latter experiments precludes a spin-glass transition. This anomaly could be a signature of a Jahn-Teller transition. The broadening of the Bragg peaks observed for  $T \leq 20$  K as well as an anomalous lattice parameter expansion [233] support this scenario. However, these conclusions are not confirmed by our synchrotron measurements and X-ray powder diffraction results of Ref. [234]. Therefore, no evidence of such a transition is revealed, at least down to 4 K.

As pictured in the left panel of Fig. 5.4, the elastic constants decrease below  $\approx 50$  K [232]. This property was also evidenced in Ref. [249] where the Young modulus strongly decreases in the same temperature range. Therefore strong magneto-elastic

effects are at play in  $\text{Tb}_2\text{Ti}_2\text{O}_7$  and should be considered.

# Chapter 6

## General conclusions

This work was dedicated to the study of geometrically frustrated magnets on a pyrochlore lattice of chemical formula  $R_2M_2O_7$ , where  $R$  is a rare earth and  $M = \text{Ti}$  or  $\text{Sn}$ . We have focused our attention in this manuscript on the crystal-electric-field acting at the rare earth site, the characterisation of the compound  $\text{Nd}_2\text{Sn}_2\text{O}_7$  with a large panel of bulk and microscopic measurements, and finally added some information on the puzzling compound  $\text{Tb}_2\text{Ti}_2\text{O}_7$ . In this final chapter, we sum up some important results and discuss some perspectives of interest.

### 6.1 Beyond the Stevens Hamiltonian

We have first studied the crystal-electric-field acting at the rare earth site in the pyrochlore series  $R_2M_2O_7$ . The aim was to analyse simultaneously, using a simple scaling law, published inelastic neutron scattering data and our own neutron time-of-flight measurements in the case of the titanate or stannate compounds, respectively, in order to determine a single set of CEF parameters. The analysis of the CEF is important in order to understand the low temperature properties of frustrated magnets: it provides information on the magnetic ground state through the CEF energy levels: influence or not of the excited energy levels as in the terbium case. It also gives the character of the spin anisotropy and the magnitude of the ground state magnetic moment: reduction of the magnetic moment in the ordered phase, strength of the dipolar interactions. Finally, it gives access to the ground state wavefunctions used to determine the presence or not of transverse exchange couplings involved in the anisotropic exchange Hamiltonian for instance. In the case of the titanate series, a reliable set of CEF parameters allows us to describe the full set of available inelastic neutron scattering spectra and provides spectroscopic factors in agreement with the spin anisotropy proposed in the literature. The case of the stannate series is slightly less conclusive: a single set of CEF parameters predicts an energy level scheme in agreement with the CEF transitions measured by inelastic neutron scattering spectroscopy and constitutes a good starting point to the analysis of the neutron intensities. However, we should note that a close but different set of CEF parameters is necessary in order to analyse inelastic neutron spectra for each investigated compound, namely  $\text{Tb}_2\text{Sn}_2\text{O}_7$ ,  $\text{Ho}_2\text{Sn}_2\text{O}_7$  and published data of  $\text{Er}_2\text{Sn}_2\text{O}_7$ .

Neutron time-of-flight measurements have also been performed on  $\text{Nd}_2\text{Sn}_2\text{O}_7$ . We did not succeed to involve it in a global analysis with the aforementioned compounds

and also did not succeed to analyse simultaneously inelastic neutron scattering spectra covering the full CEF energy levels. Since the splitting between the ground state and the first excited multiplets arising from the spin-orbit coupling  $\Delta_{\text{so}} = 236$  meV is roughly of the same order of magnitude as the overall splitting of the ground state multiplets, i.e. the highest CEF energy level lies at  $\approx 110$  meV, at least a mixing between the  ${}^4I_{9/2}$  ground state and the  ${}^4I_{11/2}$  first excited multiplet<sup>1</sup> should be considered. Therefore, the CEF Hamiltonian acting within both multiplets needs to be considered. Following the work of Ref. [250], matrix elements within the two multiplets are computed as:

$$\langle J, m_J | \mathcal{H}_{\text{CEF}}^{(J)} | J, m'_J \rangle = \sum_{n,m} B_n^m \langle J, m_J | O_n^m | J, m'_J \rangle, \quad (6.1)$$

and,

$$\begin{aligned} \langle (J+1), m_{(J+1)} | \mathcal{H}_{\text{CEF}}^{(J+1)} | (J+1), m'_{(J+1)} \rangle &= \Delta_{\text{so}} \delta_{m_{(J+1)}, m'_{(J+1)}} + \\ \sum_{n,m} B_n^m \langle (J+1), m_{(J+1)} | O_n^m | (J+1), m'_{(J+1)} \rangle, \end{aligned} \quad (6.2)$$

where  $\mathcal{H}_{\text{CEF}}^{(J)}$  and  $\mathcal{H}_{\text{CEF}}^{(J+1)}$  refer to the Stevens Hamiltonian determined in Eq. 3.12 and acting on the ground state and first excited multiplets within the Zeeman basis  $|J, m_J\rangle$  and  $|(J+1), m_{(J+1)}\rangle$ , respectively.<sup>2</sup> The  $J$ -mixing effect arising from the coupling between the two multiplets is accounted for with the mixing Hamiltonian  $\mathcal{H}_{\text{CEF}}^{(J),\text{mix}}$  acting on the ground state multiplet. However, we cannot use anymore the CEF Hamiltonian defined in terms of Stevens operators in Eq. 3.12, since the operator equivalent method derived from the Wigner-Eckart theorem used in App. B is only available within the  $|J, m_J\rangle$  basis. Here, we have to calculate off-diagonal matrix elements between the  $|J, m_J\rangle$  and  $|(J+1), m_{(J+1)}\rangle$  basis: we need to go back to a general expression of the CEF Hamiltonian introduced in Eq. B.11, and combining Eq. B.10 and Eq. B.12:

$$\mathcal{H}_{\text{CEF}} = -\frac{e}{4\pi\epsilon_0} \sum_j \sum_n \sum_{m=-n}^n \gamma_{nm} p_n^m f_n^m(x_j, y_j, z_j), \quad (6.3)$$

where  $p_n^m$  is a prefactor,  $f_n^m(x_j, y_j, z_j)$  a polynomial function, and the index  $j$  refers to the sum over the  $4f$  electrons (see App. B). Therefore,  $\mathcal{H}_{\text{CEF}}^{(J),\text{mix}}$  is computed as:

$$\begin{aligned} \langle J, m_J | \mathcal{H}_{\text{CEF}}^{(J),\text{mix}} | (J+1), m''_{(J+1)} \rangle &= \\ -\frac{e}{4\pi\epsilon_0} \sum_{n,m} \gamma_{nm} p_n^m \langle J, m_J | \sum_j f_n^m(x_j, y_j, z_j) | (J+1), m''_{(J+1)} \rangle. \end{aligned} \quad (6.4)$$

The latter equation is simplified using the Wigner-Eckart theorem in its more general form:

<sup>1</sup>For a given ion with a  $4f$  electric shell less than half-filled, the total angular momentum of the first excited multiplet is equal to  $(J+1)$  [163].

<sup>2</sup>We recall that  $-J \leq m_J \leq J$  and  $-J-1 \leq m_{(J+1)} \leq J+1$

$$\begin{aligned} \langle J, m_J | \sum_j f_n^m(x_j, y_j, z_j) | (J+1), m_{(J+1)}'' \rangle = \\ (-1)^{J-m_J} \sqrt{2J+1} \langle J | f_n^0(x_j, y_j, z_j) | J+1 \rangle \begin{pmatrix} J & n & J+1 \\ -m_J & m & m_{(J+1)}'' \end{pmatrix}, \end{aligned} \quad (6.5)$$

where  $\langle J | f_n^0(x_j, y_j, z_j) | J+1 \rangle$  are coefficients tabulated in Ref. [163], and the matrix element is the  $3j$  Wigner coefficient. These coefficients vanish if  $m_{(J+1)}'' + m_J - m \neq 0$ . Therefore, the total CEF Hamiltonian can be written in the following matrix form:

$$\begin{pmatrix} \langle J, m_J | \mathcal{H}_{\text{CEF}}^{(J)} | J, m_J' \rangle & \langle J, m_J | \mathcal{H}_{\text{CEF}}^{(J, \text{mix})} | (J+1), m_{(J+1)}'' \rangle \\ \langle (J+1), m_{(J+1)} | \mathcal{H}_{\text{CEF}}^{(J+1, \text{mix})} | J, m_J' \rangle & \langle (J+1), m_{(J+1)} | \mathcal{H}_{\text{CEF}}^{(J+1)} | (J+1), m_{(J+1)}'' \rangle \end{pmatrix}.$$

Note that in the case of the neodymium compound, the dimension of this matrix is  $d = (2J+1)(2J+2) = 110$ . To compare with the approximation made in Chapter. 3, the highest matrix dimension is in the case of the holmium ion where  $d = 2J+1 = 17$ .

## 6.2 Observation of spontaneous oscillations

We have reported in this work that the pyrochlore compound  $\text{Nd}_2\text{Sn}_2\text{O}_7$  exhibits a second-order magnetic transition at  $T_c = 0.91$  K. Neutron diffraction experiments reveal an all-in-all-out spin configuration. The long-range nature of the magnetic order is confirmed by the observation of spontaneous oscillations in zero-field  $\mu\text{SR}$  measurements. If the latter result is not surprising for a magnetically ordered compound as seen in  $\text{Gd}_2\text{Ti}_2\text{O}_7$  [112] and  $\text{Gd}_2\text{Sn}_2\text{O}_7$  [116], other pyrochlore compounds do not display any spontaneous wiggles despite the presence of magnetic Bragg peaks such as  $\text{Yb}_2\text{Ti}_2\text{O}_7$ ,  $\text{Yb}_2\text{Sn}_2\text{O}_7$  and  $\text{Tb}_2\text{Sn}_2\text{O}_7$ . An explanation for the latter compound has been put forward considering the dynamical nature of the local field jumping between two opposite configurations [75]. Following the picture of the dumbell model introduced in Chapter 1, the authors of Ref. [251] generalise in a recent paper the concept of fragmentation of the magnetic field associated to the magnetic moments for Ising-like pyrochlore compounds. Focusing on a single tetrahedron, the magnetic moment density  $\mathbf{M}$  can be written according to the Helmholtz decomposition, i.e. a curl-free — or divergence-full — and a divergence-free components [251] that is to say a transverse and a longitudinal part of the local magnetisation:

$$\mathbf{M} = \nabla\Psi + \nabla \times \mathbf{Q} = \mathbf{M}_m + \mathbf{M}_d. \quad (6.6)$$

The first contribution  $\mathbf{M}_m$  arises from the gradient of a scalar potential and represents the resulting magnetic charge of the dumbell model, and the second one  $\mathbf{M}_d$ , the divergence-free part, is a dipolar field. In the trivial case of the ice rule, i.e. the two-in/two-out spin configuration, the longitudinal part of the decomposition vanishes, i.e.  $\mathbf{M}_m = \mathbf{0}$  and we have  $\nabla \cdot \mathbf{B} = \nabla \cdot \mathbf{M} = 0$ . In the spin-ice case, an excitation consists on breaking the ice-rule by flipping a spin, and thus lead to the nucleation of a pair of magnetic monopoles. The two components of the decomposition of Eq. 6.6 do not

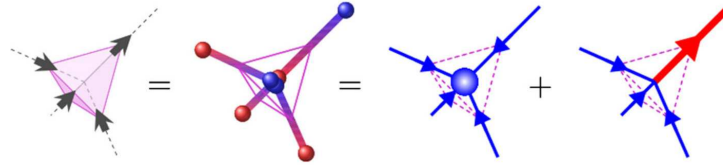


Figure 6.1: Illustration of the three-in-one-out spin configuration (left) in terms of the dumbbell model (middle) and Helmholtz decomposition into a static magnetic charge modelling the long-range order and a fluctuating dipolar field illustrating monopole dynamics. Picture taken from Ref. [251].

vanish, as illustrated in Fig. 6.1, leading to the coexistence of a static field arising from the magnetic charge at the center of the tetrahedron and a dipolar field illustrating the dynamical nature of a fluid of magnetic monopoles. Then, when two monopoles are nucleated, i.e. the all-in-all-out spin configuration, the divergence-free part is suppressed and only the longitudinal part of the decomposition survives, i.e. a local static field arising from the central magnetic charge leading to a magnetic long-range order, without a dynamical dipolar field. Therefore, since the muon spin precession occurs around only a static field, spontaneous oscillations are observed as in the case of  $\text{Nd}_2\text{Sn}_2\text{O}_7$ . On the other side, the fluctuations of the dipolar field driven by the magnetic monopole dynamics could lead to the absence of the expected oscillations in zero-field  $\mu\text{SR}$  measurements. Let us focus on the case of  $\text{Yb}_2\text{Ti}_2\text{O}_7$  and  $\text{Yb}_2\text{Sn}_2\text{O}_7$  where the spontaneous magnetic moment  $m_{\text{sp}}(0)$  has been found to lie at  $44^\circ$  and  $65^\circ$  with a magnitude of  $1.15$  and  $1.1 \mu_{\text{B}}$ , respectively, see Chapter 1. The projection of the spontaneous magnetic moment over the  $[111]$  axis lead to  $m_{111}(0) = 0.83$  and  $0.46 \mu_{\text{B}}$ , respectively. Hence, the magnitude of the transverse part of the Helmholtz decomposition is not negligible and may explain the absence of spontaneous oscillations in the magnetic ordered state. In contrast,  $m_{111}(0) = 5.3 \mu_{\text{B}}$  for  $\text{Tb}_2\text{Sn}_2\text{O}_7$  and the origin of the dynamical nature of the local field could not be supported with this interpretation.

Note that we do not discuss the case of  $\text{Er}_2\text{Sn}_2\text{O}_7$  since the long-range nature is not fully established at the time of writing, and  $\text{Er}_2\text{Ti}_2\text{O}_7$  where the shape of the  $\mu\text{SR}$  spectra is misunderstood and could be associated to a complex field distribution at the muon site.

### 6.3 Origin of spin dynamics

In the case of Ising spins with antiferromagnetic interactions, the all-in-all-out magnetic structure has been predicted with a magnetic propagation wavevector  $\mathbf{k}_{\text{mag}} = (0, 0, 0)$ , see Chapter 1, in agreement with our neutron diffraction analysis on  $\text{Nd}_2\text{Sn}_2\text{O}_7$ . However, this picture is barely compatible with first, the persistence of spin dynamics revealed by the temperature independent behaviour of the spin-lattice relaxation rate inferred from  $\mu\text{SR}$  experiments and ascribed to one-dimensional spin loops excitations, and secondly with the magnon-like dependence observed in the low temperature range of the specific heat.

$\text{Nd}_2\text{Sn}_2\text{O}_7$  is a Kramers ion, i.e. energy levels are at least double degenerate. Hence,

the ground state doublet can be described by an effective spin  $S^\mu$  ( $\mu = x, y, z$ ) [163]. As mentioned in Chapter 3, wavefunctions of a given doublet are related by an odd time reversal operator. However, the nature of the Kramers ground state doublet is defined by the symmetries of the local point group at the rare earth site, here  $D_{3d}$  which are generated by a threefold symmetry axis  $C_3$ , a mirror  $M$  and an inversion center  $I$ . Looking how the effective spin operator is transformed under these symmetries defines the nature of the doublet. In most cases, these transformations operate as follows:

$$\begin{aligned} C_3, I : S^\mu &\rightarrow S^\mu \\ M : S^\mu &\rightarrow -S^\mu. \end{aligned} \quad (6.7)$$

Therefore, the effective spin behaves as a magnetic dipole and the ground state doublet is called dipolar. The authors of Ref. [252] have considered an other kind of Kramers doublet, the dipolar-octupolar doublet where the symmetries of the point group act on the effective spin in the same manner as defined in Eq. 6.7 except for the  $y$  component of the effective spin under a mirror operation:

$$M : S^y \rightarrow S^y. \quad (6.8)$$

The authors of Ref. [252] have expressed  $S^y$  in terms of an octupolar tensor, hence the doublet denomination. Moreover, they have shown that in the case of the point group  $D_{3d}$ , if  $J = 9/2$  or  $15/2$ , if the crystal field parameter  $B_0^2 < 0$ , and if this parameter is larger than the other crystal-electric-field parameters involved in the Stevens Hamiltonian of Eq. 3.12, then the Kramers ground state is a dipolar-octupolar doublet. As seen in Chapter 3, this is the case of  $\text{Dy}_2(\text{Ti,Sn})_2\text{O}_7$ . Whether  $\text{Nd}_2\text{Sn}_2\text{O}_7$  is a dipolar-octupolar ground state doublet or not is an open question. Despite the fact that we do not succeed to include this compound in our global analysis looking for a single set of CEF parameters, and since considering the effect of excited multiplets was out of the scope of this work, we may assume that  $\text{Nd}_2\text{Sn}_2\text{O}_7$  is closely related to  $\text{Nd}_2\text{Ir}_2\text{O}_7$ , the latter compound fulfilling the condition of a dipolar-octupolar Kramers ground state [253].

The aim is to diagonalise the general anisotropic exchange Hamiltonian introduced in Eq. 1.12 in the specific case of a dipolar-octupolar doublet. This Hamiltonian can be reduced by means of the symmetry properties of the effective spin to the so-called XYZ model:

$$\mathcal{H}_{\text{XYZ}} = \sum_{i,j} \tilde{J}_x S_i^x S_j^x + \tilde{J}_y S_i^y S_j^y + \tilde{J}_z S_i^z S_j^z, \quad (6.9)$$

where  $\mathcal{I}_{zz} = \tilde{J}_z$ ,  $\mathcal{I}_{\pm\pm} = -\frac{1}{4}(\tilde{J}_x + \tilde{J}_y)$ ,  $\mathcal{I}_{\pm\pm\pm} = \frac{1}{4}(\tilde{J}_x - \tilde{J}_y)$ , and  $\mathcal{I}_{z\pm} = 0$ . Therefore, using quantum Monte Carlo calculations, the authors of Ref. [252] have computed the XYZ phase diagram, illustrated in Fig. 6.2. In a specific range of parameters the all-in-all-out phase is predicted, thus coexisting with the presence of transverse exchange coupling constants and could slightly tilt the spins away from its Ising direction, explaining the dynamics observed in the ordered phase. Therefore, the determination of these exchange parameters should be interesting for  $\text{Nd}_2\text{Sn}_2\text{O}_7$ .

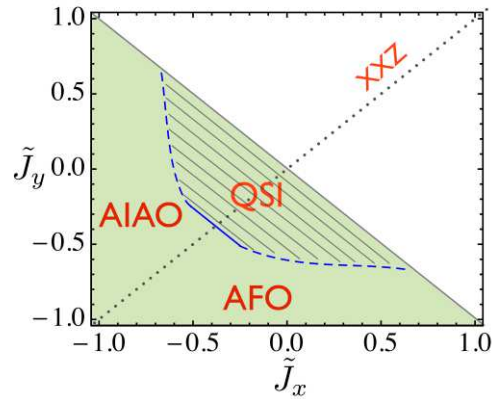


Figure 6.2: Phase diagram resulting from the XYZ model. The dotted line refers to the XXZ model introduced by Hermele *et al.* [54], see Chapter 1. All-in-all-out, quantum spin ice, and octupolar antiferromagnetic phases are predicted. Reprinted figure with permission from Ref. [252]. Copyright 2015 by the American Physical Society.

## 6.4 A magneto-elastic mode: solving the $Tb_2Ti_2O_7$ case

We have seen in Chapter. 5 that no broadening of Bragg peaks exist down to  $T = 4$  K and thus the Jahn-Teller transition expected at lower temperatures is not confirmed. The scenario proposing that  $Tb_2Ti_2O_7$  is a realisation of a quantum spin ice is put in a difficult position since no clear evidence of a magnetisation plateau has been evidenced. Using polarised neutrons on a triple-axis spectrometer, a recent work [236] has revealed the existence of a dispersive excitation slightly above the first excited crystal-electric-field energy level at  $T = 50$  mK. This mode carries magnetic transverse fluctuations in the wavevector region (220) whereas a transverse phonon-like mode contributes at higher  $q$ -values. Since these two contributions overlap, the authors of Ref. [236] suggest they have a common origin, i.e. a magneto-elastic mode (MEM) as it carries both magnetic and structural fluctuations.

## 6.5 New perspectives: the spinel compounds

An interesting direction to prospect is the study of spinel compounds of chemical formula  $CdR_2X_4$  where  $R$  is a lanthanide and  $X = S$  or  $Se$ . They have the same magnetic frustrated lattice as the pyrochlore compounds, i.e. magnetic ions sit on a corner-sharing tetrahedra network, but the local environment around the rare earth ion is different leading to different crystal-electric-field properties, see the left panel of Fig. 6.3. For instance, whereas the pyrochlore counterpart  $Er_2Ti_2O_7$  exhibits a magnetic long-range order at  $T_c = 1.2$  K, see Chapter 1, a spin-ice behaviour has been discovered in  $CdEr_2Se_4$  [254] since no long-range order is evidenced by specific heat measurements and the residual magnetic entropy is in agreement with the prediction of the two-in/two-out classical spin ice ground state. Hence, the spin anisotropies in spinel compounds that arise from the crystal-electric-field seem drastically different to those of the pyrochlore

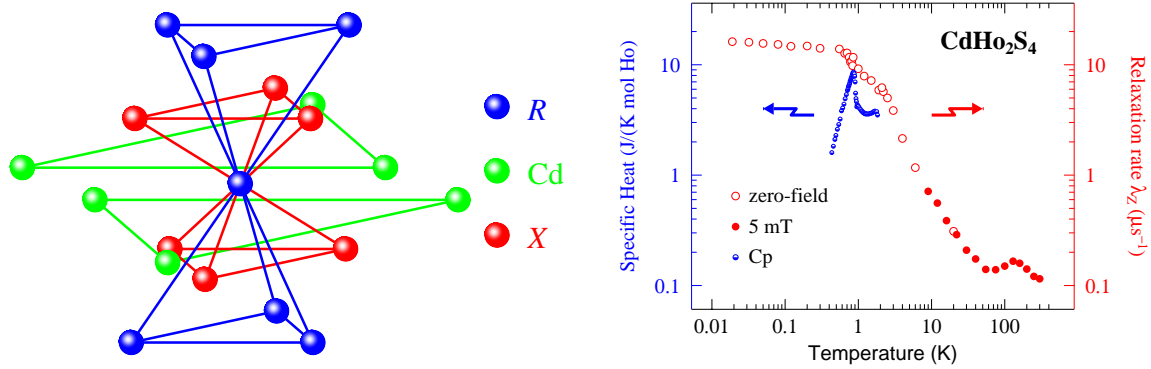


Figure 6.3: *Left: local environment at the rare earth site of spinel compounds of chemical formula  $\text{CdR}_2\text{X}_4$ , where  $R$  is a lanthanide and  $X = \text{S}, \text{Se}$ .  $\text{Cd}$ ,  $R$ , and  $X$  are displayed by green, blue, and red spheres respectively. Right: temperature dependence of the specific heat measured on  $\text{CdHo}_2\text{S}_4$  showing the magnetic transition at  $T_c = 0.87$  K, and displayed on the left ordinate axis by half-filled blue circles. The temperature behaviour of the spin-lattice relaxation rate deduced from zero and 5 mT longitudinal field  $\mu\text{SR}$  measurements is reported on the right ordinate axis with empty and full red circles, respectively. Picture modified from Ref. [212].*

compounds. Therefore, looking for new exotic magnetic ground states, a systematic study of the compounds  $\text{Cd}_2\text{R}_2\text{X}_4$  (where  $R = \text{Ho}$  or  $\text{Yb}$  and  $X = \text{S}$  or  $\text{Se}$ ) has been undertaken during this PhD thesis including bulk and  $\mu\text{SR}$  measurements. As an example, if holmium based pyrochlore compounds are undoubtedly classified as classical spin-ice,  $\text{CdHo}_2\text{S}_4$  shows a magnetic transition at  $T_c = 0.87$  K. In addition, and similarly to  $\text{Nd}_2\text{Sn}_2\text{O}_7$ , unidimensional spin loops excitations are argued to be at the origin of spin dynamics, since the spin lattice relaxation rate inferred from  $\mu\text{SR}$  experiments is temperature independent, as shown in the right panel of Fig. 6.3.

# Appendix A

## Crystallography of the pyrochlore compounds

Details of the crystallographic structure of the pyrochlore compounds are provided in this appendix. We recall that magnetic ions lie at the vertices of a corner-sharing tetrahedra network giving rise to a realisation of a three dimensional geometrically frustrated lattice. The generic chemical formula is  $R_2M_2(O1)_6(O2)$  — the two nonequivalent crystallographic sites for oxygen atoms are labelled O1 and O2 — where  $R$  is a magnetic ion, a rare earth, and  $M = \text{Ti}$  or  $\text{Sn}$  in this work. The pyrochlore compounds crystallise in the face centred cubic lattice (fcc), labelled  $F$  in the Bravais notation. The space group is  $Fd\bar{3}m$ , where the rare earth ions occupy the trigonal Wyckoff site  $16c$ , characterised by the local point group  $D_{3d}$ . We have chosen the origin of the lattice at the site symmetry  $\bar{3}m$ , and at the Wyckoff site  $16c$  of the atom  $M$ : this corresponds to the origin 2 in the International Tables for Crystallography. The list of the atomic positions in the Wyckoff notations, the local site symmetry and coordinates in the unit cell are given in Tab. A.1. To recover all the atomic positions in the unit cell, one has to apply the lattice translations associated to the fcc structure  $(\frac{1}{2}, \frac{1}{2}, 0)$ ,  $(\frac{1}{2}, 0, \frac{1}{2})$ , and  $(0, \frac{1}{2}, \frac{1}{2})$ . The unit cell gathering all the atoms is shown in the left panel of Fig. A.1. Oxygen atoms O1 located in the  $48f$  site in Wyckoff notations have a parameter  $x$  to be defined, i.e.  $x \approx 1/3$  in our case, and are rare-earth neighbours located in the vicinity of a plane perpendicular to the local trigonal  $[111]$  axis, as illustrated in the right panel of Fig. A.1, where the local environment at the rare earth site is shown. We will define this direction as the quantisation axis  $z$ . In Fig. A.2 is displayed a projection along the  $[111]$  axis of the pyrochlore structure revealing a sequence of alternatively triangular and Kagome planes, where the magnetic ions sit.

Atoms	Wyckoff sites	Site symmetry	coordinates
$R$	$16d$	$\bar{3}m$	$\frac{1}{2}, \frac{1}{2}, \frac{1}{2}$ $\frac{1}{4}, \frac{3}{4}, 0$ $\frac{3}{4}, 0, \frac{1}{4}$ $0, \frac{1}{4}, \frac{3}{4}$
$M$	$16c$	$\bar{3}m$	$0, 0, 0$ $\frac{3}{4}, \frac{1}{4}, \frac{1}{2}$ $\frac{1}{4}, \frac{1}{2}, \frac{3}{4}$ $\frac{1}{2}, \frac{3}{4}, \frac{1}{4}$
$O1$	$48f$	$2.mm$	$x, \frac{1}{8}, \frac{1}{8}$ $\bar{x} + \frac{3}{4}, \frac{1}{8}, \frac{5}{8}$ $\frac{1}{8}, x, \frac{1}{8}$ $\frac{5}{8}, \bar{x} + \frac{3}{4}, \frac{1}{8}$ $\frac{1}{8}, \frac{1}{8}, x$ $\frac{1}{8}, \frac{5}{8}, \bar{x} + \frac{3}{4}$ $\frac{7}{8}, x + \frac{1}{4}, \frac{3}{8}$ $\frac{7}{8}, \bar{x}, \frac{7}{8}$ $x + \frac{3}{4}, \frac{3}{8}, \frac{3}{8}$ $\bar{x} + \frac{1}{2}, \frac{7}{8}, \frac{3}{8}$ $\frac{7}{8}, \frac{3}{8}, \bar{x} + \frac{1}{2}$ $\frac{3}{8}, \frac{3}{8}, x + \frac{3}{4}$
$O2$	$8b$	$\bar{4}3m$	$\frac{3}{8}, \frac{3}{8}, \frac{3}{8}$ $\frac{1}{8}, \frac{5}{8}, \frac{1}{8}$

Table A.1: Atomic positions in Wyckoff notations, point symmetry and Cartesian coordinates of atoms belonging to the primitive cell. The two types of oxygen atoms are labelled  $O1$  and  $O2$ . Note that  $x$ , which is used to specify the  $O1$  oxygen coordinates, is a free parameter. Both the rare earth ions  $R$  and the atoms  $M$  are located at positions of symmetry  $\bar{3}m$ . We take the atom  $M$  at the origin of the lattice.

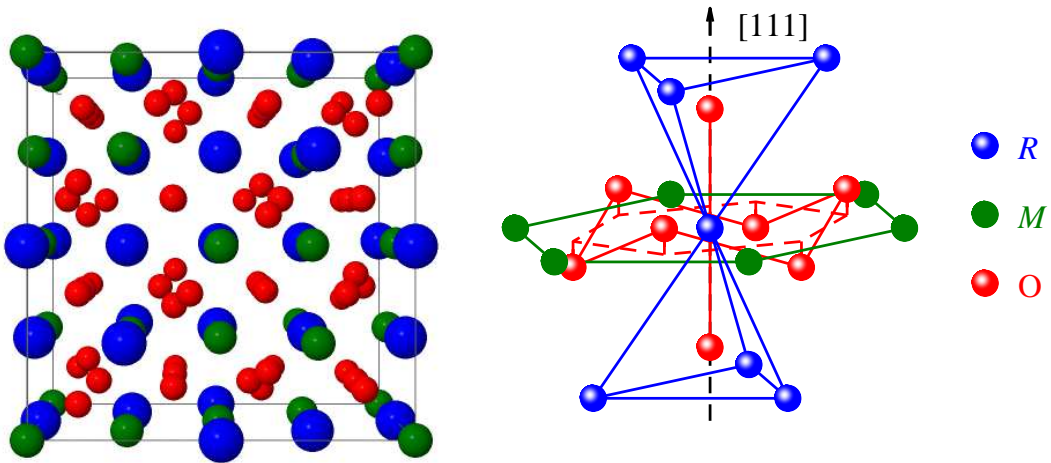


Figure A.1: Left: Crystallographic structure of the pyrochlore compound  $R_2M_2O_7$ . The blue, red and green spheres show the rare earth magnetic ions, the atoms  $M = \text{Ti}$  or  $\text{Sn}$ , and the oxygen atoms, respectively. Right: Local environment at the rare earth site. The threefold symmetry axis  $[111]$  is the quantisation axis.

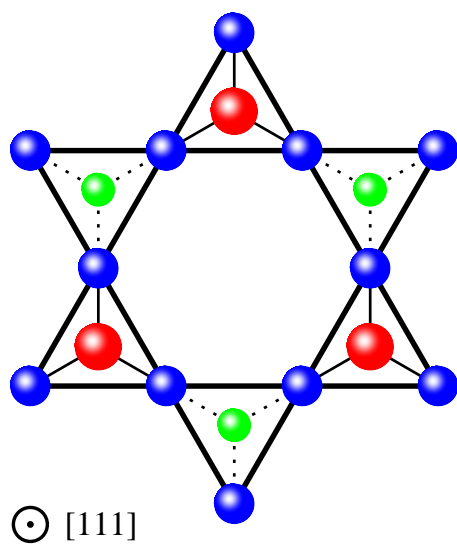


Figure A.2: Projection of the pyrochlore structure along the  $[111]$  axis: in this panel is only shown magnetic ions belonging alternatively to triangular (red and green spheres) and Kagome (blue spheres) planes.

# Appendix B

## The point charge model

In this appendix, we focus our attention on the determination of the crystal-electric-field Hamiltonian  $\mathcal{H}_{\text{CEF}}$ . The crystal-electric-field acting at the rare earth site results from the surrounding electric charge distribution, see the left panel of Fig. 3.1. The symmetry at the rare earth site is defined by the point group  $D_{3d}$ . The  $z$  axis is taken to be the local trigonal axis [111]. We will assume that the electric field distribution results from point charges surrounding the magnetic ions. The CEF potential taken at a lattice point  $(r, \theta, \phi)$  close to a magnetic ion is calculated as:

$$V_{\text{CEF}}(r, \theta, \phi) = \sum_i \frac{q_i}{|\mathbf{R}_i - \mathbf{r}|}, \quad (\text{B.1})$$

where the sum runs over the surrounding charges located at a distance  $\mathbf{R}_i$  from the rare earth site. The origin is taken at the rare earth site. Fig. B.1 sketches the different spatial variables of the problem. Thus, within the assumption that  $R_i \gg r$  the Coulombic potential can be developed as [255]:

$$\frac{1}{|\mathbf{R}_i - \mathbf{r}|} = \sum_{n=0}^{\infty} \frac{r^n}{R_i^{n+1}} P_n(\cos \omega_i), \quad (\text{B.2})$$

where  $P_n(\cos \omega_i)$  are the Legendre polynomials,  $\omega_i$  is the angle between  $\mathbf{R}_i$  and  $\mathbf{r}$  and related to their spherical coordinates as:

$$\cos \omega_i = \cos \theta \cos \theta_i + \sin \theta \sin \theta_i \cos(\phi - \phi_i) \quad (\text{B.3})$$

Thus, using the formula known as the spherical harmonic addition theorem, see for instance Ref. [256], Legendre polynomials are related to the spherical harmonics as:

$$P_n(\cos \omega_i) = \frac{4\pi}{(2n+1)} \sum_{m=-n}^n (-1)^m Y_n^{-m}(\theta_i, \phi_i) Y_n^m(\theta, \phi). \quad (\text{B.4})$$

The Legendre polynomials are defined with the Rodriguez formula [256]:

$$P_n(z) = \frac{1}{2^n n!} \frac{d^n}{dz^n} (z^2 - 1)^n, \quad (\text{B.5})$$

where here  $z = \cos \omega_i$ . The associated Legendre polynomials are defined as:

$$P_n^m(z) = (-1)^m (1 - z^2)^{m/2} \frac{d^m}{dz^m} P_n(z). \quad (\text{B.6})$$

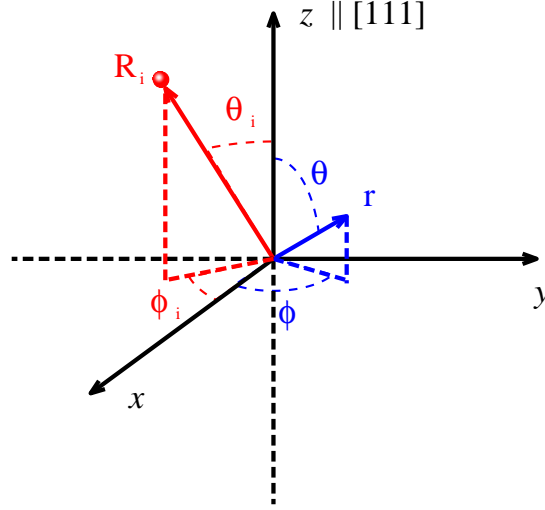


Figure B.1: Local frame with the origin taken at the rare earth site. The  $z$  axis is parallel to the  $[111]$  direction, a local trigonal symmetry axis at the rare earth site. The crystal-electric-field potential is calculated at the lattice point  $(r, \theta, \phi)$ , displayed in blue. The coordinates  $(R_i, \theta_i, \phi_i)$  of a surrounding electric charge are shown in red.

Note that  $P_n(z) \equiv P_n^0(z)$ . Thus, the spherical harmonics result from the associated Legendre polynomials as [164]:

$$Y_n^m(\theta, \phi) = (-1)^{(m+|m|)/2} \left[ \frac{(2n+1)(n-|m|)!}{2(n+|m|)!} \right]^{\frac{1}{2}} \frac{1}{(2\pi)^{\frac{1}{2}}} P_n^{|m|}(\cos \theta) \exp(im\phi). \quad (\text{B.7})$$

Therefore the CEF potential is written as:

$$\begin{aligned} V_{\text{CEF}}(r, \theta, \phi) &= \sum_n \sum_{m=-n}^n r^n \gamma'_{nm} Y_n^m(\theta, \phi) \quad \text{where,} \\ \gamma'_{nm} &= \sum_i \frac{4\pi}{(2n+1)} \frac{q_i}{R_i^{(n+1)}} (-1)^m Y_n^{-m}(\theta_i, \phi_i). \end{aligned} \quad (\text{B.8})$$

Looking at Eq. B.7, imaginary coefficients are present. In order to avoid them later, we recast Eq. B.8 in terms of tesseral harmonics  $Z_n^l$  defined as:

$$\begin{aligned} Z_n^0 &= Y_n^0, \\ Z_n^{\pm|m|} &= \sqrt{\frac{\pm 1}{2}} [Y_n^{-|m|} \pm (-1)^{|m|} Y_n^{|m|}], \end{aligned} \quad (\text{B.9})$$

where we use the convention  $\sqrt{-1} = i$ . Therefore, Eq. B.8 transforms into:

$$\begin{aligned} V_{\text{CEF}}(r, \theta, \phi) &= \sum_n \sum_{m=-n}^n r^n \gamma_{nm} Z_n^m(\theta, \phi), \quad \text{where} \\ \gamma_{nm} &= \sum_i \frac{4\pi}{(2n+1)} \frac{q_i}{R_i^{(n+1)}} Z_n^m(\theta_i, \phi_i). \end{aligned} \quad (\text{B.10})$$

Then, the perturbative CEF Hamiltonian acting on the magnetic ion is:

$$\mathcal{H}_{\text{CEF}} = -\frac{e}{4\pi\epsilon_0} \sum_j V_{\text{CEF}}(r_j, \theta_j, \phi_j), \quad (\text{B.11})$$

where the summation runs over electrons of the unfilled  $4f$  electronic shell.

We focus in the following on the ground state multiplet defined by the basis  $|L, S, J, m_J\rangle$ . In order to calculate matrix elements of  $\mathcal{H}_{\text{CEF}}$  within this basis, we use the operator equivalent method which derives from the Wigner-Eckart theorem [163]. The tesseral harmonics can be expressed in terms of Cartesian coordinates:

$$\sum_j r^n Z_n^m(\theta_j, \phi_j) = \sum_j p_n^m f_n^m(x_j, y_j, z_j), \quad (\text{B.12})$$

where  $p_n^m$  is a prefactor and  $f_n^m(x_j, y_j, z_j)$  a polynomial function (see Tab.8 of Ref. [164] for instance). The expressions of  $Z_n^m$  can be found for instance in Ref. [164]. The method consists in replacing coordinates  $x$ ,  $y$ , and  $z$  by the operators  $J_x$ ,  $J_y$ , and  $J_z$ .<sup>1</sup> Note that we must take into account the noncommutation of these operators. Therefore, products involving for instance  $xy$  must be replaced by a linear combination of  $J_x J_y$ . Consequently, we have:

$$\langle L, S, J, m_J | \sum_j r^n Z_n^m(\theta_j, \phi_j) | L, S, J, m_J \rangle \equiv \Theta_n \langle r^n \rangle \langle L, S, J, m_J | O_n^m | L, S, J, m_J \rangle, \quad (\text{B.15})$$

where  $\Theta_n$  (denoted in Ref. [164] as  $\alpha_J$ ,  $\beta_J$  and  $\gamma_J$  for  $n = 2, 4, 6$ , respectively) are the Stevens multiplicative factors given in Tab. B.1,  $\langle r^n \rangle$  is the expectation value of the  $n$ th power distance between the nucleus of the magnetic ion and the  $4f$  electronic shell. The latter has been computed in Ref. [257] and is listed in Tab. B.2.

The Stevens operators are labelled  $O_n^m$  and are expressed in terms of powers of  $J_z$ ,  $J_+$ , and  $J_-$ . As example, we focus on  $Z_2^0$ :

$$\sum_j r_j^2 Z_2^0(\theta_j, \phi_j) = \sum_j f_2^0(x_j, y_j, z_j) = \frac{1}{4} \sqrt{\frac{5}{\pi}} (3z^2 - r^2) \equiv \Theta_2 \langle r^2 \rangle [3J_z^2 - J(J+1)]. \quad (\text{B.16})$$

Therefore, the CEF Hamiltonian can be expressed in terms of Stevens operators:

$$\mathcal{H}_{\text{CEF}} = \sum_{nm} [A_n^m \langle r^n \rangle \Theta_n] O_n^m \quad (\text{B.17})$$

---

<sup>1</sup>Rather than using  $J_x$  and  $J_y$ , we introduce the raising and lowering spin operators defined as:

$$\begin{aligned} J_+ &= J_x + iJ_y, \\ J_- &= J_x - iJ_y. \end{aligned} \quad (\text{B.13})$$

Therefore, matrix elements can be computed as:

$$\begin{aligned} J_+ |L, S, J, m_J\rangle &= \sqrt{J(J+1) - m_J(m_J+1)} |L, S, J, m_J+1\rangle, \\ J_- |L, S, J, m_J\rangle &= \sqrt{J(J+1) - m_J(m_J-1)} |L, S, J, m_J-1\rangle, \\ J_z |L, S, J, m_J\rangle &= m_J |L, S, J, m_J\rangle. \end{aligned} \quad (\text{B.14})$$

Rare earth	Pr <sup>3+</sup>	Nd <sup>3+</sup>	Tb <sup>3+</sup>	Dy <sup>3+</sup>
$\Theta_2(-)$	$-2.101 \cdot 10^{-2}$	$-6.428 \cdot 10^{-3}$	$-1.010 \cdot 10^{-2}$	$-6.349 \cdot 10^{-3}$
$\Theta_4(-)$	$-7.346 \cdot 10^{-4}$	$-2.911 \cdot 10^{-4}$	$1.224 \cdot 10^{-4}$	$-5.920 \cdot 10^{-5}$
$\Theta_6(-)$	$6.099 \cdot 10^{-5}$	$-3.799 \cdot 10^{-5}$	$-1.121 \cdot 10^{-6}$	$1.035 \cdot 10^{-6}$
Rare earth	Ho <sup>3+</sup>	Er <sup>3+</sup>	Tm <sup>3+</sup>	Yb <sup>3+</sup>
$\Theta_2(-)$	$-2.222 \cdot 10^{-3}$	$2.540 \cdot 10^{-3}$	$1.010 \cdot 10^{-2}$	$3.175 \cdot 10^{-2}$
$\Theta_4(-)$	$-3.330 \cdot 10^{-5}$	$4.440 \cdot 10^{-5}$	$1.633 \cdot 10^{-4}$	$-1.732 \cdot 10^{-3}$
$\Theta_6(-)$	$-1.294 \cdot 10^{-6}$	$2.070 \cdot 10^{-6}$	$-5.606 \cdot 10^{-6}$	$1.480 \cdot 10^{-4}$

Table B.1: Stevens multiplicative factor  $\Theta_n$  for some rare earths of interest [258].

$\langle r^n \rangle (a_0^n)$	Pr <sup>3+</sup>	Nd <sup>3+</sup>	Gd <sup>3+</sup>	Tb <sup>3+</sup>	Dy <sup>3+</sup>	Ho <sup>3+</sup>	Er <sup>3+</sup>	Tm <sup>3+</sup>	Yb <sup>3+</sup>
$\langle r^2 \rangle (a_0^2)$	1.086	1.114	0.8671	0.8220	0.7814	0.7446	0.7111	0.6804	0.6522
$\langle r^4 \rangle (a_0^4)$	2.822	2.910	1.820	1.651	1.505	1.379	1.270	1.174	1.089
$\langle r^6 \rangle (a_0^6)$	15.73	15.03	7.831	6.852	6.048	5.379	4.816	4.340	3.932

Table B.2: List of the expectation values of the  $n$ th power distance between the nucleus of the magnetic ion and the  $4f$  electronic shell for some rare earths of interest. They are expressed in atomic units ( $a_0 = 52.9$  pm). Data are taken from Ref. [257].

where we have introduced:

$$A_n^m = -\frac{e}{4\pi\epsilon_0} p_n^m \gamma_n^m = -\frac{e}{4\pi\epsilon_0} p_n^m \sum_i \frac{4\pi}{(2n+1)} \frac{q_i}{R_i^{(n+1)}} Z_n^m(\theta_i, \phi_i). \quad (\text{B.18})$$

# Appendix C

## Neutron absorption correction

Here are presented how the neutron absorption has been taken into account in the neutron time-of-flight experiments. The powder samples fill an annular sample holder. We first introduce the case of a rectangular sample since, in the following, we will consider an elementary rectangular section to calculate the absorption in a more complex geometry.

### C.1 Rectangular geometry

First we consider a rectangular sample of thickness  $d$ . An incident neutron with a wavevector  $\mathbf{k}_i$  is scattered at the position  $x$  with a wavevector  $\mathbf{k}_f$ , see Fig.C.1.

Assuming a scattering angle  $\phi = 0$ , the absorption correction factor is calculated as the inverse of the transmission factor  $A = \frac{I}{I_0}$  [259]:

$$A = \frac{1}{d} \int_0^d e^{-\Sigma x} e^{-\Sigma'(d-x)} dx = \frac{1}{d} \frac{e^{-\Sigma'd} - e^{-\Sigma d}}{\Sigma - \Sigma'}, \quad (\text{C.1})$$

where  $\Sigma$  and  $\Sigma'$  are respectively the incident and final total absorption cross sections defined as:

$$\Sigma = \frac{N_f}{v_0} f \frac{\lambda}{1.8} \sum_i c_i \sigma_{a,i}, \quad (\text{C.2})$$

where  $N_f$  is the number of formula units in the cell of volume  $v_0$ ,  $f$  is the filling factor defined as the ratio of the powder density over the crystal density,  $\sigma_{a,i}$  is the absorption cross section of atom  $i$  contained  $c_i$  times in the chemical formula. Note that  $\lambda = \lambda_i$  (in Å in the formula) for the calculation of  $\Sigma$  and  $\lambda = \lambda_f$  for  $\Sigma'$ .

### C.2 Annular geometry

One of the advantages to choose a annular geometry is that the angular dependence of the absorption correction factor is very small, as shown by simulations. We will neglect it in the following which permits to calculate analytically the absorption correction factor. A section of a half-cylinder is displayed in Fig. C.2. We first consider an elementary area with a length  $d$  where the neutron scattering process occurs. The sample mass has been calculated such that the probability of neutron scattering is lower

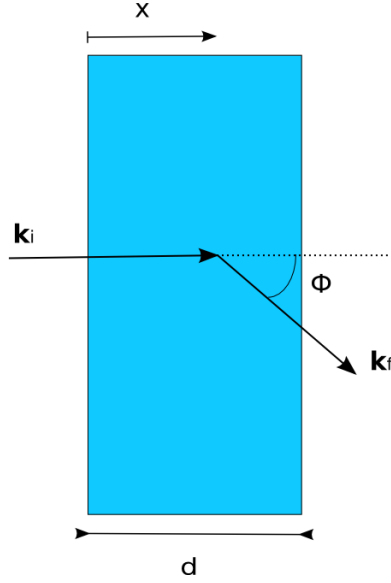


Figure C.1: Neutron scattering in a rectangular sample.

than 10 % and therefore multiple scattering processes are neglected. As  $R_{\text{in}} \rightarrow R_{\text{out}}$ , we estimate the elementary section to be rectangular and the absorption correction factor is then calculated as the inverse of the transmission factor  $\alpha' = \int \alpha(y) dy$ , where  $\alpha(y)$  is the elementary rectangular transmission factor calculated with the help of Eq. C.1. Two cases are considered, see Fig.C.2: either the neutron passes through the sample without discontinuity (1) or not (2). In the first case, the neutron path is calculated as:

$$d_1(y) = 2\sqrt{R_{\text{out}}^2 - y^2} \quad (\text{C.3})$$

In the second case, two situations have to be taken into account whether the neutron is scattered in its first or second path in the sample. In both cases the neutron path is calculated as:

$$d_2(y) = L = \sqrt{R_{\text{out}}^2 - y^2} - \sqrt{R_{\text{in}}^2 - y^2} \quad (\text{C.4})$$

Then, integrating over the half-cylinder, we get the transmission factor:

$$\begin{aligned} \frac{A'}{2} &= \\ & \frac{2}{\pi(R_{\text{out}}^2 - R_{\text{in}}^2)} \left\{ \int_0^{R_{\text{in}}} dy \frac{e^{-\Sigma'(\sqrt{R_{\text{out}}^2 - y^2} - \sqrt{R_{\text{in}}^2 - y^2})} - e^{-\Sigma(\sqrt{R_{\text{out}}^2 - y^2} - \sqrt{R_{\text{in}}^2 - y^2})}}{\Sigma - \Sigma'} \right. \\ & \quad \times e^{-\Sigma(\sqrt{R_{\text{out}}^2 - y^2} - \sqrt{R_{\text{in}}^2 - y^2})} \\ & + \int_0^{R_{\text{in}}} dy \frac{e^{-\Sigma'(\sqrt{R_{\text{out}}^2 - y^2} - \sqrt{R_{\text{in}}^2 - y^2})} - e^{-\Sigma(\sqrt{R_{\text{out}}^2 - y^2} - \sqrt{R_{\text{in}}^2 - y^2})}}{\Sigma - \Sigma'} e^{-\Sigma'(\sqrt{R_{\text{out}}^2 - y^2} - \sqrt{R_{\text{in}}^2 - y^2})} \\ & \left. + \int_{R_{\text{in}}}^{R_{\text{out}}} dy \frac{e^{-2\Sigma'\sqrt{R_{\text{out}}^2 - y^2}} - e^{-2\Sigma\sqrt{R_{\text{out}}^2 - y^2}}}{\Sigma - \Sigma'} \right\} \quad (\text{C.5}) \end{aligned}$$

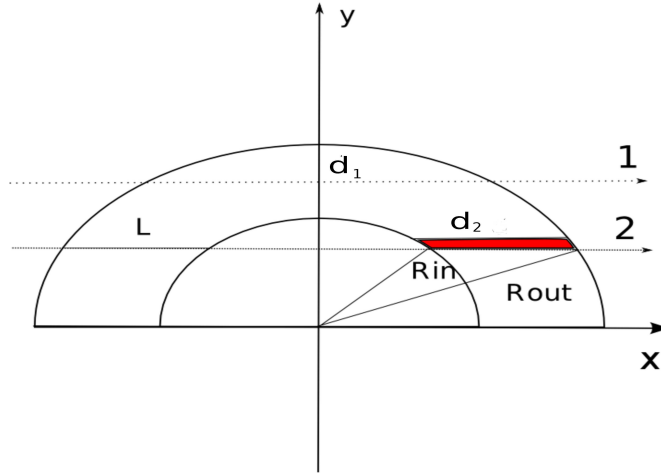


Figure C.2: Scheme of a section of a half-cylinder where neutron scattering occurs in an elementary surface (red).  $R_{\text{in}}$  and  $R_{\text{out}}$  are the internal and external radii, respectively. The index (1) and (2) refer to the two possible neutron paths, as explained in the text.

The first and second integrals of Eq. C.5 account for the neutron path labelled (2) in Fig.C.2. Two integrals are needed to take into account whether the neutron is inelastically scattered the first or second time it encounters the sample. The third integral accounts for the neutron path labelled (1). Thus Eq. C.5 is simplified as:

$$\frac{A'}{2} = \frac{1}{\pi(R_{\text{out}}^2 - R_{\text{in}}^2)} \left\{ \int_0^{R_{\text{in}}} dy \frac{e^{-2\Sigma'(\sqrt{R_{\text{out}}^2 - y^2} - \sqrt{R_{\text{in}}^2 - y^2})} - e^{-2\Sigma(\sqrt{R_{\text{out}}^2 - y^2} - \sqrt{R_{\text{in}}^2 - y^2})}}{\Sigma - \Sigma'} \right. \\ \left. + \int_{R_{\text{in}}}^{R_{\text{out}}} dy \frac{e^{-2\Sigma'\sqrt{R_{\text{out}}^2 - y^2}} - e^{-2\Sigma\sqrt{R_{\text{out}}^2 - y^2}}}{\Sigma - \Sigma'} \right\} \quad (\text{C.6})$$

# Appendix D

## Complements to magnetic diffraction

### D.1 Elements of group theory

In this section, some basic concepts of group theory applied to the determination of the magnetic structure of a pyrochlore compound are introduced.

In the paramagnetic phase, magnetic moments are disordered but magnetic fluctuations exist at short length and are classified by modes compatible with the crystal symmetries. When a compound undergoes a second-order magnetic phase transition, according to the Landau theory, one of these modes is selected while the others vanish. Using group theory, to each mode corresponds an Irreducible Representation (IR) of the group symmetry. Thus the symmetry in the ordered phase is lowered to a subgroup of the crystallographic group.

The pyrochlore compounds crystallise in the face-centred cubic lattice ( $Fd\bar{3}m$  space group). This space group gathers 48 symmetry operations  $g_i$ . Considering a magnetic propagation wavevector  $\mathbf{k}_{\text{mag}} = (0, 0, 0)$ , the subgroup  $G_k$ , called the *little group* is determined by gathering all the symmetry operations leaving  $\mathbf{k}_{\text{mag}}$  invariant, i.e. it is the whole space group  $Fd\bar{3}m$ . With the help of Kovalev's book [260], we find the IR  $\Gamma_\nu^{(\mu)}$  where  $\mu$  is the order of the representation and  $\nu$  an arbitrary index to label the different IRs. Note that in this book are actually tabulated the loaded representations  $\hat{\Gamma}_\nu^{(\mu)}$  defined as:

$$d_\nu^{(\mu)}(g_i) = \hat{d}_\nu^{(\mu)}(g_i) \exp(-\mathbf{k}_{\text{mag}} \cdot \mathbf{h}), \quad (\text{D.1})$$

where  $d_\nu^{(\mu)}(g_i)$  and  $\hat{d}_\nu^{(\mu)}(g_i)$  are respectively the matrix representation of the symmetry element  $g_i$  in the representation  $\Gamma_\nu^{(\mu)}$  and  $\hat{\Gamma}_\nu^{(\mu)}$ , and  $\mathbf{h}$  represents the translational part of the symmetry operator to which  $d_\nu^{(\mu)}(g_i)$  is associated [261].  $G_k$  can be decomposed into ten one-, two- or three-dimensional IR  $\Gamma_\nu^{(\mu)}$  ( $\mu = 1, 2, 3$ ). Calculating the trace of the matrix representations of all the symmetry operators written for a IR permits to extract the character  $\chi_{\Gamma^{(\mu)}}$  of the considered IR.

On the other hand, we determine the magnetic representation  $\Gamma(G_k)$  of  $G_k$  describing the results of the symmetry operators on the components of the magnetic moments. As the crystallographic cell contains four magnetic ions, the 48 symmetry operators are described by matrices of dimension  $4 \times 3 = 12$ . To get the character table of  $\Gamma(G_k)$ , we calculate the trace  $\chi_\Gamma$  for each matrix representation of symmetry operators. This

IR	basis vector	Atom $j = 1$			Atom $j = 2$			Atom $j = 3$			Atom $j = 4$		
		$m_x$	$m_y$	$m_z$	$m_x$	$m_y$	$m_z$	$m_x$	$m_y$	$m_z$	$m_x$	$m_y$	$m_z$
$\Gamma_3$	$\Psi_{1,j}$	1	1	1	-1	-1	1	-1	1	-1	1	-1	-1
$\Gamma_5$	$\Psi_{2,j}$	1	$e^{\frac{4i\pi}{3}}$	$e^{\frac{2i\pi}{3}}$	-1	$e^{\frac{i\pi}{3}}$	$e^{\frac{2i\pi}{3}}$	-1	$e^{\frac{4i\pi}{3}}$	$e^{\frac{5i\pi}{3}}$	1	$e^{\frac{i\pi}{3}}$	$e^{\frac{5i\pi}{3}}$
	$\Psi_{3,j}$	$e^{\frac{2i\pi}{3}}$	1	$e^{\frac{4i\pi}{3}}$	$e^{\frac{5i\pi}{3}}$	-1	$e^{\frac{4i\pi}{3}}$	$e^{\frac{5i\pi}{3}}$	1	$e^{\frac{i\pi}{3}}$	$e^{\frac{2i\pi}{3}}$	-1	$e^{\frac{i\pi}{3}}$
$\Gamma_7$	$\Psi_{4,j}$	1	-1	0	-1	1	0	1	1	0	-1	-1	0
	$\Psi_{5,j}$	0	1	-1	0	1	1	0	-1	-1	0	-1	1
	$\Psi_{6,j}$	-1	0	1	-1	0	-1	1	0	-1	1	0	1
$\Gamma_9$	$\Psi_{7,j}$	1	1	0	-1	-1	0	1	-1	0	-1	1	0
	$\Psi_{8,j}$	0	0	1	0	0	1	0	0	1	0	0	1
	$\Psi_{9,j}$	0	1	1	0	1	-1	0	-1	1	0	-1	-1
	$\Psi_{10,j}$	1	0	0	1	0	0	1	0	0	1	0	0
	$\Psi_{11,j}$	1	0	1	1	0	-1	-1	0	-1	-1	0	1
	$\Psi_{12,j}$	0	1	0	0	1	0	0	1	0	0	1	0

Table D.1: The non-normalised basis vectors associated to the IRs using the BasIREPS program [130]. The rare-earth atoms 1, 2, 3 and 4 are located respectively at positions  $(x, y, z)$ ,  $(-x + \frac{3}{4}, -y + \frac{1}{4}, z + \frac{1}{2})$ ,  $(-x + \frac{1}{4}, y + \frac{1}{2}, -z + \frac{3}{4})$ , and  $(x + \frac{1}{2}, -y + \frac{3}{4}, -z + \frac{1}{4})$ .

representation is reducible if

$$\frac{1}{d} \sum_{g_i} |\chi_{\Gamma}|^2 \neq 1, \quad (\text{D.2})$$

where  $d$  is the order of  $G_k$  (in our case,  $d = 12$ ). Expressing the matrix of  $\Gamma(G_k)$  in a block form permits to decompose it along the allowed irreducible representations  $\Gamma_{\nu}^{(\mu)}$ :

$$\Gamma(G_k) = \sum_{\nu} a_{\nu} \Gamma_{\nu}^{(\mu)}, \quad (\text{D.3})$$

with

$$a_{\nu} = \frac{1}{d} \sum_{g_i \in G_k} \chi_{\Gamma}(g_i) \chi_{\Gamma_{\nu}^{(\mu)}}^*(g_i), \quad (\text{D.4})$$

which denotes the number of times a IR appears in the decomposition. In the case considered, we get:

$$\Gamma(G_k) = 1\Gamma_3^{(1)} + 1\Gamma_5^{(2)} + 1\Gamma_7^{(3)} + 2\Gamma_9^{(3)}. \quad (\text{D.5})$$

IR  $\Gamma_3$ ,  $\Gamma_5$ ,  $\Gamma_7$  and  $\Gamma_9$  are respectively of dimension 1, 2, 3 and 3. Thus the basis vectors  $\Psi_{\nu,j}$  ( $\nu$  labelling the basis vector and  $j$  referring to the atom considered) of each IR are calculated with the projection operator formula [261, 262]. These group-theory calculations are accomplished for instance by the BasIREPS [130] or SARAh [263] programs. The basis vectors  $\Psi_{\nu,j}$  of each IR of interest are listed in Tab D.1.

The magnetic moment  $\mathbf{m}_j$  at site  $j$  is a linear combination of the basis vectors  $\Psi_{\nu,j}$  of the IR of interest. Recalling that  $\mathbf{k}_{\text{mag}} = (0,0,0)$ , when the components of  $\Psi_{\nu,j}$  are real numbers,

$$\mathbf{m}_j = \sum_{\mu} a_{\mu} \Psi_{\mu,j}, \quad (\text{D.6})$$

where  $a_\mu$  are real numbers to be determined. There are as many  $\mu$  values as the number of  $\Psi_{\mu,j}$  vectors in the selected IR. For example,  $\mu$  runs from 4 to 6 for the  $\Gamma_7$  IR; see Table D.1. In the case where the components of  $\Psi_{\mu,j}$  have imaginary parts, the magnetic moment being a real quantity, we have to introduce a corresponding basis vector for propagation vector  $-\mathbf{k}_{\text{mag}}$  (see, e.g. Ref. [137]) with

$$\mathbf{m}_j = \sum_{\mu} \frac{a_\mu}{2} \left[ 2\mathcal{R}e\{\Psi_{\mu,j}^{\mathbf{k}_{\text{mag}}}\} \cos(-2\pi\mathbf{k}_{\text{mag}} \cdot \boldsymbol{\tau}) + 2\mathcal{I}m\{\Psi_{\mu,j}^{\mathbf{k}_{\text{mag}}}\} \sin(-2\pi\mathbf{k}_{\text{mag}} \cdot \boldsymbol{\tau}) \right], \quad (\text{D.7})$$

where  $\boldsymbol{\tau}$  is a lattice translation vector. Since here  $\mathbf{k}_{\text{mag}} = (0, 0, 0)$ :

$$\mathbf{m}_j = \sum_{\mu} a_\mu \mathcal{R}e\{\Psi_{\mu,j}^{\mathbf{k}_{\text{mag}}}\}, \quad (\text{D.8})$$

where  $a_\mu$  are real numbers.

## D.2 BasIREPS vs SARAh

For the sake of clarity, we report here some minor differences in the use of the two programs previously cited.

For a magnetic ion placed in  $(x, y, z)$ , BasIREPS calculates the positions of the three other magnetic ions in  $(-x + \frac{3}{4}, -y + \frac{1}{4}, z + \frac{1}{2})$ ,  $(-x + \frac{1}{4}, y + \frac{1}{2}, -z + \frac{3}{4})$ , and  $(x + \frac{1}{2}, -y + \frac{3}{4}, -z + \frac{1}{4})$  for atomic sites labelled 1, 2, 3 and 4 respectively. Using SARAh, with the same labelling, the three other magnetic ions are located in  $(x + \frac{1}{2}, -y + \frac{3}{4}, -z + \frac{1}{4})$ ,  $(-x + \frac{1}{4}, y + \frac{1}{2}, -z + \frac{3}{4})$  and  $(-x + \frac{3}{4}, -y + \frac{1}{4}, z + \frac{1}{2})$  (atomic sites 2 and 4 are inverted). Furthermore, for IR  $\Gamma_5$ ,  $\Gamma_7$  and  $\Gamma_9$ , the basis vectors  $\Psi^S$  given by SARAh are a linear combination of basis vectors  $\Psi$  given by BasIREPS:

$$\left\{ \begin{array}{ll} \Psi_2^S = \frac{1}{3}(\Psi_2 - \Psi_3), & \Psi_8^S = -\Psi_9 + 2\Psi_{10}, \\ \Psi_3^S = \Psi_2 + \Psi_3, & \Psi_9^S = \Psi_{11} + \Psi_{12}, \\ \Psi_4^S = -\Psi_5, & \Psi_{10}^S = -\Psi_{11} + 2\Psi_{12}, \\ \Psi_5^S = -\Psi_6, & \Psi_{11}^S = \Psi_7 + \Psi_8, \\ \Psi_6^S = -\Psi_4, & \Psi_{12}^S = -\Psi_7 + 2\Psi_8, \\ \Psi_7^S = \Psi_9 + \Psi_{10}. \end{array} \right. \quad (\text{D.9})$$

## D.3 Analytical evidence for IR $\Gamma_3$ selection in $\text{Nd}_2\text{Sn}_2\text{O}_7$

In the following, using analytical computations we show that only the  $\Gamma_3$  IR can provide a proper description of  $\text{Nd}_2\text{Sn}_2\text{O}_7$  magnetic diffraction data. Our derivation is based on the experimental fact that a large magnetic intensity is observed at Bragg reflection (220), while no magnetic intensity is found at positions (111), (200), and (400) (see left panel of Fig. 4.8).<sup>1</sup>

We first recall the definition of the magnetic structure factor  $\mathbf{F}_{\text{mag}}(\mathbf{q})$  introduced in Eq. 2.18, when only one type of magnetic ion is present as in our case,

$$\mathbf{F}_{\text{mag}}(\mathbf{q}) = \text{pf}_{\text{mag}}(\mathbf{q})\mathbf{S}_{\text{mag}}(\mathbf{q}), \quad (\text{D.10})$$

<sup>1</sup>Magnetic reflections (111), (200), (220), and (400) are expected at angles  $2\theta = 23.9, 27.7, 39.5$ , and  $57.1$  degrees respectively.

where the magnetic scattering length  $p$  is defined in Eq. 2.15, and we have introduced:

$$\mathbf{S}_{\text{mag}}(\mathbf{q}) = \sum_j \mathbf{m}_j^{\text{kmag}} \exp(i\mathbf{q} \cdot \mathbf{r}_j) \exp(-W_j(\mathbf{q})). \quad (\text{D.11})$$

Here  $\mathbf{r}_j$  labels the  $j$  magnetic ion position in the unit cell. We have introduced the magnetic form factor  $f_{\text{mag}}(\mathbf{q})$  of the magnetic ion. The Fourier component of the magnetic moment  $\mathbf{m}_j^{\text{kmag}}$  has been introduced in Eq. 2.16. We will neglect in the following the Debye-Waller factor  $\exp(-W_j(\mathbf{q}))$ . Obviously the computed scattered intensity does not depend on the choice of the origin for the atomic positions. Therefore, up to the end of this section we take a rare-earth ion at position (0,0,0). From the site positions mentioned in the caption of Table D.1, and after applying the lattice translation of the face-centred-cubic structure, the three other magnetic ions are in the relative positions  $(\frac{1}{4}, \frac{1}{4}, 0)$ ,  $(\frac{1}{4}, 0, \frac{1}{4})$ , and  $(0, \frac{1}{4}, \frac{1}{4})$ . Note that for the sake of simplicity the direct lattice coordinates are given here in units of  $a_{\text{lat}}$  and those in the reciprocal lattice will be expressed in units of  $2\pi/a_{\text{lat}}$ . We also recall that the magnetic cross section is only sensitive to the components of  $\mathbf{F}_{\text{mag}}(\mathbf{q})$  perpendicular to  $\mathbf{q}$ , i.e. to the component of  $\mathbf{S}_{\text{mag}}(\mathbf{q})$  perpendicular to  $\mathbf{q}$  since  $\mathbf{F}_{\text{mag}}(\mathbf{q})$  and  $\mathbf{S}_{\text{mag}}(\mathbf{q})$  are collinear.

We begin with the  $\Gamma_5$  IR. We note that the basis vectors associated to this IR have complex number components; see Table D.1. Applying Eq. D.8 together with Eq. D.11 for  $\mathbf{q} = (111)$  we compute

$$\mathbf{S}_{\text{mag}}(111) = \begin{pmatrix} 2a_2 - a_3 \\ -a_2 + 2a_3 \\ -a_2 - a_3 \end{pmatrix}. \quad (\text{D.12})$$

Except for the trivial case  $a_2 = a_3 = 0$ ,  $\mathbf{S}_{\text{mag}}(111)$  is never collinear to (111). Therefore, a non vanishing magnetic intensity is expected at the scattering vector  $\mathbf{q} = (111)$  in contrast to the experimental observation, ruling out the  $\Gamma_5$  IR.

Looking at the  $\Gamma_7$  IR, we write  $\mathbf{m}_j^{\text{kmag}} = a_4\Psi_{4,j} + a_5\Psi_{5,j} + a_6\Psi_{6,j}$  (Eq. D.6). For  $\mathbf{q} = (200)$ , we compute

$$\mathbf{S}_{\text{mag}}(200) = \begin{pmatrix} 0 \\ -4a_4 \\ 4a_6 \end{pmatrix}. \quad (\text{D.13})$$

Unless  $a_4 = a_6 = 0$ , the vector  $\mathbf{S}_{\text{mag}}(200)$  is perpendicular to (200), yielding magnetic intensity. Since no magnetic intensity is experimentally observed at reflection (200), we must set  $a_4 = a_6 = 0$ . Then only the basis vectors  $\Psi_{5,j}$  are involved. Let us compute  $\mathbf{S}_{\text{mag}}(\mathbf{q})$  at  $\mathbf{q} = (111)$ . We get

$$\mathbf{S}_{\text{mag}}(111) = \begin{pmatrix} 0 \\ 2a_5 \\ -2a_5 \end{pmatrix}. \quad (\text{D.14})$$

Obviously,  $\mathbf{S}_{\text{mag}}(111)$  is not collinear to (111). This implies a non vanishing magnetic intensity at this  $\mathbf{q}$ -value, in contrast to experimental result. Therefore the magnetic structure cannot be represented by the  $\Gamma_7$  IR.

We now consider the  $\Gamma_9$  IR. We write  $\mathbf{m}_j^{\mathbf{k}_{\text{mag}}} = a_7\Psi_{7,j} + a_8\Psi_{8,j} + a_9\Psi_{9,j} + a_{10}\Psi_{10,j} + a_{11}\Psi_{11,j} + a_{12}\Psi_{12,j}$ . Then at  $\mathbf{q} = (200)$ ,

$$\mathbf{S}_{\text{mag}}(200) = \begin{pmatrix} 0 \\ 4a_7 \\ 4a_{11} \end{pmatrix}. \quad (\text{D.15})$$

Since no intensity is measured at this Bragg position, we set  $a_7 = a_{11} = 0$ . Considering now the  $\mathbf{q} = (020)$  reflection which would give intensity at the same angle as  $\mathbf{q} = (200)$  in our powder measurement, we deduce  $a_9 = 0$ .

At  $\mathbf{q} = (400)$  we calculate

$$\mathbf{S}_{\text{mag}}(400) = \begin{pmatrix} 4a_{10} \\ 4a_{12} \\ 4a_8 \end{pmatrix}. \quad (\text{D.16})$$

Since no magnetic intensity is detected at this position, we derive  $a_8 = a_{12} = 0$ . If we add the condition that no intensity is observed at  $\mathbf{q} = (040)$  we have  $a_{10} = 0$ .

Altogether, the magnetic moments  $\mathbf{m}_j^{\mathbf{k}_{\text{mag}}}$  vanish. Hence the magnetic structure of  $Nd_2Sn_2O_7$  cannot be described by the  $\Gamma_9$  IR.

We are left with the  $\Gamma_3$  IR. According to Table D.1 and Eq. D.6,  $\mathbf{m}_j^{\mathbf{k}_{\text{mag}}} = a_1\Psi_{1,j}$ . For  $\mathbf{q} = (111)$  we get,

$$\mathbf{S}_{\text{mag}}(111) = 2a_1 \begin{pmatrix} 1 \\ 1 \\ 1 \end{pmatrix}. \quad (\text{D.17})$$

Hence  $\mathbf{S}_{\text{mag}}(\mathbf{q} = (111))$  is collinear to  $\mathbf{q}$ . This is also the case for all the wavevectors equivalent to  $\mathbf{q} = (111)$ , e.g.  $\mathbf{q} = (\bar{1}11)$ . For the  $\mathbf{q} = (200)$  and symmetry equivalent positions we also find that  $\mathbf{S}_{\text{mag}}(\mathbf{q})$  is collinear to  $\mathbf{q}$ . Concerning  $\mathbf{q} = (400)$  and equivalent reflections,  $\mathbf{S}_{\text{mag}}(\mathbf{q}) = 0$ . Therefore no magnetic intensity is expected at positions (111), (200) and (400) in the case of the  $\Gamma_3$  IR, in accord with the experimental result.

Now, for  $\mathbf{q} = (220)$  we compute

$$\mathbf{S}_{\text{mag}}(220) = \begin{pmatrix} 0 \\ 0 \\ 4a_1 \end{pmatrix}, \quad (\text{D.18})$$

which is perpendicular to  $\mathbf{q}$ . A similar results holds for the Braggs reflection equivalent to (220). Therefore the magnetic neutron intensity will not vanish for this wavevector since  $\mathbf{q}$  is obviously perpendicular to  $\mathbf{S}_{\text{mag}}(\mathbf{q})$ .

# Appendix E

## Complements to $\mu$ SR

In this appendix, we give some details about the spin-lattice relaxation rate  $\lambda_Z$  involved in the analysis of  $\mu$ SR experiments. In the following, the  $Z$  axis refers to the direction of the muon polarisation, see Sec.2.6.

### E.1 Derivation of the spin lattice relaxation rate

From the strong collision model, the polarisation function  $P_Z(t)$  is controlled by the following integral equation:

$$P_Z(t) = P_Z^{\text{stat}}(t) \exp(-\nu_c t) + \nu_c \int_0^t P_Z(t-t') P_Z^{\text{stat}}(t') \exp(-\nu_c t'), \quad (\text{E.1})$$

where  $\nu_c$  is the field correlation rate. In the case of a static Gaussian field distribution, with a field variance  $\Delta_G^2$ , the longitudinal static polarisation function is given by the Kubo-Toyabe function [160]:

$$P_Z^{\text{stat}}(t) = \frac{1}{3} + \frac{2}{3}(1 - \gamma_\mu^2 \Delta_G^2 t^2) \exp\left(-\frac{\gamma_\mu^2 \Delta_G^2 t^2}{2}\right), \quad (\text{E.2})$$

where  $\gamma_\mu = 8.51616 \times 10^8 \text{ rad s}^{-1} \text{ T}^{-1}$  is the muon gyromagnetic ratio. In the motional narrowing limit, i.e.  $\nu_c \gg \gamma_\mu \Delta_G$ , Eq. E.1 becomes:

$$P_Z(t) = \exp(-\lambda_Z t), \quad (\text{E.3})$$

where the spin-lattice relaxation rate is  $\lambda_Z = 2\gamma_\mu^2 \Delta_G^2 \tau_c$  and  $\tau_c = 1/\nu_c$ . A physical interpretation of  $\lambda_Z$  is given in Sec. 4.8.2. In the case where a longitudinal field  $B_{\text{ext}} = \omega_\mu/\gamma_\mu$  is applied, the longitudinal polarisation function remains an exponential function within the extreme motional narrowing limit, i.e.  $\nu_c t \gg 1$  and the spin-lattice relaxation rate is given by the Redfield formula:

$$\lambda_Z(\omega_\mu = \gamma_\mu B_{\text{ext}}) = \frac{2\gamma_\mu^2 \Delta_G^2 \nu_c}{\omega_\mu^2 + \nu_c^2}, \quad (\text{E.4})$$

Within a quantum approach, the longitudinal polarisation function is expressed as [160]:

$$P_Z(t) = \exp[-\Psi_Z(t)], \quad (\text{E.5})$$

where:

$$\Psi_Z(t) = 2\pi^2\gamma_\mu^2 \int_0^t (t-\tau) \cos(\omega_\mu t) [\Phi^{XX}(\tau) + \Phi^{YY}(\tau)] d\tau, \quad (\text{E.6})$$

where  $(X, Y)$  refers to the coordinates perpendicular to the  $Z$  axis. The symmetrised correlation function of the fluctuating part of the local magnetic field at the muon site is introduced as:

$$\Phi^{\alpha\beta}(t) = \frac{1}{2\pi} \langle \{ \delta B_{\text{loc}}^\alpha(t) \delta B_{\text{loc}}^\beta \} \rangle, \quad (\text{E.7})$$

where  $\{\alpha, \beta\} = \{X, Y, Z\}$  and the symbol  $\langle \{AB\} \rangle$  stands for the thermal average of the symmetrised correlation function of operators  $A$  and  $B$  defined as:

$$2\langle \{AB\} \rangle = \langle AB \rangle + \langle BA \rangle. \quad (\text{E.8})$$

The fluctuations of the local field  $\delta \mathbf{B}_{\text{loc}}(t)$  are responsible for the transitions between the two muon states, see Fig 4.19. From Eq.E.6, the approximation that the characteristic time of the spin correlation is much shorter than the experimental time window, i.e.  $\tau \ll t$ , and assuming that  $\Phi^{\alpha\alpha}(t)$  are even functions of time, leads to  $\Psi_Z(t) = \lambda_Z t$  with:

$$\lambda_Z = \frac{\gamma_\mu^2}{2} \int_{-\infty}^{\infty} d\tau [\Phi^{XX}(\tau) + \Phi^{YY}(\tau)]. \quad (\text{E.9})$$

Therefore, Eq. E.9 can be written in terms of a time Fourier transform:

$$\lambda_Z = \pi\gamma_\mu^2 [\Phi^{XX}(\omega) + \Phi^{YY}(\omega)]. \quad (\text{E.10})$$

Following the work of Ref. [160], we express the fluctuating part of the local field at the muon site in terms of a tensor  $\mathbf{G}$  which represents the coupling between the muon spin and the spins of the system:

$$\delta B_{\text{loc}}^\alpha = \frac{\mu_0}{4\pi} \frac{g\mu_B}{v_c} \sum_i \sum_\beta G_{\mathbf{r}_i}^{\alpha\beta} \delta J_i^\beta, \quad (\text{E.11})$$

where only one type of magnetic ion per unit cell is considered,  $v_c$  is the volume of the unit cell,  $g$  the spectroscopic splitting factor, and  $\mu_B$  the electronic Bohr magneton. The index  $i$  runs over the lattice sites,  $\delta J_i^\beta$  is the component of the fluctuation of spin  $\mathbf{J}_i$ , located at site  $i$  and at a distance  $\mathbf{r}_i$  from the muon site. Therefore the symmetrised field correlation function can be expressed in terms of the symmetrised spin correlation function as:

$$\Phi^{\alpha\beta}(\omega) = \frac{1}{2\pi} \left( \frac{\mu_0}{4\pi} \right)^2 \frac{(g\mu_B)^2}{v_c^2} \sum_{\gamma, \gamma'} \sum_{i, i'} G_{\mathbf{r}_i}^{\alpha\gamma} G_{\mathbf{r}_{i'}}^{\beta\gamma'} \Lambda_{i, i'}^{\gamma\gamma'}(\omega), \quad (\text{E.12})$$

where  $\{\gamma, \gamma'\} = \{X, Y, Z\}$ . The symmetrised spin correlation function has been defined as:

$$\Lambda_{i, i'}^{\gamma\gamma'}(\omega) = \langle \{ \delta J_i^\gamma(\omega) \delta J_{i'}^{\gamma'} \} \rangle. \quad (\text{E.13})$$

The spin correlation function in the  $(\mathbf{q}, \omega)$  space is expressed as follows:

$$\Lambda^{\gamma\gamma'}(\mathbf{q}, \omega) = \int_{-\infty}^{\infty} \langle \{ \delta J^\gamma(\mathbf{q}, t) \delta J^{\gamma'}(-\mathbf{q}) \} \rangle \exp(i\omega t) dt, \quad (\text{E.14})$$

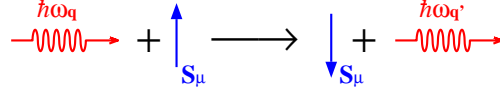


Figure E.1: *Illustration of the Raman process involved in the muon spin relaxation. A magnon of energy  $\hbar\omega_q$  is absorbed allowing the spin flip of the muon and the emission of another magnon with an energy  $\hbar\omega_{q'}$ . Picture reproduced with kind permission from Ref. [160].*

where the Fourier transformation of the component of the spin fluctuation is set as:

$$\delta J_i^\gamma = \frac{1}{\sqrt{n_c}} \sum_{\mathbf{q}} \exp(i\mathbf{q} \cdot \mathbf{i}) \delta J^\gamma(\mathbf{q}). \quad (\text{E.15})$$

Assuming  $\mathbf{q}$  as a continuous variable leads to the following formula of the spin-lattice relaxation rate:

$$\lambda_Z = \frac{\mathcal{D}}{2} \int_{v_c^*} \sum_{\beta, \gamma} \mathcal{A}^{\beta\gamma}(\mathbf{q}) \Lambda^{\beta\gamma}(\mathbf{q}, \omega) \frac{d^3\mathbf{q}}{(2\pi^3)}, \quad (\text{E.16})$$

where  $\mathcal{D} = (\mu_0/4\pi)^2 \gamma_\mu^2 (g\mu_B)^2 / v_c$ . The integration runs over the first Brillouin zone of volume  $v_c^*$  and we have introduced for simplicity:

$$\mathcal{A}^{\beta, \gamma}(\mathbf{q}) = G^{X, \beta}(\mathbf{q}) G^{\gamma, X}(-\mathbf{q}) + G^{Y, \beta}(\mathbf{q}) G^{\gamma, Y}(-\mathbf{q}). \quad (\text{E.17})$$

## E.2 Relaxation by excitations

We will focus here on the temperature behaviour of  $\lambda_Z$  in the ordered phase. The most common excitations are spin waves. We recall that the energy splitting of the muon spin states has been found to be  $\approx 70$  neV in  $\text{Nd}_2\text{Sn}_2\text{O}_7$ , which is much lower than the energy gap of spin waves. Thus, a single excitation cannot be at the origin of the relaxation of the muon spin. Therefore, a Raman scattering process involving two magnetic excitations has been put forward, where a magnon is absorbed and another one is emitted to achieve the muon spin flip, see Fig E.1.

### E.2.1 Ferromagnetic magnons

Let us consider a ferromagnetic system ruled by the following Hamiltonian [193]:

$$\mathcal{H}_{\text{FM}} = -\mathcal{I} \sum_{\langle i, i' \rangle} \mathbf{J}_i \cdot \mathbf{J}_{i'} + \Delta \sum_i J_i^Z, \quad (\text{E.18})$$

where  $\mathcal{I}$  is the isotropic exchange integral between nearest neighbour, and  $\Delta$  is an energy gap related to the anisotropy of the spin. We recall the dispersion law at small wavevector for ferromagnetic magnons:

$$E(q) = D_{\text{FM}} q^2 + \Delta, \quad (\text{E.19})$$

where  $D_{\text{FM}} = 2\mathcal{I}J a_{\text{lat}}^2$ . Following Eq. E.19, the magnon energy is minimum at small wavevectors. Recalling that the energy splitting between the two states of the muon

spin is extremely small, only magnons at low energy are involved during the relaxation process, i.e. only magnons with a small wavevector. We will consider the case of  $\mathbf{q} \rightarrow \mathbf{0}$  in the following. Let us focus now on the muon-system coupling tensor  $\mathbf{G}(\mathbf{q})$ . Since the pyrochlore compounds are insulators (no conduction electrons), we neglect the hyperfine interaction and therefore the muon spin and the spins of the system interact only through a dipolar field. According to Ref. [160, 264]:

$$G^{\alpha,\beta}(\mathbf{q} \rightarrow \mathbf{0}) = -4\pi \left[ \frac{q^\alpha q^\beta}{q^2} - C^{\alpha,\beta}(\mathbf{q} = \mathbf{0}) \right], \quad (\text{E.20})$$

where  $C^{\alpha,\beta}(\mathbf{q})$  is an analytical function of  $\mathbf{q}$ . Note that in face-centered cubic (fcc) crystal structure, if the muon is located at a tetragonal or octahedral site,  $C^{\alpha,\beta}(\mathbf{q} = \mathbf{0}) = \frac{1}{3}\delta^{\alpha\beta}$  [264]. Because of the energy conservation during a flipping process, the components of  $\mathbf{J}$  perpendicular to  $Z$  do not contribute to the muon spin flip. Therefore, only  $\Lambda^{ZZ}$  is needed. Furthermore, we will assume in the following that the symmetrised spin correlation tensor probes the relaxation at zero energy, i.e.  $\hbar\omega_\mu = 0$ . The wavevector is defined in spherical coordinates as:

$$q^X = q \sin \theta \cos \phi, \quad q^Y = q \sin \theta \sin \phi, \quad q^Z = q \cos \theta. \quad (\text{E.21})$$

Combining Eq. E.20 and Eq. E.16, with  $\beta = \gamma = Z$  in Eq. E.16, leads to:

$$\begin{aligned} \lambda_Z &= \frac{\mathcal{D}}{2} \frac{1}{(2\pi)^3} \int_0^{q_{\text{BZ}}} q^2 \Lambda^{ZZ}(q, \omega = 0) dq \int_0^\pi d\theta \sin \theta \int_0^{2\pi} d\phi (4\pi)^2 \{ \sin^2 \theta \cos^2 \theta - 2 \sin \theta \cos \theta \\ &\quad \times [\cos \phi C^{XZ}(\mathbf{q} = \mathbf{0}) + \sin \phi C^{YZ}(\mathbf{q} = \mathbf{0})] + [C^{XZ}(\mathbf{q} = \mathbf{0})]^2 + [C^{YZ}(\mathbf{q} = \mathbf{0})]^2 \} \\ &= 4\mathcal{D} \left\{ \frac{2}{15} + [C^{XZ}(\mathbf{q} = \mathbf{0})]^2 + [C^{YZ}(\mathbf{q} = \mathbf{0})]^2 \right\} \int_0^{q_{\text{BZ}}} \Lambda^{ZZ}(q, \omega = 0) q^2 dq, \end{aligned} \quad (\text{E.22})$$

where it is assumed that  $\Lambda^{ZZ}(\mathbf{q}, \omega = 0)$  only depends on the modulus of  $\mathbf{q}$ . We have considered the first Brillouin zone to be a sphere with a radius  $q_{\text{BZ}}$ . We will focus now on the symmetrised spin correlation tensor, recalling its expression in the  $(\mathbf{q}, \omega)$  space:

$$\Lambda^{ZZ}(\mathbf{q}, \omega = 0) = \frac{1}{2} [\langle \delta J^Z(\mathbf{q}, \omega = 0) \delta J^Z(-\mathbf{q}) \rangle + \langle \delta J^Z(-\mathbf{q}) \delta J^Z(\mathbf{q}, \omega = 0) \rangle]. \quad (\text{E.23})$$

Using the linear approximation of the Holstein-Primakoff transformation:

$$\delta J^Z(\mathbf{q}) = \frac{1}{\sqrt{n_c}} \sum_{\mathbf{q}_1, \mathbf{q}_2} \delta_{\mathbf{q}+\mathbf{q}_1-\mathbf{q}_2, 0} a_{\mathbf{q}_1}^\dagger a_{\mathbf{q}_2}, \quad (\text{E.24})$$

where  $n_c$  is the number of unit cells,  $a_{\mathbf{q}_1}^\dagger$  refers to the creation of a boson with wavevector  $\mathbf{q}_1$  and  $a_{\mathbf{q}_2}$  to the annihilation of a boson with wavevector  $\mathbf{q}_2$ . The Kronecker symbol  $\delta_{i,j}$  is defined such as  $\delta_{i,j} = 1$  if  $i = j$ , and  $\delta_{i,j} = 0$  otherwise. It stands here for the conservation of the momentum, i.e.  $\mathbf{q} = \mathbf{q}_2 - \mathbf{q}_1$ . Considering that  $a_{\mathbf{q}}(t) = \exp(-i\omega_{\mathbf{q}}t)a_{\mathbf{q}}$  and  $a_{\mathbf{q}}^\dagger(t) = \exp(i\omega_{\mathbf{q}}t)a_{\mathbf{q}}^\dagger$ , we derive:

$$\delta J^Z(\mathbf{q}, \omega = 0) = \frac{2\pi}{\sqrt{n_c}} \sum_{\mathbf{q}_1, \mathbf{q}_2} \delta_{\mathbf{q}+\mathbf{q}_1-\mathbf{q}_2, 0} \delta(\omega_{\mathbf{q}_1} - \omega_{\mathbf{q}_2}) a_{\mathbf{q}_1}^\dagger a_{\mathbf{q}_2}, \quad (\text{E.25})$$

where  $\delta(\omega) = \frac{1}{2\pi} \int_{-\infty}^{\infty} \exp(i\omega t) dt$  is the Dirac distribution. It follows that:

$$\begin{aligned} \langle \delta J^Z(\mathbf{q}, \omega = 0) \delta J^Z(-\mathbf{q}) \rangle &= \sum_{\mathbf{q}_1, \mathbf{q}_2} \sum_{\mathbf{q}'_1, \mathbf{q}'_2} \delta_{\mathbf{q}+\mathbf{q}_1-\mathbf{q}_2, 0} \delta_{-\mathbf{q}+\mathbf{q}'_1-\mathbf{q}'_2, 0} \\ &\quad \times \delta(\omega_{\mathbf{q}_1} - \omega_{\mathbf{q}_2}) \langle a_{\mathbf{q}_1}^\dagger a_{\mathbf{q}_2} a_{\mathbf{q}'_1}^\dagger a_{\mathbf{q}'_2} \rangle. \end{aligned} \quad (\text{E.26})$$

The mode coupling approximation states that:

$$\begin{aligned} \langle a_{\mathbf{q}_1}^\dagger a_{\mathbf{q}_2} a_{\mathbf{q}'_1}^\dagger a_{\mathbf{q}'_2} \rangle &\approx \delta_{\mathbf{q}_1-\mathbf{q}'_2, 0} \delta_{\mathbf{q}_2-\mathbf{q}'_1, 0} \langle a_{\mathbf{q}_1}^\dagger a_{\mathbf{q}_1} \rangle \langle a_{\mathbf{q}_2} a_{\mathbf{q}_2}^\dagger \rangle \\ &\quad + \delta_{\mathbf{q}_1-\mathbf{q}_2, 0} \delta_{\mathbf{q}'_1-\mathbf{q}'_2, 0} \langle a_{\mathbf{q}_1}^\dagger a_{\mathbf{q}_1} \rangle \langle a_{\mathbf{q}'_1} a_{\mathbf{q}'_1}^\dagger \rangle. \end{aligned} \quad (\text{E.27})$$

The Kronecker symbols in the second term of Eq. E.27 lead to  $\mathbf{q}_1 = \mathbf{q}_2$  and  $\mathbf{q}'_1 = \mathbf{q}'_2$ , combined with Kronecker symbols of Eq. E.26 give  $\mathbf{q} = 0$  which obviously is not of interest. We focus on the first term of Eq. E.27. On the first hand, we have  $\langle a_{\mathbf{q}}^\dagger a_{\mathbf{q}} \rangle = n_{\text{P}}(x)$  where  $n_{\text{P}}$  refers to the Planck distribution, see Eq. 4.4, and  $x = \frac{\hbar\omega_{\mathbf{q}}}{k_{\text{B}}T}$ . On the other hand, the well-known commutation relation  $[a_i^\dagger, a_j] = \delta_{ij}$  leads to  $\langle a_{\mathbf{q}} a_{\mathbf{q}}^\dagger \rangle = \langle a_{\mathbf{q}}^\dagger a_{\mathbf{q}} \rangle + 1$ . Consequently, we derive:

$$\begin{aligned} \int_0^{q_{\text{BZ}}} \Lambda^{ZZ}(q, \omega = 0) q^2 dq &= \quad (\text{E.28}) \\ \frac{1}{2} \frac{v_c}{(2\pi)^3} \int_{v_c^*} n_{\text{P}} \left( \frac{\hbar\omega(q)}{k_{\text{B}}T} \right) \left[ n_{\text{P}} \left( \frac{\hbar\omega(q)}{k_{\text{B}}T} \right) + 1 \right] \left\{ \int_{v_c^*} \delta[\omega(q) - \omega(q_1)] d^3 \mathbf{q}_1 \right\} d^3 \mathbf{q}. \end{aligned}$$

An ingenious method is to introduce the magnetic density of states such as:

$$g_m[E(q)] = \int_{v_c^*} \delta[E(q) - E(q_1)] \frac{d^3 \mathbf{q}_1}{(2\pi)^3}, \quad (\text{E.29})$$

where  $E(q) = \hbar\omega(q)$  and therefore Eq. E.28 becomes:

$$\int_0^{q_{\text{BZ}}} q^2 \Lambda^{ZZ}(q, \omega = 0) dq = \frac{\hbar v_c}{2} \int_{v_c^*} n_{\text{P}} \left( \frac{\hbar\omega(q)}{k_{\text{B}}T} \right) \left[ n_{\text{P}} \left( \frac{\hbar\omega(q)}{k_{\text{B}}T} \right) + 1 \right] g_m[E(q)] d^3 \mathbf{q}. \quad (\text{E.30})$$

For convenience, we should pass from an integration over the first Brillouin zone to an integration over the energy. Assuming a dispersion law of the form  $E = f(q)$  and the usual relation for a density of states  $g(E) dE = 4\pi q^2 dq / (2\pi)^3$ , we use the following expression for a substitution of variables in a function  $A$  [160]:

$$\int_{v_c^*} A(q) d^3 \mathbf{q} = (2\pi)^3 \int A[f^{-1}(E)] g(E) dE. \quad (\text{E.31})$$

Therefore, Eq. E.28 becomes:

$$\int_0^{q_{\text{BZ}}} q^2 \Lambda^{ZZ}(q, \omega = 0) dq = \frac{(2\pi)^3 \hbar v_c}{2} \int n_{\text{P}} \left( \frac{E}{k_{\text{B}}T} \right) \left[ n_{\text{P}} \left( \frac{E}{k_{\text{B}}T} \right) + 1 \right] g_m^2(E) dE. \quad (\text{E.32})$$

We thus obtain the expression of the spin relaxation rate in the case of a relaxation induced by ferromagnetic magnons:

$$\lambda_Z = 2(2\pi)^3 \hbar \mathcal{D} v_c \left\{ \frac{2}{15} + [C^{XZ}(\mathbf{q} = \mathbf{0})]^2 + [C^{YZ}(\mathbf{q} = \mathbf{0})]^2 \right\}$$

$$\times \int n_{\text{P}} \left( \frac{E}{k_{\text{B}}T} \right) \left[ n_{\text{P}} \left( \frac{E}{k_{\text{B}}T} \right) + 1 \right] g_m^2(E) dE. \quad (\text{E.33})$$

From Eq. E.19 we derive the associated magnetic density of states:

$$g_m(E) = \frac{1}{4\pi^2} \frac{1}{D_{\text{FM}}^{\frac{3}{2}}} \sqrt{E - \Delta}. \quad (\text{E.34})$$

Assuming  $\Delta \ll k_{\text{B}}T \ll E_{\text{max}}$ , where  $E_{\text{max}}$  is the maximal energy of a magnon excitation, and introducing  $x = E/k_{\text{B}}T$ , allows to calculate the following integral:

$$\begin{aligned} I &= \int_{\frac{\Delta}{k_{\text{B}}T}}^{\frac{E_{\text{max}}}{k_{\text{B}}T}} n(x)[n(x) + 1] g_m^2(x) k_{\text{B}}T dx \\ &= \frac{1}{(4\pi^2)^2} \frac{1}{D_{\text{FM}}^3} \int_{\frac{\Delta}{k_{\text{B}}T}}^{\frac{E_{\text{max}}}{k_{\text{B}}T}} \frac{\exp(x)}{[\exp(x) - 1]^2} (k_{\text{B}}Tx - \Delta) k_{\text{B}}T dx. \end{aligned} \quad (\text{E.35})$$

We use the following equation:

$$\int \frac{(ax - b) \exp(x)}{(\exp(x) - 1)^2} dx = \frac{b - ax}{\exp(x) - 1} - ax + a \ln[\exp(x) - 1], \quad (\text{E.36})$$

to obtain:

$$\begin{aligned} \frac{(4\pi^2)^2 D_{\text{FM}}^3}{k_{\text{B}}T} \times I &= (\Delta - E_{\text{max}}) \left[ \frac{\exp\left(\frac{E_{\text{max}}}{k_{\text{B}}T}\right)}{\exp\left(\frac{E_{\text{max}}}{k_{\text{B}}T}\right) - 1} \right] + k_{\text{B}}T \ln \left[ \exp\left(\frac{E_{\text{max}}}{k_{\text{B}}T}\right) - 1 \right] \\ &\quad - k_{\text{B}}T \ln \left[ \exp\left(\frac{\Delta}{k_{\text{B}}T}\right) - 1 \right]. \end{aligned} \quad (\text{E.37})$$

Since  $k_{\text{B}}T \ll E_{\text{max}}$ , we set  $\exp\left(\frac{E_{\text{max}}}{k_{\text{B}}T}\right) / \left[\exp\left(\frac{E_{\text{max}}}{k_{\text{B}}T}\right) - 1\right] \approx 1$  and  $\ln \left[\exp\left(\frac{E_{\text{max}}}{k_{\text{B}}T}\right) - 1\right] \approx E_{\text{max}}/k_{\text{B}}T$ . Since  $\Delta \ll k_{\text{B}}T$ , we neglect the residual term  $\Delta$  and with a linear expansion of  $\exp\left(\frac{\Delta}{k_{\text{B}}T}\right) \approx 1 + \frac{\Delta}{k_{\text{B}}T}$  in the last logarithm expression, we get:

$$I = \frac{1}{(4\pi^2)^2} \frac{(k_{\text{B}}T)^2}{D_{\text{FM}}^3} \ln \left( \frac{k_{\text{B}}T}{\Delta} \right), \quad (\text{E.38})$$

and we derive  $\lambda_Z$  in the case of ferromagnetic magnons:

$$\begin{aligned} \lambda_Z &= \frac{\hbar \mathcal{D} v_c}{\pi} \left\{ \frac{2}{15} + [C^{XZ}(\mathbf{q} = \mathbf{0})]^2 + [C^{YZ}(\mathbf{q} = \mathbf{0})]^2 \right\} \frac{k_{\text{B}}^2 T^2}{D_{\text{FM}}^3} \ln \left( \frac{k_{\text{B}}T}{\Delta} \right) \\ &\propto T^2 \ln \left( \frac{k_{\text{B}}T}{\Delta} \right). \end{aligned} \quad (\text{E.39})$$

This result has some importance since it predicts that the relaxation of the muon spin induced by ferromagnetic magnons has a vanishing spin-lattice relaxation rate when  $T \rightarrow 0$ .

## E.2.2 Antiferromagnetic magnons

The derivation of  $\lambda_Z$  in the case of antiferromagnetic magnons is a bit more complicated and we only give some pieces of the derivation of  $\lambda_Z$ , referring to the work of Ref. [160] for a complete study. We will also introduce some equations that will be needed elsewhere. For simplicity, we consider an antiferromagnetic lattice which can be viewed as two interlaced sublattices  $d_1$  and  $d_2$ , each containing magnetic atoms with opposite spins. This implies that all the nearest neighbours of a magnetic ion belonging to a magnetic sublattice belong to the other magnetic sublattice. We consider the following Hamiltonian:

$$\mathcal{H}_{\text{AF}} = \sum_{i,i'} \sum_{d_1,d_2} \mathcal{I}_{i+d_1,i'+d_2} \mathbf{J}_{i+d_1} \cdot \mathbf{J}_{i'+d_2} + g\mu_B \sum_i \sum_{d_1} \mathbf{B}_{\text{ani},d_1} \cdot \mathbf{J}_{i+d_1}, \quad (\text{E.40})$$

where  $\mathcal{I}_{i+d_1,i'+d_2} \equiv \mathcal{I}$  is the exchange integral. The notation  $i+d_1$  and  $i'+d_2$  refers to two nearest neighbours belonging to each sublattice.

The Holstein-Primakoff transformations need to be introduced for the two types of magnetic ions, i.e. two magnon modes are introduced:

$$\begin{aligned} J_{i+d_1}^+ &= \sqrt{2J} a_{i+d_1}^\dagger, & J_{i+d_1}^- &= \sqrt{2J} a_{i+d_1}, & J_{i+d_1}^Z &= a_{i+d_1}^\dagger a_{i+d_1} - J, \\ J_{i+d_2}^+ &= \sqrt{2J} b_{i+d_2}, & J_{i+d_2}^- &= \sqrt{2J} b_{i+d_2}^\dagger, & J_{i+d_2}^Z &= J - b_{i+d_2}^\dagger b_{i+d_2}, \end{aligned} \quad (\text{E.41})$$

where  $a^\dagger, b^\dagger$  and  $a, b$  are the boson creation and annihilation operators for the magnetic sublattices  $d_1, d_2$  respectively. The space Fourier transform of the boson operators is defined as:

$$\begin{aligned} a_{i+d_1} &= \frac{1}{\sqrt{n_c}} \sum_{\mathbf{q}} a_{\mathbf{q}} \exp[i\mathbf{q} \cdot (\mathbf{i} + \mathbf{d}_1)], \\ a_{i+d_1}^\dagger &= \frac{1}{\sqrt{n_c}} \sum_{\mathbf{q}} a_{\mathbf{q}}^\dagger \exp[-i\mathbf{q} \cdot (\mathbf{i} + \mathbf{d}_1)]. \end{aligned} \quad (\text{E.42})$$

We also introduce the Bogoliubov transformation:

$$\begin{aligned} a_{\mathbf{q}} &= u_{\mathbf{q}} \alpha_{\mathbf{q}} + v_{\mathbf{q}} \beta_{\mathbf{q}}^\dagger, & b_{\mathbf{q}} &= u_{\mathbf{q}} \beta_{\mathbf{q}} + v_{\mathbf{q}} \alpha_{\mathbf{q}}^\dagger, \\ a_{\mathbf{q}}^\dagger &= u_{\mathbf{q}} \alpha_{\mathbf{q}}^\dagger + v_{\mathbf{q}} \beta_{\mathbf{q}}, & b_{\mathbf{q}}^\dagger &= u_{\mathbf{q}} \beta_{\mathbf{q}}^\dagger + v_{\mathbf{q}} \alpha_{\mathbf{q}}, \end{aligned} \quad (\text{E.43})$$

where  $\alpha_{\mathbf{q}}, \alpha_{\mathbf{q}}^\dagger, \beta_{\mathbf{q}}, \beta_{\mathbf{q}}^\dagger$  are bosons operators fulfilling the relations:

$$[\alpha_{\mathbf{q}}, \alpha_{\mathbf{q}'}^\dagger] = \delta_{\mathbf{q}-\mathbf{q}',0}, \quad \text{and} \quad [\beta_{\mathbf{q}}, \beta_{\mathbf{q}'}^\dagger] = \delta_{\mathbf{q}-\mathbf{q}',0}. \quad (\text{E.44})$$

Note that  $\alpha_{\mathbf{q}_1}, \alpha_{\mathbf{q}_2}^\dagger$  commutes with  $\beta_{\mathbf{q}_3}, \beta_{\mathbf{q}_4}^\dagger$ . This leads to the relation:

$$u_{\mathbf{q}}^2 - v_{\mathbf{q}}^2 = 1. \quad (\text{E.45})$$

Therefore, we can introduce a function  $x_{\mathbf{q}}$  such as:

$$u_{\mathbf{q}} = \cosh(x_{\mathbf{q}}) \quad \text{and} \quad v_{\mathbf{q}} = \sinh(x_{\mathbf{q}}). \quad (\text{E.46})$$

The Hamiltonian defined in Eq. E.40 can be reduced as:

$$\mathcal{H}_{\text{AF}} = \sum_{\mathbf{q}} \hbar\omega_{\mathbf{q}}(\alpha_{\mathbf{q}}^{\dagger}\alpha_{\mathbf{q}} + \beta_{\mathbf{q}}^{\dagger}\beta_{\mathbf{q}} + 1). \quad (\text{E.47})$$

The most general dispersion law for antiferromagnetic magnons is:

$$(\hbar\omega_{\mathbf{q}})^2 = (\hbar\omega_{\text{ex}} + \Delta)^2 - (\hbar\omega_{\text{ex}}\gamma_{\mathbf{q}})^2, \quad (\text{E.48})$$

where  $\Delta$  is the energy gap of the magnons due to the anisotropy of the spins, and  $\hbar\omega_{\text{ex}} = 2\mathcal{I}z_{\text{nn}}J$ . We have introduced:

$$\gamma_{\mathbf{q}} = \frac{1}{z_{\text{nn}}} \sum_{\mathbf{d}_{\text{pair}}} \exp(i\mathbf{q} \cdot \mathbf{d}_{\text{pair}}), \quad (\text{E.49})$$

where  $\mathbf{d}_{\text{pair}}$  is the vector joining a magnetic ion to one of its nearest neighbours. At small wave vectors for a cubic compound, we simplify Eq. E.48 to the well-known dispersion law for antiferromagnetic magnons, assuming the energy to only depend on the modulus of  $\mathbf{q}$ :

$$(\hbar\omega_{\mathbf{q}})^2 = D_{\text{AF}}^2 q^2 + \Delta^2, \quad (\text{E.50})$$

where  $D_{\text{AF}} = 4\sqrt{3}\mathcal{I}Ja_{\text{lat}}$ . Note that the Hamiltonian has been rendered diagonal with  $\alpha_{\mathbf{q}}^{\dagger}\beta_{\mathbf{q}}^{\dagger} + \alpha_{\mathbf{q}}\beta_{\mathbf{q}} = 0$  which leads to:

$$\tanh(2x_{\mathbf{q}}) = -\gamma_{\mathbf{q}} \frac{\omega_{\text{ex}}}{\omega_{\text{ex}} + \Delta}, \quad (\text{E.51})$$

After the introduction of these definitions, let us go back to the derivation of the spin-lattice relaxation rate which is rewritten as:

$$\lambda_Z = \frac{\mathcal{D}}{2} \frac{1}{V} \sum_{\mathbf{q}} \sum_{d_1 d_2} (G_{d_1}^{X,Z}(\mathbf{q})G_{d_2}^{Z,X}(-\mathbf{q}) + G_{d_1}^{Y,Z}(\mathbf{q})G_{d_2}^{Z,Y}(-\mathbf{q}))\Lambda_{d_1 d_2}^{ZZ}(\mathbf{q}, \omega = 0). \quad (\text{E.52})$$

Note that we have directly considered that only the spins correlations along the  $Z$  axis come at play in the Raman process. To evaluate the spin correlation tensor, we need to introduce:

$$\begin{aligned} \delta J_{d_1}^Z(\mathbf{q}) &= \frac{1}{\sqrt{n_c}} \sum_{\mathbf{q}_1, \mathbf{q}_2} \delta_{\mathbf{q}_1 + \mathbf{q}_2 - \mathbf{q}, 0} a_{\mathbf{q}_1}^{\dagger} a_{\mathbf{q}_2}, \\ \delta J_{d_2}^Z(\mathbf{q}) &= \frac{1}{\sqrt{n_c}} \sum_{\mathbf{q}_1, \mathbf{q}_2} \delta_{\mathbf{q}_1 + \mathbf{q}_2 - \mathbf{q}, 0} b_{\mathbf{q}_1}^{\dagger} b_{\mathbf{q}_2}, \end{aligned} \quad (\text{E.53})$$

After some calculations, the following expression is derived [160]:

$$\lambda_Z = \frac{8}{15} (2\pi)^3 \hbar \mathcal{D} v_c \int n_{\text{P}} \left( \frac{E}{k_{\text{B}}T} \right) \left[ n_{\text{P}} \left( \frac{E}{k_{\text{B}}T} \right) + 1 \right] g_m^2(E) dE. \quad (\text{E.54})$$

From Eq. E.50, we infer the associated magnetic density of states as:

$$g_m(E) = \frac{1}{2\pi^2} \frac{E}{D_{\text{AF}}^3} \sqrt{E^2 - \Delta^2} \quad (\text{E.55})$$

Introducing  $x = \frac{E}{k_B T}$ , we derive:

$$\begin{aligned}\lambda_Z &\propto 2(2\pi)^3 \hbar \mathcal{D}v_c \frac{1}{4\pi^4} \frac{1}{D_{\text{AF}}^6} k_B T \int_{\frac{\Delta}{k_B T}}^{\infty} \left\{ \frac{\exp(x)}{[\exp(x) - 1]^2} (k_B T x)^2 [(k_B T)^2 x^2 - \Delta^2] \right\} dx \\ &\propto \frac{1}{\pi} \hbar \mathcal{D}v_c \frac{(k_B T)^3}{D_{\text{AF}}^6} [(k_B T)^2 I_4 - \Delta^2 I_2]\end{aligned}\quad (\text{E.56})$$

where we have introduced the following integral:

$$I_{2m} = \int_0^{\infty} \frac{x^{2m} \exp(x)}{[\exp(x) - 1]^2} dx \quad (\text{E.57})$$

Note that compared to the ferromagnetic case, we do not introduce a maximum energy for the magnons since no convergence problem appears in the integral. We also assumed that  $\Delta \ll k_B T$ , leading us to neglect the term containing  $I_2$ . Since  $I_4 = 4\pi^2/15$ , we get the expression of  $\lambda_Z$  in the antiferromagnetic case:

$$\lambda_Z \propto \frac{4\pi^3}{15} \hbar \mathcal{D}v_c \frac{1}{D_{\text{AF}}^6} (k_B T)^5. \quad (\text{E.58})$$

Once again, the muon spin relaxation driven by antiferromagnetic magnons has a vanishing spin lattice relaxation rate when  $T \rightarrow 0$ .

# List of publications

- **Nd<sub>2</sub>Sn<sub>2</sub>O<sub>7</sub>: an all-in all-out pyrochlore magnet with no divergence-free field and anomalously slow paramagnetic spin dynamics**  
*A. Bertin, P. Dalmas de Réotier, B. Fåk, C. Marin, A. Yaouanc, A. Forget, D. Sheptyakov, B. Frick, C. Ritter, A. Amato, C. Baines, and P.J.C. King*  
Submitted to Physical Review B
- **Crystal electric field in the R<sub>2</sub>Ti<sub>2</sub>O<sub>7</sub> pyrochlore compounds**  
*A. Bertin, Y. Chapuis, P. Dalmas de Réotier, and A. Yaouanc*  
J. Phys.: Cond. Matter **24**, 256003 (2012)
- **Evidence for unidimensional low-energy excitations as the origin of persistent spin dynamics in geometrically frustrated magnets**  
*A. Yaouanc, P. Dalmas de Réotier, A. Bertin, C. Marin, E. Lhotel, A. Amato, C. Baines*  
Phys. Rev. B **91**, 104427 (2015)
- **Low temperature crystal structure and local magnetometry for the geometrically frustrated pyrochlore Tb<sub>2</sub>Ti<sub>2</sub>O<sub>7</sub>**  
*P. Dalmas de Réotier, A. Yaouanc, A. Bertin, C. Marin, S. Vanishri, D. Sheptyakov, A. Cervellino, B. Roessli, and C. Baines*  
Journal of Physics: Conference Series **551**, 012021 (2014)
- **Study for the dynamical nature of the ordered and paramagnetic ground state of Er<sub>2</sub>Ti<sub>2</sub>O<sub>7</sub> by neutron spin echo spectroscopy**  
In preparation
- **Crystal-electric-field study in the geometrically frustrated pyrochlores R<sub>2</sub>Sn<sub>2</sub>O<sub>7</sub>**  
In preparation

# Bibliography

- [1] G. H. Wannier, Phys. Rev., **79**, 357 (1950), erratum: Phys. Rev. B **7**, 5017 (1973).
- [2] P. Dalmas de Réotier *et al.*, Phys. Rev. B, **86**, 104424 (2012).
- [3] P. Schiffer *et al.*, Phys. Rev. Lett., **73**, 2500 (1994).
- [4] J. N. Reimers, Phys. Rev. B, **45**, 7287 (1992).
- [5] R. Moessner and J. T. Chalker, Phys. Rev. Lett., **80**, 2929 (1998).
- [6] R. Moessner and J. T. Chalker, Phys. Rev. B, **58**, 12049 (1998).
- [7] S. E. Palmer and J. T. Chalker, Phys. Rev. B, **62**, 488 (2000).
- [8] N. P. Raju *et al.*, Phys. Rev. B, **59**, 14489 (1999).
- [9] A. S. Wills *et al.*, J. Phys.: Condens. Matter, **18**, L37 (2006).
- [10] R. Moessner, Phys. Rev. B, **57**, R5587 (1998).
- [11] S. T. Bramwell and M. J. Harris, J. Phys.: Condens. Matter, **10**, L215 (1998).
- [12] G. Ferey *et al.*, Rev. Chim. Miner., **23**, 474 (1986).
- [13] M. J. Harris *et al.*, Phys. Rev. Lett., **81**, 4496 (1998).
- [14] M. E. Zhitomirsky *et al.*, Phys. Rev. Lett., **109**, 077204 (2012).
- [15] J. Villain *et al.*, J. Phys. France, **41**, 1263 (1980).
- [16] S. T. Bramwell, M. J. P. Gingras, and J. N. Reimers, J. Appl. Phys., **75**, 5523 (1994).
- [17] L. Savary *et al.*, Phys. Rev. Lett., **109**, 167201 (2012).
- [18] M. J. Harris *et al.*, Phys. Rev. Lett., **79**, 2554 (1997).
- [19] M. J. Harris *et al.*, J. Magn. Magn. Mater., **177**, 757 (1998).
- [20] A. P. Ramirez *et al.*, Nature, **399**, 333 (1999).
- [21] H. Kadowaki *et al.*, Phys. Rev. B, **65**, 144421 (2002).

- [22] K. Matsuhira, Y. Hinatsu, and T. Sakakibara, *Journal of Physics: Condensed Matter*, **13**, L737 (2001).
- [23] D. Bernal and R. H. Fowler, *J. Chem. Phys.*, **1**, 515 (1933).
- [24] J. S. Gardner, M. J. P. Gingras, and J. E. Greedan, *Rev. Mod. Phys.*, **82**, 53 (2010).
- [25] R. Moessner and A. P. Ramirez, *Physics Today*, pp. 24–29 (February 2006).
- [26] L. Pauling, *J. Am. Chem. Soc.*, **57**, 2680 (1935).
- [27] S. T. Bramwell *et al.*, *Phys. Rev. Lett.*, **87**, 047205 (2001).
- [28] G. Prando *et al.*, *J. Phys: Conf. Ser.*, **145**, 012033 (2009).
- [29] X. Ke *et al.*, *Phys. Rev. B*, **76**, 214413 (2007).
- [30] J. Snyder *et al.*, *Phys. Rev. B*, **69**, 064414 (2004).
- [31] K. Matsuhira *et al.*, *Journal of Physics: Condensed Matter*, **12**, L649 (2000).
- [32] B. C. den Hertog and M. J. P. Gingras, *Phys. Rev. Lett.*, **84**, 3430 (2000).
- [33] K. Matsuhira *et al.*, *J. Phys. Soc. Jpn.*, **71**, 1576 (2002).
- [34] S. T. Bramwell and M. J. P. Gingras, *Science*, **294**, 1495 (2001).
- [35] R. Siddharthan *et al.*, *Phys. Rev. Lett.*, **83**, 1854 (1999).
- [36] R. Siddharthan, B. S. Shastry, and A. P. Ramirez, *Phys. Rev. B*, **63**, 184412 (2001).
- [37] M. J. P. Gingras and B. C. den Hertog, *Can. J. Phys.*, **79**, 1339 (2000).
- [38] R. G. Melko and M. J. P. Gingras, *Journal of Physics: Condens. Matter*, **16**, R1277 (2004).
- [39] C. L. Henley, *Phys. Rev. B*, **71**, 014424 (2005).
- [40] J. P. Clancy *et al.*, *Phys. Rev. B*, **79**, 014408 (2009).
- [41] T. Fennell *et al.*, *Phys. Rev. B*, **70**, 134408 (2004).
- [42] T. Fennell *et al.*, *Science*, **326**, 415 (2009).
- [43] I. A. Ryzhkin, *JETP*, **101**, 481 (2005).
- [44] C. Castelnovo, R. Moessner, and S. L. Sondhi, *Nature*, **451**, 42 (2008).
- [45] C. Castelnovo, R. Moessner, and S. L. Sondhi, *Annu. Rev. Cond. Matter Phys.*, **1**, 179 (2012).
- [46] C. L. Henley, *Ann. Rev. Condens. Matter Phys.*, **1**, 179 (2010).

- [47] S. T. Bramwell *et al.*, *Nature*, **461**, 956 (2009).
- [48] L. Onsager, *J. Chem. Phys.*, **2**, 599 (1934).
- [49] L. J. Chang *et al.*, *Sci. Rep.*, **3**, 1881 (2013).
- [50] S. R. Dunsiger *et al.*, *Phys. Rev. Lett.*, **107**, 207207 (2011).
- [51] S. J. Blundell, *Phys. Rev. Lett.*, **108**, 147601 (2012).
- [52] D. J. P. Morris *et al.*, *Science*, **326**, 411 (2009).
- [53] L. D. C. Jaubert and P. C. W. Holdsworth, *Nature Phys.*, **5**, 258 (2009).
- [54] M. Hermele, M. P. A. Fisher, and L. Balents, *Phys. Rev. B*, **69**, 064404 (2004).
- [55] M. J. P. Gingras and P. A. McClarty, *Rep. Prog. Phys.*, **77** (2014).
- [56] O. Benton, O. Sikora, and N. Shannon, *Phys. Rev. B*, **86**, 075154 (2012).
- [57] N. Shannon *et al.*, *Phys. Rev. Lett.*, **108**, 067204 (2012).
- [58] S. H. Curnoe, *Phys. Rev. B*, **78**, 094418 (2008).
- [59] S. Onoda, *Journal of Physics: Conference Series*, **320**, 012065 (2011).
- [60] K. A. Ross *et al.*, *Phys. Rev. X*, **1**, 021002 (2011).
- [61] P. McClarty, S. Curnoe, and M. Gingras, *J. Phys.: Conf. Series*, **145**, 012032 (2009).
- [62] M. Elhajal, B. Canals, and C. Lacroix, *J. Phys.: Cons. Matter*, **16**, S917 (2004).
- [63] M. Elhajal *et al.*, *Phys. Rev. B*, **71**, 094420 (2005).
- [64] T. Moriya, *Phys. Rev.*, **120**, 91 (1960).
- [65] L. Savary and L. Balents, *Phys. Rev. Lett.*, **108**, 037202 (2012).
- [66] S. Lee, S. Onoda, and L. Balents, *Phys. Rev. B*, **86**, 104412 (2012).
- [67] L. Savary and L. Balents, *Phys. Rev. B*, **87**, 205130 (2013).
- [68] K. Kimura *et al.*, *Nat. Commun.*, **4**, 1934 (2013).
- [69] A. J. Princep *et al.*, *Phys. Rev. B*, **88**, 104421 (2013).
- [70] H. D. Zhou *et al.*, *Phys. Rev. Lett.*, **101**, 227204 (2008).
- [71] K. Matsuhira *et al.*, *J. Phys. Soc. Jpn.*, **272-276**, e981 (2004).
- [72] S. Onoda and Y. Tanaka, *Phys. Rev. Lett.*, **105**, 047201 (2010).
- [73] I. Mirebeau, P. Bonville, and M. Hennion, *Phys. Rev. B*, **76**, 184436 (2007).

- [74] I. Mirebeau *et al.*, Phys. Rev. Lett., **94**, 246402 (2005).
- [75] P. Dalmas de Réotier *et al.*, Phys. Rev. Lett., **96**, 127202 (2006).
- [76] I. Mirebeau *et al.*, Physica B, **385**, 307 (2006).
- [77] F. Bert *et al.*, Phys. Rev. Lett., **97**, 117203 (2006).
- [78] Y. Chapuis *et al.*, J. Phys.: Condens. Matter, **19**, 446206 (2007).
- [79] K. C. Rule *et al.*, J. Phys.: Condens. Matter, **21**, 486005 (2009).
- [80] K. C. Rule *et al.*, Phys. Rev. B, **76**, 212405 (2007).
- [81] I. Mirebeau *et al.*, Phys. Rev. B, **78**, 174416 (2008).
- [82] H. W. J. Blöte, R. F. Wielinga, and W. J. Huiskamp, Physica, **43**, 549 (1969).
- [83] J. A. Hodges *et al.*, J. Phys.: Condens. Matter, **13**, 9301 (2001).
- [84] J. A. Hodges *et al.*, Phys. Rev. Lett., **88**, 077204 (2002).
- [85] J. S. Gardner *et al.*, Phys. Rev. B, **70**, 180404(R) (2004).
- [86] R. Applegate *et al.*, Phys. Rev. Lett., **109**, 097205 (2012).
- [87] N. R. Hayre *et al.*, Phys. Rev. B, **87**, 184423 (2013).
- [88] Y. Yasui *et al.*, J. Phys. Soc. Jpn., **72**, 3014 (2003).
- [89] L.-J. Chang *et al.*, Nat. Commun., **3**, 992 (2012).
- [90] K. A. Ross *et al.*, Phys. Rev. B, **86**, 174424 (2012).
- [91] A. Yaouanc *et al.*, Phys. Rev. B, **84**, 172408 (2011).
- [92] A. Yaouanc *et al.*, Phys. Rev. Lett., **110**, 127207 (2013).
- [93] Z. L. Dun *et al.*, Phys. Rev. B, **87**, 134408 (2013).
- [94] J. Lago *et al.*, Phys. Rev. B, **89**, 024421 (2014).
- [95] S. T. Bramwell *et al.*, J. Phys.: Condens. Matter, **12**, 483 (2000).
- [96] J. D. M. Champion *et al.*, Phys. Rev. B, **68**, 020401 (2003).
- [97] A. Poole, A. S. Wills, and E. Lelièvre-Berna, J. Phys.: Condens. Matter, **19**, 452201 (2007).
- [98] J. D. M. Champion and P. C. W. Holdsworth, J. Phys. Condens. Matter, **16**, S665 (2004).
- [99] M. E. Zhitomirsky, P. C. W. Holdsworth, and R. Moessner, Phys. Rev. B, **89**, 140403 (2014).

- [100] S. Petit *et al.*, Phys. Rev. B, **90**, 060410 (2014).
- [101] J. P. C. Ruff *et al.*, Phys. Rev. Lett., **101**, 147205 (2008).
- [102] J. Lago *et al.*, J. Phys.: Condens. Matter, **17**, 979 (2005).
- [103] H. B. Cao *et al.*, Phys. Rev. B, **82**, 104431 (2010).
- [104] S. Guitteny *et al.*, Phys. Rev. B, **88**, 134408 (2013).
- [105] P. M. Sarte *et al.*, J. Phys.: Condens. Matter, **23**, 382201 (2011).
- [106] S. T. Bramwell, M. Shirai, and C. Ritter, Search for a quantum critical point in a geometrically frustrated magnet (2004), Institut Laue Langevin Experimental Report No 5-31-1496.
- [107] V. N. Glazkov *et al.*, Phys. Rev. B, **72**, 020409 (2005).
- [108] V. N. Glazkov *et al.*, J. Phys.: Condens. Matter, **18**, 2285 (2006).
- [109] G. Luo, S. T. Hess, and L. R. Corruccini, Phys. Lett. A, **291**, 306 (2001).
- [110] V. Bondah-Jagalu and S. T. Bramwell, Can. J. Phys., **79**, 1381 (2001).
- [111] A. P. Ramirez *et al.*, Phys. Rev. Lett., **89**, 067202 (2002).
- [112] A. Yaouanc *et al.*, Phys. Rev. Lett., **95**, 047203 (2005).
- [113] J. D. M. Champion *et al.*, Phys. Rev. B, **64**, 140407 (2001).
- [114] J. R. Stewart *et al.*, J. Phys.: Condens. Matter, **16**, L321 (2004).
- [115] G. Ehlers, J. Phys.: Condens. Matter, **18**, R231 (2006).
- [116] Y. Chapuis *et al.*, Physica B, **404**, 686 (2009).
- [117] P. Bonville *et al.*, J. Phys.: Condens. Matter, **15**, 7777 (2003).
- [118] P. Bonville *et al.*, Hyperfine Interactions, **156-157**, 103 (2004).
- [119] E. Bertin *et al.*, Eur. Phys. J. B, **27**, 347 (2002).
- [120] P. Bonville *et al.*, Phys. Rev. Lett., **92**, 167202 (2004).
- [121] J. C. Lashley, Cryogenics, **43**, 369 (2003).
- [122] D. R. Gaskell, *Introduction to the thermodynamics of materials* (Taylor and Francis Group, LLC, New York, 2008), fifth edition.
- [123] Y. Chapuis, *Frustration géométrique, transitions de phase et ordre dynamique*, Ph.D. thesis, Université Joseph Fourier, Grenoble (2009).
- [124] S. Tumanski, Phys. Rev. B, **24**, 5363 (2007).
- [125] <http://peach.center.ous.ac.jp/>.

- [126] [http://www.icmmo.u-psud.fr/Labos/LCI/Service\\_SQUID/](http://www.icmmo.u-psud.fr/Labos/LCI/Service_SQUID/).
- [127] <http://hyperphysics.phy-astr.gsu.edu/hbase/solids/squid.html>.
- [128] *The ILL yellow book, guide to neutron research facilities* (2008).
- [129] <http://www.psi.ch>.
- [130] J. Rodriguez-Carvajal, *Physica B*, **192**, 55 (1993).
- [131] [http://www.met.reading.ac.uk/pplato2/h-flap/phys7\\_1.html](http://www.met.reading.ac.uk/pplato2/h-flap/phys7_1.html).
- [132] <http://xray0.princeton.edu/phil/Facility/Guides/XrayDataCollection.html>.
- [133] L. H. Schwartz and J. B. Cohen, *Diffraction from Materials* (Academic Press, 1987).
- [134] M. Schlenker, in J. Baruchel *et al.*, eds., *Neutron and synchrotron radiation for condensed matter studies* (EDP Sciences, Springer-Verlag, 1993).
- [135] M. J. Buerger, *Physics*, **26**, 637 (1940).
- [136] V. F. Sears, *Neutron News*, **3**, 26 (1992), issue No 3.
- [137] A. S. Wills, *J. Phys. IV France*, **11**, 133 (2001).
- [138] G. L. Squires, *Introduction to the Theory of Thermal Neutron Scattering*, chap. 7 (Cambridge University Press, London, 1976).
- [139] J. Rossat-Mignod, in K. Sköld and D. L. Price, eds., *Methods of Experimental Physics*, vol. 23, part C (Academic Press, Inc, New York, 1987).
- [140] P. R. Willmott *et al.*, *J. Synchrotron Rad.*, **20**, 667 (2013).
- [141] <http://pd.chem.ucl.ac.uk/pdnn/inst1/optics1.htm>.
- [142] <http://www.psi.ch/sls/ms/pd-description>.
- [143] <http://www.psi.ch/sinq/hrpt/description>.
- [144] J. Rodriguez-Carvajal, *An introduction to the program FullProf* (2001).
- [145] B. H. Toby, *Powder Diffraction*, **21** (2006).
- [146] P. Thompson, D. Cox, and J. Hastings, *J. Appl. Crystallogr.*, **20**, 79 (1987).
- [147] L. W. Finger and D. E. Cox, *J. Appl. Cryst.*, **27**, 892 (1994).
- [148] <http://www.isis.stfc.ac.uk/instruments/mari/technical/>.
- [149] S. Ikeda and J. M. Carpenter, *Nucl. Instr. and Meth. A*, **239**, 536 (1985).
- [150] M. Marseguerra and G. Pauli, *Nucl. Instr. and Meth.*, **4**, 140 (1959).
- [151] K. H. Andersen, *Nucl. Instr. and Meth. A*, **371**, 472 (1996).

- [152] C. K. Loong, S. Ikeda, and J. Carpenter, *Nucl. Instr. and Meth.*, **A260**, 381 (1987).
- [153] R. Eccleston, in F. Hippert *et al.*, eds., *Neutron and X-ray spectroscopy* (Springer, 2006).
- [154] C. Windsor, *Pulsed Neutron scattering* (Taylor and Francis LTD, London, 1981).
- [155] <http://www.isis.stfc.ac.uk/instruments/mari/software/mari-software4777.html>.
- [156] <https://www.ill.eu/sites/BS-review>.
- [157] C. G. Darwin, *Phil. Mag.*, **27**, 315675 (1914).
- [158] P. Ewald, *Z. Phys.*, **30**, 1 (1924).
- [159] B. Frick, in F. Hippert *et al.*, eds., *Neutron and X-ray spectroscopy* (Springer, 2006).
- [160] A. Yaouanc and P. Dalmas de Réotier, *Muon Spin Rotation, Relaxation, and Resonance: Applications to Condensed Matter*, International Series of Monographs on Physics 147 (Oxford University Press, Oxford, 2011).
- [161] A. Amato and H. Luetkens, *GPS User Guide* (2014), <http://www.psi.ch/smusc/gps>.
- [162] J. Jensen and A. R. Mackintosh, *Rare Earth Magnetism; Structures and Excitations* (Clarendon, Oxford, 1991).
- [163] A. Abragam and B. Bleaney, *Electron paramagnetic resonance of transition ions* (Clarendon, Oxford, 1970).
- [164] M. T. Hutchings, in F. Seitz and D. Turnbull, eds., *Solid State Physics*, vol. 16, p. 227 (Academic Press, New York, 1964).
- [165] K. B. Helean *et al.*, *J. Solid State Chem.*, **177**, 1858 (2004).
- [166] B. Z. Malkin, in A. A. Kaplyanskii and R. M. Macfarlane, eds., *Spectroscopy of solids containing rare earth ions*, chap. 12, p. 13 (North-Holland, Amsterdam, 1987).
- [167] C. Mazumdar *et al.*, *Phys. Rev. B*, **78**, 144422 (2008).
- [168] S. Rosenkranz *et al.*, *J. Appl. Phys.*, **87**, 5914 (2000).
- [169] B. Z. Malkin *et al.*, *Phys. Rev. B*, **70**, 075112 (2004).
- [170] J. Zhang *et al.*, *Phys. Rev. B*, **89**, 134410 (2014).
- [171] M. Shirai, Ph.D. thesis, University College London (2006).
- [172] M. P. Zinkin *et al.*, *J. Phys.: Condens. Matter*, **8**, 193 (1996).

- [173] A. Bertin *et al.*, J. Phys.: Condens. Matter, **24**, 256003 (2012).
- [174] Code developed in Fortran by Bertin A.
- [175] M. Mączka *et al.*, Phys. Rev. B, **79**, 214437 (2009).
- [176] T. T. A. Lummen *et al.*, Phys. Rev. B, **77**, 214310 (2008).
- [177] K. Kanada *et al.*, Journal of the Physical Society of Japan, **68** (1999).
- [178] J. S. Gardner *et al.*, Phys. Rev. Lett., **82**, 1012 (1999).
- [179] M. J. P. Gingras *et al.*, Phys. Rev. B, **62**, 6496 (2000).
- [180] M. Mączka *et al.*, Phys. Rev. B, **78**, 134420 (2008).
- [181] V. V. Klekovkina and B. Z. Malkin, Optics and Spectroscopy, **116**, 849 (2014).
- [182] A. J. Princep *et al.*, Crystal field states of  $\text{tb}^{3+}$  in the pyrochlore spin liquid  $\text{tb}_2\text{ti}_2\text{o}_7$  from neutron spectroscopy (2015), arXiv:1501.04927.
- [183] <http://www.isis.stfc.ac.uk/instruments/prisma/technical/prisma-technical-information7295.html>.
- [184] J. S. Gardner and G. Ehlers, J. Phys.: Condens. Matter, **21**, 436004 (2009).
- [185] H. Cao *et al.*, Phys. Rev. Lett., **103**, 056402 (2009).
- [186] H. Armon, E. R. Bauminger, and S. Ofer, Phys. Lett. B, **43**, 380 (1973).
- [187] J. D. Cashion, D. B. Prowse, and A. Vas, J. Phys. C: Solid State Phys., **6**, 2611 (1973).
- [188] R. Pöttgen and K. Łątka, Z. Anorg. Allg. Chem, **636**, 2244 (2010).
- [189] R. P. Gupta and S. K. Sen, Phys. Rev. A, **7**, 850 (1973).
- [190] B. J. Kennedy, B. A. Hunter, and C. J. Howard, J. Sol. State Chem., **130**, 58 (1997).
- [191] M. A. Subramanian, G. Aravamudan, and G. V. S. Rao, Prog. Solid St. Chem., **15**, 55 (1983).
- [192] P. Dalmas de Réotier *et al.*, Phys. Rev. Lett., **91**, 167201 (2003).
- [193] C. Kittel, *Quantum Theory of Solids* (J. Wiley & Sons, New York, 1963).
- [194] I. S. Gradshteyn and I. M. Ryzhik, *Table of integrals, series and products* (Academic Press, San Diego, 1985), corrected and enlarged edition.
- [195] P. Dalmas de Réotier *et al.*, Phys. Rev. B, **85**, 140407 (2012).
- [196] A. Kornblit and G. Ahlers, Phys. Rev. B, **8**, 5163 (1973).

- [197] M. E. Fisher, *J. Math. Phys.*, **5**, 944 (1964).
- [198] A. Pelissetto and E. Vicari, *Physics Reports*, **368**, 549 (2002).
- [199] C. Kittel, *Introduction to Solid State Physics* (J. Wiley & Sons, New York, 1986), sixth edition.
- [200] H. Sagayama *et al.*, *Phys. Rev. B*, **87**, 100403 (2013).
- [201] C. Hohenemser, N. Rosov, and A. Kleinhammes, *Hyp. Int.*, **49**, 267 (1989).
- [202] R. K. Harris *et al.*, *Pure Appl. Chem.*, **73**, 1795 (2001).
- [203] G. E. Barberis *et al.*, *Phys. Rev. B*, **19**, 5495 (1979).
- [204] A. Heidemann, *Z. Phys.*, **238**, 208 (1970).
- [205] G. L. Squires, *Introduction to the Theory of Thermal Neutron Scattering*, chap. 7 (Cambridge University Press, London, 1978).
- [206] W. G. Stirling and K. A. McEwen, in K. Sköld and D. L. Price, eds., *Methods of Experimental Physics: Neutron Scattering*, vol. 23C, chap. 20 (Academic Press, New York, 1987).
- [207] Code developed in Fortran by Bertin A.
- [208] W. Marshall and S. W. Lovesey, *Theory of thermal neutron scattering* (Clarendon, Oxford, 1971).
- [209] N. Bloembergen, *Physica*, **15**, 386 (1949).
- [210] L. Van Hove, *Phys. Rev.*, **95**, 1374 (1954).
- [211] H. Benner and J. P. Boucher, in L. J. de Jongh, ed., *Magnetic properties of layered transition metal compounds*, pp. 323–378 (Kluwer Academic Publishers, 1990).
- [212] A. Yaouanc *et al.*, *Phys. Rev. B*, **91**, 104427 (2015).
- [213] S. W. Lovesey, *Theory of Neutron Scattering from Condensed Matter*, vol. 2 (Clarendon, Oxford, 1986).
- [214] R. S. Hayano *et al.*, *Phys. Rev. B*, **20**, 850 (1979).
- [215] P. J. Baker *et al.*, *Phys. Rev. B*, **86**, 094424 (2012).
- [216] A. Zorko *et al.*, *Phys. Rev. Lett.*, **100**, 147201 (2008).
- [217] A. Abragam, *C. R. Acad. Sci.*, **299**, 95 (1984).
- [218] M. Enjalran and M. J. P. Gingras, *Phys. Rev. B*, **70**, 174426 (2004).
- [219] A. Yaouanc *et al.*, *Phys. Rev. B*, **84**, 184403 (2011).
- [220] A. Keren *et al.*, *Phys. Rev. Lett.*, **92**, 107204 (2004).

- [221] J. S. Gardner *et al.*, Phys. Rev. B, **68**, 180401(R) (2003).
- [222] J. S. Gardner *et al.*, Phys. Rev. B, **64**, 224416 (2001).
- [223] Y. Yasui *et al.*, J. Phys. Soc. Jpn., **71**, 599 (2002).
- [224] S. Legl *et al.*, Phys. Rev. Lett., **109**, 047201 (2012).
- [225] E. Lhotel *et al.*, Phys. Rev. B, **86**, 020410(R) (2012).
- [226] L. Yin *et al.*, Phys. Rev. Lett., **110**, 137201 (2013).
- [227] K. Binder and A. P. Young, Rev. Mod. Phys., **58**, 801 (1986).
- [228] Y. Chapuis *et al.*, Phys. Rev. B, **82**, 100402(R) (2010).
- [229] P. Bonville *et al.*, Phys. Rev. B, **84**, 184409 (2011).
- [230] B. D. Gaulin *et al.*, Phys. Rev. B, **84**, 140402(R) (2011).
- [231] Y. Luan, *Elastic properties of complex transition metal oxides studied by resonance ultrasound spectroscopy*, Ph.D. thesis, University of Tennessee (2011).
- [232] Y. Nakanishi *et al.*, Phys. Rev. B, **83**, 184434 (2011).
- [233] J. P. C. Ruff *et al.*, Phys. Rev. Lett., **99**, 237202 (2007).
- [234] K. Goto *et al.*, J. Phys. Soc. Jpn, **81**, 015001 (2012).
- [235] P. Dalmas de Réotier *et al.*, J. Phys.: Conf. Ser., **551**, 012021 (2014).
- [236] T. Fennell *et al.*, Phys. Rev. Lett., **112**, 017203 (2014).
- [237] S. H. Curnoe, Phys. Rev. B, **88**, 014429 (2013).
- [238] S. P. Mukherjee and S. H. Curnoe, Phys. Rev. B, **90**, 214404 (2014).
- [239] H. R. Molavian, M. J. P. Gingras, and B. Canals, Phys. Rev. Lett., **98**, 157204 (2007).
- [240] Y.-J. Kao *et al.*, Phys. Rev. B, **68**, 172407 (2003).
- [241] T. Fennell *et al.*, Phys. Rev. Lett., **109**, 017201 (2012).
- [242] K. Fritsch *et al.*, Phys. Rev. B, **87**, 094410 (2013).
- [243] S. Guitteny *et al.*, Phys. Rev. Lett., **111**, 087201 (2013).
- [244] R. Moessner and S. L. Sondhi, Phys. Rev. B, **68**, 064411 (2003).
- [245] K. Matsuhira *et al.*, J. Phys.: Condens. Matter, **14**, L559 (2002).
- [246] S. Sakakibara *et al.*, Phys. Rev. Lett., **90**, 207205 (2003).

- [247] H. R. Molavian and M. J. P. Gingras, *J. Phys.: Condens. Matter*, **21**, 172201 (2009).
- [248] C. Dekker *et al.*, *Phys. Rev. B*, **40**, 11243 (1989).
- [249] L. G. Mamsurova, K. S. Pigal'skii, and K. K. Pukhov, *JETP Lett.*, **43**, 755 (1986).
- [250] N. Magnani *et al.*, *Phys. Rev. B*, **71**, 054405 (2005).
- [251] M. E. Brooks-Bartlett *et al.*, *Phys. Rev. X*, **4**, 011007 (2014).
- [252] Y. Huang, G. Chen, and M. Hermele, *Phys. Rev. Lett.*, **112**, 167203 (2014).
- [253] M. Watahiki *et al.*, *J. Phys.: Conf. Ser.*, **320**, 012080 (2011).
- [254] J. Lago *et al.*, *Phys. Rev. Lett.*, **104**, 247203 (2010).
- [255] H. Margenau and G. M. Murphy, *The mathematics of physics and chemistry* (Van Nostrand, Princeton, New Jersey, 1956), 2<sup>nd</sup> edition.
- [256] M. Stone and P. Goldbart, *Mathematics for physics, a guided tour for graduate students* (Cambridge University Press, New York, 2009).
- [257] A. J. Freeman and J. P. Desclaux, *J. Mag. Mag. Mat*, **12**, 11 (1979).
- [258] K. W. H. Stevens, *Proc. Phys. Soc. London, Sect.*, **A 65**, 209 (1951).
- [259] D. Schmitt and B. Ouladdiaf, *J. Appli. Cryst.*, **31**, 620 (1998).
- [260] O. V. Kovalev, *Irreducible representations of the space groups* (Gordon and Breach, Science Publishers, 1961).
- [261] A. S. Wills, *Phys. Rev. B*, **63**, 064430 (2001).
- [262] C. Bradley and A. Cracknell, *The mathematical theory of symmetry in solids* (Clarendon Press, Oxford, 1972).
- [263] A. S. Wills, *Physica B*, **276**, 680 (2000).
- [264] A. Yaouanc, P. Dalmas de Réotier, and E. Frey, *Phys. Rev. B*, **47**, 796 (1993).

# Abstract

This Phd thesis focuses on the study of magnetically frustrated compounds where magnetic ions lie at the vertices of a corner-sharing tetrahedra network: the pyrochlore compounds. The two series of chemical formula  $R_2M_2O_7$ , where  $R$  is a lanthanide and  $M = \text{Ti, Sn}$ , are of peculiar interest since they display a large variety of exotic magnetic ground states. First, we have studied the crystal-electric-field acting at the rare earth within the Stevens approximation where only the ground state multiplet is considered. A single set of parameters for each families of interest has been determined through a global analysis including several inelastic neutron scattering spectra of various compounds. Then, we have characterised with a large panel of techniques the low temperature physical properties of  $\text{Nd}_2\text{Sn}_2\text{O}_7$ . This compound enters a long-range magnetic order at transition temperature  $T_c = 0.91$  K with an “all-in-all-out” spin configuration. A persistence of spin dynamics has been found in the ordered phase, ascribed to one-dimensional spin loops excitations. Anomalously slow paramagnetic spin fluctuations are also reported. Finally, we have brought information on the two proposed ground states of the widely studied compound  $\text{Tb}_2\text{Ti}_2\text{O}_7$ : first, a Jahn-Teller transition is claimed to occur at low temperatures but no broadening of the Bragg peaks is seen down to  $T = 4$  K precluding premises of a structural transition. Secondly, this compound could be a realisation of a quantum spin-ice but no definitive evidence of a magnetisation plateau is found down to  $T = 20$  mK.

**Key words:** magnetism - geometrical frustration - pyrochlore - crystal-electric-field - spin dynamics - diffraction - inelastic neutron scattering - muon spin relaxation

# Résumé

Cette thèse se concentre sur l'étude de composés magnétiques géométriquement frustrés où les ions magnétiques se situent aux sommets d'un réseau de tétraèdres partageant leurs sommets: les composés pyrochlores. Deux familles de formule chimique  $R_2M_2O_7$ , où  $R$  est un lanthanide et  $M = \text{Ti, Sn}$ , sont particulièrement intéressantes puisqu'elles présentent une grande variété d'états magnétiques exotiques. Premièrement, nous avons étudié le champ cristallin agissant au site de la terre rare dans l'approximation de Stevens où uniquement le terme fondamental est considéré. Un jeu unique de paramètres a été déterminé pour chaque famille considérée grâce à une analyse globale incluant des spectres de neutrons inélastiques de plusieurs composés. Ensuite, nous avons caractérisé avec un large éventail de techniques les propriétés physiques à basse température de  $\text{Nd}_2\text{Sn}_2\text{O}_7$ . En dessous de la température de transition  $T_c = 0.91$  K, ce composé possède un ordre magnétique à longue portée dans la configuration de spins dite “all-in-all-out”. Une persistance de la dynamique de spins a été révélée dans la phase ordonnée, attribuée à des excitations unidimensionnelles de spins. Une dynamique de spins anormalement lente est également reportée dans la phase paramagnétique. Enfin, nous avons apporté quelques informations sur les deux états fondamentaux proposés pour le composé très étudié  $\text{Tb}_2\text{Ti}_2\text{O}_7$ : premièrement, l'apparition d'une transition Jahn-Teller à basse température est suggérée mais l'absence d'élargissement des pics de Bragg réfute la présence d'une transition structurale. Enfin ce composé pourrait être un exemple d'une glace de spin quantique mais l'existence d'un plateau d'aimantation n'est pas évident jusqu'à  $T = 20$  mK.

**Mots clefs:** magnétisme - frustration géométrique - pyrochlore - champ cristallin - dynamique de spins - diffraction - diffusion inélastique de neutrons - relaxation du spin du muon